

UNIVERSITY OF CRETE

PHD THESIS

**Strong transitions driven by stochastic
fields and open quantum systems'
dynamics**

Author:
G. Mouloudakis

Supervisor:
Prof. P. Lambropoulos
Dr. G. M. Nikolopoulos



*A thesis submitted in fulfillment of the requirements
for the degree of Doctor of Philosophy*

in the

Department of Physics
University of Crete

*Supported by the Hellenic Foundation for Research and Innovation (HFRI) under the 3rd
Call for HFRI PhD Fellowships (Fellowship Number: 5525).*



Abstract

This thesis explores aspects on two broad parts of the field of quantum system dynamics, namely, the strong interaction between matter and stochastically fluctuating radiation and the dynamics of open quantum systems. In the first topic, we investigate atomic transitions under strong driving using squeezed radiation, which is known to exhibit photon super-bunching properties and explore its effects on double optical resonance (DOR) in pump and probe setups. Additionally, we study the phenomenon of electron-positron pair creation in presence of stochastic radiation and explore the possibility of observing a non-linear enhancement of the process in the multi-photon regime due to photon correlation effects of the radiation. In the second topic, we analyze various aspects, including qubit correlations in non-Markovian environments, fidelity of quantum state transfer in the presence of non-Markovian dissipation, new methods of quantitatively evaluating non-Markovianity in open quantum systems, the relationship between the Quantum Zeno effect and exceptional points in non-Markovian open quantum systems, as well as the phenomenon of single-resonance autoionization viewed from the perspective of non-Hermitian physics. This thesis contributes to our understanding of strong driving effects and the dynamics of open quantum systems, shedding light on fundamental quantum phenomena and paving the way for future advancements in intriguing areas of active research.

Acknowledgements

I would like to express my deepest gratitude to the following individuals who have played a crucial role in the completion of my PhD thesis:

First and foremost I would like to thank Prof. Peter Lambropoulos for his invaluable support and insightful feedback throughout the entire shaping of my career as a researcher. The collaboration with Prof. Lambropoulos is a long-lasting collaboration that began back to the date I was an undergraduate student and has been pivotal for me since then. His expertise and mentorship have been really instrumental and enlightening all these years. I am honestly grateful to him, not only due to the innumerable theoretical tools I acquired under his supervision, but mostly due to the way he influenced my intuition and the process of my analytical thinking in physics. I would also like to thank Dr. Georgios M. Nikolopoulos for his insightful comments and vital help, as well as Prof. Iannis Kominis for his essential guidance and support during all these years. Furthermore, I would like to thank my colleagues, Theodoros Ilias and Ioannis Stergou, for our stimulating discussions and our successful collaborations, as well as Dimitrios Kaltsas for insights that helped me reshape some of my ideas and refine parts of my work presented in the final chapter of my thesis. Besides the interesting discussions I had with my colleagues, I would also like to acknowledge the endless enlightening discussions I had with my brother, Kostas Mouloudakis, regarding the subject of my thesis as well as its presentation. Last but not least, I would like to express my gratitude to my family and friends for their love as well as the psychological support they provided me all these years, without which the completion of my PhD thesis would not have been possible. For these reasons, I dedicate the thesis to them.

Contents

Abstract	v
Acknowledgements	vii
1 Introduction	1
I Strong transitions driven by stochastic fields	3
2 Theoretical Background	5
2.1 Quantum states of radiation	5
2.1.1 Coherent states	6
2.1.2 Chaotic states	8
2.1.3 Squeezed states	8
Squeezed vacuum states	9
Squeezed coherent states	11
2.2 Strong field phenomena	12
2.2.1 General Description	12
2.2.2 Double Optical Resonance	13
2.2.3 Electron-positron pair creation	15
2.3 Atomic transitions induced by stochastic radiation	17
2.3.1 General properties	17
2.3.2 Two-level system subject to stochastic radiation	18
Phase-Diffusion field	19
Chaotic field	20
3 Photon statistics effects in double optical resonance	25
3.1 Squeezed coherent states in single-photon double optical resonance . .	25
3.2 Multi-photon double optical resonance in presence of bunched and superbunched radiation	35
3.2.1 Two-photon transition strongly driven by chaotic and squeezed vacuum radiation: The absence of splitting	41
4 Photon statistics effects in multi-photon Schwinger pair production	47
4.1 Possibility of multi-photon enhancement under strong FEL radiation .	47
4.2 Conservation laws and the standing wave hypothesis	50
4.3 Multi-photon enhancement of vacuum e^-e^+ pair creation	51
II Open quantum systems' dynamics	59
5 Theoretical Background	61
5.1 Markovian and non-Markovian processes	61
5.1.1 General Description	61

5.1.2	The Nakajima-Zwanzig method	63
5.1.3	The time-convolutionless projection operator method	65
5.2	Elements of quantum information	66
5.2.1	Quantum entanglement	66
5.2.2	Quantum state transfer	68
5.3	The quantum Zeno effect	71
5.4	Single-qubit coupled to an external environment	74
5.5	Exceptional points in open quantum systems	76
6	Entanglement dynamics of two interacting qubits coupled with a common non-Markovian environment	81
6.1	Overview of the existing literature	81
6.2	Theoretical description of the system	82
6.3	Two-qubit entanglement dynamics and the phenomenon of entanglement "instability"	85
7	Arbitrary-length XX spin chains boundary-driven by non-Markovian environments	93
7.1	Introduction	93
7.2	Theoretical formulation	94
7.3	Dynamical and state transfer properties of XX spin chains boundary-driven by non-Markovian environments	98
7.3.1	Lorentzian environments	98
7.3.2	Ohmic environments	103
7.3.3	Comparing Lorentzian to Ohmic environments	106
8	Non-Markovianity in the time evolution of open quantum systems assessed by means of quantum state distance	111
8.1	General description of our methodology	111
8.2	Brief summary and necessary modifications of QSD measures	112
8.3	Theoretical formulation	115
8.3.1	Markovian system: construction of $\sigma(t)$	117
8.3.2	Non-Markovian system (construction of $\rho(t)$)	117
8.4	Quantitative evaluation of non-Markovianity for various non-Markovian reservoirs	119
8.4.1	Single qubit	120
8.4.2	Five mutually interacting qubits	122
9	Coalescence of non-Markovian dissipation, quantum Zeno effect, and non-Hermitian physics in a simple realistic quantum system	127
9.1	Introduction	127
9.2	Description of the system under consideration	129
9.3	Exceptional points and the onset of the quantum Zeno regime	131
9.3.1	Markovian environment	131
9.3.2	Lorentzian environment	137
9.3.3	Ohmic environment	139
10	The non-Hermitian landscape of autoionization	143
10.1	Brief introductory overview	143
10.2	Theoretical formulation	144
10.3	Exceptional points in single-resonance autoionization	146

A	Photon statistics enhancement of e^-e^+ pair production	151
B	Derivation of the functions $R(t)$ and $B(s)$ for special types of non-Markovian reservoirs	153
B.1	Lorentzian spectral density	153
B.2	Lorentzian squared spectral density	154
B.3	Ohmic spectral density	154
C	Derivation of the effective Hamiltonian $\hat{\mathcal{H}}_{\text{eff}}$	155

List of Figures

2.1	Semi-classical Autler-Townes splitting in " Λ -type" three-level system	15
2.2	Representation of Eq. (2.78) in terms of diagrams	22
3.1	Squeezed coherent states in single-photon DOR: Schematic representation of the system at study	27
3.2	Photon number distribution of a squeezed coherent state	30
3.3	Probe state population dynamics for various values of Δ_2 and probe state population as a function of Δ_2 in the case of coherent driving, for various values of $ \alpha ^2$	31
3.4	Probe state population as a function of Δ_2 in the case of SQCS driving for various values of r	32
3.5	Probe state population as a function of Δ_2 in the case of SQCS driving for extreme values of r (extreme squeezing), and probe state population as a function of Δ_2 in the case of SQVS driving	33
3.6	Probe state population as a function of Δ_2 for various values of Φ	34
3.7	Multi-photon DOR in presence of bunched and superbunched radiation: Schematic representation of the system at study	36
3.8	Single-photon Stark splitting for various types of radiation fields, modeled with Cesium parameters	40
3.9	Two-photon Stark splitting for various types of radiation fields, modeled with Lithium parameters	41
3.10	Probe state population under single-photon driving as a function of Δ_2 and n	42
3.11	Probe state population under two-photon driving as a function of Δ_2 and n	43
3.12	Photon probability distributions of the coherent, chaotic and squeezed vacuum radiation fields for mean photon number $\bar{n} = 20$	44
4.1	Ratio of the number of e^-e^+ pairs created by a field that results from the collision of two counter-propagating FEL beams that undergo Gaussian amplitude fluctuations over the number of e^-e^+ pairs created by a harmonically oscillating field of the form $\mathcal{E}\cos(\omega t)$, as a function of the intensity, for different values of N_0	54
4.2	Number of e^-e^+ pairs created by a field that results from the collision of two counter-propagating FEL beams that undergo Gaussian amplitude fluctuations, compared to the respective number of pairs created by a harmonically oscillating field of the form $\mathcal{E}\cos(\omega t)$, for minimum number of photons $N_0 = 10$ and interaction time $\tau = 50fs$	55
5.1	Schematic representation of a single-qubit coupled to an external environment	75

6.1	Schematic representation of two interacting qubits coupled to a common non-Markovian environment	83
6.2	Dynamics of the two-qubit concurrence for various initial two-qubit states. The two-qubits are assumed to be non-interacting ($\mathcal{J} = 0$). . . .	86
6.3	Steady state value of the two-qubit concurrence as a function of the qubit-environment couplings g_1 and g_2 , for various initial two-qubit states. The two-qubits are assumed to be non-interacting ($\mathcal{J} = 0$). . . .	87
6.4	Steady state value of the two-qubit concurrence as a function of the qubit-environment couplings g_1 and g_2 , for various initial two-qubit states. The two-qubits are assumed to be interacting with a coupling strength $\mathcal{J}/\gamma = 1$	88
6.5	Steady state value of the two-qubit concurrence as a function of the qubit-environment couplings g_1 and g_2 for the initial two-qubit state $ \Psi(0)\rangle_{12} = g\rangle_1 e\rangle_2$	89
6.6	Effects of the detuning Δ_c on the value of the two-qubit steady state concurrence	90
7.1	Schematic presentation of an arbitrary-length XX spin chain coupled to non-Markovian reservoirs at its boundaries.	95
7.2	Dynamics of the populations of the first qubit, N^{th} qubit and channel qubits of the XX chain as well as the long-time dynamics of the sum of all qubit populations.	99
7.3	Long-time dynamics of the qubit populations of the chain, as well as their sum, for spin chains of small length.	100
7.4	Long-time dynamics of the sum of all qubit populations in the spin chain and initial excitation in the central qubit of the chain	101
7.5	Dynamics of the average-state fidelity of state transfer between the two edges of the spin chain and maximum average fidelity as a function of the number of spin sites	102
7.6	Dynamics of the sum of all qubit populations in a XX chain boundary driven by reservoirs characterized by Ohmic spectral densities	104
7.7	Dynamics of the populations of the first qubit, N^{th} qubit and channel qubits of a XX chain boundary driven by reservoirs characterized by Ohmic spectral densities	105
7.8	Comparison between Lorentzian and Ohmic spectral densities and of the resulting dynamics of the sum of all qubit populations of a XX chain boundary-driven by reservoirs characterized by those two spectral densities.	107
8.1	Schematic representation of a XX spin chain coupled to a non-Markovian at its one end and schematic description of the evaluation of the degree of non-Markovianity of the system.	116
8.2	Dynamics of the excitation survival probability of a single qubit coupled to various types of reservoirs	120
8.3	QSD measures between the Markovian-damped and the non-Markovian-damped system using various types of non-Markovian reservoirs in the single-qubit case	121
8.4	Dynamics of the excitation survival probability of the first qubit of a chain consisting of $N = 5$ qubits	123

8.5	QSD measures between the Markovian-damped and the non-Markovian-damped system using various types of non-Markovian reservoirs for the case of $N = 5$ qubits	124
9.1	Schematic representation of the system at study. Two non-identical qubits are interacting with a coupling strength \mathcal{J} , while one of them is also coupled to an external environment E via a coupling g	130
9.2	Imaginary parts of the eigenvalues λ_3 and λ_4	134
9.3	Population of qubit 1 as a function of the time for various values of $\tilde{\gamma}$ and time dynamics of the effective decay Γ_{eff}	135
9.4	Effective decay rate and its derivative with respect to $\tilde{\gamma}$, as function of $\tilde{\gamma}$, for various qubit energy differences ε	136
9.5	Time dynamics of the effective decay rate, effective decay rate as function of g , and location of the exceptional point g_{EP} as a function of γ , for a Lorentzian boundary environment	138
9.6	Effective decay rate as function of g for various values of ε , derivative of the effective decay rate with respect to g , as a function g , for various values of ε , and location of the exceptional point as a function of ε , for a Lorentzian boundary environment	139
9.7	Effective decay rate as function of g for various Ohmic parameters S , effective decay rate as function of g for various cut-off frequencies ω_c , and effective decay rate as function of g for various energy differences ε between the two qubits, for Ohmic boundary environment	141
10.1	Schematic representation of single-resonance autoionization	145
10.2	Dependence of the exceptional points on the asymmetry parameter q	146
10.3	Real and imaginary parts of the eigenvalues λ_1 and λ_2 as a function of the parameters $\tilde{\Omega}$ and Δ	147
10.4	Ionization probability as a function of Δ for various interaction times T	147
10.5	Effective decay rate of the ground state as a function of $\tilde{\Omega}$ and Δ	148

Dedicated to my family and
friends

Chapter 1

Introduction

The field of quantum optics has transformed our understanding of light-matter interactions, providing important insights of the interplay between atoms and photons on the quantum level [1]. Over the years, significant steps have been made in utilizing the potential of quantum systems for various technological applications, ranging from quantum computing [2] to secure communication protocols [3]. One key aspect of quantum optics research lies in the investigation of transitions strongly driven by external radiation, which form the foundation of numerous strong-field quantum phenomena. Contrary to the case of weak driving, it has been well established that in the regime of high laser intensities, interesting non-linear effects come into play, substantially altering the response of the driven systems [4]. Although simple models involving monochromatic coherent radiation of zero bandwidth may capture the basic dynamics of the driven systems, more often than not, the available radiation sources used in experimental setups are subject to stochastic fluctuations in phase or/and intensity, that have been shown to leave a significant imprint on the response of the driven systems [5, 6]. These quantum stochastic properties of electromagnetic radiation, embodied in its correlation functions may arguably be viewed as the "trade mark" of quantum optics and have been a topic of ongoing research since the pioneering works of R. Glauber in 1963 [7, 8].

Notwithstanding the substantial progress in this field spanning nearly six decades, several fundamental questions pertaining to the interplay between matter and stochastic radiation have remained unexplored. This knowledge gap has been primarily attributed to the lack of access to the requisite intensities within experimental setups, as well as the inherent inability to precisely control the statistical properties of radiation sources employed in these investigations. However, the landscape has undergone a dramatic transformation in recent years with the advent of high-intensity, short-wavelength sources such as free electron lasers (FELs) [9], along with the development of methods enabling effective manipulation of the statistical properties of generated quantum states of light [10]. Among these generated states of radiation, a particular class has gathered significant theoretical and experimental attention due to its important applications in modern quantum technologies, i.e. the "squeezed" states of radiation [11], which lack any classical analog and, thus, demand description through a quantized field framework. In view of the above groundbreaking advancements, novel aspects of the strong interaction between matter and stochastic radiation have once again taken center stage, ultimately paving the way for achievements in the manipulation and effective control of quantum systems.

Along with the advent of strong field quantum optics in presence of stochastic radiation, a parallel field was gradually emerging as a cornerstone in the study of complex quantum phenomena, namely, the field of open quantum system dynamics [12]. In contrast to idealized closed systems, isolated from external influences, open quantum systems are inherently entangled with their surroundings, which are often

characterized by stochasticity, resulting in complex dynamics involving dissipation. The study of open quantum systems has gained significant attention due to its fundamental implications for a wide range of fields, including quantum information processing [13], condensed matter physics [14], quantum chemistry [15], and quantum biology [16]. Open systems dynamics plays a pivotal role in elucidating the processes of decoherence, relaxation, dissipation, and noise-induced effects, which are crucial in determining the stability, coherence, and performance of quantum systems [17].

In the field of quantum information processing, open quantum systems dynamics poses both challenges and opportunities. On the one hand, environmental interactions can induce detrimental effects such as information loss, reduced fidelity, and increased susceptibility to errors. On the other hand, effectively controlling open systems' dynamics can facilitate novel quantum error correction schemes [18], enable fault-tolerant quantum computing [19], and pave the way for resilient quantum communication protocols [20]. Over the past decades, a rich theoretical framework has been developed to describe the dynamics of open quantum systems. Techniques such as master equations, quantum trajectories, and non-Markovian dynamics methods have provided powerful tools to capture the interplay between the system of interest and its environment [21]. Furthermore, advances in experimental techniques and technologies have made it possible to probe, manipulate, and engineer open quantum systems, offering important tools for studying and exploiting their dynamics [22]. Despite remarkable progress, several key challenges and open questions remain in the field of open quantum systems dynamics. Understanding the interplay between coherent evolution and environmental interactions is a central focus. Exploring the role of non-Markovianity, memory effects, and system-environment correlations in shaping the dynamics of open systems presents an ongoing research frontier [23, 24]. Additionally, developing robust strategies for controlling and mitigating the detrimental effects of environmental noise on quantum systems is of great importance for advancing practical applications [25].

The role of this thesis is twofold as it covers and contributes to aspects in both fields of strong field quantum optics under stochastic radiation and open quantum system dynamics. As such, the thesis is organized in two main parts. In the first part we investigate the phenomenon of double optical resonance (DOR) using strong squeezed radiation that exhibits photon super-bunching properties and compare the resulting effects with the case of strong driving using radiation initially prepared in a coherent state. The phenomenon is investigated also under two-photon driving with fields of various photon statistics, revealing an intricate interplay between the stochastic character of radiation and the non-linear character of the process. In addition, we study the phenomenon of electron-positron pair creation in the multi-photon regime under the presence of stochastic radiation and explore the conditions of observing a non-linear enhancement of the process attributed to photon correlation effects of the radiation field. In the second part we investigate various systems consisting of single qubits or chains of interacting qubits that are coupled to non-Markovian reservoirs and explore aspects such as qubit correlations, fidelity of quantum state transfer, exceptional points, the Quantum Zeno effect, the evaluation of non-Markovianity as well as several other facets of open quantum system dynamics. Finally, we explore the phenomenon of single-resonance autoionization viewed from the perspective of non-Hermitian physics, showing novel effects and opening up an interesting and fruitful territory for further exploration.

Part I

Strong transitions driven by stochastic fields

Chapter 2

Theoretical Background

2.1 Quantum states of radiation

The study of quantum states of radiation lies at the intersection of quantum mechanics and electromagnetism, and provides insights on the fundamental nature of light and its interactions with matter. Contrary to classical physics that describes light as a continuous wave, in quantum theory the light is described in terms of excitations of the electromagnetic field, called photons, that exhibit both wave-like and particle-like properties, and their behavior is described by quantum states. Quantum states of radiation are characterized by their wave function, which describes the probability distribution of finding a photon in a particular state. In quantum optics, the most commonly used formalism is the so-called "second quantization" formalism, which treats the electromagnetic field as an ensemble of harmonic oscillators [26]. The central concept behind "second quantization" is that the electric field can be expressed as a sum of individual modes, each associated with a specific frequency and direction of polarization.

The quantum states of radiation most often are expressed in terms of Fock states or number states, which correspond to different numbers of photons occupying a particular mode of the electromagnetic field. Those states are usually denoted as $|n\rangle$ and obey the relation

$$\hat{\mathcal{N}} |n\rangle = n |n\rangle, \quad (2.1)$$

where $\hat{\mathcal{N}}$ is the photon number operator and n is the number of photons. Fock states are orthogonal to each other, and they are widely used in quantum optics, since every quantum state of radiation can be expressed as a superposition of the former.

One important concept in quantum optics is the creation and annihilation operators, \hat{a}^\dagger and \hat{a} , respectively. These operators act on the quantum states and change the number of photons present in a particular mode. The creation operator adds a photon to the mode, while the annihilation operator removes a photon, as reflected by the following equations:

$$\hat{a}^\dagger |n\rangle = \sqrt{n+1} |n+1\rangle, \quad (2.2a)$$

$$\hat{a} |n\rangle = \sqrt{n} |n-1\rangle. \quad (2.2b)$$

The creation and annihilation operators are non-Hermitian with \hat{a}^\dagger being the Hermitian adjoint of \hat{a} , and they follow the bosonic commutation relation

$$[\hat{a}, \hat{a}^\dagger] = 1. \quad (2.3)$$

The photon number operator $\hat{\mathcal{N}}$ is expressed in terms of \hat{a} and \hat{a}^\dagger as $\hat{\mathcal{N}} = \hat{a}^\dagger \hat{a}$.

Quantum states of radiation can also be entangled, a phenomenon that arises from the inherent correlations between different modes of the electromagnetic field [27]. Entanglement allows for a variety of non-classical effects such as quantum teleportation [28], quantum cryptography [3], quantum computing [2], etc. Overall, the study of different quantum states of radiation is important as it provides the necessary framework for understanding the behavior of light and its interactions with matter in its various forms. In what follows, we review the properties of three main quantum states of radiation that we encounter in most experimental as well as theoretical works.

2.1.1 Coherent states

The concept of coherent states originated from the pioneering works of Roy J. Glauber in the 1960s where he introduced these states as the quantum counterparts of classical states of light [7, 8]. Coherent states exhibit unique properties that make them particularly useful for describing the dynamics of light fields and their interactions with matter, especially in fields like laser theory. They possess several desirable features, including a well-defined phase, a minimum uncertainty product, and the ability to exhibit interference phenomena similar to classical waves.

Formally, coherent states are eigenstates of the annihilation operator. If we denote by $|\alpha\rangle$ such a state, with $\alpha \in \mathbb{C}$ being its eigenvalue, then by definition we have:

$$\hat{a} |\alpha\rangle = \alpha |\alpha\rangle. \quad (2.4)$$

Coherent states can always be expressed in terms of Fock states via the relation

$$|\alpha\rangle = \sum_{n=0}^{\infty} \langle n|\alpha\rangle |n\rangle. \quad (2.5)$$

The coefficients $\langle n|\alpha\rangle$ of this decomposition can be calculated using the definition (2.4), i.e.

$$\langle n|\hat{a}|\alpha\rangle = \alpha \langle n|\alpha\rangle, \quad (2.6)$$

and since

$$\langle n|\hat{a}|\alpha\rangle = \langle \alpha|\hat{a}^\dagger|n\rangle^* = \sqrt{n+1} \langle \alpha|n+1\rangle^* = \sqrt{n+1} \langle n+1|\alpha\rangle, \quad (2.7)$$

we find that

$$\langle n+1|\alpha\rangle = \frac{\alpha}{\sqrt{n+1}} \langle n|\alpha\rangle, \quad (2.8)$$

via which, by mathematical induction, we obtain

$$\langle n|\alpha\rangle = \frac{\alpha^n}{\sqrt{n!}} \langle 0|\alpha\rangle. \quad (2.9)$$

Substituting back to Eq. (2.5), we get

$$|\alpha\rangle = \langle 0|\alpha\rangle \sum_{n=0}^{\infty} \frac{\alpha^n}{\sqrt{n!}} |n\rangle, \quad (2.10)$$

where the multiplicative constant $\langle 0|\alpha\rangle$ can be calculated by requiring $|\alpha\rangle$ to be normalized, i.e.

$$\langle \alpha|\alpha\rangle = |\langle 0|\alpha\rangle|^2 \sum_{n=0}^{\infty} \frac{|\alpha|^{2n}}{n!} = |\langle 0|\alpha\rangle|^2 e^{|\alpha|^2} = 1, \quad (2.11)$$

through which we find that $\langle 0|\alpha\rangle = e^{i\theta} e^{-\frac{1}{2}|\alpha|^2}$, where θ is a real number representing the phase of the state vector. Therefore, $|\alpha\rangle$ is expressed in terms of Fock states as:

$$|\alpha\rangle = e^{-\frac{1}{2}|\alpha|^2} \sum_{n=0}^{\infty} \frac{\alpha^n}{\sqrt{n!}} |n\rangle. \quad (2.12)$$

Formally, coherent states can be also generated by the action of the so-called displacement operator $\hat{D}(\alpha) \equiv e^{-\frac{1}{2}|\alpha|^2} e^{\alpha\hat{a}^\dagger - \alpha^*\hat{a}}$ on the lowest (ground) energy state of the harmonic oscillator, $|0\rangle$, since

$$|\alpha\rangle = e^{-\frac{1}{2}|\alpha|^2} \sum_{n=0}^{\infty} \frac{\alpha^n}{\sqrt{n!}} |n\rangle = e^{-\frac{1}{2}|\alpha|^2} \sum_{n=0}^{\infty} \frac{(\alpha\hat{a}^\dagger)^n}{n!} |0\rangle = e^{-\frac{1}{2}|\alpha|^2} e^{\alpha\hat{a}^\dagger} |0\rangle = \hat{D}(\alpha) |0\rangle, \quad (2.13)$$

where we used the fact that $\hat{a}|0\rangle = |0\rangle$ and therefore $e^{-\alpha^*\hat{a}}|0\rangle = |0\rangle$. Note that the displacement operator can be written in three equivalent forms, i.e. $\hat{D}(\alpha) = e^{\alpha\hat{a}^\dagger - \alpha^*\hat{a}} = e^{-\frac{1}{2}|\alpha|^2} e^{\alpha\hat{a}^\dagger - \alpha^*\hat{a}} = e^{\frac{1}{2}|\alpha|^2} e^{-\alpha^*\hat{a} + \alpha\hat{a}^\dagger}$, in which the creation and annihilation operators appear in what is called symmetric, normal and anti-normal order, respectively.

Using the expansion of a coherent state in terms of Fock states, we can calculate the probability to find n photons in the field as:

$$P_\alpha(n) = \langle \alpha | \hat{\Pi}_n | \alpha \rangle = e^{-|\alpha|^2} \frac{|\alpha|^{2n}}{n!}, \quad (2.14)$$

where $\hat{\Pi}_n$ is a projection operator defined as $\hat{\Pi}_n \equiv |n\rangle \langle n|$. As becomes evident the probability follows a Poissonian distribution with average photon number $\bar{n} = \sum n P_\alpha(n) = |\alpha|^2$ and root mean square deviation

$$\Delta\mathcal{N} = \sqrt{\langle \alpha | \hat{a}^\dagger \hat{a} \hat{a}^\dagger \hat{a} | \alpha \rangle - \langle \alpha | \hat{a}^\dagger \hat{a} | \alpha \rangle^2} = \sqrt{\bar{n}} = |\alpha|. \quad (2.15)$$

Contrary to Fock states, coherent states are non-orthogonal to each other. It is straightforward to prove this by considering the scalar product of two coherent states $|\alpha\rangle$ and $|\beta\rangle$,

$$\langle \alpha | \beta \rangle = e^{-\frac{1}{2}(|\alpha|^2 + |\beta|^2)} \sum_{n=0}^{\infty} \frac{(\alpha^*)^n \beta^n}{n!} = \exp \left[\alpha^* \beta - \frac{1}{2}(|\alpha|^2 + |\beta|^2) \right], \quad (2.16)$$

from which we have that

$$|\langle \alpha | \beta \rangle|^2 = e^{-|\alpha - \beta|^2}. \quad (2.17)$$

Since $|\alpha - \beta|^2$ is never zero for $\alpha \neq \beta$, coherent states are always non-orthogonal to each other and in that sense, each coherent state "contains" all of the others. Despite the fact that the set of coherent states is non-orthogonal and overcomplete, it is a continuous, normalized set that can be used as a basis, and has been proven to be extremely useful in calculating correlation functions that involve the photon creation and annihilation operators when used as such [7, 8].

2.1.2 Chaotic states

Chaotic states of radiation, also known as thermal states, play a fundamental role in the study of quantum systems. These states are characterized by their high degree of disorder and randomness, reflecting the behavior of an ensemble of particles or a large number of quantum modes at thermal equilibrium. In a thermal state the majority of particles or modes are populating the lower energy levels, while a smaller fraction occupies higher ones. The chaotic nature of thermal states arises due to the inherent fluctuations in the occupation of energy levels, resulting in fluctuations in the emitted or absorbed radiation. Thermal radiation, often referred as black body radiation, was studied extensively by Max Planck at the beginning of twentieth century marking the birth of quantum theory [29].

A chaotic field is by definition in thermal equilibrium with the surrounding environment at a finite temperature, which we denote by T . Therefore, its state is necessarily describable in terms of a density operator, which acquires the form:

$$\rho_{Th} = \frac{\exp(-\hat{\mathcal{H}}/k_B T)}{\text{Tr} [\exp(-\hat{\mathcal{H}}/k_B T)]}, \quad (2.18)$$

where $\hat{\mathcal{H}}$ is the system Hamiltonian operator and k_B is Boltzmann's constant. For a single-mode of frequency ω , Eq. (2.18) becomes:

$$\rho_{Th} = \frac{\exp(-\hbar\omega\hat{a}^\dagger\hat{a}/k_B T)}{\text{Tr} [\exp(-\hbar\omega\hat{a}^\dagger\hat{a}/k_B T)]}. \quad (2.19)$$

The probability to find n photons in the field is

$$P_{Th}(n) = \text{Tr}(\rho\hat{\Gamma}_n) = \frac{e^{-\hbar\omega n/k_B T}}{\sum_n e^{-\hbar\omega n/k_B T}} = e^{-\hbar\omega n/k_B T} (1 - e^{-\hbar\omega/k_B T}), \quad (2.20)$$

which can also be written in the form

$$P_{Th}(n) = \frac{1}{1 + \bar{n}} \left(\frac{\bar{n}}{1 + \bar{n}} \right)^n = \frac{\bar{n}^n}{(1 + \bar{n})^{n+1}}, \quad (2.21)$$

since the mean photon number \bar{n} is expressed as

$$\bar{n} = \sum_n n P_{Th}(n) = \frac{1}{e^{\hbar\omega/k_B T} - 1}. \quad (2.22)$$

The root mean square deviation of the photon number is given by

$$\Delta\mathcal{N} = \sqrt{\langle\hat{\mathcal{N}}^2\rangle - \langle\hat{\mathcal{N}}\rangle^2} = \sqrt{\bar{n}^2 + \bar{n}}, \quad (2.23)$$

which can be approximated by $\Delta\mathcal{N} \approx \bar{n}$ in the limit of high mean photon numbers $\bar{n} \gg 1$.

2.1.3 Squeezed states

Squeezed states of radiation are quantum states that exhibit reduced quantum uncertainty in one of two physical observables characterized by non-commutative operators, such as amplitude or phase, at the expense of increased uncertainty in the

conjugate property [11]. This phenomenon is a consequence of the Heisenberg uncertainty principle, which states that certain pairs of physical properties (like position and momentum, or amplitude and phase) cannot be simultaneously measured with arbitrary precision. The phenomenon of squeezing was first predicted in the second half of twentieth century and is linked to the presence of quantum fluctuations [30] in the field. Quantum fluctuations are inherent to any quantum system and arise due to the uncertainty principle. In the case of squeezed states, the fluctuations are manipulated such that they become non-uniform, resulting in squeezing along a specific property [31].

The squeezed states of radiation find applications across a broad spectrum of different fields, ranging from quantum optics and quantum information science to gravitational wave detection [32–34]. These states possess remarkable features that make them particularly appealing for various technological advancements. For instance, they can be utilized in high-precision interferometry to enhance the measurement accuracy beyond the classical limit imposed by shot noise [35]. or used for their applications in quantum communication, quantum computing, and quantum metrology [36].

Squeezed states of radiation field are generated in non-linear processes in which an electromagnetic field drives a non-linear medium [37]. In such a medium, pairs of correlated photons of the same frequency are generated. In the interaction picture, this process can be described by the effective Hamiltonian [38, 39]

$$\hat{H} = \varepsilon(\hat{a}^\dagger)^2 + \varepsilon^* \hat{a}^2. \quad (2.24)$$

This Hamiltonian describes how a pump field is down-converted to its sub-harmonics at half the driving frequency, with the parameter ε containing the amplitude of the driving field and the second-order susceptibility for the down-conversion. Since the total Hamiltonian is time-independent, the time evolution operator (also called squeeze operator) is

$$\hat{U}(t) = \exp\left(-\frac{i\hat{H}t}{\hbar}\right) = \exp\left(\frac{\zeta}{2}(\hat{a}^\dagger)^2 - \frac{\zeta^*}{2}\hat{a}^2\right) \equiv \hat{S}(\zeta), \quad (2.25)$$

where $\zeta = -\frac{i\varepsilon t}{\hbar}$ is the so-called squeezing parameter, which can also be written as $\zeta = re^{i\theta}$, and the factor of $\frac{1}{2}$ was introduced for reasons of mathematical convenience. The squeezing parameter characterizes the degree of squeezing and depends on the amplitude of the driving field and the interaction time, i.e. the time that takes for light to travel via the non-linear medium.

Squeezed vacuum states

The action of the squeeze operator on the vacuum state $|0\rangle$, results to the so-called squeezed vacuum state denoted by

$$|\zeta\rangle \equiv \hat{S}(\zeta)|0\rangle. \quad (2.26)$$

In order to obtain the photon number probability distribution of the squeezed vacuum state [38, 39], we decompose $|\zeta\rangle$ in the Fock basis,

$$|\zeta\rangle = \sum_{n=0}^{\infty} C_n |n\rangle, \quad (2.27)$$

and seek an expression for the relevant coefficients. Starting with the vacuum state, which satisfies the relation

$$\hat{a} |0\rangle = 0, \quad (2.28)$$

we multiply by $\hat{S}(\zeta)$ from the left and use the fact that $\hat{S}(\zeta)$ is unitary, to obtain

$$\hat{S}(\zeta)\hat{a}\hat{S}^\dagger(\zeta)\hat{S}(\zeta)|0\rangle = 0 \Leftrightarrow \hat{S}(\zeta)\hat{a}\hat{S}^\dagger(\zeta)|\zeta\rangle = 0. \quad (2.29)$$

Using the definition of ζ we find that

$$\hat{S}(\zeta)\hat{a}\hat{S}^\dagger(\zeta) = \hat{a} \cosh r + e^{i\theta}\hat{a}^\dagger \sinh r. \quad (2.30)$$

In view of Eq. (2.29), Eq. (2.30) becomes:

$$(\hat{a} \cosh r + \hat{a}^\dagger e^{i\theta} \sinh r) |\zeta\rangle = 0. \quad (2.31)$$

By substituting Eq. (2.27) in Eq. (2.31), we obtain a relation for the coefficients C_n :

$$C_{n+1} = -e^{i\theta} \tanh r \left(\frac{n}{n+1} \right)^{1/2} C_{n-1}, \quad (2.32)$$

which can be solved recursively, yielding:

$$C_{2n} = (-1)^n (e^{i\theta} \tanh r)^n \left[\frac{(2n-1)!!}{(2n)!!} \right]^{1/2} C_0. \quad (2.33)$$

If we demand from C_{2n} to satisfy the normalization condition $\sum_{n=0}^{\infty} |C_{2n}|^2 = 1$, we obtain

$$|C_0|^2 \left(1 + \sum_{n=0}^{\infty} \frac{[\tanh r]^{2n} (2n-1)!!}{(2n)!!} \right) = 1, \quad (2.34)$$

which takes the simple form $C_0 = \sqrt{\cosh r}$, using the identity

$$1 + \sum_{n=0}^{\infty} z^n \left(\frac{(2n-1)!!}{(2n)!!} \right) = (1-z)^{-1/2}. \quad (2.35)$$

Finally, in view of the following two identities

$$(2n)!! = 2^n n!, \quad (2.36)$$

$$(2n-1)!! = \frac{1}{2^n} \frac{(2n)!}{n!}, \quad (2.37)$$

one obtains the final expression for the coefficients

$$C_{2n} = (-1)^n \frac{\sqrt{(2n)!}}{2^n n!} \frac{(e^{i\theta} \tanh r)^n}{\sqrt{\cosh r}}. \quad (2.38)$$

Substitution of Eq. (2.38) back to Eq. (2.27), gives the decomposition of the squeezed vacuum state in the Fock basis:

$$|\zeta\rangle = \frac{1}{\sqrt{\cosh r}} \sum_{n=0}^{\infty} (-1)^n \frac{\sqrt{(2n)!}}{2^n n!} e^{in\theta} (\tanh r)^n |2n\rangle. \quad (2.39)$$

The probability of detecting $2n$ photons in the field is

$$P_{2n} = |\langle 2n | \zeta \rangle|^2 = \frac{(2n)!}{2^{2n}(n!)^2} \frac{(\tanh r)^{2n}}{\cosh r}, \quad (2.40)$$

while the probability of detecting $2n + 1$ photons is

$$P_{2n+1} = |\langle 2n + 1 | \zeta \rangle|^2 = 0. \quad (2.41)$$

Equations (2.40) and (2.41) indicate that the photon probability distribution of a squeezed vacuum state is oscillatory, with the probability for all odd photon numbers to be zero. The probability can also be expressed in terms of the mean photon number $\bar{n} = \sum_{n=0}^{\infty} P_{2n}(2n) = \sinh^2 r$, as:

$$P_{2n} = \frac{1}{\sqrt{1 + \bar{n}}} \frac{(2n)!}{(n!)^2 2^{2n}} \left(\frac{\bar{n}}{1 + \bar{n}} \right)^n. \quad (2.42)$$

Squeezed coherent states

A squeezed coherent state (SQCS) is defined as the state resulting upon acting on the vacuum state with the squeeze operator $\hat{S}(\zeta)$ followed by the displacement operator $\hat{D}(\alpha)$, i.e.

$$|SQCS\rangle \equiv \hat{D}(\alpha) \hat{S}(\zeta) |0\rangle. \quad (2.43)$$

The squeeze and displacement operators are given by the relations $\hat{S}(\zeta) = \exp \left[\frac{\zeta}{2} \hat{a}^{\dagger 2} - \frac{\zeta^*}{2} \hat{a}^2 \right]$ and $\hat{D}(\alpha) = \exp (\alpha \hat{a}^{\dagger} - \alpha^* \hat{a})$, respectively, where $\zeta = r e^{i\theta}$ is the complex squeezing parameter and $\alpha = |\alpha| e^{i\phi}$ is the complex displacement parameter. In terms of the above parameters, the normally-ordered form of the density operator of a SQCS can be expressed as [40]:

$$\rho_{SQCS} = \frac{1}{\cosh r} \exp \left\{ \frac{1}{2} \tanh r \left[e^{-i\theta} (\hat{a} - \alpha)^2 + e^{i\theta} (\hat{a}^{\dagger} - \alpha^*)^2 \right] - (\hat{a}^{\dagger} - \alpha^*) (\hat{a} - \alpha) \right\}. \quad (2.44)$$

The probability of finding n photons in the field is:

$$P_{SQCS}(n) = \text{Tr}(\rho_{SQCS} \hat{\Pi}_n) = \text{Tr}(\rho_{SQCS} |n\rangle \langle n|). \quad (2.45)$$

Using the relation $|n\rangle = (n!)^{-1/2} \frac{d^n}{dz^n} |z\rangle \Big|_{z=0}$, where $|z\rangle$ is the un-normalized coherent state $|z\rangle = \exp(z \hat{a}^{\dagger}) |0\rangle$, that satisfies $\langle z_2 | z_1 \rangle = \exp(z_1 z_2^*)$, we find that

$$\begin{aligned} P_{SQCS}(n) &= \frac{1}{n!} \frac{d^n}{dz_2^{*n}} \frac{d^n}{dz_1^n} \langle z_2 | \rho_{SQCS} | z_1 \rangle_{z_1=z_2=0} \\ &= \frac{\exp(B)}{n! \cosh r} \frac{d^n}{dz_2^{*n}} \frac{d^n}{dz_1^n} \exp \left[A z_1 + A^* z_2^* + \frac{\tanh r}{2} \left(e^{-i\theta} z_1^2 + e^{i\theta} z_2^{*2} \right) \right]_{z_1=z_2=0} \\ &= \frac{\tanh^n r \exp(B)}{2^n n! \cosh r} \left| H_n \left(\frac{i A e^{i\theta/2}}{\sqrt{2 \tanh r}} \right) \right|^2, \end{aligned} \quad (2.46)$$

where

$$A \equiv \alpha^* - \tanh r e^{-i\theta} \alpha, \quad (2.47a)$$

$$B \equiv \frac{\tanh r}{2} \left(e^{-i\theta} \alpha^2 + e^{i\theta} \alpha^{*2} \right) - |\alpha|^2, \quad (2.47b)$$

and by $H_n(x)$ we denote the n^{th} -degree Hermite polynomial. Using the following generating function of Hermite polynomials,

$$H_n(x) = \frac{\partial^n}{\partial t^n} \exp[2xt - t^2]_{t=0}, \quad (2.48)$$

the SQCS photon probability distribution can be expressed as

$$P_{\text{SQCS}}(n) = \frac{(\tanh r)^n}{2^n n! \cosh r} \exp \left[\frac{\tanh r}{2} \left(e^{-i\theta} \alpha^2 + e^{i\theta} \alpha^{*2} \right) - |\alpha|^2 \right] \times \left| H_n \left(\frac{e^{i\theta/2} \alpha^* - e^{-i\theta/2} \alpha \tanh r}{-i\sqrt{2} \tanh r} \right) \right|^2. \quad (2.49)$$

By substituting $\alpha = |\alpha|e^{i\phi}$ in Eq. (2.49) and adopting the definition $\Phi \equiv \phi - \theta/2$, one finally gets:

$$P_{\text{SQCS}}(n) = \frac{(\tanh r)^n}{2^n n! \cosh r} \exp \left[|\alpha|^2 \cos(2\Phi) \tanh r - |\alpha|^2 \right] \left| H_n \left(\frac{|\alpha|e^{-i\Phi} - |\alpha|e^{i\Phi} \tanh r}{-i\sqrt{2} \tanh r} \right) \right|^2. \quad (2.50)$$

The mean photon number of the distribution is given by

$$\bar{n} = |\alpha|^2 + (\sinh r)^2, \quad (2.51)$$

which is independent of Φ , while the photon number variance is given by

$$(\Delta n)^2 = |\alpha|^2 [e^{2r} \cos^2 \Phi + e^{-2r} \sin^2 \Phi] + 2(\sinh r \cosh r)^2. \quad (2.52)$$

2.2 Strong field phenomena

2.2.1 General Description

Quantum optics has witnessed remarkable advancements in recent years. The advent of intense laser sources, opened up the field of strong field physics, where the interaction between light and matter becomes inherently non-linear [41] and paved the way for important applications in the fields of attosecond science [42], precision spectroscopy [43], and quantum information processing [13].

In the regime of strong field interactions, the electric field of an intense laser pulse can induce significant modifications in the behavior of atoms, molecules, and condensed matter systems. The electric field strengths involved are typically on the order of the atomic field strength, where the ponderomotive potential dominates over other energy scales. Consequently, the dynamics of electrons and the associated quantum states are dramatically altered, leading to unique phenomena that are absent in the weak field regime [44].

One of the most known effects in strong field quantum optics is high-order harmonic generation (HHG) [45]. HHG refers to the process where atoms or molecules exposed to intense laser fields emit high-energy photons that are harmonics of the driving laser frequency [46]. This phenomenon left important impact on the field of ultra-fast dynamics, as it enabled the generation of coherent bursts of extreme ultraviolet (XUV) and soft X-ray radiation with attosecond durations [47]. The ability

to manipulate and control these attosecond pulses has opened up new possibilities for investigating electronic dynamics on their natural timescales, probing electronic structure, and initiating a wide range of time-resolved experiments [48].

Another captivating aspect of strong field phenomena is the exploration of strong-field ionization (SFI) [49]. When subjected to intense laser fields, atoms and molecules can be ionized, leading to the creation of free electrons. The ionization process in strong fields exhibits intriguing characteristics such as above-threshold ionization [50], tunnel ionization [51], and the generation of electron wave packets with complex quantum interference patterns [52]. Understanding these ionization mechanisms is crucial for various applications, including the development of advanced imaging techniques [53], the manipulation of chemical reactions [54], and the exploration of attosecond dynamics in complex molecular systems [55].

With the advent of novel light sources, as well as of new theoretical models describing the intricate interplay between light and matter in the regime of high intensities, the list of strong field phenomena is constantly growing. Besides, HHG and SFI, another two very popular phenomena in the world of strong fields are the double optical resonance (DOR) in atomic physics and the electron-positron pair creation in high-energy physics. To what follows, we review each of them in more detail, since a basic theoretical understanding of these phenomena is necessary for the following chapters of the thesis.

2.2.2 Double Optical Resonance

Double resonance refers to a strong field phenomenon observed in pump and probe setups, and it is essentially based on the phenomenon of AC Stark splitting [56]. The term optical is often used since the systems of investigation are usually atoms that emit or absorb photons whose frequencies lie in the optical range.

The pump and probe experimental setups typically involves two synchronized laser pulses: the pump pulse and the probe pulse [57]. The pump pulse is the initial pulse that excites the sample under investigation, inducing a change in its physical properties or electronic structure. This excitation leads to the formation of transient states or non-equilibrium conditions within the system. Subsequently, the probe pulse, delayed by a controlled time interval, interacts with the excited sample and measures the resulting changes in its properties, such as absorption, reflectivity, or emission. By varying the time delay between the pump and probe pulses, a temporal evolution of the sample's response can be recorded. Pump-probe experiments enable the investigation of fundamental processes such as energy relaxation [58], charge transfer [59], molecular dynamics [60], and phase transitions [61], shedding light on the underlying mechanisms governing the behavior of complex systems.

If the pump pulse is sufficiently strong, it induces an AC Stark effect in the system. AC Stark splitting, also known as the Autler-Townes effect, refers to the modification of energy levels in a quantum system induced by the presence of an oscillating electric field [62]. When atoms or molecules interact with a strong laser field, the energy levels that were once discrete become modified, leading to the emergence of new energy states. This effect arises due to the interaction between the electric field of the laser and the charge distribution within the atom or molecule. The AC Stark effect is an important consequence of the interaction between light and matter, and it is closely related to the more well-known phenomenon of the Stark effect, which describes the energy level shifts induced by static electric fields [63]. While the Stark effect is observed in the presence of a steady electric field, the AC Stark effect arises when the electric field is oscillating in time. One of the features of AC Stark splitting

is the possibility of creating "avoided level crossings" in the energy level diagram of a quantum system [64]. These avoided crossings occur when two or more energy levels come close to each other but do not actually cross due to the influence of the laser field. As a result, new dressed states are formed, which are superpositions of the original energy states. This effect is the basis of several phenomena and is utilized for manipulating quantum systems in the atomic level [65].

Considering a two-level system driven by a radiation field of strong intensity, the splitting of the atomic states involved in the process can be probed either by the observation of the spectrum of spontaneous emission from the upper state or through a pump probe arrangement, as described above. In the second case we have the phenomenon of DOR, in which the splitting is probed through a second weak-field transition to a third level. To formulate the phenomenon of DOR, we consider a three-level system in a " Λ -type" configuration, that consists of a ground state, an excited state as well as a third state that acts as a probe, denoted by $|g\rangle$, $|e\rangle$ and $|p\rangle$, respectively. The ground state is by definition stable while $|p\rangle$ is considered to be meta-stable, i.e. it is characterized by a long lifetime. A schematic representation of the system is depicted in Fig. 2.1(a). The Hamiltonian of the system is [26]

$$\hat{\mathcal{H}} = \hat{\mathcal{H}}_A + \hat{\mathcal{V}}, \quad (2.53)$$

where $\hat{\mathcal{H}}_A$ is the atomic Hamiltonian given by

$$\hat{\mathcal{H}}_A = \hbar\omega_g\hat{\sigma}_{gg} + \hbar\omega_e\hat{\sigma}_{ee} + \hbar\omega_p\hat{\sigma}_{pp}, \quad (2.54)$$

with $\hat{\sigma}_{ii} \equiv |i\rangle\langle i|$, ($i = g, e, p$), while $\hat{\mathcal{V}}$ is the atom-field interaction Hamiltonian given by

$$\hat{\mathcal{V}} = -\vec{\rho} \cdot [\vec{E}_1(t) + \vec{E}_2(t)], \quad (2.55)$$

with $\vec{E}_j(t) = \hat{e}_j E_j(t)$ and $E_j(t) = \mathcal{E}_j e^{-i\omega_j t} + c.c.$, ($j = 1, 2$). E_1 is assumed to be the electric field with polarization \hat{e}_1 and frequency ω_1 that drives the $|g\rangle \longleftrightarrow |e\rangle$ transition, while E_2 is assumed to be the electric field with polarization \hat{e}_2 and frequency ω_2 that drives the $|e\rangle \longleftrightarrow |p\rangle$ transition. $\vec{\rho}$ is assumed to be the dipole moment operator of the atom. The state of the system at any time can be written as:

$$|\Psi(t)\rangle = c_g(t) |g\rangle + c_e(t) |e\rangle + c_p(t) |p\rangle, \quad (2.56)$$

where $c_i(t)$ is the time-dependent amplitude of state $|i\rangle$, ($i = g, e, p$). In view of the above relations, the time-dependent Schrödinger equation $i\hbar \frac{\partial}{\partial t} |\Psi(t)\rangle = \hat{\mathcal{H}} |\Psi(t)\rangle$ within the rotating wave approximation (RWA) leads to the following set of equations:

$$\frac{\partial}{\partial t} c_g(t) = -i\omega_g c_g(t) + ic_e(t) \Omega_1 e^{i\omega_1 t}, \quad (2.57a)$$

$$\frac{\partial}{\partial t} c_e(t) = -i\omega_e c_e(t) + ic_g(t) \Omega_1 e^{-i\omega_1 t} + ic_p(t) \Omega_2 e^{-i\omega_2 t}, \quad (2.57b)$$

$$\frac{\partial}{\partial t} c_p(t) = -i\omega_p c_p(t) + ic_e(t) \Omega_2 e^{i\omega_2 t}, \quad (2.57c)$$

where $\Omega_1 \equiv \wp_{ge} \mathcal{E}_1 / \hbar$ and $\Omega_2 \equiv \wp_{ep} \mathcal{E}_2 / \hbar$ are the Rabi frequencies of the $|g\rangle \longleftrightarrow |e\rangle$ and $|e\rangle \longleftrightarrow |p\rangle$ transitions respectively, and $\wp_{\mu\nu} \equiv \langle \mu | \vec{\rho} \cdot \hat{e}_j | \nu \rangle$ is the dipole matrix element of the corresponding $|\mu\rangle \longleftrightarrow |\nu\rangle$ transition with $\mu, \nu \in \{g, e, p\}$ and $\mu \neq \nu$. Note that $\wp_{\mu\nu} \mathcal{E}_j$ is assumed to be real without loss of generality. The set of Eqs. (2.57) can be simplified by introducing the transformations $c_g(t) = \tilde{c}_g(t) e^{-i\omega_g t}$,

$c_e(t) = \tilde{c}_e(t)e^{-i(\omega_g+\omega_1)t}$ and $c_p(t) = \tilde{c}_p(t)e^{-i(\omega_g+\omega_1-\omega_2)t}$, in view of which we obtain:

$$\frac{\partial}{\partial t}\tilde{c}_g(t) = i\Omega_1\tilde{c}_e(t), \quad (2.58a)$$

$$\frac{\partial}{\partial t}\tilde{c}_e(t) = i\Delta_1\tilde{c}_e(t) + i\Omega_1\tilde{c}_g(t) + i\Omega_2\tilde{c}_p(t), \quad (2.58b)$$

$$\frac{\partial}{\partial t}\tilde{c}_p(t) = i(\Delta_1 - \Delta_2)\tilde{c}_p(t) + i\Omega_2\tilde{c}_e(t), \quad (2.58c)$$

where $\Delta_1 \equiv \omega_1 - \omega_{eg} \equiv \omega_1 - (\omega_e - \omega_g)$ and $\Delta_2 \equiv \omega_2 - \omega_{ep} \equiv \omega_2 - (\omega_e - \omega_p)$ are the detunings of the $|g\rangle \longleftrightarrow |e\rangle$ and $|e\rangle \longleftrightarrow |p\rangle$ transitions, respectively. By solving numerically the above set of differential equations we obtain the time evolution of the transformed amplitudes $\tilde{c}_i(t)$, ($i = g, e, p$). The population of the probe state $|p\rangle$ can then be easily calculated as:

$$P_p(t) = |c_p(t)|^2 = |\tilde{c}_p(t)|^2 = \tilde{c}_p(t)\tilde{c}_p^*(t). \quad (2.59)$$

In Fig. 2.1(b) we plot the probe state population calculated after an interaction time T , as a function of Δ_2 , for various values of Ω_1 . For simplicity we assume that the frequency ω_1 is resonant with the $|g\rangle \longleftrightarrow |e\rangle$ transition, i.e. $\Delta_1 = 0$. The probe field is assumed to be much weaker than the field that drives the $|g\rangle \longleftrightarrow |e\rangle$ transition. As becomes evident, increasing the value of Ω_1 eventually leads to the splitting of the excited state (as well as the ground state) to two states, energetically separated by $\hbar\Omega_1$. The splitting is monitored by measuring the population of the probe state for varying frequencies ω_2 , i.e. varying detunings Δ_2 .

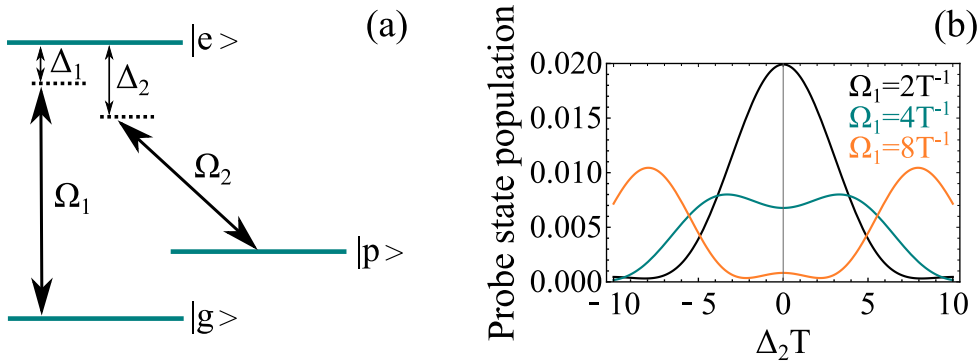


FIGURE 2.1: (a) Schematic representation of a "Lambda-type" three-level system where the first transition is driven by a strong radiation field, while the second one by a weak probe field. (b) Probe state population as a function of Δ_2 for $\Delta_1 = 0$ and $\Omega_2 = 0.1T^{-1}$. T is the atom-field interaction time. Black line: $\Omega_1 = 2T^{-1}$, teal line: $\Omega_1 = 4T^{-1}$, orange line: $\Omega_1 = 8T^{-1}$.

2.2.3 Electron-positron pair creation

The spontaneous production of electron-positron pairs in vacuum in the presence of ultrastrong electromagnetic radiation, is one of the most intriguing non-linear phenomena predicted by Quantum Electrodynamics (QED) theory, which still has not been confirmed experimentally. The analysis of this strong-field phenomenon was presented in 1931 in the work of Sauter [66] who was the first to calculate the leading order expression of the pair creation rate for fields smaller than the critical value

$\mathcal{E}_c = \frac{m_e^2 c^3}{e\hbar} = 1.32 \times 10^{16}$ V/cm, whereas Schwinger extended his work by calculating the full result [67]. The critical value \mathcal{E}_c is defined as the value of the electric field such that the spontaneous creation of an e^-e^+ pair in vacuum, often referred to as Schwinger mechanism, acquires a sizable rate [67]. Due to the practical impossibility of creating such an ultrastrong static and homogeneous field in the laboratory, there was a lot of theoretical activity in the decade of 1970 on the analysis of vacuum pair creation using time-dependent electric fields [68–75]. However, within the available optical laser technology at that time, the resulting rate would be far too small to be experimentally observable, due to insufficient power density necessary for breaking the vacuum.

The more recent advent of the free-electron laser (FEL), in facilities such as the European XFEL [76], DESY [77], SLAC [78] and SACLA [79], revived the interest in this problem over the last twenty years or so [80–94], because FEL's can provide strong, tightly focused radiation with energies up to the hard X-rays regime. At the same time, many authors have in addition explored possible ways to effectively enhance the pair creation yield by using consecutive pulses with time delay [95], combinations of weak high-frequency and strong low-frequency fields [96–99], strong fields combined with thermal backgrounds [100], as well as fields with frequency [101] or amplitude [102] modulations. Treatments based on effective electron and positron mass models have also received considerable attention the last few years [103–105]. It is important to note here that most of the studies mentioned above distinguish pair creation into two regimes depending on the field parameters, i.e. the tunneling and the multi-photon regime. For a harmonically oscillating field $E(t) = \mathcal{E} \cos(\omega t)$, these two regimes are reflected in the value of $\gamma = \frac{m_e c \omega}{e \mathcal{E}}$, which is the exact analog of the Keldysh parameter in strong-field laser-atom interactions. In particular, for $\gamma \ll 1$ (high-field, low-frequency limit) e^-e^+ pairs are mainly created via the tunneling effect, whereas for $\gamma \gg 1$ (low-field, high frequency limit) the pairs are created via multi-photon absorption with the corresponding formulas resembling a perturbative result. Pair creation in the intermediate regime between those two, often referred as non-perturbative multi-photon regime, has also been considered in a number of papers [106–111]. It must always be kept in mind that the notion of strong non-perturbative regime depends not only on the intensity but also on the wavelength. For example, infrared radiation of intensity 10^{14} W/cm² induces non-perturbative behavior, whereas the same intensity at XUV belongs to the multi-photon regime [112]. Moreover, in all strong-field laser interactions, there are no sharp demarcation lines between the multi-photon and tunneling regimes.

Although pair creation via the Schwinger mechanism has not been experimentally observed so far, creation of e^-e^+ pairs via the so-called Breit-Wheeler mechanism [113] has been reported since the mid 1990s in pioneering experiments at Stanford (SLAC) [114, 115]. In those experiments, a high-energy photon created through Compton backscattering of optical photons by a 46.6 GeV electron beam, collided with laser photons of wavelength 527nm to produce electron-positron pairs. The reported measured signal of 106 ± 14 positrons were the first data involving the creation of e^-e^+ pairs in the laboratory. The theoretical analysis of SLAC's data was based on the existing non-perturbative theory of the multi-photon Breit-Wheeler reaction available at the time [116, 117], whereas further theoretical insights of the measurements were added many years later [118, 119]. Production of electron-positron pairs can also be achieved via the Bethe-Heitler mechanism where the pairs are created by laser radiation in the vicinity of an atomic nucleus [120–122].

2.3 Atomic transitions induced by stochastic radiation

In this section we present the main properties of stochastically fluctuating electromagnetic fields and some basic theoretical tools that enable us to account for these in atomic transitions [5, 6]. In particular, we focus on two well-known models of stochastically fluctuating fields and explore their strong-driving effects on a two-level system.

2.3.1 General properties

Consider an atom described by an atomic density matrix operator ρ coupled to a stochastically fluctuating field of amplitude $\mathcal{E}(t)$. The stochastic character of the field leads to equations of motion which are also stochastic. Therefore these equations have to be averaged over the field fluctuations. The averaging process for a N -photon transition leads to atomic-field correlations of the type $\langle \mathcal{E}^{*N}(t_1) \mathcal{E}^N(t_2) \rho_{ii}(t_2) \rangle$, that cannot be generally evaluated without first solving the stochastic differential equations describing the time evolution of the density matrix elements. Note that the angular brackets denote the averaging over the fluctuations of the radiation field. As an approximation valid under certain conditions, one could decorrelate the atomic-field dynamics [123] by taking

$$\langle \mathcal{E}^{*N}(t_1) \mathcal{E}^N(t_2) \rho_{ii}(t_2) \rangle = \langle \mathcal{E}^{*N}(t_1) \mathcal{E}^N(t_2) \rangle \langle \rho_{ii}(t_2) \rangle. \quad (2.60)$$

However, as described below, there are specific models of fluctuating fields where the decorrelation is mathematically rigorous and does not stand only as an approximation. In what follows, we describe two well-known and mostly used models for stochastic fields, namely the phase-diffusion and the chaotic field model.

In the phase-diffusion (PD) model the field has non-fluctuating amplitude but its phase is a Wiener-Levy stochastic process [124]. In this case the n^{th} -order correlation function of the field is equal to [125]:

$$\langle \mathcal{E}^*(t_1) \mathcal{E}(t_2) \dots \mathcal{E}^*(t_{2n-1}) \mathcal{E}(t_{2n}) \rangle = \prod_{j \rightarrow \text{odd}}^{2n-1} \langle \mathcal{E}^*(t_j) \mathcal{E}(t_{j+1}) \rangle, \quad (2.61)$$

with $t_j > t_{j+1}$.

This represents a stationary Markovian process, with an exponential first-order correlation function given by [124]:

$$\langle \mathcal{E}^*(t_1) \mathcal{E}(t_2) \rangle = \langle |\mathcal{E}(t)|^2 \rangle \exp \left[-\frac{1}{2} \gamma_L |t_1 - t_2| \right], \quad (2.62)$$

where γ_L is the bandwidth of the field. The mean value of the field amplitude in the PD model is zero, i.e. $\langle \mathcal{E}(t) \rangle = 0$. A short note should be made at this point regarding the use of the term "Markovian" in the context of stochastically fluctuating fields. Although, strictly speaking, the term Markovian refers to memoryless processes, i.e. processes in which for a given time the field has no memory of its past values (implying a delta-like field correlation function), more often than not, the term "Markovian" is also used for short memory fluctuating fields. In such case the memory of the field usually decays exponentially fast as happens for example in the case of Eq. (2.62). Although the finite memory may, strictly speaking, imply

a non-Markovian process, it is essentially the relative magnitude between the bandwidth of the field and the rates that appear in the context of particular problem, that determine whether the memory effects of the field play significant role in the dynamics of a given system. Given the above, in what follows, by using the term "Markovian" we will be also referring to stochastically fluctuating fields with short memory and not only for fields described by delta-like field correlation functions.

It has been established [124] that in the case of the phase-diffusion model the decorrelation of the atom-field dynamics (See Eq. (2.60)) is rigorous without any approximation. Physically, this is easy to understand, because for a constant amplitude, the fluctuations of the phase of the field cannot affect the evolution of the populations, but only the coherence, i.e. the relative phase of the coefficients representing the superposition of the states coupled by the field. And it is the correlation between the time evolution of populations that is factorized in the process of decorrelation. Formally, the decorrelation is justified due to the statistical independence of the increments of a Wiener-Levy process.

In the chaotic field model the field undergoes both amplitude and phase fluctuations. Its amplitude is a complex Gaussian stochastic process with its n^{th} -order correlation function obeying [125]:

$$\langle \mathcal{E}^*(t_1) \mathcal{E}(t_2) \dots \mathcal{E}^*(t_{2n-1}) \mathcal{E}(t_{2n}) \rangle = \sum_P \prod_{j \rightarrow \text{odd}}^{2n-1} \langle \mathcal{E}^*(t_j) \mathcal{E}(t_{P(j+1)}) \rangle, \quad (2.63)$$

where the sum is over all possible permutations P , with $t_j > t_{j+1}$. The field amplitude is usually written in the form $\mathcal{E}(t) = \mathcal{E}_x(t) + i\mathcal{E}_y(t)$, where $\mathcal{E}_x(t)$ and $\mathcal{E}_y(t)$ are two independent Gaussian processes with mean values equal to zero. For reasons of analytical simplification, in what follows, we assume the chaotic field to be Markovian with an exponential first-order correlation function given by Eq. (2.62), a property not necessarily satisfied by a general chaotic field.

Contrary to the case of the phase diffusion model, the decorrelation of atomic-field dynamics is not mathematically rigorous for a chaotic field, but stands only as an approximation, valid in the weak field regime. The relative errors of this approximation have been evaluated in a very interesting recent theoretical work [126, 127] that also includes systematical methods of describing fluctuating SASE-FEL pulses driving single Auger resonances.

2.3.2 Two-level system subject to stochastic radiation

In this section we describe a method of finding the time evolution of a two-level system driven by a stochastically fluctuating field as presented in [5]. We begin by considering a two-level atom with a ground state $|1\rangle$ and an excited state $|2\rangle$ subject to an electric field of the form $E(t) = \mathcal{E}(t)e^{i\omega t} + \mathcal{E}^*(t)e^{-i\omega t}$. The complex field amplitude is generally assumed to undergo fluctuations and can be written in the form $\mathcal{E}(t) \equiv |\mathcal{E}(t)|e^{i\varphi(t)}$, with $|\mathcal{E}(t)|$ and $\varphi(t)$ the real amplitude and the phase of the field, respectively. The electric dipole between the two states is μ_{12} and the transition frequency is ω_{21} . The equations of motion of the density matrix in the RWA are

$$\left(\frac{d}{dt} + i\Delta + \frac{1}{2}\gamma_{21}\right)\sigma_{12}(t) = \frac{1}{2}i\Omega_R(t)D(t), \quad (2.64)$$

$$\left(\frac{d}{dt} + \gamma_2\right)D(t) = -\gamma_2 - 2\text{Im}[\Omega_R^*(t)\sigma_{12}(t)], \quad (2.65)$$

where we introduced the slowly varying amplitudes $\rho_{ii}(t) = \sigma_{ii}(t)$, $i = 1, 2$ and $\rho_{12}(t) = \sigma_{12}(t)e^{i\omega t}$, and used the property $\sigma_{11}(t) + \sigma_{22}(t) = 1$, implying a closed system with no population loss. By $D(t) \equiv \sigma_{22}(t) - \sigma_{11}(t)$, we denote the population difference and by Δ the detuning from the resonance, i.e. $\Delta = \omega - \omega_{21}$. γ_2 is the spontaneous decay rate of the excited state, while γ_{21} the off-diagonal relaxation that may include decays other than γ_2 as for example in the case of elastic collisions. The Rabi frequency $\Omega_R(t) = 2\hbar^{-1}\mu_{12}\mathcal{E}(t)$ is stochastic and its mean value will be denoted by $\bar{\Omega}_R(t) = 2\hbar^{-1}\mu_{12}\mathcal{E}_0$.

We integrate both equations formally and eliminate $\sigma_{12}(t)$ to obtain:

$$D(t) = -1 - \text{Re} \int_0^t e^{\gamma_2(t_1-t)} dt_1 \int_0^{t_1} e^{(i\Delta + \frac{1}{2}\gamma_{21})(t_2-t_1)} \Omega_R^*(t_1) \Omega_R(t_2) D(t_2) dt_2, \quad (2.66)$$

under the initial conditions $\sigma_{11}(0) = 1$, $\sigma_{22}(0) = 1$ and $\sigma_{12}(0) = 0$.

Phase-Diffusion field

At first, let us assume that field is described by a phase-diffusion model. The stochastic average of Eq. (2.66) over the fluctuating phase, in view of Eq. (2.62), yields:

$$\langle D(t) \rangle = -1 - \text{Re} \int_0^t e^{\gamma_2(t_1-t)} dt_1 \int_0^{t_1} e^{(i\Delta + \frac{1}{2}\gamma_{21} + \gamma_L)(t_2-t_1)} \bar{\Omega}_R^2(t_2) \langle D(t_2) \rangle dt_2, \quad (2.67)$$

where γ_L the field bandwidth. Taking the Laplace transform on both sides of Eq. (2.67) yields:

$$\langle \mathcal{D}(s) \rangle = -\frac{1}{s} - \text{Re} \left\{ \frac{\bar{\Omega}_R^2}{(s + \gamma_2) [s + i\Delta + \frac{1}{2}(\gamma_{21} + \gamma_L)]} \langle \mathcal{D}(s) \rangle \right\}, \quad (2.68)$$

where by $\langle \mathcal{D}(s) \rangle$ we denoted the Laplace transform of $\langle D(t) \rangle$. The steady state value of the population difference can be evaluated using the final value theorem for the Laplace transform, namely, $\lim_{s \rightarrow 0} s \langle \mathcal{D}(s) \rangle = \langle D(t = \infty) \rangle \equiv \langle D_\infty \rangle$. Using this theorem one obtains:

$$\langle D \rangle_\infty^{PD} = -1/(1 + S), \quad (2.69)$$

where S is the saturation parameter given by

$$S = \frac{(\bar{\Omega}_R^2/\gamma_2) \frac{1}{2}(\gamma_{21} + \gamma_L)}{\Delta^2 + \frac{1}{4}(\gamma_{21} + \gamma_L)^2} \quad (2.70)$$

In view of the above equation we conclude that the effect of the fluctuating phase on the dynamics of the two-level system is the addition of the field bandwidth γ_L to the atomic linewidth γ_{21} . The averaged population of the second state is given by the expression

$$\langle \sigma_{22} \rangle_\infty^{PD} = \frac{\frac{1}{2}S}{1 + S} = \frac{\frac{1}{4}(\gamma_{21} + \gamma_L)^2}{\frac{\Delta^2}{1+S_0} + \frac{1}{4}(\gamma_{21} + \gamma_L)^2} \frac{\frac{1}{2}S_0}{1 + S_0}, \quad (2.71)$$

where S_0 is the value of S when the field is exactly on resonance with the $|1\rangle \leftrightarrow |2\rangle$ transition. The profile of Eq. (2.71) is Lorentzian with FWHM equal to $\sqrt{1 + S_0}(\gamma_{21} +$

γ_L).

Chaotic field

For chaotic fields the stochastic average of Eq. (2.66) is generally a very challenging task. As a result, one has to obtain a perturbation series expansion for the correction to the decorrelation approximation [5]. Only in the case of zero bandwidth the exact correction can be found.

Let us first consider that the field has zero bandwidth. Note that $\gamma_L = 0$ implies an infinite correlation time and the field is random with statistics independent of time. In this case the phase of the field is characterized by a uniform distribution from 0 to 2π and its real amplitude follows a Rayleigh distribution. Hence, the stochastic average of the population difference is given by:

$$\langle D(t) \rangle = \int_0^{2\pi} \int_0^\infty \frac{2|\Omega_R| e^{-\left(\frac{|\Omega_R|}{\Omega_R}\right)^2}}{2\pi\Omega_R^2} D(|\Omega_R|, \varphi, t) d|\Omega_R| d\varphi. \quad (2.72)$$

Taking the derivative of both sides of Eq. (2.72) with respect to $\bar{\Omega}_R^2 = \langle \Omega_R^* \Omega_R \rangle$ one finds:

$$\langle \Omega_R^* \Omega_R D(t) \rangle = \langle \Omega_R^* \Omega_R \rangle \langle D(t) \rangle + \langle \Omega_R^* \Omega_R \rangle^2 \frac{d \langle D(t) \rangle}{d \langle \Omega_R^* \Omega_R \rangle}. \quad (2.73)$$

Moving the first term of the right-hand side of Eq. (2.73) to left-hand side, we form the term $\langle \Omega_R^* \Omega_R \delta D(t) \rangle$ which represents the correlation between the intensity of the chaotic field and the fluctuations of the population difference around its mean value, i.e. $\delta D(t) = D(t) - \langle D(t) \rangle$. If we calculate the stochastic average of Eq. (2.66) using Eq. (2.73), take its Laplace transform and use the Laplace final value theorem as described in the case of the phase-diffusion model, we find:

$$S^2 \frac{d \langle D \rangle_\infty^{CH}}{dS} + (1 + S) \langle D \rangle_\infty^{CH} + 1 = 0, \quad (2.74)$$

where S is given by Eq. (2.70) with $\gamma_L = 0$. Eq. (2.74) is differential and its solution can be written in the various forms:

$$\langle D \rangle_\infty^{CH} = -\frac{e^{1/S}}{S} \int_1^\infty \frac{e^{-t/S}}{t} dt \equiv -\frac{e^{1/S}}{S} E_1(1/S) = \int_0^\infty \left(\frac{-1}{1+S'} \right) \frac{e^{-S'/S}}{S} dS. \quad (2.75)$$

Eq. (2.75) indicates that the mean value of the population difference of a chaotic field with zero bandwidth can be calculated by first finding the solution for a coherent field, i.e. phase-diffusion field with zero bandwidth, and then average the result over the exponential intensity distribution of the chaotic field.

For $S \ll 1$ the asymptotic expansion of $E_1(1/S)$ results $\langle D \rangle_\infty^{CH} = -\sum_{k=0}^\infty k!(-S)^k$

while in the case of the phase-diffusion field we have $\langle D \rangle_\infty^{PD} = -\sum_{k=0}^\infty (-S)^k$. The two results agree only to first order perturbation theory. For $S \gg 1$ the series expansion of $E_1(1/S)$ leads to the result $\langle D \rangle_\infty^{CH} \simeq -(\ln S)/S$ while $\langle D \rangle_\infty^{PD} \simeq -1/S$. This indicates that the chaotic field is less effective in saturating a single-photon transition than a coherent field.

We now consider the more complex case of arbitrary bandwidth, where a non-perturbative relation between $\langle \Omega_R^*(t_1) \Omega_R(t_2) D(t_2) \rangle$ and $\langle D(t_2) \rangle$ cannot be found by simply knowing the statistics of the Rabi frequency. For Markovian chaotic fields with exponential first-order correlation function one can show that $\langle \Omega_R^*(t_1) \Omega_R(t_2) D(t_2) \rangle = \exp[-\frac{1}{2}\gamma_L(t_1 - t_2)] \langle \Omega_R^*(t_2) \Omega_R(t_2) D(t_2) \rangle$ but no further progress can be made. However, using a systematic method presented here, we can develop a perturbation series of the correlation $\langle \Omega_R^*(t_1) \Omega_R(t_2) D(t_2) \rangle$ that can be summed up to all orders [5]. We begin by writing $D(t) = \langle D(t) \rangle + \delta D(t)$, which also implies $\langle \delta D(t) \rangle = 0$. Substituting this relation back to Eq. (2.66) and taking its stochastic average one finds:

$$\begin{aligned} \langle D(t) \rangle = & -1 - \text{Re} \int_0^t e^{\gamma_2(t_1-t)} dt_1 \int_0^{t_1} e^{[i\Delta + \frac{1}{2}\gamma_{21}](t_2-t_1)} \\ & \times [\langle \Omega_R^*(t_1) \Omega_R(t_2) \rangle \langle D(t_2) \rangle + \langle \Omega_R^*(t_1) \Omega_R(t_2) \delta D(t_2) \rangle] dt_2. \end{aligned} \quad (2.76)$$

By subtracting Eq. (2.76) from Eq. (2.66), one finds:

$$\begin{aligned} \delta D(t_2) = & -\text{Re} \int_0^{t_2} e^{\gamma_2(t_3-t_2)} dt_3 \int_0^{t_3} e^{[i\Delta + \frac{1}{2}\gamma_{21}](t_4-t_3)} \\ & \times \{ [\Omega_R^*(t_3) \Omega_R(t_4) - \langle \Omega_R^*(t_3) \Omega_R(t_4) \rangle] \langle D(t_4) \rangle \\ & + [\Omega_R^*(t_3) \Omega_R(t_4) \delta D(t_4) - \langle \Omega_R^*(t_3) \Omega_R(t_4) \delta D(t_4) \rangle] \} dt_4. \end{aligned} \quad (2.77)$$

Iterating Eq. (2.77) and substitution of $\delta D(t_2)$ back in Eq. (2.76), leads to the following series integral equation:

$$\begin{aligned} \langle D(t) \rangle = & -1 - \text{Re} \int_0^t e^{\gamma_2(t_1-t)} dt_1 \int_0^{t_1} e^{[i\Delta + \frac{1}{2}\gamma_{21}](t_2-t_1)} dt_2 \\ & \times \left\{ \langle \Omega_R^*(t_1) \Omega_R(t_2) \rangle \langle D(t_2) \rangle - \text{Re} \int_0^{t_2} e^{\gamma_2(t_3-t_2)} dt_3 \int_0^{t_3} e^{[i\Delta + \frac{1}{2}\gamma_{21}](t_4-t_3)} dt_4 \right. \\ & \times \left[\langle \Omega_R^*(t_1) \Omega_R(t_4) \rangle \langle \Omega_R^*(t_3) \Omega_R(t_2) \rangle \langle D(t_4) \rangle - \text{Re} \int_0^{t_4} e^{\gamma_2(t_5-t_4)} dt_5 \int_0^{t_5} e^{[i\Delta + \frac{1}{2}\gamma_{21}](t_6-t_5)} dt_6 \right. \\ & \times (\langle \Omega_R^*(t_1) \Omega_R(t_6) \rangle \langle \Omega_R^*(t_3) \Omega_R(t_4) \rangle \langle \Omega_R^*(t_5) \Omega_R(t_2) \rangle \\ & + \langle \Omega_R^*(t_1) \Omega_R(t_4) \rangle \langle \Omega_R^*(t_3) \Omega_R(t_6) \rangle \langle \Omega_R^*(t_5) \Omega_R(t_2) \rangle \\ & \left. \left. + \langle \Omega_R^*(t_1) \Omega_R(t_6) \rangle \langle \Omega_R^*(t_3) \Omega_R(t_2) \rangle \langle \Omega_R^*(t_5) \Omega_R(t_4) \rangle \langle D(t_6) \rangle - \dots) \right] \right\}. \end{aligned} \quad (2.78)$$

Since we assumed that the field is Markovian with exponential first order correlation function, the above equation is generally solvable using Laplace transform. However due to the complexity of Eq. (2.78), one should develop a systematic way of calculating its Laplace transform. One useful way is to express our equation in terms of diagrams [128, 129], as depicted in Fig. 2.2. The straight line between two successive vertices at t_j and t_{j+1} is associated with the factor $\exp[\gamma_2(t_{j+1} - t_j)]$ while the wavy line with the factor $\frac{1}{2} \exp[(i\Delta + \frac{1}{2}\gamma_{21})(t_{j+1} - t_j)] + c.c.$ A loop connecting two vertices at t_j and t'_j , with $t_j > t'_j$ and $j < j'$ is associated with the factor

$\bar{\Omega}_R^2 \exp \left[-\frac{1}{2} \gamma_L (t_j - t'_j) \right]$. It is important to notice that although Eq. (2.78) may contain intersecting loops, the exponential form of the first-order correlation function allows us to replace these loops by non-intersecting ones. In example, the part of the diagram that represents the term $\langle \Omega_R^*(t_1) \Omega_R(t_4) \rangle \langle \Omega_R^*(t_3) \Omega_R(t_6) \rangle \langle \Omega_R^*(t_5) \Omega_R(t_2) \rangle$ can be replaced equivalently by $\langle \Omega_R^*(t_1) \Omega_R(t_6) \rangle \langle \Omega_R^*(t_3) \Omega_R(t_4) \rangle \langle \Omega_R^*(t_5) \Omega_R(t_2) \rangle$.

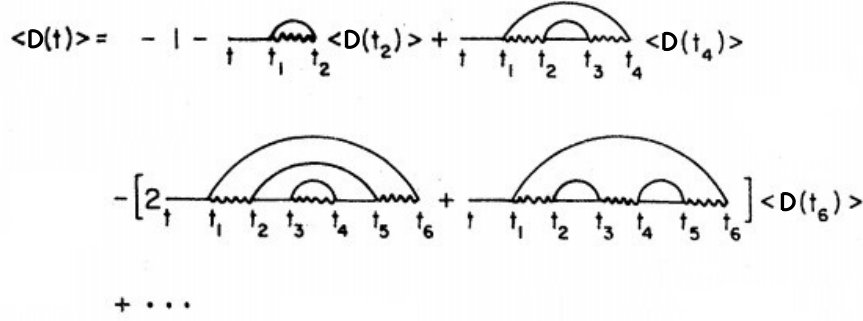


FIGURE 2.2: Representation of Eq. (2.78) in terms of diagrams [5].

Taking the Laplace transform of the diagram in Fig. 2.2 and applying the Laplace frequency-shift theorem we find:

$$\langle D(s) \rangle = -(1/s) / \left[1 + \sum_1(s) \right], \quad (2.79)$$

where

$$\begin{aligned} \sum_1(s) &= \text{Re} \frac{\bar{\Omega}_R^2}{(s + \gamma_2) [s + i\Delta + \frac{1}{2}(\gamma_{21} + \gamma_L)]} \times \left(1 - \text{Re} \frac{\bar{\Omega}_R^2}{(s + \gamma_2 + \gamma_L) [s + i\Delta + \frac{1}{2}(\gamma_{21} + \gamma_L)]} + \dots \right) \\ &\equiv \text{Re} \frac{\bar{\Omega}_R^2}{(s + \gamma_2) [s + i\Delta + \frac{1}{2}(\gamma_{21} + \gamma_L)]} \frac{1}{1 + \sum_2(s)}, \end{aligned} \quad (2.80)$$

is the first irreducible function corresponding to the set of diagrams in Eq. (2.78). Eq. (2.80) also defines $\sum_2(s)$. The recursion relation between the functions $\sum_i(s)$ is

$$\sum_m(s) = \frac{S_m(s)}{1 + \sum_{m+1}(s)}, \quad (2.81)$$

with

$$S_m(s) = \text{Re} \frac{(m+1)\bar{\Omega}_R^2}{2 [s + \gamma_2 + \frac{1}{2}(m-1)\gamma_L] [s + i\Delta + \frac{1}{2}(\gamma_{21} + m\gamma_L)]}, \quad (2.82)$$

for m odd, or

$$S_m(s) = \text{Re} \frac{m\bar{\Omega}_R^2}{2 (s + \gamma_2 + \frac{1}{2}m\gamma_L) \{s + i\Delta + \frac{1}{2}[\gamma_{21} + (m-1)\gamma_L]\}}, \quad (2.83)$$

for m even. The coefficients S_m are called saturation coefficients. The steady state value of the population difference is given by

$$\langle D \rangle_{\infty}^{CH} = -\frac{1}{1 + \sum_1} = \frac{-1}{1 + \frac{S_1}{1 + \frac{S_2}{1 + \dots}}}, \quad (2.84)$$

where \sum_m and S_m are given by Eqs. (2.81), (2.82) and (2.83) by applying $s = 0$. The first saturation coefficient S_1 is identical to the saturation parameter defined in Eq. (2.70) for the case of the phase-diffusion field. Therefore the relation $\sum_1 < S_1$ implies the known result, that a chaotic field is always less effective in saturating a single-photon transition than a phase-diffusion field. If we set $\gamma_L = 0$ in Eq. (2.84) we get the continued fraction result $-\frac{e^{1/S}}{S} E_1(1/S)$ of Eq. (2.75). For non-zero bandwidth Eq. (2.84) converges and can be suitably truncated and summed to any desired accuracy.

Before closing this section we should note that there also other methods that can be used to describe the interaction between atoms and stochastic radiation. For example, one could use the perturbative method of multi-time cumulants [130] which, depending on the specific details of the considered problem, may be useful in describing the interaction between atoms and stochastic fields with Gaussian first-order correlation functions. However, we should always keep in mind that methods such as the above are of limit usefulness for non-stationary processes, i.e. processes with varying mean value or/and variance over time. In such cases, where most methods are not directly applicable, the problem is usually approached solely via numerical Monte-Carlo methods.

Chapter 3

Photon statistics effects in double optical resonance

A benchmark problem encapsulating the interplay between non-linearity and photon correlations is the dynamics of a transition between two bound states driven resonantly by fields with different quantum stochastic properties, such as coherent state, chaotic (thermal) or squeezed. The dynamics can be probed either by the observation of the spectrum of spontaneous emission from the upper state or through a pump probe arrangement, as in DOR, where a second weak-field transition to a third level serves as a probe.

The case of weak field absorption of a two-level atom by states of various photon statistics in the narrow bandwidth limit has been studied in great detail [131], as has the case of strong driving in the context of both resonance fluorescence and DOR [5, 6]. The problems of resonance fluorescence into a squeezed vacuum (SQV) reservoir [132–140], the calculation of the absorption spectrum in a squeezed state of non-zero bandwidth [141, 142] and the interaction of a three-level system with a broadband squeezed vacuum field [143, 144] have also been investigated. In addition to intensity fluctuations, a transition between two discrete states is also sensitive to the bandwidth of the radiation. The bandwidth is of course part of the stochastic properties of the field, but not a uniquely quantum feature, as the intensity fluctuations are in certain sources such as SQV. For coherent and chaotic fields (ChF), which are amenable to modelling in terms of classical fields, with Gaussian stochastic properties, this has been treated in considerable detail [5, 6, 145, 146]. The theory of a single-photon transition, driven strongly by coherent or ChF, including arbitrary bandwidth, is well understood for both fluorescence and DOR; although experimentally much remains to be explored, especially for driving by ChF. To the best of our knowledge, no experimental data exist for that case, for which the theory predicts [5, 6, 145, 146] a rich variety of counter-intuitive effects due to intensity fluctuations mirrored in the concomitant fluctuations of the Rabi frequency. Given that photon bunching, inherent in chaotic radiation, is responsible for those effects, would those effects be more pronounced in the presence of superbunching? In the light of the recent achievement by Spasibko et al. [147] and Lu Zhang et al. [148, 149], theoretical predictions to those questions appear to be within experimental reach, which has served as the principal motivation for this work.

3.1 Squeezed coherent states in single-photon double optical resonance

As we mentioned in section 2.1.3, a quantum state is referred as "squeezed" if the variance of one of the quadrature amplitudes of the state is modified in such a way

that becomes smaller than the respective variance of a vacuum or a coherent state. Such a state is referred in the bibliography under the term "Squeezed vacuum state" (SQVS) and "Squeezed coherent state" (SQCS), respectively. Due to Heisenberg's uncertainty principle, squeezing always results to the increase of the conjugated quadrature variance above the variance of vacuum, in the case of a SQVS, and the variance of a coherent state in the case of a SQCS [38].

The first experimental observation of squeezed light was reported back in 1985 in the pioneering work of Slusher et al. [150] who achieved four-wave-mixing in an atomic vapor of sodium atoms. Since then, significant advances in the generation and detection of squeezed light [30] gave the green light for the implementation of squeezing as a resource in a series of different applications in several fields. Among these applications, the ones that stand out are related to the reduction of quantum noise in optical communications [151], the detection of sub-shot-noise phase shifts [152, 153], the ability to achieve maximum sensitivity in interferometry at lower laser powers [154] that was implemented in the detection scheme of gravitational waves [155], the storage of quantum memory [156, 157] necessary for quantum information tasks, and most recently, the ability for quantum-enhanced microscopy and effective bio-imaging without the danger of damaging the cell sample [158, 159].

The underlying physical mechanism behind the last application is thoroughly intriguing since it is based on the effective yield enhancement that one can achieve by inducing non-linear processes with squeezed radiation. As has been known since the 1960's [7, 8] any non-linear light-matter interaction depends on the quantum statistical properties of the radiation that are embodied in its correlation functions. This realization naturally led to a series of studies [160–173] on non-linear phenomena induced by fields that may exhibit photon bunching or superbunching properties resulting to higher correlation functions than those of a coherent field. The simplest example illustrating this dependence is the transition from a bound state to a continuum via the absorption of N photons, i.e. N -photon ionization. The derivation of the transition probability per unit time for N -photon ionization when all real bound atomic intermediate states are assumed sufficiently far from resonance [174–177], indicates that the rate of the process is proportional to an effective N -photon matrix element multiplied by the N^{th} -order intensity correlation function [7, 8]. And in view of the dependence of the correlation functions on the stochastic properties of the radiation, the rate of such a process can be affected dramatically by the intensity fluctuations of the source [178]. As a prototype example one can take an 11-photon ionization process induced by thermal radiation whose N^{th} order intensity correlation function is given by $N! \times I^N$, where I is the average intensity, i.e. $N!$ times larger than the respective correlation function of the coherent field. For $N = 11$, the $N!$ factor arising from the strong intensity fluctuations of the chaotic field, gives us an enormous enhancement of around seven orders of magnitude, that in fact has been observed experimentally in the past for process of such a high-order [179, 180]. The situation becomes even more interesting if one considers squeezed radiation, which under certain values of parameters may exhibit superbunching properties resulting to correlation functions even larger than those of the chaotic field [181].

The main hindrance in the experimental investigation of such phenomena using squeezed radiation has been the difficulty of producing stable, high intensity squeezed sources with controllable stochastic properties in the lab. However, in view of recent works [182] providing novel methods to overcome experimental difficulties associated with the generation of squeezed coherent radiation, the study of some of these effects are timely.

In what follows we investigate the strong driving of a bound-bound transition

by a radiation field initially prepared in a SQCS [183]. For that matter, we consider a " Λ -type" three-level system where the first transition is driven by a radiation field initially prepared in a squeezed coherent state, while the second one by a weak probe field. If the squeezed field is sufficiently strong to cause Stark splitting of the states it connects, such a splitting can be monitored through the population of the probe state, as we explored in Section 2.2.1. Since squeezed light is not amenable to simulation in terms of classical stochastic processes, we adopt a fully quantum mechanical treatment in terms of the resolvent operator, involving averaging over the photon number distribution of the SQCS, a method valid in the limit where the bandwidth of the source is sufficiently smaller than the natural decay of the excited state.

We begin by considering an atom initially resting in its ground state $|g\rangle$ in the presence of a quantized radiation field in a two-mode Fock state with n photons in the first mode with frequency ω_1 and m photons in the second mode with frequency ω_2 . The atom can absorb one photon from the first mode and move to the excited state $|a\rangle$, while the latter is coupled to another excited state $|b\rangle$ via the emission of one of the m photons. The Hamiltonian of the system consists of three parts; namely, the atomic Hamiltonian $\hat{H}^A = \sum_j \hbar\omega_j |j\rangle \langle j|$ ($j = g, a, b$), the Hamiltonian of the radiation field $\hat{H}_R = \sum_{i=1}^2 \hbar\omega_i \hat{a}_i^\dagger \hat{a}_i$ and the interaction Hamiltonian under the rotating wave approximation, $\hat{V} = \sum_{i=1}^2 \hbar g_i (\hat{\sigma}_+^{(i)} \hat{a}_i + \hat{a}_i^\dagger \hat{\sigma}_-^{(i)})$, where $\hbar\omega_g$, $\hbar\omega_a$ and $\hbar\omega_b$ are the energies of the atomic states $|g\rangle$, $|a\rangle$ and $|b\rangle$, respectively, g_1 and g_2 represent the coupling strengths between those states in units of frequency, while \hat{a}_i and \hat{a}_i^\dagger , ($i = 1, 2$) are photon annihilation and creation operators, respectively. The atomic operators $\hat{\sigma}_+^{(i)}$ and $\hat{\sigma}_-^{(i)}$, ($i = 1, 2$), are the raising and lowering operators, respectively, given by the relations $\hat{\sigma}_+^{(1)} = |a\rangle \langle g|$, $\hat{\sigma}_-^{(1)} = |g\rangle \langle a|$, $\hat{\sigma}_+^{(2)} = |a\rangle \langle b|$ and $\hat{\sigma}_-^{(2)} = |b\rangle \langle a|$.

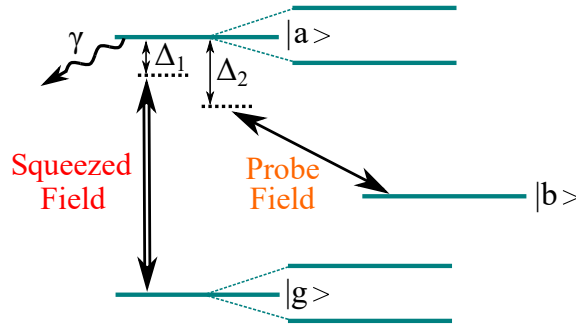


FIGURE 3.1: Schematic presentation of the system at study. A strong radiation field prepared initially in a squeezed coherent state drives the $|g\rangle \leftrightarrow |a\rangle$ transition resulting to a Stark splitting of both states. This splitting is monitored through the calculation of the population of state $|b\rangle$ as a function of Δ_2 , which is assumed to be weakly coupled to state $|a\rangle$ through a probe field.

The eigenstates of the unperturbed Hamiltonian $\hat{H}^0 \equiv \hat{H}^A + \hat{H}^R$ of the compound system "atom + radiation", are $|I\rangle = |g\rangle |n\rangle_1 |m\rangle_2$, $|A\rangle = |a\rangle |n-1\rangle_1 |m\rangle_2$ and $|B\rangle = |b\rangle |n-1\rangle_1 |m+1\rangle_2$, with energies $\hbar\omega_I = \hbar\omega_g + n\hbar\omega_1 + m\hbar\omega_2$, $\hbar\omega_A = \hbar\omega_a + (n-1)\hbar\omega_1 + m\hbar\omega_2$ and $\hbar\omega_B = \hbar\omega_b + (n-1)\hbar\omega_1 + (m+1)\hbar\omega_2$, respectively. The detunings from resonance of the two transitions are defined as $\Delta_1 \equiv \omega_1 - \omega_{ag} \equiv \omega_1 - (\omega_a - \omega_g)$ and $\Delta_2 \equiv \omega_2 - \omega_{ab} \equiv \omega_2 - (\omega_b - \omega_a)$.

To account for the spontaneous decay of the excited state $|a\rangle$, we make the substitution $\omega_A \rightarrow \tilde{\omega}_A = \omega_A - \frac{i}{2}\gamma$, in view of which, our system now becomes open. Note that this method introduces a decay rate without accounting for the repopulation of the ground state. It is however a good approximation as long as the first transition is sufficiently strong so that the Rabi frequency Ω_1 of the first transition is sufficiently larger than the decay rate γ . In such a case, the interaction between the uncoupled states of the compound system $|I\rangle$ and $|A\rangle$, causes a splitting into doublets energetically separated by $\hbar\Omega_1$ (Stark splitting). Such a splitting can be monitored through the calculation of the probe state population (state $|b\rangle$) as a function of Δ_2 . Our ultimate goal is the study of the splitting profile in the case where the $|g\rangle \leftrightarrow |a\rangle$ transition is driven by a strong field prepared in a squeezed coherent state. The switch-over from the initial Fock state to a squeezed coherent state can be realized through appropriate averaging of the probe state population over the photon statistics distribution of the squeezed coherent field, as will be described in detail below. A schematic representation of the system we study is depicted in Fig 3.1.

Our problem is formulated in terms of the resolvent operator, which is the Laplace transform of the time-evolution operator $\hat{U}(t) = \exp(-i\hat{H}t)$. Taking the Laplace transform with s being the usual Laplace variable and making the change of variables $s = -iz$, we obtain the relation $\hat{G}(z) = (z - \hat{H})^{-1}$, where $\hat{G}(z)$ is the resolvent operator [164, 184, 185]. Using the relation $\hat{H} = \hat{H}^0 + \hat{V}$, it is straightforward to show that $\hat{G}(z)$ obeys the equation $\hat{G}(z) = \hat{G}^0(z) + \hat{G}^0(z)\hat{V}\hat{G}(z)$, where $\hat{G}^0(z) \equiv \frac{1}{z - \hat{H}^0}$ is the unperturbed resolvent operator. In view of this equation, the matrix elements of the resolvent operator in the compound system basis, satisfy the equations

$$(z - \hbar\omega_I)G_{II} = 1 + V_{IA}G_{AI}, \quad (3.1)$$

$$(z - \hbar\tilde{\omega}_A)G_{AI} = V_{AI}G_{II} + V_{AB}G_{BI}, \quad (3.2)$$

$$(z - \hbar\omega_B)G_{BI} = V_{BA}G_{AI}. \quad (3.3)$$

Solving for G_{BI} , one obtains:

$$G_{BI} = \frac{V_{BA}V_{AI}}{(z - \hbar\omega_I)(z - \hbar\tilde{\omega}_A)(z - \hbar\omega_B) - (z - \hbar\omega_I)|V_{BA}|^2 - (z - \hbar\omega_B)|V_{AI}|^2}. \quad (3.4)$$

The matrix elements of the time evolution operator in the compound system basis, i.e. $U_{ij}(t)$, ($i, j = I, A, B$) are related to the respective matrix elements of the resolvent operator through the inverse transform [164]

$$U_{ij}(t) = -\frac{1}{2\pi i} \int_{-\infty}^{+\infty} e^{-ixt} G_{ij}(x^+) dx, \quad (3.5)$$

where $x^+ = x + i\eta$, with $\eta \rightarrow 0^+$. In order to calculate the integral of Eq. (3.5) one should first calculate the roots of the third order polynomial appearing in the denominator of Eq. (3.4). If we denote these three roots by z_1, z_2 and z_3 , the resulting expression is

$$U_{BI}(t) = V_{BA}V_{AI} \left[\frac{\exp(-iz_1 t)}{(z_1 - z_2)(z_1 - z_3)} + \frac{\exp(-iz_2 t)}{(z_2 - z_1)(z_2 - z_3)} + \frac{\exp(-iz_3 t)}{(z_3 - z_1)(z_3 - z_2)} \right]. \quad (3.6)$$

The population of the probe state $|b\rangle$ at times $t > 0$, is given by

$$P_b(t) = |U_{BI}(t)|^2. \quad (3.7)$$

The population of $|b\rangle$ depends non-linearly on the photon numbers n and m through the expressions of the compound system energies $\hbar\omega_I$, $\hbar\tilde{\omega}_A$ and $\hbar\omega_B$, as well as the matrix elements V_{AI} and V_{BA} that reflect the Rabi frequencies of the $|g\rangle \leftrightarrow |a\rangle$ and $|a\rangle \leftrightarrow |b\rangle$ transitions, respectively, via the relations $2V_{AI} \equiv \hbar\Omega_1 = \hbar g_1 \sqrt{n}$ and $2V_{BA} \equiv \hbar\Omega_2 = \hbar g_2 \sqrt{m+1}$.

We focus on the dependence of $P_b(t)$ on n and t , by adopting the notation $P_b(n, t)$. The dependence on m is not of particular importance as long as the probe field coupling strength g_2 is chosen to be sufficiently smaller than all the other rates that appear in the problem at hand. To capture the case where the field driving the $|g\rangle \leftrightarrow |a\rangle$ is initially prepared in a state other than Fock, one can average the desired quantity (probe state population in our problem) over the corresponding photon number distribution of the initial field state. This is a standard method in quantum optics [26]. However, one should note that it is strictly valid in the limit where the field bandwidth is much smaller than the natural decay γ . We are particularly interested in the case where the field driving the first transition is initially prepared in a SQCS.

As shown in section 2.1.3, the photon number probability distribution of a SQCS is given by

$$P_{\text{SQCS}}(n) = \frac{(\tanh r)^n}{2^n n! \cosh r} \exp \left[|\alpha|^2 \cos(2\Phi) \tanh r - |\alpha|^2 \right] \left| H_n \left(\frac{|\alpha| e^{-i\Phi} - |\alpha| e^{i\Phi} \tanh r}{-i\sqrt{2} \tanh r} \right) \right|^2. \quad (3.8)$$

where $H_n(x)$ is the n^{th} -order Hermite polynomial, $\Phi \equiv \phi - \theta/2$, while ϕ and θ are the phases of the displacement and squeezing parameters, respectively, i.e. $\alpha = |\alpha| e^{i\phi}$ and $\zeta = r e^{i\theta}$. In Fig. 3.2(a) we plot the photon number distribution of a SQCS with a squeezing parameter $r = 0.5$ and compare it to the distribution of a coherent field ($r = 0$). As becomes evident, depending on the phase difference Φ , the distribution deviates from its Poissonian form, by exhibiting Super-Poissonian (red line) or Sub-Poissonian statistics (teal line). The situation becomes even more interesting for larger values of r . In Fig. 3.2(b) we plot the photon number distribution of a SQCS with a squeezing parameter $r = 2$ for two values of Φ and observe an obvious non-classical behaviour with vivid oscillations in both cases. These oscillations have been interpreted in the past by Schleich and Wheeler [186] as resulting from the interference of error contours in phase space. In the $\Phi = 0$ case (red line) the distribution is peaked at $n = 0$ and the oscillations are much faster compared to the $\Phi = \pi/2$ case (teal line) where the distribution is peaked at a slightly higher photon number than the peak of the Poissonian distribution and the oscillations appear only for photon numbers larger than the position of the peak. It should be noted that the photon number distributions of Fig. 3.2 acquire discrete values for each value of the integer n , but are depicted as continuous since the photon number scale over which they are plotted is large. To avoid any misconception, there is another form of Eq. (3.8) often found in bibliography where the distribution is essentially the same but it exhibits sub-Poissonian statistics for $\Phi = 0$ and super-Poissonian statistics for $\Phi = \pi/2$. This is a reflection of whether the SQCS is defined as $|\text{SQCS}\rangle \equiv \hat{D}(\alpha) \hat{S}(\zeta) |0\rangle$ or $|\text{SQCS}\rangle \equiv \hat{S}(\zeta) \hat{D}(\alpha) |0\rangle$, which are not equal since the operators $\hat{D}(\alpha)$ and $\hat{S}(\zeta)$ do not commute. In any case one can go from the one definition to the other through the relation:

$$\hat{S}(\zeta) \hat{D}(\alpha) = \hat{D}(\alpha \cosh r + \alpha^* e^{i\theta} \sinh r) \hat{S}(\zeta). \quad (3.9)$$

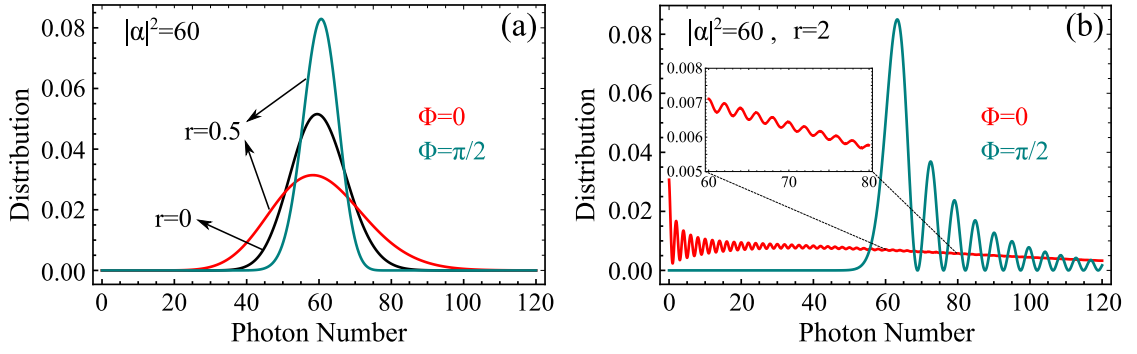


FIGURE 3.2: (a) Photon number distribution of a squeezed coherent state with $|\alpha|^2 = 60$ and $r = 0.5$, compared the respective distribution of a coherent state ($r = 0$, black line). (b) Photon number distribution of a squeezed coherent state with $|\alpha|^2 = 60$ and $r = 2$. In both panels the red lines correspond to $\Phi = 0$, while the teal lines correspond to $\Phi = \pi/2$.

Returning back to our problem, we average the population of the probe state $|b\rangle$ over the photon number distribution of Eq. (3.8), according to:

$$P_b^{SQCS}(t) = \sum_{n=1}^{\infty} P_b(n, t) P_{SQCS}(n). \quad (3.10)$$

In what follows we will be concerned about the behaviour of $P_b^{SQCS}(t)$ as a function of Δ_2 for different parameters of the SQCS, or put otherwise, the effects of various schemes of squeezing on the resulting Stark splitting profile imprinted on the population of the probe state.

Among other parameters, Eq. (3.10) depends also on the time. Therefore, in order to study the behaviour of the probe state population as a function of Δ_2 , one should first make a choice of the interaction time $t = T$ during which the driven system is exposed to the radiation. In Fig. 3.3(a) we plot $P_b^{SQCS}(t)$ as a function of the time for various detunings Δ_2 and $r = 0$. Under this choice of parameters, we notice that the population of the probe state reaches its steady state value at about $t = 25\gamma^{-1}$. Numerical investigations of the behaviour of $P_b^{SQCS}(t)$ as a function of the time for different combinations of the parameters Δ_2 , $|\alpha|^2$, r and Φ , revealed that the choice of $t = 30\gamma^{-1} \equiv T$ always guarantees that the system is well within its steady state regime. Therefore we adopt this choice of time for the calculations throughout this chapter. In Fig. 3.3(b) we plot $P_b^{SQCS}(T)$ as a function of Δ_2 for various $|\alpha|^2$ and $r = 0$, parameters corresponding to a coherent state. Note that, as expected, for $r = 0$ the distribution does not depend on the choice of Φ . We confirm that as $|\alpha|^2$ increases and the mean Rabi frequency $\bar{\Omega}_1 = g_1 |\alpha|$ becomes larger than the spontaneous decay rate γ , the single peak structure (black line) splits into two peaks forming the well-known Autler-Towns doublet structure [187]. The distance between the two peaks is equal to the mean Rabi frequency $\bar{\Omega}_1$ which is proportional to the square root of the mean photon number of the coherent state $\bar{n} = |\alpha|^2$. As long as $\bar{\Omega}_1$ is smaller than γ , the increase of $|\alpha|^2$ will result to power broadening of the profile [188] until it splits into the doublet.

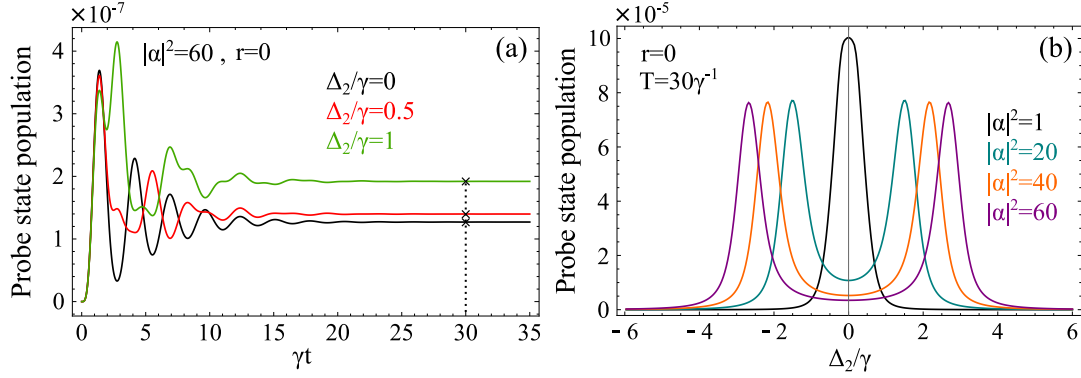


FIGURE 3.3: (a) Population of the probe state $|b\rangle$ as a function of the time for various detunings Δ_2 . The parameters of the strong field are: $|\alpha|^2 = 60$, $r = 0$, $g_1 = 0.7\gamma$ and $\Delta_1 = 0$. The vertical dashed line corresponds to the time $T = 30\gamma^{-1}$ where the system is well within its steady state regime. (b) Population of the probe state $|b\rangle$ as a function of Δ_2 for various values of $|\alpha|^2$. The chosen parameters are: $r = 0$, $g_1 = 0.7\gamma$, $T = 30\gamma^{-1}$ and $\Delta_1 = 0$.

Before continuing to the case of strong driving by a SQCS, we should note that the exact choice of the Rabi frequency of the probe transition is not of direct relevance to our problem, as long as it is sufficiently weaker than all of the other rates that appear in the derivation. If this condition is satisfied, then the only effect of changing the Rabi frequency of the probe will be a linear change in the total population of the probe state (y-axis) but not in the ratio between individual peaks or widths. And since our aim is the study of the form of the splitting profile, the exact values of the probe state population are of no importance. For the same reason we are not concerned about the possible natural decay of the probe state $|b\rangle$ to some other unobserved state.

In Fig. 3.4(a) we plot the population of the probe state as a function of Δ_2 for various degrees of squeezing and $\Phi = 0$. The splitting profile shows great sensitivity to the value of the squeezing parameter r , becoming significantly broader as the latter increases. The physics behind this broadening of the profile is related to the strong amplitude fluctuations of the field that are translated into fluctuations in the value of the Rabi frequency of the transition that cause partial smearing of the doublet structure after taking the average over the SQCS distribution. However, as seen in Fig. 3.4(b), under the same choice of parameters but with $\Phi = \pi/2$, the profile only slightly deviates from the profile exhibited under coherent state driving ($r = 0$). An effective way of interpreting this sensitivity on the phase difference Φ is through the form of the SQCS photon number variance. In particular, the photon number variance of the SQCS is given by the relation:

$$(\Delta n)^2 = |\alpha|^2 [e^{2r} \cos^2 \Phi + e^{-2r} \sin^2 \Phi] + 2(\sinh r \cosh r)^2. \quad (3.11)$$

For $\Phi = 0$, Eq. (3.11) reduces to $(\Delta n)^2 = |\alpha|^2 e^{2r} + 2(\sinh r \cosh r)^2$. In this case it is straightforward to show that the increase of the squeezing parameter will always lead to the increase of the variance of the SQCS (inset of Fig. 3.4(a)) and therefore to the broadening of the total profile after averaging over the SQCS distribution. However the picture is drastically different if $\Phi = \pi/2$, where Eq. (3.11) takes the form $(\Delta n)^2 = |\alpha|^2 e^{-2r} + 2(\sinh r \cosh r)^2$. It is easy to check that in this case the variance is not increasing monotonically as a function of r , but it acquires a minimum value at a position that depends upon the choice of $|\alpha|^2$. In the considered case

$|\alpha|^2 = 60$, the minimum is positioned at $r = 0.91$. The variance remains smaller than its value at $r = 0$ (corresponds to a coherent state) up to the position $r = 1.53$, and becomes larger than that thereafter (inset of Fig. 3.4(b)). Also the value of the variance in the vicinity of the minimum is not much smaller than its $r = 0$ value. This behaviour explains why for the squeezing parameters considered in Fig. 3.4(b), the SQCS splitting profile does not exhibit significant deviations from the corresponding coherent profile. It also explains why the peaks of the teal and orange lines corresponding to the values $r = 1$ and $r = 1.5$, respectively, appear larger than the peaks of the black line (coherent field), due to the sub-Poissonian form of the SQCS photon number distribution.

As r increases, for $\Phi = 0$, the peaks of the splitting profile appear at slightly smaller detunings than the coherent splitting, contrary to the $\Phi = \pi/2$ case where the peaks tend towards higher detunings. This can be attributed to the behaviour of the mode of the SQCS distribution (most probable value) as a function of r in each case. In particular, for $\Phi = 0$ the mode of the distribution tends towards the zero photon number, while for $\Phi = \pi/2$ it is positioned at photon numbers slightly higher than $|\alpha|^2$, depending on the value of r . This tendency is also evident in Fig. 3.2. We should note that the peaks of the resulting profile are not separated by the Rabi frequency corresponding to the mode of the photon number distribution, nor the Rabi frequency corresponding to its mean photon number, given by the relation $\bar{n} = |\alpha|^2 + (\sinh r)^2$, for every Φ . As will become evident in the next chapter of the thesis, the exact shape of the resulting profile stems from a complex interplay between properties of the probe state population function associated with the order of the process, and the structure of the photon probability distributions of the driving field. The behaviour of the mode as a function of r and different values of Φ can however give us good evidence for the expected behaviour of the position of the peaks.

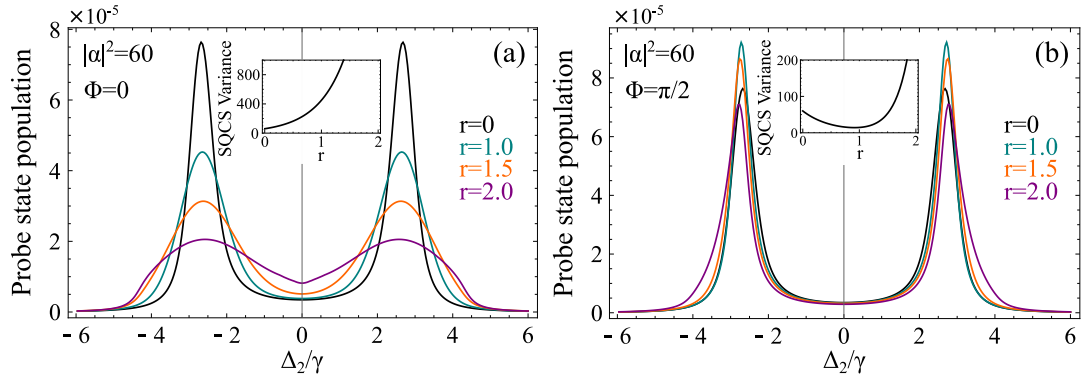


FIGURE 3.4: (a) Population of the probe state $|b\rangle$ as a function of Δ_2 for different degrees of squeezing and $\Phi = 0$. Inset: Variance of the SQCS according to Equation (2.52) for $\Phi = 0$. (b) Population of the probe state $|b\rangle$ as a function of Δ_2 for different degrees of squeezing and $\Phi = \pi/2$. Inset: Variance of the SQCS according to Equation (2.52) for $\Phi = \pi/2$. In both panels $|\alpha|^2 = 60$, $T = 30\gamma^{-1}$, $g_1 = 0.7\gamma$ and $\Delta_1 = 0$. Black lines: $r = 0$, teal lines: $r = 1$, orange lines: $r = 1.5$ and purple lines: $r = 2$.

This tendency of the peaks towards slightly higher (absolute) detunings for $\Phi = \pi/2$ as r is increased, i.e. the increasing in the frequency distance between the two peaks, becomes even more evident by inspecting Fig. 3.5(a). In this figure we examine the resulting profile for very large values of the squeezing parameter corresponding to well beyond the state of the art squeezing. At this point we should

mention that squeezing is most usually measured in the bibliography in terms of the squeezing factor in dB units. The connection between the squeezing factor R and the squeezing parameter r used in our work, is given by the relation

$$R[dB] = -10 \log_{10}(e^{-2r}). \quad (3.12)$$

Therefore, the extremely large squeezing factor of $20dB$ reported back in 2016 [189] corresponds approximately to a squeezing parameter $r = 2.3$. As becomes evident in Fig. 3.5(a), under extreme squeezing, the resulting profile is distorted in a rather unusual way. The peaks of the profile are positioned at slightly higher detunings from the respective peak for coherent driving ($r = 0$) and the total profile is broadened mainly towards one direction. This effect can be interpreted through the particular form of the SQCS photon number distribution for $\Phi = \pi/2$. As seen in Fig. 3.2(b) the distribution exhibits a large peak at a photon number slightly higher than $|\alpha|^2$, followed by an oscillatory behaviour for larger photon numbers. As r increases, the distribution maintains its form qualitatively, but the probability of the mode (most probable value) of the distribution tends towards larger values, while the ratio of the probabilities between subsequent peaks of the distribution is decreased. This indicates that as r is increased the weight of the distribution is transferred from its mode towards the peaks of higher photon numbers, leading also to the increase of the variance of the distribution. Therefore, the splitting profile after averaging over the SQCS distribution exhibits smaller peaks but it is more broadened towards higher (absolute) detunings.

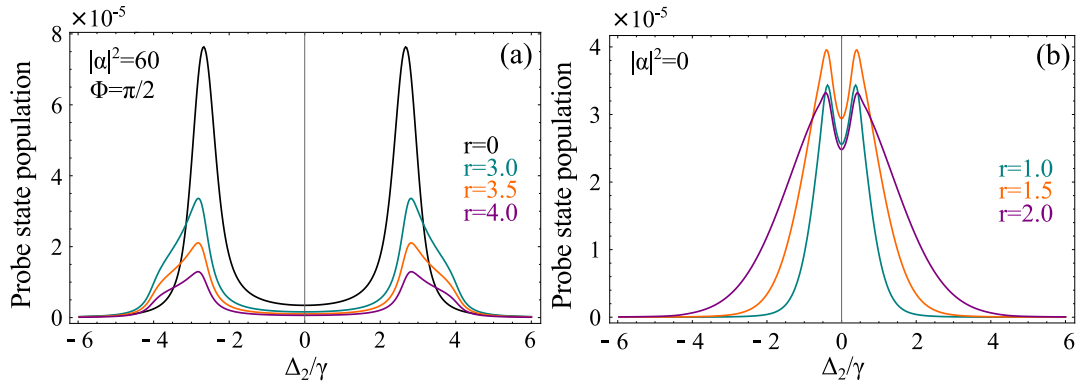


FIGURE 3.5: (a) Population of the probe state $|b\rangle$ as a function of Δ_2 for different degrees of extreme squeezing, $\Phi = \pi/2$ and $|\alpha|^2 = 60$. Black line: $r = 0$, teal line: $r = 3$, orange line: $r = 3.5$ and purple line: $r = 4$. In both panels $T = 30\gamma^{-1}$, $g_1 = 0.7\gamma$ and $\Delta_1 = 0$. (b) Population of the probe state $|b\rangle$ as a function of Δ_2 for different degrees of squeezing and $|\alpha|^2 = 0$, corresponding to a squeezed vacuum state. Teal line: $r = 1$, orange line: $r = 1.5$ and purple line: $r = 2$.

Another interesting scenario occurs for $|\alpha|^2 = 0$ but a non-zero squeezing parameter. This choice of parameters corresponds to what is widely known as a squeezed vacuum state (SQVS). The SQVS is defined as $|SQVS\rangle \equiv \hat{S}(\zeta)|0\rangle$ and its photon number distribution is given by:

$$P_{SQVS}(n) = \begin{cases} \frac{1}{\sqrt{1+\bar{n}}} \frac{(2n)!}{(n!)^2 2^{2n}} \left(\frac{\bar{n}}{1+\bar{n}} \right)^n, & n \rightarrow \text{even} \\ 0, & n \rightarrow \text{odd} \end{cases}, \quad (3.13)$$

where $\bar{n} = (\sinh r)^2$ is the mean photon number of the distribution. As seen from Eq. 3.13, the SQVS distribution exhibits oscillatory behaviour with zero values for odd photon numbers. The mode of the distribution is sharply peaked at $n = 0$ and its variance is given by the relation $(\Delta n)^2 = 2\bar{n}(\bar{n} + 1)$. In Fig. 3.5(b) we plot the population of the probe state when the strong field is initially prepared in a SQVS and notice that the position of the peaks is rather insensitive to the increasing of the squeezing parameter, while the width of the peaks are significantly increased, as one would expect by inspecting the SQVS variance for increasing r . From a physical viewpoint this sharp increase of the width is due to the superbunching effect inherent in squeezed vacuum sources, translated to strong intensity fluctuations that smear out the profile. Note that the exact shape of the profile also depends on the choice of the coupling strength g_1 , which is however chosen to be the same through all of our calculations ($g_1 = 0.7\gamma$) providing us the ability for straightforward comparison between the profiles of different figures.

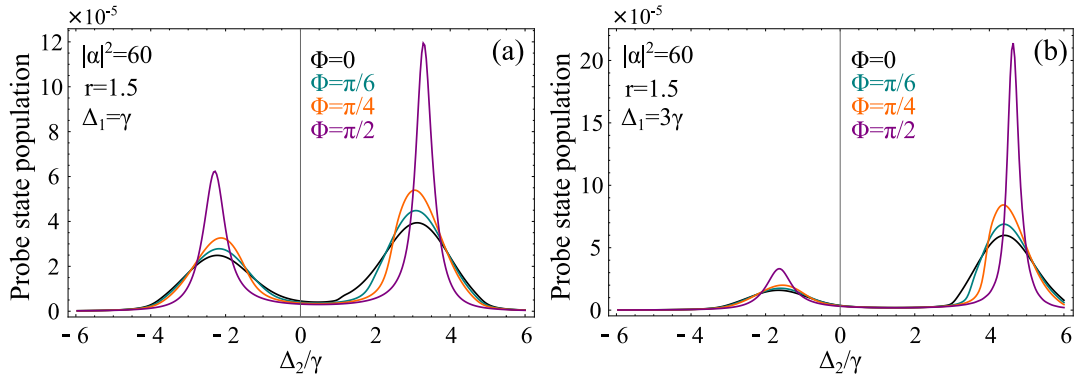


FIGURE 3.6: (a) Population of the probe state $|b\rangle$ as a function of Δ_2 for various angles Φ . The squeezed field is detuned from resonance with the $|g\rangle \leftrightarrow |a\rangle$ transition by $\Delta_1 = \gamma$. (b) Population of the probe state $|b\rangle$ as a function of Δ_2 for various angles Φ . The squeezed field is detuned from resonance with the $|g\rangle \leftrightarrow |a\rangle$ transition by $\Delta_1 = 3\gamma$. In both panels $|\alpha|^2 = 60$, $T = 30\gamma^{-1}$, $g_1 = 0.7\gamma$ and $r = 1.5$. Black lines: $\Phi = 0$, teal lines: $\Phi = \pi/6$, orange lines: $\Phi = \pi/4$ and purple lines: $\Phi = \pi/2$.

Lastly, in Fig. 3.6(a) and Fig. 3.6(b) we consider the case where the squeezed field is detuned from resonance with the $|g\rangle \leftrightarrow |a\rangle$ transition. Similarly to the case of coherent driving, the profile exhibits an asymmetry with the larger peak appearing at positive detunings for positive Δ_1 , and vice versa. This asymmetry can be interpreted in terms of the dressed states of the strong field transition [190]. The resulting doublets are expressed as linear combinations of the ground and the first excited state of the atom, with equal weights in the case of exact resonance ($\Delta_1 = 0$). However, as Δ_1 is increased, one can show that the upper dressed state of the doublet contains more of the state $|a\rangle$ and less of the ground state, while the opposite is true for the lower dressed state. In this case the probe state is connected through a larger dipole moment to the upper state of the doublet than the lower, resulting to an asymmetry in the splitting profile. The asymmetry is examined for $r = 1.5$ and various values of the phase difference Φ . As Φ is increased, the width of the two peaks is decreased and the peaks move towards slightly higher detunings (their frequency distance is increased). The width of each peak also depends on Δ_1 . Increasing Δ_1 results to the decrease of the width of the large peak and the increase of the width of the smaller one. Finally, we report that the asymmetry ratio (peak-to-peak) does not remain constant, but it increases with the increase of Φ .

To summarize, in this section we examined the Autler-Townes splitting profile resulting from the strong driving of two bound atomic states by a SQCS. The splitting was probed through a third state assumed to be weakly coupled to the upper bound state in a three-level " Λ -type" system. Since squeezed radiation is not amenable to modeling in terms of classical stochastic processes, we adopted a fully quantum mechanical treatment in terms of the resolvent operator and averaged the population of the probe state over the photon number distribution of the SQCS in the limit where the bandwidth of the squeezed field is sufficiently smaller than the natural decay of the excited state. Our results indicate that the resulting splitting profile is greatly affected by the parameters of the SQCS, i.e. the squeezing parameter r and its phase difference Φ from the complex displacement parameter. In particular, we showed that for $\Phi = 0$ the profile becomes significantly broader with the increase of r , while under the same values of parameters but with $\Phi = \pi/2$, increasing r up to 2 results to a profile resembling the one acquired with coherent driving. This degree of squeezing is well-within today's squeezing capabilities while the intensities necessary for the observation of single-photon Stark splitting in atomic systems are more or less of the order of 1 W/cm^2 [191, 192]. The case of extreme squeezing was also investigated, revealing unusual distortions of the splitting profile, as well as the cases of SQVS driving and off-resonant strong driving resulting to an asymmetric profile. To the best of our knowledge, the strong driving of a bound-bound atomic transition by a SQCS has not been experimentally tested yet. Meanwhile, the investigation of finite bandwidth effects on the system remain still an open and interesting theoretical problem.

3.2 Multi-photon double optical resonance in presence of bunched and superbunched radiation

As we saw earlier, the most conspicuous effect of intensity fluctuations on a strongly driven transition is the distortion of the profile of AC Stark splitting. When probed in double optical resonance as a function of the probe frequency, in the absence of intensity fluctuations, the profile consists of two peaks separated by the Rabi frequency. But the Rabi frequency itself, is affected by the intensity fluctuations, in a manner that depends on the order of the transition that couples the two levels and of course the stochastic properties of the field.

In what follows, we investigate the role of photon bunching and superbunching in both single-photon and two-photon transitions and apply our theory in realistic atomic transitions, exploring the effects of the order of the process in the Autler-Townes splitting profile [191]. In contrast to a single-photon transition, where the non-linearity sets in upon strong driving, two or more photon strong driving involves a non-linearity imposed on an already non-linear process. It is this "escalation", so to speak, of non-linearity in combination with the stochastic character of the driving field that introduces new effects in the system. As before, in order to single-out the role of intensity fluctuations, we have chosen to consider a source of zero bandwidth. To forestall misinterpretation of that condition, zero bandwidth here simply implies a source bandwidth sufficiently smaller than the width of the excited state; a situation which is well within experimental accessibility. Our work was motivated by the recent groundbreaking work by Spasibko et al. in which they reported the observation of up to 2 orders of magnitude enhancement in the generation of optical harmonics due to ultrafast photon-number fluctuations of a bright

squeezed vacuum source, paving the way for the experimental investigation of the role of superbunching in multi-photon transitions [147].

A schematic representation of our system is depicted in Fig. 3.7. Contrary to the system investigated in the previous section, the strongly-driven $|g\rangle \longleftrightarrow |a\rangle$ transition is now considered to be multi-photon. Since we want to apply our theory in realistic atomic transitions, the ionization of the excited state $|a\rangle$ is also included. Our aim is the exploration of the role of photon bunching and super-bunching in such "doubly" non-linear processes. To that end, the cases of chaotic and squeezed vacuum field driving are investigated and compared with the case of strong-driving by a coherent radiation field.

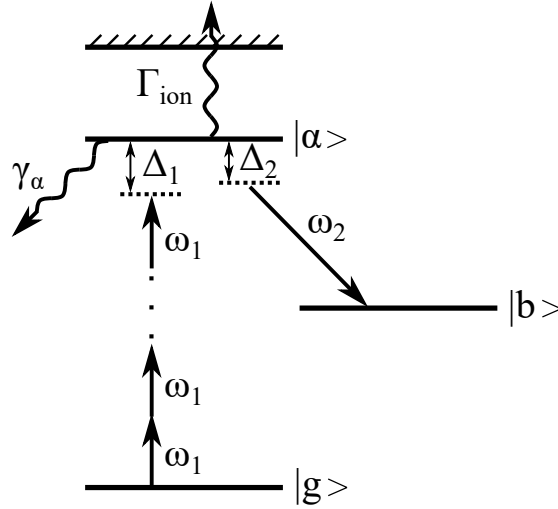


FIGURE 3.7: Schematic representation of the system under consideration. The considered system is the same as the one presented in Fig. 3.1, with the exception that the strong transition between the states $|g\rangle$ and $|a\rangle$, is considered to be a multi-photon transition. The cases of bunched and superbunched radiation are investigated. The ionization of state $|a\rangle$ is also included in the formulation.

The formulation of the problem is exactly the same as in the previous section, therefore the repetition of the theory in terms of the resolvent operator is unnecessary. The only differences are two: The first is that we make the substitution $\omega_A \rightarrow \tilde{\omega}_A = \omega_A - \frac{i}{2}(\gamma_a + \Gamma_{ion})$ to account for the spontaneous decay γ_a , as well as the ionization rate Γ_{ion} of state $|a\rangle$ via the absorption of an additional photon. Note that this method of introducing the spontaneous decay is approximate in the sense that it does not take into account the repopulation of energetically lower levels to which it decays. However, since we focus on a strong transition between $|g\rangle$ and $|a\rangle$, the induced Rabi frequency of that transition is by definition much larger than the spontaneous decay γ_a . As a result, the relative error caused by that approximation is practically negligible. The second is that the Rabi frequency of the first transition is a N -photon effective Rabi frequency and therefore is proportional to $\sqrt{n(n-1)\dots(n-N)} \approx n^N$ for large photon numbers. For that matter we adopt the notation $\Omega_1^{(N)}$ where N is the order of the process. Ω_2 is simply proportional to \sqrt{m} , since it represents a single-photon transition. Note that the matrix element V_{AI} and V_{BA} are related to the Rabi frequencies $\Omega_1^{(N)}$ and Ω_2 via the relations $\Omega_1^{(N)} = 2V_{AI}$ and $\Omega_2 = 2V_{BA}$ ($\hbar = 1$), respectively.

As before, the population of $|b\rangle$ is a function of the time as well as the photon number of the radiation field modes. The dependence on the photon numbers n

and m , comes from both, the compound system energies $\hbar\omega_I$, $\hbar\tilde{\omega}_A$ and $\hbar\omega_B$, as well as the interaction Hamiltonian matrix elements V_{AI} and V_{BA} . The ionization rate Γ_{ion} introduced in the expression of $\tilde{\omega}_A$, also depends linearly on n . The quantity of interest in this problem is the population of state $|b\rangle$ given by $P_b(t)$. Since it is solely its dependence on n and t that matters, we adopt the notation $P_b(n, t)$. If the first transition is driven strongly, i.e. if $\Omega_1^{(N)} \gg \gamma_a, \Gamma_{ion}, \Delta_1$, the interaction V between the uncoupled "atom+field" states $|I\rangle$ and $|A\rangle$, causes a splitting into doublets (Stark splitting). This splitting is here monitored through the population of state $|b\rangle$ as a function of Δ_2 , which is assumed to be coupled to $|a\rangle$ weakly, acting thus as a probe. The first transition is assumed to be on resonance, i.e. $\Delta_1 = 0$.

Following the same method as in the previous section, we find $P_b(n, t)$ by assuming the radiation field to be initially prepared in a Fock state and then average over the photon number distributions of desired field states. It should be emphasised again that this method, convenient as it may be, is strictly valid in the limit where the field bandwidth is much smaller than the natural decay of the atomic states involved in the calculation. Adopting this method, we average $P_b(n, t)$ over the photon number distributions corresponding to a coherent (Coh) field, a chaotic field (ChF) and a squeezed vacuum (SV) field state, through the formal expressions:

$$P_b^{Coh}(t) = \sum_{n=1}^{\infty} e^{-\bar{n}} \frac{\bar{n}^n}{n!} P_b(n, t) \quad (3.14)$$

$$P_b^{ChF}(t) = \sum_{n=1}^{\infty} \frac{\bar{n}^n}{(1 + \bar{n})^{n+1}} P_b(n, t) \quad (3.15)$$

$$P_b^{SV}(t) = \sum_{n=1}^{\infty} \frac{1}{\sqrt{1 + \bar{n}}} \frac{(2n)!}{(n!)^2 2^{2n}} \left(\frac{\bar{n}}{1 + \bar{n}} \right)^n P_b(2n, t) \quad (3.16)$$

Note that for an N -photon process all $P_b(n < N, t)$ terms are zero owing to the presence of V_{AI} in the numerator of Eq. (3.6), and its proportionality to $\sqrt{n(n-1)\dots(n-N)}$. The first non-zero term in Eqs. (3.14) and (3.15) is the $n = N$ term. Similarly, in the summation over the squeezed vacuum photon number distribution, the first non-zero term is the $n = N/2$ or $n = (N+1)/2$ term, depending on whether N is even or odd, respectively. The SV photon number distribution contains only even number of photons and therefore the increment of $P_b(n, t)$ in Eqn. (3.16) is $2n$.

In order for the Stark splitting to develop in realistic transitions, we need to consider large mean photon numbers ($\bar{n} \approx 10^6$ or even much larger, as the order N of the coupling is increased). This entails a serious numerical task since the averages over the photon number distributions extend far beyond \bar{n} and therefore, performing the summation through increments of n by 1 is computationally futile. One efficient way to overcome this obstacle, is to scale the problem by multiplying the photon number n , in the expression of $P_b(n, t)$, by a dimensionless scaling factor [174, 175]. The scaling renders the averaging numerically feasible, so that we can calculate the population profiles for values of \bar{n} , which correspond realistically to mean photon numbers around \bar{n} multiplied by the scaling factor. Owing to the non-linear dependence of $P_b(n, t)$ on n , the connection between realistic and scaled intensities is not straightforward. A discrepancy of a few percent [175] that may be involved is far from significant for the effects discussed herein.

In order to ensure the connection of our calculations with transitions in actual physical systems, it is important to obtain the connection between number of photons in the quantized radiation field and photon fluxes in laser pulses employed in experiments. As a calibration for our scaled parameters, we have chosen as systems

of reference the atoms of Cesium for single-photon driving and Lithium for two-photon driving. Our choice is based on earlier work [177] in which we have shown that the validity of that calibration extends beyond the specific reference systems. In that task, we need to obtain the expressions connecting $\bar{\Omega}_1^{(N)}$ and $\bar{\Gamma}_{ion}$ (mean Rabi frequency and mean ionization rate) to \bar{n} , pertaining to the $6s \rightarrow 7p$ and $2s \rightarrow 4s$ transitions in Cs and Li, respectively, including the ionization channels. Note that we do not need to calculate the exact value of the matrix element connecting $|a\rangle$ to $|b\rangle$ ($7p$ to $7s$ in Cs and $4s$ to $3p$ in Li), since $|b\rangle$ serves as a probe (weak coupling). Therefore we simply need a value for $\bar{\Omega}_2$ connecting the two excited resonances, compatible with weak coupling. Given that the averaging does not include summation with respect to m , one may always choose the proper m , which means adjusting the probe laser intensity, so as to obtain the desired weak Rabi frequency $\bar{\Omega}_2$, irrespective of the value of the atomic matrix element.

The relations that connect $\bar{\Omega}_1^{(N)}$ and $\bar{\Gamma}_{ion}$ to intensity can be found by calculating the corresponding atomic parameters [193–197]. Then, it is only the connection between the intensity and the mean photon number that is needed, in order to obtain them as a function of the latter. An approximate connection between the two is given by $\bar{n} = \frac{8\pi^3 c^2}{\omega^2} \frac{F}{\gamma_L}$ [164], where γ_L is the bandwidth of the source, ω its frequency, and F is the photon flux, connected to the intensity via the relation $F = I/N\hbar\omega$, with N being the order of the process. Note that with this definition of F , the photon flux is expressed in terms of N -tuples of photons, which means pairs of photons for two-photon driving, accounting for the fact that an N -photon transition can be completed only through the absorption/emission of N photons. It is simply a logistically convenient normalization of the number of photons driving the transition. We shall nevertheless continue using the term flux for F , as defined above. The approximation inherent in the equation connecting \bar{n} to F is such that it does not account for the exact line shape of the source. It is, however, sufficient for our purposes of this work, as it provides a relation between \bar{n} and F to within more or less a factor of 2. As pointed out at the outset, for the averaging over the photon distributions to be valid, the bandwidth of the source should be much smaller than the natural decay of state $|a\rangle$. We have therefore chosen, for both transitions, a bandwidth 100 times smaller than γ_a . The resulting parameters used for the $6s \rightarrow 7p$ ($7s$ probe) transition in Cs are: $\omega_g = 0$, $\omega_a = 2.698\text{eV}$, $\omega_b = 2.298\text{eV}$, $\Delta_1 = 0$, $\gamma_a = 0.82 \times 10^7\text{Hz}$, $\bar{\Omega}_1^{(1)} = 1.884 \times 10^4 \sqrt{\bar{n}}\text{Hz}$, $\bar{\Gamma}_{ion} = 1.181 \times 10^{-7} \bar{n}\text{Hz}$, $\gamma_L = 0.82 \times 10^5\text{Hz}$, while for the $2s \rightarrow 4s$ ($3p$ probe) transition in Li are: $\omega_g = 0$, $\omega_a = 4.372\text{eV}$, $\omega_b = 3.835\text{eV}$, $\gamma_a = 1.78 \times 10^7\text{Hz}$, $\Delta_1 = 0$, $\bar{\Omega}_1^{(2)} = 11.225 \times 10^{-7} \bar{n}\text{Hz}$, $\bar{\Gamma}_{ion} = 3.09 \times 10^{-7} \bar{n}\text{Hz}$, $\gamma_L = 1.78 \times 10^5\text{Hz}$. In both transitions the Rabi frequency connecting the excited state to the probe state is chosen to be equal to the spontaneous decay of the former. The effective two-photon dipole matrix element for the transition was calculated using the values of the single-photon dipole moments between allowed transitions in Li, via the relation [196] $\mu_{ga}^{(2)} = \sum_l \frac{\mu_{gl}\mu_{la}}{\omega_{la} + \omega_1}$. Using now the aforementioned relation between the intensity and the mean photon number we obtain the expression for $\bar{\Omega}_1$ as a function of \bar{n} .

A few explanatory remarks may be useful at this point. First, the inclusion of the ionization channels in both systems is dictated by the fact that zero detuning from resonance of the first transition ($\Delta_1 = 0$) implies that $\omega_1 = 2.698\text{eV}$ in Cs and $\omega_1 = 2.186\text{eV}$ in Li. Since the ionization thresholds lie at 3.894eV and 5.392eV in Cs and Li, respectively, the absorption of an additional photon of the first mode, while the atom is at the excited state $|a\rangle$, leads to ionization in both cases.

Second, the possible complication due to the fine structure splitting of the $7p$

state in Cs needs to be examined. Since we are working with a bandwidth much smaller than the fine structure splitting of the P line, which lies in the THz range, the spectral resolution of the source allows us to resolve such a splitting. In that case, a complete theoretical description should include both $J = 1/2$ and $J = 3/2$ states. However, since we tune exactly on resonance ($\Delta_1 = 0$) with one of the states of the doublet (for example the $J = 1/2$ state), the effect of the neighbouring state is negligible and can be safely neglected, provided the Rabi frequency is much smaller than the fine structure splitting; a condition fully satisfied in our calculations. Similarly, the fine structure splitting of the $3p$ probe state in Li does not affect our results, since we consider detunings Δ_2 in the vicinity of 10^8 Hz, much smaller than the fine structure splitting of the line.

Third, it should be noted that the description of the $2s \rightarrow 4s$ transition in Li, in terms of an effective two-photon Rabi frequency is, in general, not straightforward since the states between the $2s$ and $4s$ may introduce additional complications to the system. Our description is valid as long as the first photon in the two-photon process is sufficiently far from resonance with the nearest intermediate state. In our case the first photon with energy $\omega_1 = 2.186$ eV is detuned by $\Delta_{2p} = 0.338$ eV $\simeq 81$ THz from the $2p$ resonance in Li, which is sufficiently larger than the values of the scaled two-photon Rabi frequency we consider, which are in the vicinity of 10^8 Hz, ensuring thus the validity of our parametrization.

Finally, we should note that by calculating the population of the probe state at a time $t = T$, (referred to as interaction time) using the formalism of section II is approximately equivalent to calculating the probe state population under a square pulse of the same duration T . It is moreover well known that the difference of results under a square pulse from those under, say, a Gaussian of the same effective duration is of order 2. The only constrain on the duration is that it must not be so short that its Fourier bandwidth violates the small bandwidth condition adopted at the outset. In any case, extremely short pulses of a few cycles, such as those employed in strong field laser-matter physics [198], are Fourier limited without any stochastic fluctuations and therefore of no relevance to the matter of this chapter. Otherwise, the longer the pulse, the more signal will be collected, until of course the initial state is depleted, which is beyond typical experimental conditions of relevance to our calculations. The values of T employed in our illustrative calculations have been chosen so as to correspond to typical experimental conditions pertaining to the effects discussed herein.

In Fig. 3.8 we present the population of the probe state as a function of Δ_2 , for the case of the $|g\rangle \leftrightarrow |a\rangle$ transition driven on resonance ($\Delta_1 = 0$) by single photon coupling. It has been calculated for initial radiation fields with different quantum stochastic properties (i.e. coherent-solid black lines, chaotic-dashed teal lines and squeezed vacuum-dotted orange lines). For the comparison to be meaningful the average photon number \bar{n} is the same for all field states. In the regime of intensities corresponding to Rabi frequencies comparable to, or only a few times larger than the natural width of the upper state (Fig. 3.8(a)), increasing the intensity leads to the broadening of the profile (power broadening) [188], until it eventually splits into two peaks, exhibiting the profile of the well known Autler-Towns doublet [187], evident for all three initial field states (Fig. 3.8(b)). For the sake of calibration, we note that for the transition $6s \rightarrow 7p$ in Cs and the time of interaction assumed for Fig. 3.8, the splitting would begin becoming noticeable around $I \approx 0.17$ W/cm²; which is reasonable for a single-photon transition.

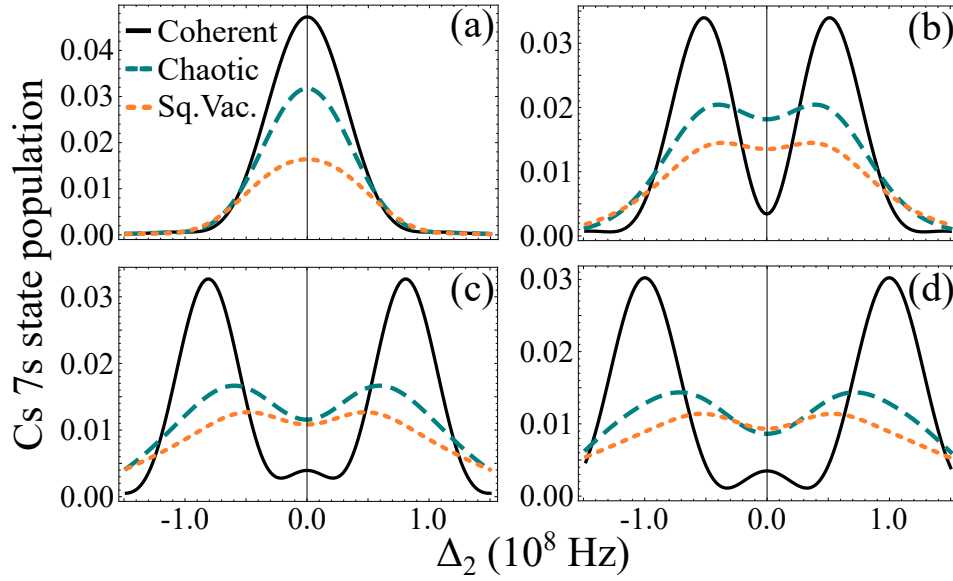


FIGURE 3.8: Single-photon Stark splitting modeled with Cesium parameters. The calculation is carried out for various types of radiation fields: coherent (solid black line), chaotic (dashed teal line) and squeezed vacuum (dotted orange line). The values of the relevant parameters used are: detuning from the first resonance $\Delta_1 = 0$, interaction time $T = 10^{-7}$ sec, laser bandwidth $\gamma_L = 0.82 \times 10^5$ Hz, scaling factor $= 4 \times 10^6$, corresponding to the intensity: (a) $I = 0.086$ W/cm², (b) $I = 0.43$ W/cm², (c) $I = 0.86$ W/cm², (d) $I = 1.29$ W/cm².

For a coherent field state, the splitting is equal to the mean Rabi frequency $\bar{\Omega}_1$ of the driven single-photon transition, while for a ChF state, with increasing intensity, it tends to the value of $\bar{\Omega}_1 / \sqrt{2}$, in agreement with earlier work [5, 6, 145, 146]. For an initial (bright) SV field state, as shown in Figs. 3.8(b) to 3.8(d), the splitting turns out to be even smaller than the one for chaotic field, at the same average intensity. In addition, both the chaotic and the SV fields induce a smearing out of the profile, as compared to that for the coherent field. This smearing stems from the strong amplitude fluctuations, entailing fluctuations of the Rabi frequency and therefore partial smearing of the doublet structure [199]. Physically, it is a consequence of the fact that, during the Rabi oscillations, two successive transitions between the two states are driven by intensities whose values have undergone a random change. A measure of that randomness is reflected in the values of the intensity correlations functions characterizing the field. Thus, in accordance with that physical picture, the smearing turns out to be more pronounced for the SV as compared to that for the ChF, compatible with the so-called superbunching of SV; a term implying intensity fluctuations stronger than those of the ChF. Therefore, in general, the behavior of a single-photon bound-bound transition driven strongly by a SV field is in overall agreement with expectations based on the combination of the results of previous studies for the ChF [5, 6, 145, 146] and the superbunching properties of the squeezed radiation. The differences in the behavior depicted in Fig. 3.8 from those earlier results turn out to be of a quantitative but not qualitative degree.

The situation changes drastically when a strongly driven two-photon transition is examined, as illustrated with the results shown in Fig. 3.9. For weak to moderate driving field strengths, again a gradual (power) broadening [200] appears (Fig. 3.9(a)), developing eventually into a doublet. Under stronger driving, however, at least two glaring surprises stand out. First, in contrast to the single-photon case,

with increasing intensity, the splitting present under driving by a coherent state, is totally absent under driving by chaotic or squeezed vacuum fields, giving rise to a single peak (Fig. 3.9(b)). Second, the width of that peak is significantly smaller than the average Rabi frequency. Moreover, inspection of Fig. 3.9(d) reveals that the width of the peak for SV driving, if anything tends to be smaller than the one for ChF driving; a rather unexpected feature since SV undergoes stronger fluctuations, in the sense that its intensity correlation functions are larger [30, 39, 147]. This counter-intuitive effect persists for even higher intensities, corresponding to mean Rabi frequencies many times larger than the spontaneous decay of the excited state (Figs. 3.9(c) and 3.9(d)).

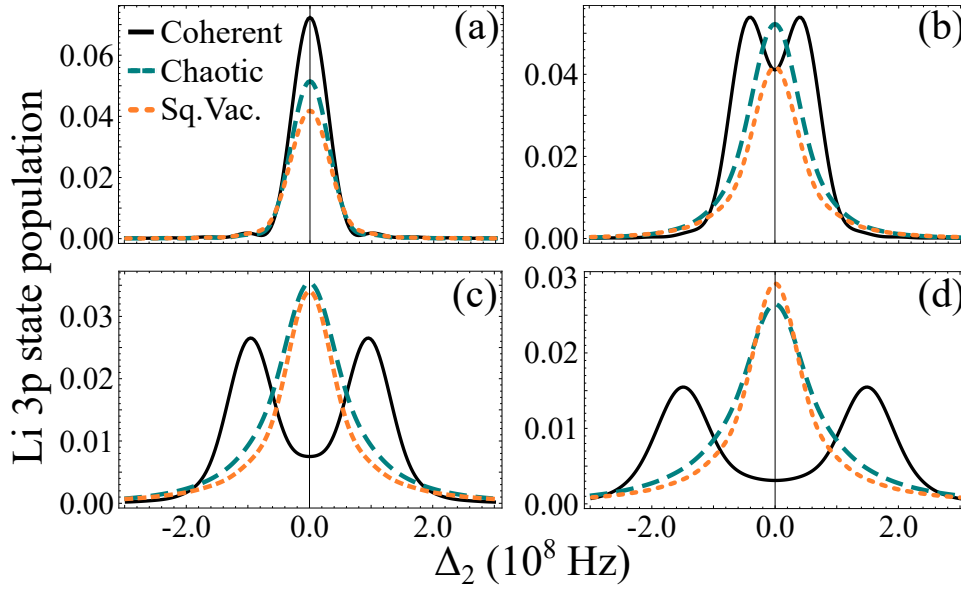


FIGURE 3.9: Two-photon Stark splitting modeled with Lithium parameters. The calculation is carried for various types of radiation fields: coherent (solid black line), chaotic (dashed teal line) and squeezed vacuum (dotted orange line). The values of the relevant parameters used are: detuning from the first resonance $\Delta_1 = 0$, interaction time $T = 10^{-7}$ sec, laser bandwidth $\gamma_L = 1.78 \times 10^5$ Hz, scaling factor $= 10^{13}$, corresponding to the intensity: (a) $I = 0.49 \times 10^6$ W/cm², (b) $I = 2.47 \times 10^6$ W/cm², (c) $I = 4.95 \times 10^6$ W/cm², (d) $I = 7.43 \times 10^6$ W/cm².

Its interpretation defies straightforward extrapolation from the physical picture for single- to two-photon transition. As detailed in the next subsection, the unexpected profile for two-photon driving results from a combination of the structure of the photon number distributions and certain features of the probe state population, associated with the order of the process. The apparent difference from earlier predictions [5, 6, 145] has to do more with the scheme of observation of the splitting than with the underlying physical picture. It does nevertheless point to an intricate interplay between the non-linearity of the transition itself and that induced by the strong driving; hence our term "compounded non-linearity".

3.2.1 Two-photon transition strongly driven by chaotic and squeezed vacuum radiation: The absence of splitting

Theory has demonstrated the absence of Stark splitting under strong two-photon driving by ChF and SV fields, but the single-peaked profile is much narrower than

the Rabi frequency. This result was unexpected for at least two reasons: (a) Since both of those sources involve strong intensity fluctuations, entailing strong fluctuations of the non-linear Rabi frequency, on physical grounds, one would have thought that the profile would be broadened by the fluctuating Rabi frequency. (b) Earlier calculations [5, 6, 145] for the case of driving by a ChF had supported that interpretation. In this subsection, we elaborate on the interpretation of the results presented above.

As will become evident, this counter-intuitive phenomenon results from the interplay between properties of the probe state population function associated with the order of the process, and the structure of the photon probability distributions of the driving fields. For the sake of contrast, we provide here calculations for single-photon driving as well.

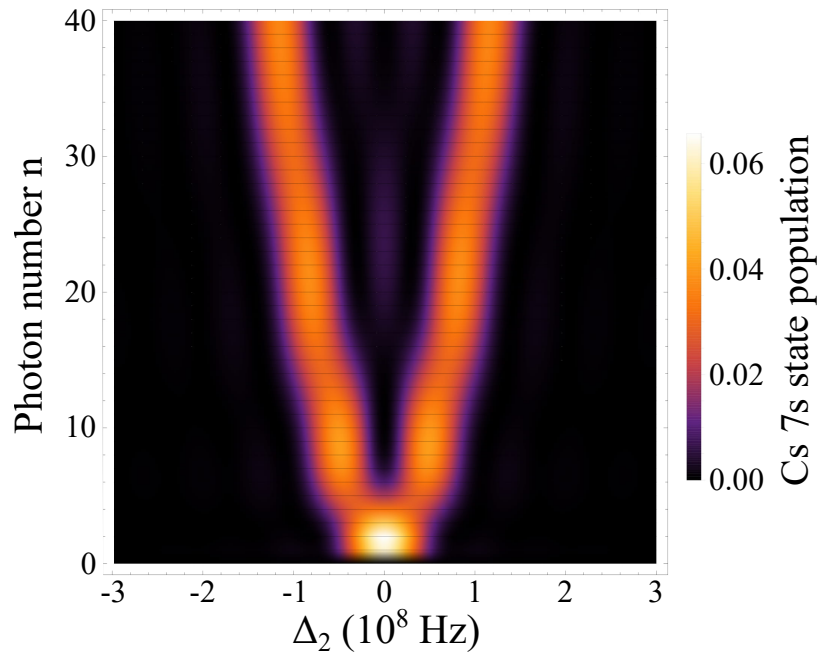


FIGURE 3.10: Probe state population under single-photon driving. Population of the 7s probe state of Cs as a function of the detuning from resonance, Δ_2 , and the photon number of the first mode, n . The quantity we plot is the population of the probe state $P_b(n, T)$ before averaging it over the photon probability distributions according to Eqs. (3.14)-(3.16). The values of the relevant parameters used are: detuning from the first resonance $\Delta_1 = 0$ and interaction time $T = 10^{-7}$ sec.

In Figs. 3.10 and 3.11 we plot the probe state population for single-photon and two-photon driving, respectively, as a function of Δ_2 and the photon number n . Note that the population of the probe state is here calculated before averaging over the photon probability distributions given by Eqs. (3.14)-(3.16), with the results corresponding to the case where the external driving field is initially prepared in a number (Fock) state.

The comparison between Figs. 3.10 and 3.11 reveals two main differences/features of the resulting profile, that are associated with the order of each process:

(I) In Fig. 3.11, under two-photon driving, the splitting of the profile for increasing photon numbers is larger and occurs much earlier than the respective splitting of the profile in Fig. 3.10 under single-photon driving. This effect is expected since

the splitting is equal to the Rabi frequency which grows as \sqrt{n} and $\sqrt{n(n-1)} \approx n$ (for large n) in the single-photon and two-photon cases, respectively.

(II) The population of the probe state for two-photon driving decreases much faster with increasing photon numbers, in comparison to single-photon driving. Even though for two-photon driving the probe state population may overall be slightly higher than the population for single-photon driving (see colour bars in 2D graphs), the population in the latter case remains almost constant for increasing n .

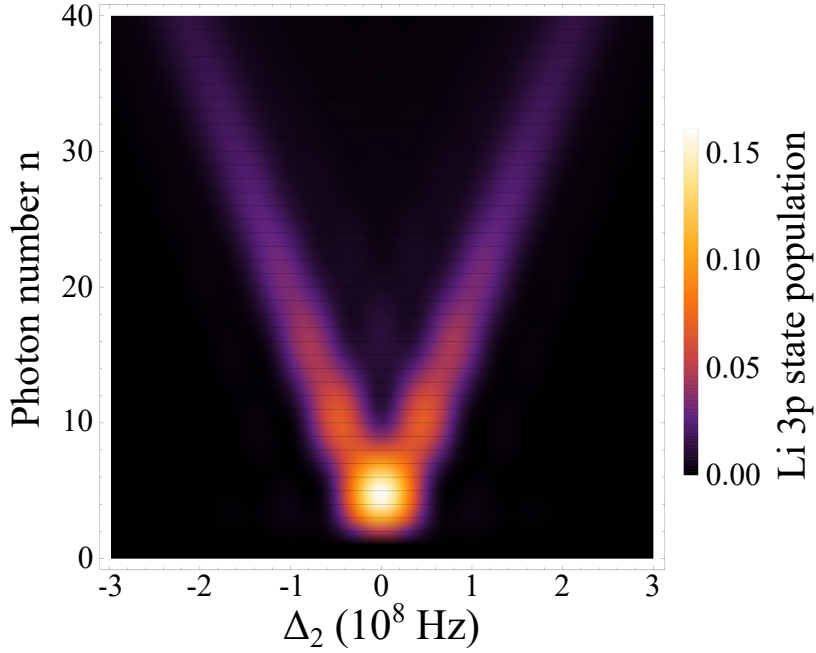


FIGURE 3.11: Probe state population under two-photon driving. Population of the 3p probe state of Li as a function of the detuning from resonance, Δ_2 , and the photon number of the first mode, n . The quantity we plot is the population of the probe state $P_b(n, T)$ before averaging it over the photon probability distributions according to Eqs. (3.14)-(3.16). The values of the relevant parameters used are: detuning from the first resonance $\Delta_1 = 0$ and interaction time $T = 10^{-7}$ sec.

Averaging over a photon probability distribution translates into performing a sum of all $P_b(n, t)$ terms, for n up to infinity, with each term weighted by the photon number probability distribution of the driving radiation field. For example, for the radiation field in a coherent state we have:

$$P_b^{coh}(t) = \sum_{n=1}^{\infty} p_{coh}(n) P_b(n, t) = p_{coh}(1) P_b(1, t) + p_{coh}(2) P_b(2, t) + \dots \quad (3.17)$$

With that in mind, the results depicted in Figs. 3.10 and 3.11 can be thought as the consequence of summing (superimposing) different stripes of the 2D plots with each stripe corresponding to a different photon number n , weighted according to the corresponding photon number probability of the field distribution.

In view of the above, the structure of the distribution is expected to play a major role in determining the resulting profile after averaging. The coherent photon number probability follows a Poissonian distribution centered always at \bar{n} with root mean square deviation $\Delta n = \sqrt{\bar{n}}$. Conversely, the distributions of the ChF and SV fields are drastically different, because for every n we have $p_{ChF}(n) > p_{ChF}(n+1)$

and $p_{SV}(2n) > p_{SV}(2n+2)$ (note that the SV probability for odd photon numbers is zero). Also for a given \bar{n} , both ChF and SV distributions exhibit much longer tails of values larger than those of the coherent state distribution (see Fig. 3.12).

For both, single- and two-photon driving, averaging over the coherent state distribution, the resulting profile stems from a superposition dominated by the stripes with photon numbers that fall more or less within the range $\bar{n} \pm 2\Delta n = n \pm 2\sqrt{\bar{n}}$, i.e. the range of photon numbers in which the Poissonian differs substantially from zero. Let us, for example, consider the case with $\bar{n} = 20$, depicted in Fig. 3.12. The stripes of Figs. 3.10 and 3.11 falling within the range of $\bar{n} \pm 2\Delta n$ do exhibit splitting. As a consequence, their superimposition will result to a profile with noticeable splitting, i.e. the stripes of neighbouring photon numbers are superimposing constructively with weights giving rise to a finite width of the total profile. Keep in mind that the connection with realistic photon numbers is obtained via multiplication by the relevant scaling factor.

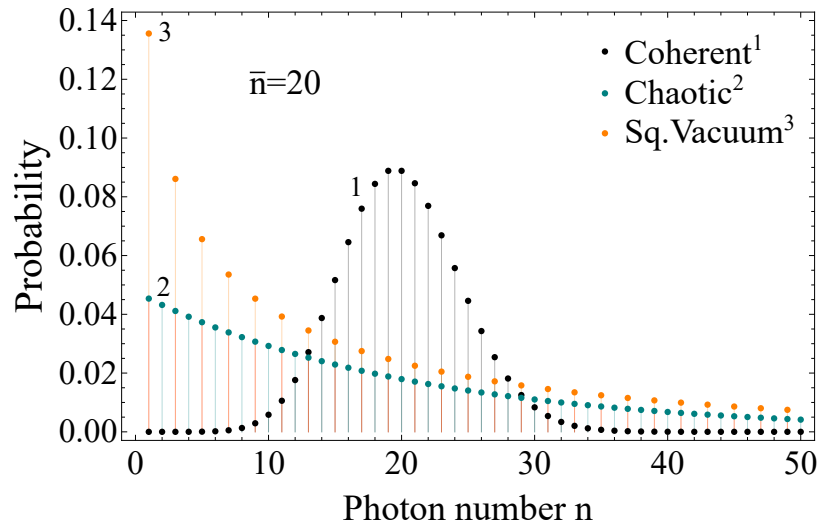


FIGURE 3.12: Photon probability distributions of the coherent¹, chaotic² and squeezed vacuum³ radiation fields for mean photon number $\bar{n} = 20$.

The situation with the SV and ChF distributions is, however, quite different, because now the contributions (weights) of low photon number stripes are always more significant than those of larger n , irrespective of the value of \bar{n} . One might then expect that in both, the single- and the two-photon, cases no splitting would appear, since the profile would be dominated by stripes corresponding to relatively low photon numbers, for which no noticeable splitting is expected. Yet, there is a striking difference between the profiles for the two cases, which should be expected in view of the properties (I) and (II) discussed above. Owing to the combination of (I) and (II), for single-photon photon driving, the stripes of neighboring photon numbers are increasingly similar to each other for increasing photon numbers. In contrast, the respective stripes for the two-photon case exhibit rapid variations, in both the magnitude of the splitting as well as the values of the probe state population. These properties in combination with the long tails of the ChF and SV field distributions conspire to the following situation: In the single-photon case, even if the weights of the low photon number stripes are larger, as n increases, the higher photon number stripes are becoming increasingly similar (see Fig. 4) leading to a constructive superimposition that results to a profile with noticeable splitting. This

constructive superimposition is minimized for very large n because the ChF and SV field distributions, depending on the choice of \bar{n} , are approaching zero. Of course the contribution of the low photon number stripes (that are not exhibiting Stark splitting) is always there, leading to a filled out profile in the vicinity of $\Delta_2 = 0$ (see Fig. 3.10 for comparison with the coherent field profile). Conversely, this constructive phenomenon cannot persist in the two-photon case where, with increasing n , the splitting is constantly increasing, whereas the probe state population is decreasing very rapidly. In that case, after averaging, the low photon number stripes (no-splitting stripes) have the dominant contribution resulting to a smeared out profile always peaked at $\Delta_2 = 0$.

It should now be evident that this complex compounded non-linearity phenomenon arises from the interplay between the order of the process (reflected in properties (I) and (II) of the probe state population profile) and the strong driving by ChF and SV fields, whose distributions have long tails, satisfying the conditions $p_{ChF}(n) > p_{ChF}(n+1)$ and $p_{SV}(2n) > p_{SV}(2n+2)$.

To sum up, in undertaking this work, we aimed at extending previous work [5, 6, 145] so that, in view of recent experimental advances [147], effects that had remained in the realm of theory could at last be explored experimentally in order to shed light into the theoretical models. The underlying physical picture according to earlier work was that the intensity fluctuations inherent in the chaotic field, imprinted on the Rabi frequency would smear out the splitting. And since squeezed vacuum radiation exhibits stronger fluctuations, the smearing of the splitting ought to be more pronounced. That smearing had been documented theoretically for single-photon driving by a chaotic field, with supporting evidence that, under driving by two or more photons, the double-peak profile would be overshadowed by a broad profile. Physically, that made sense because, beyond single-photon driving, the Rabi frequency is proportional to an intensity correlation function of second or higher order, which entails enhancement owing to bunching, as discussed previously. Yet, our results revealed a more nuanced situation, whose interpretation required a detailed examination of the probing of the splitting.

Under single-photon driving by a classical or coherent state field, the structure of the AC splitting profile, whether observed through fluorescence (to the initial or a third state) or through double resonance, exhibits similar features reflecting the Rabi frequency. The only qualitative difference is that, in resonance fluorescence there are three peaks, with the side peaks separated by two times the Rabi frequency of the strong transition, whereas in double resonance or fluorescence to a third state, there are two peaks separated by one time this Rabi frequency. This is expected to be valid, even under two or more photon driving, in compatibility with our results. It is also valid if the driving field undergoes only phase fluctuations. The situation, however, changes drastically under driving by fields undergoing intensity fluctuations. As documented in this section, an intricate interplay between population of the upper state by the strong stochastic field and depopulation by the weak (free of fluctuations) probe field, introduces a sensitivity to the detailed structure of the photon number distribution; with the consequence of a single peak much narrower than the Rabi frequency. Even more surprisingly, that single peak under driving by SV radiation, if anything, tends to be narrower than the one under driving by a chaotic field, whose fluctuations are "weaker" than those of SV. As for resonance fluorescence (which means decay to the initial state), in a two-level system driven by a two-photon transition, it entails spontaneous two-photon decay; a hopelessly weak process. The behavior of AC Stark splitting in fluorescence to a third state, which is possible and observable, should be in overall compatibility with our findings. We

should note that, nevertheless, formal models of AC Stark splitting in two-photon resonance fluorescence driven by fields without stochastic fluctuations have been published [201–203], but without quantitative connection to any specific physical system.

Finally, we should not close this section without drawing attention to a route towards the exploration of these effects at wavelengths beyond the optical range. The recent explosive development of FEL (Free Electron Lasers) short wavelength sources, extending up to hard X-rays, offers the immediate possibility of experimental investigation of strongly driven two-photon transitions at XUV wavelengths; say, at photon energies up to about 150 eV. At those wavelengths, transitions involving subvalence electrons lead to Auger decay. SASE-FEL sources are known to exhibit stochastic behavior [204, 205] similar to that of the chaotic field. The effect of that behavior on an Auger resonance strongly driven by a single photon transition, probed through double resonance, has been studied theoretically [126], with results that mirror earlier theoretical findings in the optical range [5, 6]. However, more recent state of the art advances [206] at the Fermi FEL have demonstrated the possibility of manipulating the stochastic properties of the FEL through seeding with coherent radiation. We would therefore suggest that, using that source with controllable seeding, offers the possibility of strong two-photon driving of an Auger resonance. The uniqueness of such a project lies in the combination of controllable stochastic properties with two-photon strong driving, in an entirely new wavelength range involving subvalence electrons. True, it cannot involve SV radiation, but as we have stressed throughout this section, much remains to be done experimentally even for chaotic radiation; with the additional novelty of a two-photon driven Auger resonance. Still, to start with, even the experimental investigation of single-photon driving of an Auger resonance by stochastic radiation, represents unknown territory.

Chapter 4

Photon statistics effects in multi-photon Schwinger pair production

As described in section 2.2.3, the advent of the free-electron laser (FEL) revived the interest in the problem of electron-positron pair creation in vacuum, since FEL sources provide strong, tightly focused radiation with energies up to the hard X-ray regime. Given the huge theoretical activity over the past few years on the topic of vacuum pair creation using ultrastrong radiation [207, 208], it is the purpose of this chapter to introduce and explore an aspect that seems to have escaped attention until now. That is the possibility of enhancement of the Schwinger mechanism owing to the intrinsic stochastic fluctuations of FEL sources, and if possible, to explore the range of intensities over which such enhancement could be expected to be significant.

4.1 Possibility of multi-photon enhancement under strong FEL radiation

The stochastic properties of self-amplified spontaneous emission (SASE) FEL sources have been documented quite extensively through theoretical [126, 127, 209, 210] as well as experimental studies [204, 206, 211–213]. Briefly, their stochastic properties are akin to those of chaotic (thermal) radiation [7, 8]. The feature of that radiation of direct relevance to our considerations is the strong intensity fluctuations, presently in the near sub-fs time scale, implying spiky behavior during the pulse, which is known to affect the yield of processes whose rate depends on the intensity in a non-linear fashion [126, 127, 179, 180].

Before embarking on the formal and computational details, it would be helpful to establish the qualitative context of the problem at hand. In any arrangement involving a laser for the observation of pair creation, that laser will necessarily be pulsed. The particular temporal shape is of secondary importance but the pulse duration, as characterized by the full width at half maximum (FWHM), would be of decisive importance. To clarify the reason for its importance we need to consider the various time scales at play in the underlying physical process. One of those time scales is the transition time (TT), which is the time within which the photons must be absorbed for the process to be completed. The initial state is the vacuum with the final state being the continuum of the pair e^-e^+ . The energy gap that the absorption of the photons must bridge for the pair to be created is 1.022MeV . There are no real intermediate states within the gap. The process has to proceed via virtual intermediate states of the continuum which energetically lie 1.022MeV above the initial state. Let

us take, for example, the case of 10 photon absorption which would require photons of energy a bit more than 0.1MeV , which is also the energy of the first virtual state. Its wavefunction consists of a linear superposition of all continuum states. Its "lifetime" is the inverse of its detuning from the nearest state with allowed transition, which in this case is the continuum threshold detuned by about 0.9MeV . This corresponds to a lifetime of about $4 \times 10^{-6}\text{fs}$. Obviously the process must be completed within that time. Put otherwise, the other photons must arrive before the virtual state ceases to exist. The laser pulse duration provides the second time scale, the interaction time (IT), by which we mean the time interval during which the fields are present to induce pair creation. For the time being and possibly the near future, the pulse duration of any conceivable laser at any wavelength will be orders of magnitude longer than the above TT. Therefore, the IT can be assumed to be much longer than the TT. If we are to contemplate a short wavelength laser in the X-ray range, even for photon energy of say 10keV , the field period (the third time scale) is about $4 \times 10^{-4}\text{fs}$, two orders of magnitude longer than the TT. For all practical purposes, at present the pulse duration of an X-ray FEL cannot be expected to be much shorter than $0.1 - 1\text{fs}$. In the light of the above time scales, it should be clear that the TT is so short compared to the other time scales that pair creation in the presence of a laser is essentially an instantaneous process.

Let us now examine what exactly happens during a pulse. Assume that the intensity is such that at the peak of the pulse $\gamma \ll 1$ which entails tunneling (see section 2.2.3). As the pulse rises and falls, however, it goes through ranges of intensity for which $\gamma \gg 1$ where multi-photon transition dominates and which actually is more efficient [70–72, 87]. This means that under the reality of a pulse, in the end the pairs produced will have been created via multi-photon absorption, as well as tunneling around the peak of the pulse. If the temporal pulse shape is smooth, say a Gaussian, all we need is to integrate the pair production over the pulse shape. If on the other hand the pulse is not smooth but the intensity undergoes stochastic fluctuations, integration over a pulse shape is impossible. In that case, we need to work with averaging over the stochastic fluctuations. If the equations governing the rate of the process depend on the laser intensity non-linearly, the averaging does not lead to the replacement of the instantaneous intensity by the average intensity, as would have been the case for a linear dependence. It does instead lead to a more complex dependence, the form of which depends on the stochastic properties of the source and the type of non-linearity. The possible relevance of that issue stems from a well established precedence in the long history of multi-photon processes in atomic systems. As mentioned in chapter 3, it is known that the rate of an N -photon process, far from resonance with real intermediate states, depends on the N^{th} order intensity correlation function [5, 6, 179, 180]. And since correlation functions depend on the stochastic properties of the radiation, the rate of even the simplest non-linear process such as the above can be affected dramatically by intensity fluctuations. If we consider, for example, an 11-photon process induced by thermal radiation whose N^{th} order intensity correlation function is given by $N! \times I^N$, where I is the average intensity, that process would be enhanced by a factor of about 10^7 , as compared to the same process under a smooth pulse without the fluctuations of the thermal source. That is an example of a relatively simple non-linearity, in that the dependence on intensity is proportional to a single correlation function, which reduces to a power of the intensity for a smooth pulse.

The situation becomes much more complex when for a smooth pulse the rate is a complicated function of the intensity, as that entails the dependence of the rate on a complicated function of a stochastic variable. In that case, it is far from evident

whether averaging over the fluctuations will lead to enhancement of the rate. One might expect that in the regime of multi-photon dominance in the rate, there may be some enhancement, the details of which are examined in the sections that follow. A helpful physical picture provides some insight into the role of intensity fluctuations, if we note that intensity fluctuations such as those of thermal radiation imply random spikes of intensity during the pulse. Some of those spikes will have a peak intensity much higher than the peak of the average intensity. Since a non-linear function of the intensity involves high powers of the instantaneous values, spikes with intensity higher than the average will tend to enhance disproportionately the high powers of the function. In the case of a process depending on a single power of the intensity, the enhancement caused by spikes is obvious. To summarise our basic argument, the time scales entering pair production mediated by laser radiation satisfy the conditions for the influence of intensity fluctuations on the rate of the process.

The case of short wavelength FEL is of particular interest in that context, because as already noted above, typical FEL's are known to exhibit strong intensity fluctuations very similar to those of thermal (chaotic) radiation. Although, in principle, the effect of fluctuations can be analyzed mathematically for any photon frequency, in this work we restrict our analysis to very short wavelength FEL sources of photon energies above the 10keV range. For the time being, pulse durations of FEL's are at best in the fs range, with plans underway towards sub-femtosecond pulses. Even if we were to assume pulse duration of 1 attosecond, in the photon energy range of $10 - 100\text{keV}$ such a pulse would span tens of cycles, which makes it much larger than the TT. If the pulse undergoes intensity fluctuations, the relative time scales allow their influence on the rate of pair creation. It bears repeating that whether the result is enhancement of the rate, remains to be explored through the quantitative analysis in the sections that follow.

Aside from the theoretical ideas on the possible role of intensity fluctuations in pair creation, our motivation for this work was inspired by known results in multi-photon ionization of atoms, where enhancement of the order of $N!$ has been observed a long time ago, in processes of order as high as $N = 11$ [179, 180]. In atoms, in addition to the initial ground state and the ionization potential, there are infinitely many real intermediate states which can happen to be in near resonance with the absorption of a number of photons smaller than N . When the order of the overall process is, let us say 10, at most 2 but most often 1 real intermediate states can be in near resonance to a degree that can violate the overall non-resonant condition. In that case, the enhancement will be slightly lower than $N!$, but still quite significant, as large as for example a factor 10^7 observed in [179, 180]. Curiously, there is one atomic system whose ionization bears an uncanny similarity with pair creation. That is the negative ion of hydrogen whose binding energy is 0.754eV . It has a ground state and a continuum, without any real intermediate states. Although at much lower photon energies, its multi-photon ionization (technically called detachment) has been studied theoretically as well as experimentally [214–216]. There is on the other hand a crucial difference between multi-photon break up of an atom or molecule and pair creation in vacuum. The interaction region in laser-atom interactions contains a finite number of atoms. As a result, even unlimited intensity will not help beyond the point of complete ionization of the species in the interaction volume. And this can happen even before the pulse reaches its peak [217]. Vacuum on the other hand is an infinite sea from which pairs can be created as long as there are photons present. It is therefore reasonable to expect that, at least in the multi-photon regime of $\gamma \gg 1$ an enhancement of the order of $N!$ would be obtained.

4.2 Conservation laws and the standing wave hypothesis

Electromagnetic fields can be characterized using a gauge and Lorentz invariant approach in terms of the electromagnetic field strength tensor $F^{\mu\nu}$ and its dual, $\tilde{F}^{\mu\nu} = \frac{1}{2}\epsilon^{\mu\nu\alpha\beta}F_{\alpha\beta}$ ($\epsilon^{\mu\nu\alpha\beta}$ is the rank-four Levi-Civita tensor), as:

$$\mathcal{F} = \frac{1}{4}F_{\mu\nu}F^{\mu\nu} = -\frac{1}{2}(\vec{E}^2 - \vec{B}^2), \quad (4.1a)$$

$$\mathcal{G} = \frac{1}{4}F_{\mu\nu}\tilde{F}^{\mu\nu} = c\vec{E} \cdot \vec{B}. \quad (4.1b)$$

It is generally known that e^-e^+ pair creation cannot occur either in the light-like field of a plane monochromatic wave, which is always characterized by $\mathcal{F} = 0 = \mathcal{G}$, or in a field characterized by $\mathcal{F} > 0$ and $\mathcal{G} = 0$, corresponding to a pure magnetic field. On the other hand, pair creation can occur in fields described by $\mathcal{F} < 0$ and $\mathcal{G} = 0$. Brezin and Itzykson were the first to calculate the pair production rate by a spatially uniform periodic electric field [69], stating that such a field could be realised by proper optical focusing of laser beams in the laboratory. In view of some concern about pair production using this method [218], it was argued that another more effective method of realising such a field would be via the creation of a standing wave formed by the superposition of two counter-propagating coherent laser beams of the same wavelength λ [70–72, 74, 75, 88, 106]. In this idealized scenario pair production can occur in an antinode of the standing wave at lengths $l \ll \lambda$, such that the spatial inhomogeneities of the field can be neglected to a good approximation. Extensions that take into account the temporal behavior of the resulting laser pulse [219] as well as spatial inhomogeneities [220] have also been considered, while a detailed analysis of the Schwinger pair creation using counter-propagating laser pulses can be found in the paper by G. R. Mocken et al. [107]. We should also note that pair production can occur in plasma-like media as has been discussed in a series of papers by H. K. Avetissian et al. [221, 222].

Following the lines of previous works based on the conceptual experiment of pair creation by an idealized standing wave, we generalize part of the problem by including the presence of amplitude (intensity) fluctuations in the initial beams and show that such fluctuations could eventually lead to large enhancement of the created pairs. Specifically, we focus on the study of pair creation resulting from a standing wave formed by the interference of two counter-propagating FEL beams of the same wavelength that undergo amplitude fluctuations, i.e. beams of the form $\mathcal{E}_t^{(1)}\cos(\omega t - \mathbf{k} \cdot \mathbf{r})$ and $\mathcal{E}_t^{(2)}\cos(\omega t + \mathbf{k} \cdot \mathbf{r})$, where the index "t" denotes the stochastic character of the amplitudes and \mathbf{k} is the beam wavevector. In this scenario, the resulting field is equal to $(\mathcal{E}_t^{(1)} + \mathcal{E}_t^{(2)})\cos(\omega t)\cos(\mathbf{k} \cdot \mathbf{r}) + (\mathcal{E}_t^{(1)} - \mathcal{E}_t^{(2)})\sin(\omega t)\sin(\mathbf{k} \cdot \mathbf{r})$. Adopting the approximation $\mathbf{k} \cdot \mathbf{r} \ll 1$, which is based on the assumption that pair creation occurs at lengths smaller than the wavelength of the beams [102], the resulting field is, to a good approximation, a standing wave of the form $\mathcal{E}_t\cos(\omega t)$, where $\mathcal{E}_t = \mathcal{E}_t^{(1)} + \mathcal{E}_t^{(2)}$. In particular, we consider the case in which both $\mathcal{E}_t^{(1)}$ and $\mathcal{E}_t^{(2)}$ undergo Gaussian amplitude fluctuations, corresponding to those of an ideal chaotic state. In that case, the first-order intensity correlation function \tilde{G}_1 of the resulting field is two times the first-order intensity correlation function of the chaotic

field G_1^{chao} , since:

$$\begin{aligned}\tilde{G}_1 &\equiv \langle \mathcal{E}_t^* \mathcal{E}_{t'} \rangle = \left\langle \left(\mathcal{E}_t^{(1)*} + \mathcal{E}_t^{(2)*} \right) \left(\mathcal{E}_{t'}^{(1)} + \mathcal{E}_{t'}^{(2)} \right) \right\rangle \\ &= \left\langle \mathcal{E}_t^{(1)*} \mathcal{E}_{t'}^{(1)} + \mathcal{E}_t^{(1)*} \mathcal{E}_{t'}^{(2)} + \mathcal{E}_t^{(2)*} \mathcal{E}_{t'}^{(1)} + \mathcal{E}_t^{(2)*} \mathcal{E}_{t'}^{(2)} \right\rangle \\ &= \left\langle \mathcal{E}_t^{(1)*} \mathcal{E}_{t'}^{(1)} \right\rangle + \left\langle \mathcal{E}_t^{(2)*} \mathcal{E}_{t'}^{(2)} \right\rangle = 2G_1^{chao},\end{aligned}\tag{4.2}$$

given the fact that no amplitude correlation exists between the two beams. It is straightforward to show that this result persists even for correlations functions of arbitrary order. Therefore, for the N th-order (normal-ordered) intensity correlation function of the resulting field we can prove that

$$\tilde{G}_N = 2G_N^{chao}.\tag{4.3}$$

The effects of this result on pair creation are discussed in the next section. A brief clarification should be made at this point regarding the connection with FEL radiation: As is generally known, apart from amplitude fluctuations, FEL radiation does also exhibit fluctuations in phase [126, 127, 207], making the standing wave hypothesis even more challenging to realise experimentally. The reason we do not include this type of fluctuations in the formulation is twofold: First, the problem of vacuum e^-e^+ pair creation in the presence of fields that undergo fluctuations both in amplitude and phase is considerably more complex, while the tools that have been developed for treating analogous problems in atomic transitions [5, 6, 146] are not directly applicable to the problem at hand. Second, the inclusion of phase fluctuations resulting to a finite field bandwidth is not expected to notably affect the measured signal of created pairs, since the process of pair creation, when operating in the multi-photon regime, is ultimately an N -photon escape process, involving no intermediate resonances. And in this case the role of field bandwidth is essentially irrelevant. Therefore, in what follows we are interested solely in examining how the presence of fluctuations in the amplitude of the resulting standing wave may affect the total number of created pairs [223].

4.3 Multi-photon enhancement of vacuum e^-e^+ pair creation

A few years after the paper of Brezin and Itzykson [69], Popov extended their work using the imaginary time method [224] and determined more accurately the pre-exponential factor in the expression of the rate of vacuum pair creation. For the details of this derivation we refer the reader to [70–72, 85–87]. Assuming a monochromatic laser field of the form $\mathcal{E} \cos(\omega t)$ focused down to the diffraction limit, Popov obtained the following expressions for the number of e^-e^+ created pairs in the $\gamma \ll 1$ and $\gamma \gg 1$ limits, corresponding to the tunneling and multi-photon regimes, respectively:

$$N(\mathcal{E}) = 2^{-3/2} N_0^4 \left(\frac{\mathcal{E}}{\mathcal{E}_c} \right)^{5/2} \times \exp \left[-\frac{\pi \mathcal{E}_c}{\mathcal{E}} \left(1 - \frac{1}{2N_0^2 \left(\frac{\mathcal{E}}{\mathcal{E}_c} \right)^2} \right) \right] \left(\frac{\omega \tau}{2\pi} \right), \quad \gamma \ll 1,\tag{4.4a}$$

$$N(\mathcal{E}) \approx 2\pi N_0^{3/2} \left(\frac{8\mathcal{E}_c}{N_0 e \mathcal{E}} \right)^{-2N_0} \left(\frac{\omega \tau}{2\pi} \right), \quad \gamma \gg 1,\tag{4.4b}$$

where \mathcal{E} is the amplitude of the electric field, $\mathcal{E}_c = \frac{m_e^2 c^3}{e\hbar} = 1.32 \times 10^{16}$ V/cm is the critical electric field value calculated by Schwinger [67], τ is the interaction time and $N_0 = \frac{2mc^2}{\hbar\omega}$ is the minimum number of photons needed for vacuum pair creation to occur at a given frequency. Comparison between Eqs. (4.4a) and (4.4b) reveals that pair creation in the multi-photon regime is far more effective than pair creation in the tunneling regime due to the exponential suppression of the latter for $\mathcal{E} < \mathcal{E}_c$. Given that the electric field amplitude is proportional to the square root of the intensity, Eqs. (4.4a) and (4.4b) can also be written in the form:

$$N(I) = 2^{-3/2} N_0^4 \left(\frac{I}{I_c} \right)^{5/4} \times \exp \left[-\pi \sqrt{\frac{I_c}{I}} \left(1 - \frac{1}{2N_0^2 \left(\frac{I}{I_c} \right)} \right) \right] \left(\frac{\omega\tau}{2\pi} \right), \quad \gamma \ll 1, \quad (4.5a)$$

$$N(I) \approx 2\pi N_0^{3/2} \left(\frac{8}{N_0 e} \right)^{-2N_0} \left(\frac{I}{I_c} \right)^{N_0} \left(\frac{\omega\tau}{2\pi} \right), \quad \gamma \gg 1, \quad (4.5b)$$

where e is the Euler's constant, I is the intensity of the electric field and $I_c = 4.65 \times 10^{29}$ W/cm² is the intensity corresponding to \mathcal{E}_c .

As also noted in the chapter 2, one of the key results in quantum optics when working under the zero bandwidth approximation is that the effects of any type of radiation field on a transition can be captured by first solving a problem assuming a harmonically oscillating field of constant amplitude ($\mathcal{E} \cos(\omega t)$) and then average over the intensity distribution corresponding to the radiation field considered [5]. We use this method to calculate the number of pairs created by the amplitude fluctuating standing wave field considered in the previous subsection.

Inspection of Eq. (4.5) reveals that the number of pairs created for $\gamma \gg 1$ is proportional to the intensity to the power of N_0 , i.e. the N_0 -th order intensity correlation function of the harmonically oscillating field of constant amplitude, as expected for a multi-photon transition that involves no intermediate resonances. Given that: (i) all the information about the effects of the coherence properties of a considered field on such a multi-photon transition is contained in its intensity correlation function, (ii) the N -th order intensity correlation function of the standing wave field resulting from the interference of the two counter-propagating beams with Gaussian amplitude fluctuations is twice that of the chaotic field as shown in the previous section and (iii) the intensity distribution of the chaotic field is $p(I') = \frac{e^{-I'}}{I'}$, where I is the mean intensity, it is straightforward to argue that the resulting number of e^-e^+ pairs created by such a standing wave field, in the zero bandwidth approximation, is:

$$\tilde{N}(I) = 2 \int_0^\infty N(I') \frac{e^{-I'}}{I'} dI', \quad (4.6)$$

where the factor of 2 is direct consequence of Eq. (4.3).

Using now the expressions for the number of created pairs in each regime, one can show that in the limit of zero intensities, the number of e^-e^+ pairs created by such a field is $2N_0!$ times larger than the respective number of pairs created in the case of a harmonically oscillating of constant amplitude, i.e.

$$\lim_{I \rightarrow 0^+} \frac{\tilde{N}(I)}{N(I)} = 2N_0!, \quad (4.7)$$

where N_0 is the minimum number of photons participating in the process. The details of this calculation is presented in Appendix A. Note that since γ is inversely proportional to the square root of the intensity and the integral over the intensity in Eq. (4.6) extends from zero up to infinity, we split the integration into two parts; namely from 0 to I_b (multi-photon regime) and from I_b up to infinity (tunneling regime), where I_b is the intensity corresponding to $\gamma = 1$. We should note that this method is not generally valid for arbitrary intensities since (i) there practically exists no sharp boundary between these two regimes and (ii) the considered formulas of Eqs. (4.5a) and (4.5b) give only an approximate expression of the number of created pairs in the $\gamma \sim 1$ regime in which they are joined in order of magnitude as N_0 decreases. However, in what follows we will limit our discussion to intensities lower than $I = 0.01I_c$. In this case the considered approximation is expected to give a good estimation of the total number of created pairs and the reason behind this has to do

with the specific form of the intensity distribution $p(I') = \frac{e^{-I'}}{I'}$ as a function of I' for different values of I . In particular, $p(I')$ is decreasing for increasing I' but this occurs faster for smaller values of I . And even in the maximum considered case of $I = 0.01I_c$, due to the exponential factor, the contribution of the terms with about $I' \geq 0.02I_c$ is already small. This has two consequences: Firstly, the integral corresponding to the tunneling regime, i.e. $2 \int_{I_b}^{\infty} N(I') \frac{e^{-I'}}{I'} dI'$ does not give a substantial contribution to the total number of created pairs \tilde{N} . This is due to the fact that the boundary intensity corresponding to $\gamma = 1$, which can be expressed as $I_b = \frac{4}{N_0^2} I_c$, is already larger than $0.02I_c$ for all N_0 up to 14, resulting to the suppression of the number of pairs due to the exponentially decaying factor. Therefore the main contribution to the total number of pairs generally arises from the multi-photon integral $2 \int_0^{I_b} N(I') \frac{e^{-I'}}{I'} dI'$. Secondly, as far as the multi-photon integral is concerned, even if Eq. (4.5b) gives only an order of magnitude approximation of the created pairs as we approach the $\gamma \sim 1$ regime, or in other words the intensity boundary I_b , if the considered number of photons participating in the process is approximately up to 14, the terms in the vicinity of the non-perturbative multi-photon regime ($\gamma \sim 1$) have relatively smaller weights and do not contribute significantly to the resulting number of created pairs \tilde{N} . In view of the above, we limit our discussion to photon orders up to about $N_0 = 14$ and to intensities up to about $I = 0.01I_c$ in order to ensure the validity of our approximation. Note that for arbitrary intensities and orders N_0 one cannot use this approach to the problem at hand.

Using this method, one can prove the validity of Eq. (4.7) in the zero field limit, regardless of the exact choice of the boundary (this is due to the consequence of taking the limit $I \rightarrow 0^+$ as discussed in Appendix A).

Eq. (4.7) is a direct consequence of the proportionality of the number of created pairs to the intensity correlation function of the field, which for a chaotic field is $N_0!$ larger than the respective correlation function of the coherent field. Of course in the limit of zero intensities the number of created pairs is practically zero, therefore the presence of such an enhancement factor does not seem to be useful. However, numerical calculations of the created pairs number ratio as a function of the intensity using Eq. (4.6), reveal that this enhancement factor persists over a large intensity window which depends on the order of the process, extending up to the strong field regime (Fig. 4.1).

In Fig. 4.1 we plot the ratio of the number of e^-e^+ pairs created by the field resulting from the collision of two counter-propagating FEL beams that undergo amplitude fluctuations with Gaussian statistics over the number of e^-e^+ pairs created

by a harmonically oscillating field, for various orders N_0 . Fixing N_0 in each considered case implies that the two kinds of beams have the same energy when the ratio \tilde{N}/N is calculated. As seen, there exists a large intensity plateau over which the ratio remains equal to the expected value $2N_0!$ of the zero field limit. The range of the intensity plateau strongly depends on the order of the process N_0 , as it decreases while N_0 is increased. The deviation from the $2N_0!$ factor is attributed to the presence of tunnelling whose role becomes increasingly important with the increase of intensity. In other words, in an imaginable scenario where there was no tunnelling regime present in the problem at hand and the number of created pairs were given by Eq. (4.5b) for every intensity, it would be easy to show that after averaging the enhancement factor $2N_0!$ would persist for any given intensity. Given that the enhancement factor, depending on the minimum number of photons participating in the process, can reach very high values, it is our purpose on this section to examine whether and under which combination of parameters such an enhancement could be utilized to experimentally observe the Schwinger vacuum pair creation under the considered configuration.

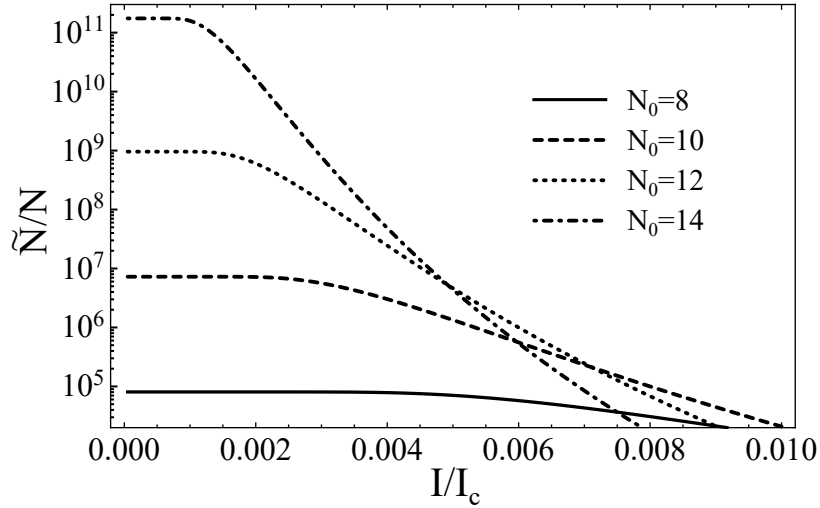


FIGURE 4.1: Ratio of the number of e^-e^+ pairs created by a field that results from the collision of two counter-propagating FEL beams that undergo Gaussian amplitude fluctuations over the number of e^-e^+ pairs created by a harmonically oscillating field of the form $\mathcal{E}\cos(\omega t)$. The ratio is plotted as a function of the intensity for different values of N_0 . The range of the intensity plateau over which the ratio remains equal to predicted low field value $2N_0!$ is increasingly larger for smaller values of N_0 . The values of N_0 used are: $N_0 = 8$ (solid line), $N_0 = 10$ (dashed line), $N_0 = 12$ (dotted line) and $N_0 = 14$ (dash-dotted line).

Given that the parameter γ is expressed in terms of the intensity as $\gamma = \frac{\hbar\omega}{mc^2} \sqrt{\frac{I_c}{I}}$ and that the minimum number of photons participating in the process is $N_0 = \frac{2mc^2}{\hbar\omega}$, we can write that:

$$\gamma = \frac{2}{N_0} \sqrt{\frac{I_c}{I}}. \quad (4.8)$$

According to Eq. (4.8), γ is inversely proportional to the order of the process N_0 . Let us for example examine the case of $N_0 = 14$, corresponding to the photon energy $\hbar\omega = 73\text{keV}$. In this case the enhancement factor \tilde{N}/N reaches the maximum value $2N_0! = 1.74 \times 10^{11}$ and persists for intensities up to $I \cong 0.001I_c$ (see Fig. 4.1). However, even if the enhancement factor seems very large, for intensities around

$I \cong 0.001I_c$ the number of created pairs by an harmonically oscillating field is of the order of 10^{-15} (for an interaction time $\tau = 50fs$), therefore an enhancement factor of the order of 10^{11} does not lead to an observable number of pairs. In this case one could try to increase the intensity in order to create more pairs. However, the drawback in this case would be that, for the intensities such that the number of created pairs is measurable, according to Eq. (4.8), the parameter γ would be such that pair creation would gradually approach the tunneling regime. On the other hand, using a much lower photon number, say $N_0 = 5$, the maximum enhancement factor would be only $2N_0! = 240$ and the corresponding energy of the photons needed to observe the process would be extremely high ($\hbar\omega \approx 204keV$).

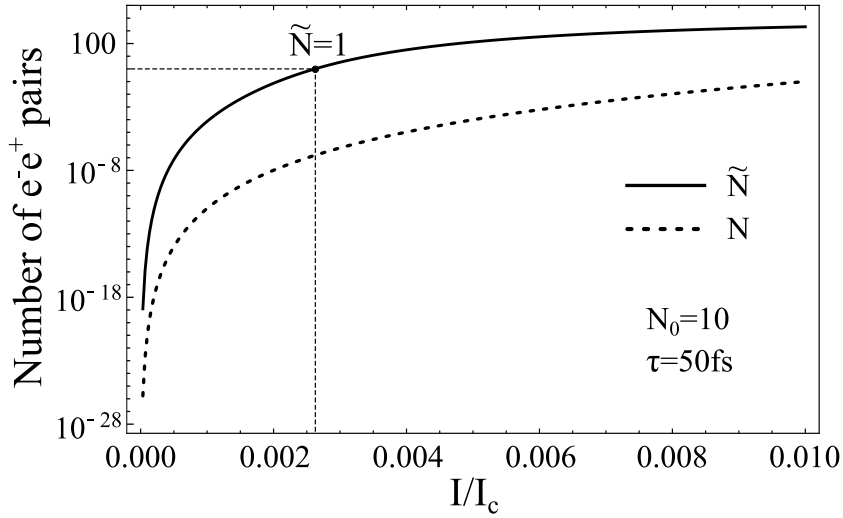


FIGURE 4.2: Number of e^-e^+ pairs created by a field that results from the collision of two counter-propagating FEL beams that undergo Gaussian amplitude fluctuations (solid line), compared to the respective number of pairs created by a harmonically oscillating field of the form $\mathcal{E}\cos(\omega t)$ (dotted line). The parameters used are: minimum number of photons $N_0 = 10$ and interaction time $\tau = 50fs$. The vertical axis is presented in logarithmic scale and the dashed line corresponds to the intensity such that $\tilde{N} = 1$.

In view of the above, we consider an intermediate scenario where $N_0 = 10$, corresponding to photon energies $\hbar\omega \approx 102keV$. The threshold of 100keV photons, even seemingly high, is expected to be reached in the near future based on recent studies on technical design plans and simulations confirming the possibility of obtaining such high-energy FEL photons in the European XFEL facilities [225, 226]. In addition to this, several years ago, works on multi-photon ionization experiments in atomic systems with chaotic radiation have reported the observation of the expected non-linear multi-photon enhancement for processes of such a high-order [179, 180]. Therefore it seems legitimate to investigate the case of pair creation via the absorption of 10 photons.

As can be seen in Fig. 4.1, for a 10-photon process, a maximum enhancement factor of $2N_0! = 7.26 \times 10^6$, for intensities up to $I \cong 0.0028I_c$ can be expected. In Fig. 4.2 we plot the actual number of the created e^-e^+ pairs as a function of the intensity, both for the harmonically oscillating field of the form $\mathcal{E}\cos(\omega t)$ (dotted line), as well as for the field resulting from the collision of two counter-propagating FEL beams that undergo amplitude fluctuations with Gaussian statistics (solid line). The calculation has assumed interaction time of $\tau = 50fs$, but one can easily obtain the resulting number of pairs for any interaction time, owing to the linear dependence

of $N(I)$ and $\tilde{N}(I)$ on τ . As is evident in Fig. 4.2, the number of pairs created using a field of the form $\mathcal{E}\cos(\omega t)$ is very low for intensities below the critical intensity I_c . However, by taking advantage of the large enhancement factor for $N_0 = 10$, \tilde{N} becomes sufficiently large to be experimentally detectable at lower intensities. The intensity at which $\tilde{N} = 1$ (dashed line), is approximately $I \cong 0.0026I_c$ and according to Eq. 4.8 corresponds to $\gamma \cong 3.9$. This intensity may become even lower as long as one can achieve larger interaction times τ . Intensities of that magnitude are likely to be available in the future in FEL facilities such as the European XFEL [225, 226] or the SULF in China [227].

A few further comments regarding the assumptions underlying this work are in order at this point. The derivation of Eqs. (4.4a) and (4.4b) for the number of created pairs provided by Popov are based on the assumption that the number of pairs are calculated in a volume equal to $\Delta V = \lambda^3$. This assumption can of course be revised by multiplying the resulting equations with the proper scaling factors. Note that one does not need to focus the radiation field down to the diffraction limit (which for high energy photons becomes increasingly difficult) in order to achieve the desired field intensity, as long as there is adequate power to balance the effect of less tight focusing. Moreover, even if the calculations are based on the standing wave hypothesis, extended in a way that includes the stochastic character of the amplitudes of the individual beams, it is obvious that one does not need a standing wave in order to observe the non-linear multi-photon enhancement in pair creation induced by the fluctuating fields. However, the adoption of this hypothesis is useful in view of the additional factor of 2 that one obtains in the resulting number of created pairs, based on Eq. (4.3). One could of course approach the problem from a solely numerical perspective, by using the quantum Vlasov equations along the lines of the work of I. Sitiwaldi and Bai-Song Xie [207], in combination with a Gaussian stochastic modulation of the amplitude, using Monte Carlo techniques. However, this method would not provide any additional insight to the present work as far as the non-linear multi-photon enhancement factor is concerned. Finally, as described in the previous section, our calculations involve the notion of an intensity boundary between the multi-photon and the tunneling regime, necessary in order to perform the integration in Eq. (4.6). Even though a sharp boundary does not really exist between these two regimes, splitting Eq. (4.6) into two integrals and calculating them separately using Eqs. (4.5a) and (4.5b) is expected to give a good estimate of the expected number of created pairs for $N_0 = 10$ and for intensities up to $I = 0.01I_c$, as discussed in the previous section.

In the light of our results, it appears that the role of intensity fluctuations in enhancing non-linear strong field phenomena may be exploited advantageously in Schwinger pair production. Our results, based as they are on approaches in the existing literature, may also be used in combination with other methods aiming at enhancing the yield of pair creation. To the best of our knowledge, the problem has so far been explored only theoretically. The stumbling block towards experimental verification has been the availability of appropriate laser sources. This is particularly crucial for FEL sources which, however, are still under constant development. The source ideally suited for the experimental exploration of our predictions would be a SASE FEL with photon energy range around 100 keV. As mentioned before, the possibility of developing FEL's in that photon energy range has been addressed in quite recent theoretical studies [225, 226]. Considering the fact that about 40 years ago an X-ray laser was viewed as science fiction, in view of the rapid development of hard X-ray FEL's within the last 15 years or so, the availability in the near future of an FEL in the above photon energy range would not seem too optimistic. Be that as

it may, intensity fluctuations are apt to play an intriguing role in pair creation under FEL radiation, if other issues related to focusing etc. can be addressed.

Part II

Open quantum systems' dynamics

Chapter 5

Theoretical Background

5.1 Markovian and non-Markovian processes

5.1.1 General Description

The study of open quantum system's dynamics is largely based on the understanding of the concept of stochastic processes, i.e. processes describing the evolution in time of a random phenomenon. Stochastic processes are divided in two big categories, namely the Markovian and the non-Markovian processes. Traditional Markovian processes assume that the present state of a system depends solely on its immediate past, independent of the entire history leading up to that point. However, many real-world phenomena exhibit intricate temporal dependencies that cannot be adequately captured by the simplifying assumption of memoryless transitions. This has given rise to the study of non-Markovian processes, which account for the influence of past events and the persistence of memory. Non-Markovian processes opened up ways to explore complex dynamics, and they are present across many phenomena in various fields of physics [24]. In this chapter, we provide a general introductory description of the Markovian and non-Markovian processes and some of their basic properties [12].

First, let us introduce the concept of a dynamical map [12]. Consider a compound system that consists of two parts denoted by S and B , standing for "System" and "Bath", respectively. In most cases, the system S is characterized by just a few degrees of freedom, in contrast to the bath, which is often assumed to be much larger than S and, more often than not, is effectively described by infinite degrees of freedom. Suppose that at $t = 0$ the compound system is prepared at an uncorrelated product state of the form $\rho(0) = \rho_S(0) \otimes \rho_B$, where $\rho_S(0)$ is the density matrix describing the initial state of system S , and ρ_B is the density matrix describing a reference state of the bath (a thermal equilibrium state in example). The change of the reduced system S from the initial state to the state at some time $t > 0$, is described by the following transformation:

$$\rho_S(0) \mapsto \rho_S(t) = \hat{V}(t)\rho_S(0) \equiv \text{Tr}_B \hat{U}(t,0)[\rho_S(0) \otimes \rho_B] \hat{U}^\dagger(t,0), \quad (5.1)$$

where $\hat{U}(t,0)$ is the time-evolution operator of the compound system and Tr_B denotes the partial trace over the degrees of freedom of the environment B . If we regard the reference state ρ_B and the final time t to be fixed, Eq. (5.1) defines a map from the space of density matrices, denoted by $\mathcal{S}(\hat{\mathcal{H}}_S)$, where $\hat{\mathcal{H}}_S$ is the Hamiltonian of the system S , into itself, i.e.

$$\hat{V}(t) : \mathcal{S}(\hat{\mathcal{H}}_S) \mapsto \mathcal{S}(\hat{\mathcal{H}}_S), \quad (5.2)$$

which is called "dynamical map" and is characterized completely in terms of operators pertaining to the Hilbert space of S . If we decompose the density matrix of B in an orthonormal basis $|\varphi_\alpha\rangle$ of \mathcal{H}_B , i.e.

$$\rho_B = \sum_{\alpha} \lambda_{\alpha} |\varphi_{\alpha}\rangle \langle \varphi_{\alpha}|, \quad (5.3)$$

where λ_{α} are non-negative real numbers satisfying $\sum_{\alpha} \lambda_{\alpha} = 1$, then Eq. (5.1), yields:

$$\hat{V}(t)\rho_S = \sum_{\alpha,\beta} \hat{W}_{\alpha\beta}(t)\rho_S \hat{W}_{\alpha\beta}^{\dagger}(t), \quad (5.4)$$

where the operators $\hat{W}_{\alpha\beta}(t)$ are defined as

$$\hat{W}_{\alpha\beta}(t) = \sqrt{\lambda_{\beta}} \langle \varphi_{\alpha} | \hat{U}(t,0) | \varphi_{\beta} \rangle. \quad (5.5)$$

and they satisfy the condition

$$\sum_{\alpha,\beta} \hat{W}_{\alpha\beta}^{\dagger}(t) \hat{W}_{\alpha\beta}(t) = \hat{\mathcal{I}}_S, \quad (5.6)$$

where $\hat{\mathcal{I}}_S$ is the identity operator acting on S . Using the above equation, it is straightforward to show that

$$\text{Tr}_S[\hat{V}(t)\rho_S] = \text{Tr}_S(\rho_S) = 1. \quad (5.7)$$

Hence, we conclude that a dynamical map $\hat{V}(t)$ represents a completely positive and trace-preserving quantum operation. If we allow t to vary, we get a family of dynamical maps, $\{\hat{V}(t)|t \geq 0\}$, with $V(0)$ being the identity map, that describes the whole time evolution of the open system. If the characteristic time scales over which the reservoir correlation functions decay are very small, to the point where it is justified to neglect memory effects in the reduced system dynamics, then the process is Markovian. The Markovian case is formalized in terms of the following dynamical map property:

$$\hat{V}(t_1)\hat{V}(t_2) = \hat{V}(t_1 + t_2), \quad t_1, t_2 \geq 0. \quad (5.8)$$

Given a family of dynamical maps, $\{\hat{V}(t)|t \geq 0\}$, there exists a linear map \mathcal{L} , which allows to express $\hat{V}(t)$ in the exponential form:

$$\hat{V}(t) = e^{(\hat{\mathcal{L}}t)}, \quad (5.9)$$

in view of which one can obtain the following first-order differential equation describing the dynamics of the reduced system:

$$\frac{d}{dt}\rho_S(t) = \hat{\mathcal{L}}\rho_S(t). \quad (5.10)$$

Note that $\hat{\mathcal{L}}$ is a superoperator acting upon $\rho_S(t)$, often called Liouville superoperator. By starting from this equation, one can derive the so-called Markovian quantum master equation, found in every open quantum systems' textbook [12], which reads:

$$\frac{d}{dt}\rho_S(t) = \hat{\mathcal{L}}\rho_S(t) = -i[\hat{\mathcal{H}}, \rho_S] + \sum_{k=1}^{N^2-1} \gamma_k \left(A_k \rho_S A_k^{\dagger} - \frac{1}{2} A_k^{\dagger} A_k \rho_S - \frac{1}{2} \rho_S A_k^{\dagger} A_k \right). \quad (5.11)$$

In the above equation, $\hat{\mathcal{H}}$ is the Hamiltonian of the system, γ_k is the relaxation rate of the k_{th} decay channel of the open system, that is expressed in terms of the correlation functions of the environment, N is the dimension of the Hilbert space \mathcal{H}_S , and A_k are the so-called Lindblad operators that describe the interaction of the subsystem with the environment. The Lindblad operators may acquire various forms, depending on the particular model considered under study. We should note that the derivation of Eq. (5.11) is based on two important approximations, namely, the Markov approximation which implies that the spectral density of the environment is slowly varying as a function of the frequency in the vicinity of the system's resonances, and the Born approximation which implies a weak coupling between B and S .

Although, Eq. (5.11) is generally successful in predicting the time evolution of the system in the Markovian limit, more often than not, the environments involved in realistic open quantum systems are not characterized by smooth spectral densities and therefore non-Markovian features come into play, resulting in a more complex dynamical behaviour of the system. In what follows we review two well-known techniques which allow the systematic description of non-Markovian dynamics of open systems, namely, the Nakajima-Zwanzig method and the time-convolutionless projection operator method [12].

5.1.2 The Nakajima-Zwanzig method

Let us consider a system S coupled to an environment B . The dynamics of the compound system ($S + B$) are described by a Hamiltonian of the form

$$\hat{\mathcal{H}} = \hat{\mathcal{H}}_0 + \alpha \hat{\mathcal{H}}_I, \quad (5.12)$$

where $\hat{\mathcal{H}}_0$ describes the time evolution of the uncoupled compound system, $\hat{\mathcal{H}}_I$ is the interaction Hamiltonian, and α is a dimensionless expansion parameter. The dynamics of the density matrix of the compound system, $\rho(t)$, in the interaction representation, are given by the following equation of motion ($\hbar = 1$):

$$\frac{\partial}{\partial t} \rho(t) = -i\alpha [\hat{\mathcal{H}}_I(t), \rho(t)] \equiv \alpha \hat{\mathcal{L}} \rho(t), \quad (5.13)$$

where by $\hat{\mathcal{L}}$ we denote the Liouville superoperator, and $\hat{\mathcal{H}}_I(t)$ is the interaction picture representation of the interaction Hamiltonian, defined by

$$\hat{\mathcal{H}}_I(t) = \exp(i\hat{\mathcal{H}}_0 t) \hat{\mathcal{H}}_I \exp(-i\hat{\mathcal{H}}_0 t). \quad (5.14)$$

Our purpose is the derivation of an exact master equation describing the dynamics of ρ_S . For that matter, it is convenient to define a superoperator $\hat{\mathcal{P}}$, that acts on ρ as follows:

$$\rho \mapsto \hat{\mathcal{P}}\rho = \text{Tr}_B(\rho) \otimes \rho_B \equiv \rho_S \otimes \rho_B, \quad (5.15)$$

where ρ_B is some fixed state of the environment. Accordingly, we define a complementary super-operator $\hat{\mathcal{Q}}$ as:

$$\hat{\mathcal{Q}}\rho = \rho - \hat{\mathcal{P}}\rho. \quad (5.16)$$

The superoperators $\hat{\mathcal{P}}$ and $\hat{\mathcal{Q}}$ are maps in the state space of the compound system Hilbert space $\hat{\mathcal{H}} = \hat{\mathcal{H}}_S \otimes \hat{\mathcal{H}}_B$ and they obey the following properties:

$$\hat{\mathcal{P}} + \hat{\mathcal{Q}} = \hat{\mathcal{I}}, \quad (5.17a)$$

$$\hat{\mathcal{P}}^2 = \hat{\mathcal{P}}, \quad (5.17b)$$

$$\hat{Q}^2 = \hat{Q}, \quad (5.17c)$$

$$\hat{P}\hat{Q} = \hat{Q}\hat{P} = 0, \quad (5.17d)$$

where \hat{I} is the identity operator. By acting with the projection operators \hat{P} and \hat{Q} in Eq. (5.13), the following coupled differential equations are obtained:

$$\frac{\partial}{\partial t}\hat{P}\rho(t) = \hat{P}\frac{\partial}{\partial t}\rho(t) = \alpha\hat{P}\hat{L}(t)\rho(t), \quad (5.18a)$$

$$\frac{\partial}{\partial t}\hat{Q}\rho(t) = \hat{Q}\frac{\partial}{\partial t}\rho(t) = \alpha\hat{Q}\hat{L}(t)\rho(t). \quad (5.18b)$$

By inserting the identity operator $\hat{I} = \hat{P} + \hat{Q}$ between $\hat{L}(t)$ and $\rho(t)$, the above set of equations can be also written as:

$$\frac{\partial}{\partial t}\hat{P}\rho(t) = \alpha\hat{P}\hat{L}(t)\hat{P}\rho(t) + \alpha\hat{P}\hat{L}(t)\hat{Q}\rho(t), \quad (5.19a)$$

$$\frac{\partial}{\partial t}\hat{Q}\rho(t) = \alpha\hat{Q}\hat{L}(t)\hat{P}\rho(t) + \alpha\hat{Q}\hat{L}(t)\hat{Q}\rho(t). \quad (5.19b)$$

Formal integration of Eq. (5.19b) yields:

$$\hat{Q}\rho(t) = \hat{G}(t, t_0)\hat{Q}\rho(t_0) + \alpha \int_{t_0}^t ds \hat{G}(t, s)\hat{Q}\hat{L}(s)\hat{P}\rho(s), \quad (5.20)$$

where t_0 is some arbitrary initial time, and $\hat{G}(t, s)$ is a propagator defined by the following equation:

$$\hat{G}(t, s) \equiv \hat{T}_{\leftarrow} \exp \left[\alpha \int_{t_0}^t ds' \hat{Q}\hat{L}(s') \right]. \quad (5.21)$$

\hat{T}_{\leftarrow} is a chronological time ordering operator that orders any product of superoperators such that their time arguments increase from right to left. Note that the propagator $\hat{G}(t, s)$ satisfies the following differential equation:

$$\frac{\partial}{\partial t}\hat{G}(t, s) = \alpha\hat{Q}\hat{L}(t)\hat{G}(t, s), \quad (5.22)$$

with the initial condition

$$\hat{G}(s, s) = \hat{I}. \quad (5.23)$$

Substitution of Eq. (5.20) back to Eq. (5.19a), yields:

$$\begin{aligned} \frac{\partial}{\partial t}\hat{P}\rho(t) = & \alpha\hat{P}\hat{L}(t)\hat{G}(t, t_0)\hat{Q}\rho(t_0) + \alpha\hat{P}\hat{L}(t)\hat{P}\rho(t) \\ & + \alpha^2 \int_{t_0}^t ds \hat{P}\hat{L}(t)\hat{G}(t, s)\hat{Q}\hat{L}(s)\hat{P}\rho(s). \end{aligned} \quad (5.24)$$

Eq. (5.24) is known as the Nakajima-Zwanzig equation. The integral term in the right-hand side of Eq. (5.24) depends on the past history of the system in the time interval $[t_0, t]$, hence Eq. (5.24) captures non-Markovian features in the dynamics of the open system. The main drawback of the Nakajima-Zwanzig method is that Eq. (5.24) may be very difficult to solve for specific systems. In this case perturbation expansions are necessary in order to capture aspects of the open system dynamics. Usually Eq. (5.24) is expanded in terms of the coupling constant α , i.e. in powers

of the interaction Hamiltonian, or in time. In some cases it might also be convenient to perform the perturbation expansion for the Laplace transform of $\rho_S(t)$ in the Schrödinger picture.

5.1.3 The time-convolutionless projection operator method

In those cases where the Nakajima-Zwanzig equation show practical disadvantages due to its complexity, a method developed by Shibata et al. [228–230] may be applicable, which provides a technique of finding a systematic expansion of the dynamics of the system of interest in terms of its coupling strength to the environment. This method is called "the time-convolutionless projection operator method" and its aim is to eliminate the dependence of the time evolution of the density matrix on the history of the system, and therefore to provide the derivation an exact master equation which is local in time [12]. Following the definitions introduced in the previous section, the density matrix $\rho(s)$ appearing in the right-hand side of Eq. (5.20) is now replaced by the relation:

$$\rho(s) = \hat{G}(t, s)(\hat{\mathcal{P}} + \hat{\mathcal{Q}})\rho(t), \quad (5.25)$$

where $\hat{G}(t, s)$ is now the backward propagator of the composite system, defined as:

$$\hat{G}(t, s) \equiv \hat{T}_{\rightarrow} \exp \left[-\alpha \int_s^t ds' \hat{\mathcal{L}}(s') \right], \quad (5.26)$$

with \hat{T}_{\rightarrow} indicating antichronological time-ordering. In view of Eq. (5.25), Eq. (5.20) can be written as:

$$\hat{\mathcal{Q}}\rho(t) = \hat{\mathcal{G}}(t, t_0)\hat{\mathcal{Q}}\rho(t_0) + \alpha \int_{t_0}^t ds \hat{\mathcal{G}}(t, s) \hat{\mathcal{Q}}\hat{\mathcal{L}}(s) \hat{\mathcal{P}}\hat{G}(t, s)(\hat{\mathcal{P}} + \hat{\mathcal{Q}})\rho(t). \quad (5.27)$$

The above equation can be further written as:

$$[1 - \hat{\Sigma}(t)]\hat{\mathcal{Q}}\rho(t) = \hat{\mathcal{G}}(t, t_0)\hat{\mathcal{Q}}\rho(t_0) + \hat{\Sigma}(t)\hat{\mathcal{P}}\rho(t), \quad (5.28)$$

by introducing the superoperator

$$\hat{\Sigma}(t) \equiv \alpha \int_{t_0}^t ds \hat{\mathcal{G}}(t, s) \hat{\mathcal{Q}}\hat{\mathcal{L}}(s) \hat{\mathcal{P}}\hat{G}(t, s), \quad (5.29)$$

that satisfies the properties $\hat{\Sigma}(t_0) = 0$ and $\hat{\Sigma}(t)|_{\alpha=0} = 0$. The factor $[1 - \hat{\Sigma}(t)]$ in Eq. (5.28) may be inverted for small α or in any case for small $t - t_0$, resulting to the following equation:

$$\hat{\mathcal{Q}}\rho(t) = [1 - \hat{\Sigma}(t)]^{-1}\hat{\Sigma}(t)\hat{\mathcal{P}}\rho(t) + [1 - \hat{\Sigma}(t)]^{-1}\hat{\mathcal{G}}(t, t_0)\hat{\mathcal{Q}}\rho(t_0). \quad (5.30)$$

Eq. (5.30) implies that the value of $\hat{\mathcal{Q}}\rho(t)$ at time t is determined by the value of $\hat{\mathcal{P}}\rho(t)$ at time t and the initial condition $\hat{\mathcal{Q}}\rho(t_0)$. The advantage of this equation is that the dependence of the history of evolution (which appears in Eq. (5.24)) has now been removed by introducing $\hat{G}(t, s)$. However, it must always be kept in mind that (5.30) is only valid for weak couplings and/or for small values of $t - t_0$. We now substitute Eq. (5.24) back to Eq. (5.19a) and find the exact time-convolutionless

(TCL) master equation,

$$\frac{\partial}{\partial t} \hat{\mathcal{P}}\rho(t) = \hat{\mathcal{K}}(t) \hat{\mathcal{P}}\rho(t) + \hat{\mathcal{M}}(t) \hat{\mathcal{Q}}\rho(t_0), \quad (5.31)$$

where we defined the time-local superoperator $\hat{\mathcal{K}}(t)$ (TCL generator) as:

$$\hat{\mathcal{K}}(t) \equiv \alpha \hat{\mathcal{P}} \hat{\mathcal{L}}(t) [1 - \hat{\Sigma}(t)]^{-1} \hat{\mathcal{P}}, \quad (5.32)$$

and the inhomogeneity superoperator $\hat{\mathcal{M}}(t)$ as:

$$\hat{\mathcal{M}}(t) = \alpha \hat{\mathcal{P}} \hat{\mathcal{L}}(t) [1 - \hat{\Sigma}(t)]^{-1} \hat{\mathcal{G}}(t, t_0) \hat{\mathcal{Q}}. \quad (5.33)$$

The TCL master equation, given by Eq. (5.31), is exact and local in time. The superoperators $\hat{\mathcal{K}}(t)$ and $\hat{\mathcal{M}}(t)$ are generally complicated objects, however they are usually expanded in powers of the coupling strength α , ultimately allowing one to find approximate solutions of Eq. (5.31) [12].

5.2 Elements of quantum information

Quantum information theory is a rather new field of physics that provides ways of manipulating information at the quantum level. It encompasses the principles of quantum mechanics to exploit quantum phenomena such as superposition and entanglement for information processing tasks. Quantum information processing holds great promise for advancements in various fields, including cryptography [3], computation [231], and communication [20]. However, the realization of practical quantum technologies faces significant challenges due to the unavoidable interaction between quantum systems and their surrounding environments. This is where the field of open quantum systems comes into play, aiming to understand and control the detrimental effects of noise and decoherence on quantum information [232]. By studying the dynamics of quantum systems coupled to their environment, open quantum systems theory provides tools for characterizing, modeling, and controlling the interactions that hinder the preservation and manipulation of quantum information [233]. The field investigates topics such as quantum error correction [18], quantum control [234], and quantum measurements in the presence of noise and decoherence [235]. Additionally, it explores novel approaches for protecting quantum information against environmental effects through the design of fault-tolerant quantum codes [236] and the implementation of error mitigation strategies [237].

In this section we aim at providing a brief overview of the phenomenon of quantum entanglement, as well as the phenomenon of quantum state transfer, as they form the basis of understanding the topics discussed in the following chapters of the thesis.

5.2.1 Quantum entanglement

The study of quantum correlations represents lies at the heart of quantum information science, revealing properties that distinguish quantum systems from classical ones. An important benchmark in the exploration of quantum correlations was the seminal work of Einstein, Podolsky, and Rosen (EPR) in 1935, which challenged the completeness of quantum mechanics by highlighting the existence of entangled states that exhibited seemingly non-local correlations [238]. This profound insight led to the development of Bell's theorem in 1964, which mathematically formalized

the notion that no local realistic theory could reproduce all the predictions of quantum mechanics [239]. Bell's theorem spurred intensive experimental efforts to test the violation of Bell inequalities and confirm the existence of non-local correlations, culminating in the groundbreaking experiments conducted by Alain Aspect and his colleagues in the 1980s [240]. These experiments provided evidence for the entanglement of distant quantum systems, solidifying the foundations of quantum correlations and opening up the potential of utilizing them in quantum technologies.

The exploration of quantum correlations has not been limited to entanglement alone. Over the years, several quantum correlations have been explored, such as quantum discord or quantum steering. Quantum discord, captures the quantumness of correlations beyond entanglement, encompassing situations where quantum systems possess non-classical correlations that cannot be explained by classical probabilistic models [241]. Quantum steering, on the other hand, investigates the possibility of one party steering the state of another party's system through local measurements [242]. These forms of quantum correlations are crucial for tasks such as quantum communication, quantum computation, and quantum sensing.

In this section we review the basic properties of quantum entanglement, which is the most known among all quantum correlations, and illustrate its connection to the phenomenon of quantum decoherence. In order to understand the phenomenon of quantum entanglement, let us first consider a multipartite system consisting of n subsystems [243]. According to the classical description, the total state space of the system is the Cartesian product of the spaces of the n subsystems. However, according to quantum theory, the total Hilbert space \mathcal{H} is a tensor product of the subsystem spaces \mathcal{H}_l , ($l = 1, \dots, n$), i.e. $\mathcal{H} = \otimes_{l=1}^n \mathcal{H}_l$. In this case, the superposition principle allows us to write the total state of the compound system in the form

$$|\Psi\rangle = \sum_{i_1, \dots, i_n} c_{i_1, \dots, i_n} |i_1\rangle \otimes |i_2\rangle \otimes \dots \otimes |i_n\rangle, \quad (5.34)$$

which obviously cannot be described in general as a product of the states of the individual subsystems. This suggests that is generally impossible to assign a single state vector to any one of the n subsystems. In this case, $|\Psi\rangle$ is called an "entangled state". Entanglement, contrary to classical superposition, allows us to construct an exponentially large superposition with only a linear amount of physical resources.

Let us now consider a simple system consisting of a pair of qubits (i.e. two-level systems) A and B prepared in the entangled state [26]

$$|\psi\rangle = \alpha |0^A\rangle |0^B\rangle + \beta |1^A\rangle |1^B\rangle, \quad (5.35)$$

where $\alpha, \beta \in \mathbb{C}$. The probability of detecting the two-qubit system in state $|0^A\rangle |0^B\rangle$ is $|\alpha|^2$, while the probability of detecting it in state $|1^A\rangle |1^B\rangle$ is $|\beta|^2$. An important inherent property of the entangled state $|\psi\rangle$ is that, if we measure the state of one of the two qubits, for example qubit B, and we find it in one of the states $|0^B\rangle$ or $|1^B\rangle$, then the act of measurement instantly prepares qubit A in the state $|0^A\rangle$ or $|1^A\rangle$, respectively. Therefore, the expectation value $\langle \hat{A} \rangle$ of an operator \hat{A} that acts only on qubit A is given by $\langle \hat{A} \rangle = \langle 0^A | \hat{A} | 0^A \rangle$ if qubit B is measured and found in state $|0^B\rangle$, and $\langle \hat{A} \rangle = \langle 1^A | \hat{A} | 1^A \rangle$ if B is found in state $|1^B\rangle$. The expectation value of \hat{A} , irrespective of any measurement on qubit B is given by:

$$\langle \hat{A} \rangle = \langle \psi | \hat{A} | \psi \rangle = |\alpha|^2 \langle 0^A | \hat{A} | 0^A \rangle + |\beta|^2 \langle 1^A | \hat{A} | 1^A \rangle = \text{Tr}(\rho^A \hat{A}), \quad (5.36)$$

where

$$\rho^A = |\alpha|^2 |0^A\rangle\langle 0^A| + |\beta|^2 |1^A\rangle\langle 1^A|, \quad (5.37)$$

is the reduced density operator of qubit A, resulting after tracing the degrees of freedom of qubit B out of the total density operator of the system, $\rho = |\psi\rangle\langle\psi|$. Note that the mixed state given by Eq. (5.37) differs from the single qubit pure state $|\varphi\rangle = \alpha |0^A\rangle + \beta |1^A\rangle$, which leads to

$$\sigma^A = |\varphi\rangle\langle\varphi| = |\alpha|^2 |0^A\rangle\langle 0^A| + |\beta|^2 |1^A\rangle\langle 1^A| + \alpha\beta^* |0^A\rangle\langle 1^A| + \alpha^*\beta |1^A\rangle\langle 0^A|. \quad (5.38)$$

As becomes evident, in the mixed state the non-diagonal elements of the density operator, also known as coherences, are zero, contrary to the non-diagonal elements of the pure state density operator that are given by $\langle 0^A | \sigma^A | 1^A \rangle = \alpha\beta^*$ and $\langle 1^A | \sigma^A | 0^A \rangle = \alpha^*\beta$. This suggests that the act of entangling two systems and discarding the information pertaining to one of them, results in the loss of coherence of the remaining system. This phenomenon is called decoherence and it is the main challenge of quantum computing and quantum information processing, as maintaining coherence is crucial for performing quantum operations and preserving quantum states.

There exist many measures of entanglement in the literature. Among them, one that stands out due to its practicality is the measure of concurrence introduced by Woiters in 1998 [244]. Mathematically, the concurrence is defined as follows:

$$\mathcal{C} = \max(\lambda_1 - \lambda_2 - \lambda_3 - \lambda_4, 0) \quad (5.39)$$

where $\lambda_1, \lambda_2, \lambda_3$, and λ_4 are the square roots of the eigenvalues of the matrix $\rho\tilde{\rho}$, arranged in decreasing order. ρ is the density matrix representing the quantum state of the two qubits, $\tilde{\rho}$ is defined as $\tilde{\rho} \equiv (\sigma_y \otimes \sigma_y)\rho^*(\sigma_y \otimes \sigma_y)$ and σ_y is the Pauli-Y matrix. The concurrence measures the "twistiness" or the degree of entanglement between the two qubits. The larger the concurrence value, the more entangled the qubits are.

5.2.2 Quantum state transfer

Quantum state transfer refers to the process of transmitting the quantum state of a system from one location to another without physically moving the particles that encode the quantum information [245]. It is perhaps one of the most important concepts in the field of quantum information and plays a crucial role in the development of quantum communication and quantum computing.

In classical systems, information can be easily transferred by copying and transmitting the state of a physical system. However, in the quantum regime, the situation is different due to the no-cloning theorem, according to which it is impossible to make an identical copy of an unknown quantum state [246]. Quantum state transfer overcomes this limitation by utilizing quantum entanglement and quantum coherence as resources of transmitting quantum information. There are different methods and protocols for quantum state transfer, depending on the physical system being used. Some common approaches include using photons in optical systems [247, 248], trapped ions [249], superconducting circuits [250–252], or spin qubits in solid-state systems [253, 254]. In general, the process of quantum state transfer involves preparing an initial quantum state at one location, typically called the sender or the source. Then, through the use of entanglement and quantum gates, the information is encoded onto a quantum system and transmitted to the receiving location, also

known as the receiver. At the receiver, the encoded quantum state is successfully transferred and can be extracted for further processing or measurement.

Quantum state transfer is a fundamental concept for various applications in quantum information processing. It enables the transmission of quantum information between different quantum devices, forming the basis for quantum communication networks and distributed quantum computing [255]. By achieving efficient and reliable quantum state transfer, we can realize long-distance quantum communication [256], secure quantum cryptography [257], and large-scale quantum computation [258, 259].

The desirable goal in quantum communication is to achieve state transfer with as high fidelity as possible. Perfect state transfer refers to a specific ideal scenario in quantum state transfer where the quantum state is transmitted from the source to the destination with perfect fidelity, without any loss or distortion of information [260]. In other words, the quantum state arrives at the destination unchanged and in its entirety. In what follows we briefly present three of the most known protocols for perfect state transfer as presented in [261].

We begin by considering a spin chain consisting of N spins, whose dynamics is described by the Hamiltonian

$$\hat{\mathcal{H}} = \frac{1}{2} \sum_{j=1}^N h_j \hat{\sigma}_j^z - \frac{1}{2} \sum_{j=1}^{N-1} J_j (\hat{\sigma}_j^x \hat{\sigma}_{j+1}^x + \hat{\sigma}_j^y \hat{\sigma}_{j+1}^y + \Delta \hat{\sigma}_j^z \hat{\sigma}_{j+1}^z). \quad (5.40)$$

Here h_j plays the role of the "magnetic field", determining the energy separation between the spin-up and spin-down states, J_j is the nearest-neighbor spin-spin coupling which in general is assumed to be time-dependent, Δ is the anisotropy parameter and $\hat{\sigma}_j^{x,y,z}$ are the Pauli spin operators. In what follows we set $\Delta = 0$, and therefore, the Hamiltonian given by Eq. (5.40) reduces to that of the XX spin chain model which is isomorphic to the Hubbard Hamiltonian for spinless fermions or hard-core bosons [262]:

$$\hat{\mathcal{H}} = \sum_{j=1}^N h_j \hat{a}_j^\dagger \hat{a}_j - \sum_{j=1}^{N-1} J_j (\hat{a}_j^\dagger \hat{a}_{j+1} + \hat{a}_{j+1}^\dagger \hat{a}_j), \quad (5.41)$$

where \hat{a}_j and \hat{a}_j^\dagger are the particle annihilation and creation operators at site j with energy h_j , respectively, and J_j is the tunneling coupling between adjacent sites.

Consider now an arbitrary single-qubit state of the form $|\psi\rangle = \alpha |0\rangle + \beta |1\rangle$. Our objective is the transfer of this state between the two ends of the spin chain. Let us assume that initially all spins are prepared in their ground state $|\downarrow\rangle_j \equiv |0\rangle_j$ and at $t = 0$ the first spin is excited to the state $|\psi\rangle_1$ (the subscript 1 implies the site of the spin). Perfect state transfer is accomplished if at some well-defined time t_{out} the last spin of the chain is found in state $|\psi\rangle_N$, up to a fixed phase factor. For the purposes of our problem we only need to consider the single-excitation subspace of the total Hilbert space, since the Hamiltonian of Eq. (5.40) (or of Eq. (5.41)) preserves the number of particle excitations. If $|0\rangle \equiv \prod_{j=1}^N |0\rangle_j$ and $|\mathbf{j}\rangle \equiv \hat{\sigma}_j^+ |0\rangle$ ($\hat{a}_j^\dagger |0\rangle$), then the initial state of the chain, i.e. $|\Psi\rangle_{\text{in}} = \alpha |0\rangle + \beta |1\rangle$, evolves in time as $|\Psi(t)\rangle = \hat{U}(t) |\Psi\rangle_{\text{in}} = \alpha |0\rangle + \beta \sum_{j=1}^N A_j(t) |\mathbf{j}\rangle$, where $\hat{U}(t) = \hat{\mathcal{T}} \exp\left[\frac{1}{i\hbar} \int_0^t \hat{\mathcal{H}}(t') dt'\right]$ is the time evolution operator, $\hat{\mathcal{T}}$ is the time-ordering operator and $A_j(t) \equiv \langle \mathbf{j} | \hat{U}(t) | 1 \rangle$. Formally, perfect state transfer is achieved if in a well-defined time $t = t_{\text{out}}$, $|A_N(t_{\text{out}})| = 1$, provided that the phase of the amplitude A_N , $\varphi = \arg(A_N)$ is fixed and known, i.e. $\varphi = \varphi_0$,

and therefore can be amended.

The performance of a state transfer protocol is usually quantified in terms of the transfer fidelity $F_\psi = \langle \psi | \rho_N | \psi \rangle$, where $\rho_N \equiv \text{Tr}_{\mathcal{N}}(|\Psi\rangle\langle\Psi|) = (1 - |\beta|^2|A_N|^2)|0\rangle\langle 0| + |\beta|^2|A_N|^2|1\rangle\langle 1| + \alpha\beta^*A_N^*|0\rangle\langle 1| + \alpha^*\beta A_N|1\rangle\langle 0|$ is the reduced density operator of the N_{th} site of the chain. Substituting ρ_N in the expression of F_ψ , we find that $F_\psi = |\alpha|^2 + |\beta|^2(1 - 2|\alpha|^2)|A_N|^2 + 2|\alpha|^2|\beta|^2|A_N|\cos\varphi$. Averaging over all possible $|\psi\rangle$ and after compensating for φ_0 , we find the following expression for the mean transfer fidelity \mathcal{F} [263]:

$$\mathcal{F} = \frac{1}{2} + \frac{|A_N|^2}{6} + \frac{|A_N|\cos(\varphi - \varphi_0)}{3}. \quad (5.42)$$

Note that for a completely random phase φ and $|A_N| = 1$, the fidelity acquires the classical value $\mathcal{F} = 2/3$, while for $|A_N| = 0$, we find that $\mathcal{F} = 1/2$, implying a totally random guess of the qubit state $|0\rangle$ or $|1\rangle$.

Let us now briefly present three of the most known protocols for perfect state transfer in spin chains described by Eq. (5.40) (or Eq. (5.41)) [261]. For what follows we set $h_j = 0 \forall j \in [1, N]$ and we assume that the individual couplings J_j can be fully controlled and are subject to the constraint $J_j \leq J_{\max} \equiv \max(J_j)$.

The first protocol is based on applying a sequence of SWAP operations implemented by π pulses between pairs of neighboring spin sites. We initially assume that all couplings J_j are set to zero, and then switch on J_1 for time $t_1 = \pi/(2J_1)$, then J_2 for time $t_2 = \pi/(2J_2)$, etc. until we reach on the N^{th} site of the chain. At the end of each interval the corresponding state amplitude is $A_j(t_{j-1}) = -i \sin(J_{j-1}t_{j-1})A_{j-1}(t_{j-2}) = (-i)^{j-1}$, ($j = 2, \dots, N$). If every coupling strength J_j can be pulsed to its maximal value J_{\max} and there are $N - 1$ steps, the total transfer time is $t_{\text{out}} = (N - 1)\pi/(2J_{\max}) \simeq (\pi/2)(N/J_{\max})$, for $N \gg 1$, and the final state amplitude is $A_N(t_{\text{out}}) = (-i)^{N-1}$.

The second protocol we consider is "static" in the sense that during the transfer the couplings strengths J_j remain fixed. However, even in this case, to initiate and to terminate (at time t_{out} the transfer process, at least J_1 and J_{N-1} should be quickly switched on and off, respectively. This protocol is known as the spin-coupling protocol and requires the spin-spin coupling strengths to follow the relation [264–268]

$$J_j = J_0 \sqrt{(N-j)j}, \quad j = 1, \dots, N. \quad (5.43)$$

This particular couplings configuration suggests that the strongest coupling is in the center of the chain at $j = N/2$, for N even, or at $j = (N \pm 1)/2$ for N odd, with values $J_{N/2} = \frac{1}{2}J_0N \equiv J_{\max}$ and $J_{(N \pm 1)/2} = \frac{1}{2}J_0\sqrt{N^2 - 1} \simeq J_{\max}$ ($N \gg 1$), respectively. Interestingly, among the infinitely many possible static protocols for perfect state transfer [260], the spin-coupling protocol was proved to be optimal in terms of its fast transfer time [269]. If the spin-spin coupling strengths J_j follow Eq. (5.43), it is easy to show that the energy spectrum is equidistant and is given the relation $\lambda_k = 2J_0k - J_0(N + 1)$, ($k = 1, \dots, N$), while $A_j(t)$ is given by

$$A_j(t) = \binom{N-1}{j-1}^{1/2} [-i \sin(J_0 t)]^{j-1} \cos(J_0 t)^{N-j}, \quad (5.44)$$

implying perfect periodic oscillations between the two ends of the chain. At the time $t = t_{\text{out}} = \pi/(2J_0)$, the amplitude of the final state is $A_N(t) = [-i \sin(J_0 t_{\text{out}})]^{N-1} = (-i)^{N-1}$. The transfer time may also be expressed in terms of J_{\max} as $t_{\text{out}} = (\pi/4)(N/J_{\max})$,

which shows that is two times shorter than the respective transfer time in the SWAP protocol presented above.

The third and final protocol we consider here is the so-called adiabatic state transfer protocol which is based on introducing slowly varying couplings J_j to achieve the transfer of the excitation between the two ends of the chain [270, 271]. Let us assume that N is odd and that the couplings J_j can be manipulated independently. The eigenstate of the Hamiltonian given by Eq. (5.40) (or Eq. (5.41)) in the single-excitation subspace, is:

$$|\Psi^{(0)}\rangle = \frac{1}{\sqrt{\mathcal{N}_0}} [J_2 J_4 \dots J_{N-1} |\mathbf{1}\rangle + (-1) J_1 J_4 \dots J_{N-1} |\mathbf{3}\rangle + \dots + (-1)^{\mathcal{J}} J_1 J_3 \dots J_{N-2} |\mathbf{N}\rangle], \quad (5.45)$$

where $\mathcal{J} \equiv \frac{1}{2}(N-1)$ and $\mathcal{N}_0 \equiv (J_2 J_4 \dots J_{N-1})^2 + \dots + (J_1 J_3 \dots J_{N-2})^2$. The eigenstate given by Eq. (5.45) is conventionally called coherent population trapping or dark state [272, 273] and its corresponding eigenvalue is $\lambda^{(0)} = 0$. As becomes evident, the amplitude of the initial state, A_1 , is proportional to the product of all the even-numbered couplings, while the amplitude of the final state, A_N , is proportional to the product of all the odd-numbered couplings. This result suggest that, if we first switch on all the even-numbered couplings and then switch them off adiabatically while we gradually switch on then odd-numbered couplings, the state system will gradually rotate from $|\mathbf{1}\rangle$ to $|\mathbf{N}\rangle$. Assuming that the even and odd "families" of couplings are described by common shape functions, i.e. $J_2, J_4, \dots, J_{N-1} = J_{\text{even}}(t)$ and $J_1, J_3, \dots, J_{N-2} = J_{\text{odd}}(t)$, the amplitudes $A_1(t)$ and $A_N(t)$ would be given by the relations

$$A_1(t) = \frac{[J_{\text{even}}(t)]^{\mathcal{J}}}{\sqrt{\mathcal{N}_0(t)}}, \quad (5.46a)$$

$$A_N(t) = (-1)^{\mathcal{J}} \frac{[J_{\text{odd}}(t)]^{\mathcal{J}}}{\sqrt{\mathcal{N}_0(t)}}, \quad (5.46b)$$

where $\mathcal{N}_0(t) \equiv \sum_{n=0}^{\mathcal{J}} [J_{\text{odd}}(t)]^{2n} [J_{\text{even}}(t)]^{2(\mathcal{J}-n)}$. Therefore, by applying first the J_{even} followed by the J_{odd} couplings, partially overlapping in time, we can achieve perfect state transfer. At the time $t = t_{\text{out}}$ the amplitude of the final state would be $A_N(t_{\text{out}}) = (-1)^{\mathcal{J}}$, that is, $|A_N(t_{\text{out}})| = 1$, with $\varphi_0 = (-\pi)(N-1)/2 \pmod{2\pi}$.

Before closing this section we should note that, although perfect state transfer can be achieved via many protocols [260], with the above three being the most well-known in the community, in realistic situations, the inevitable noise introduced due to several experimental imperfections leads to diagonal or off-diagonal disorder in the chain that may affect substantially the performance of every protocol. To that end, several studies have investigated the problem of state transfer in presence of disorder, providing a comparison of the performance of many protocols under noisy conditions [261, 274–277].

5.3 The quantum Zeno effect

The quantum Zeno effect (QZE) is a phenomenon in quantum mechanics that was named after the ancient Greek philosopher Zeno of Elea. In its simplest form, the quantum Zeno effect describes the suppression or slowing down of certain quantum processes due to frequent measurements or observations. The phenomenon is based on the fact that when a measurement is made on a quantum system, its wavefunction collapses into one of the possible eigenstates of the measuring quantity. In that

sense, if a quantum system is observed frequently and continuously, its wavefunction is constantly collapsing, preventing it from evolving and undergoing certain transitions. This repeated measurement essentially freezes the system in its initial state and prevents it from reaching other states or undergoing certain quantum processes. It is as if the system is "protected" from evolving by the act of measurement. In this section we provide a brief overview of the quantum Zeno effect [278] as its description is essential for understanding the work presented in some of the following chapters.

It is well-known that the evolution of a unstable quantum system is characterized by three regimes: a short-time region in which the decay is quadratic, an intermediate region in which the decay follows the usual exponential law, and a long-time region in which the decay is governed by a power law [279–281]. The quadratic region is an intrinsic feature of the quantum evolution of any given state at very short times under the Schrödinger equation. For this to become clear, let us consider an arbitrary initial state $|\psi_0\rangle \equiv |\psi(t=0)\rangle$ of a quantum system that evolves according to a Hamiltonian $\hat{\mathcal{H}}$ [278]. The "survival" amplitude $\mathcal{A}(t)$ and the probability $p(t)$ that the system has "survived" in its initial state after some time t are given by ($\hbar = 1$):

$$\mathcal{A}(t) = \langle \psi_0 | \psi(t) \rangle = \langle \psi_0 | e^{-i\hat{\mathcal{H}}t} | \psi_0 \rangle, \quad (5.47)$$

$$p(t) = |\mathcal{A}(t)|^2 = \left| \langle \psi_0 | e^{-i\hat{\mathcal{H}}t} | \psi_0 \rangle \right|^2. \quad (5.48)$$

After some very short time δt , the system has evolved according to the Schrödinger equation as:

$$\begin{aligned} |\psi(\delta t)\rangle &= e^{-i\hat{\mathcal{H}}\delta t} |\psi_0\rangle = |\psi_0\rangle - i\hat{\mathcal{H}} |\psi_0\rangle \delta t - \frac{1}{2} \hat{\mathcal{H}}^2 |\psi_0\rangle (\delta t)^2 + \mathcal{O}[(\delta t)^3] \\ &\equiv |\psi_0\rangle + |\delta\psi\rangle, \end{aligned} \quad (5.49)$$

where the last equation defines $|\delta\psi\rangle$. Substituting the above expression back to Eqs. (5.47) and (5.48), we find that:

$$\mathcal{A}(\delta t) = 1 - i\langle \hat{\mathcal{H}} \rangle_0 \delta t - \frac{1}{2} \langle \hat{\mathcal{H}}^2 \rangle_0 (\delta t)^2 \quad (5.50)$$

and

$$p(\delta t) = 1 - \frac{(\delta t)^2}{\tau_Z^2} + \mathcal{O}[(\delta t)^4] \quad (5.51)$$

where $\langle \dots \rangle_0 \equiv \langle \psi_0 | \dots | \psi_0 \rangle$ and

$$\tau_Z^{-2} \equiv \langle \hat{\mathcal{H}}^2 \rangle_0 - \langle \hat{\mathcal{H}} \rangle_0^2 \quad (5.52)$$

defines the so-called "Zeno time" [280, 281]. The term Zeno was first used by Misra and Sudarshan in 1977 [282], who named the initial quadratic evolution region of any system as Zeno region, since in this region one could slow down (or eventually stop) the evolution of the system. In this sense, the "frozen" system reminds us of the paradox of Zeno's arrow that never reaches its target. Note that Eq. (5.51) was derived from Eq. (5.50) using the fact that $\langle \hat{\mathcal{H}} \rangle_0$ is real which is an obvious consequence of the fact the $\hat{\mathcal{H}}$ is a Hermitian matrix. As Eq. (5.51) suggests, the survival probability for short times evolves quadratically away from unity.

Let us now explore how the act of frequent measurements on the system can slow down its quantum evolution [278]. The most famous and familiar formulation

of the QZE involves Von Neumann measurements, represented by one-dimensional projectors [283]. We assume that N projective measurements are performed, one after each time interval $\tau = t/N$, in order to check whether the system lies in its initial state $|\psi_0\rangle$. The corresponding projective measurement operator in such case is $|\psi_0\rangle\langle\psi_0|$. According to quantum mechanics, after each measurement the state of the system is projected back to $|\psi_0\rangle$ and starts a new evolution according to the Schrödinger equation. The survival probability after N measurements, i.e. at the final time $t = N\tau$, is expressed as

$$p^{(N)}(t) = p(\tau)^N = p(t/N)^N. \quad (5.53)$$

Using Eq. (5.51), the above equation can be written as

$$p^{(N)}(t) \simeq [1 - (t/N\tau_Z)^2]^N, \quad (5.54)$$

which for large N can be roughly approximated by

$$p^{(N)}(t) \approx \exp[-t^2/(N\tau_Z^2)]. \quad (5.55)$$

It is now easy to see that in the $N \rightarrow \infty$ limit (infinitely frequent measurements), the survival probability tends to unity, therefore the evolution is halted and the system remains "frozen" in its initial state. Note that the survival probability after N pulsed measurement ($t = N\tau$) is interpolated by an exponential law

$$p^{(N)}(t) = p(\tau)^N = \exp[N \log p(\tau)] = \exp(-\gamma_{\text{eff}}(\tau)t), \quad (5.56)$$

with an effective decay rate

$$\gamma_{\text{eff}}(\tau) \equiv -\frac{1}{\tau} \log p(\tau). \quad (5.57)$$

For $\tau \rightarrow 0$, i.e. $N \rightarrow \infty$, we have $p(\tau) \simeq \exp(-\tau/\tau_Z^2)$, and therefore

$$\gamma_{\text{eff}}(\tau) \simeq \tau/\tau_Z^2, \quad \tau \rightarrow 0. \quad (5.58)$$

So far we explored the QZE by considering the act of frequent von Neumann measurements on the system as a way to hinder its evolution. However, the QZE can also be exploited by considering a passive coupling between the system and a measuring apparatus, in which case the dynamics of the system can effectively be described by a non-Hermitian Hamiltonian. Let us first consider a two-level system undergoing Rabi oscillations between its two states [278]. The interaction Hamiltonian (interaction between the two levels) reads:

$$\hat{\mathcal{H}}_{\text{int}} = \Omega \hat{\sigma}_1 = \Omega(|+\rangle\langle-| + |-\rangle\langle+|) = \begin{pmatrix} 0 & \Omega \\ \Omega & 0 \end{pmatrix}, \quad (5.59)$$

where Ω is assumed to be a real number, $\hat{\sigma}_j$ ($j = 1, 2, 3$) are the Pauli matrices, and

$$|+\rangle = \begin{pmatrix} 1 \\ 0 \end{pmatrix}, \quad |-\rangle = \begin{pmatrix} 0 \\ 1 \end{pmatrix}, \quad (5.60)$$

are the eigenstates of $\hat{\sigma}_3$. In what follows we assume that system initially lies in the $|+\rangle$ state, i.e.

$$|\psi_0\rangle = |+\rangle = \begin{pmatrix} 1 \\ 0 \end{pmatrix}. \quad (5.61)$$

Let us now include a measuring apparatus that is coupled with one of the two levels of the two-level system, for example the lower level. In this case, the dynamics of the two-level system can effectively be described by a non-Hermitian Hamiltonian of the form:

$$\hat{\mathcal{H}}_{\text{int}}^{\text{eff}} = \begin{pmatrix} 0 & \Omega \\ \Omega & -i2V \end{pmatrix} \quad (5.62)$$

This Hamiltonian describes the population oscillations between the two levels of the system but at same time describes the loss of population from the lower state due to the coupling with the apparatus. Note that in the derivation of the effective Hamiltonian of Eq. (5.62), the Born-Markov approximation was applied (see section 5.1.1). In contrast to previous case where no apparatus was present, the Hamiltonian now is non-Hermitian and therefore probabilities are not conserved. Elementary algebra (and properties of SU(2)) yield [278] ($\hbar = 1$):

$$e^{-i\hat{\mathcal{H}}_{\text{int}}^{\text{eff}}t} = e^{-Vt} \left[\cosh(Gt) - i\frac{\vec{h} \cdot \hat{\sigma}}{G} \sinh(Gt) \right], \quad (5.63)$$

where $\vec{h} \equiv (\Omega, 0, iV)^T$ and $G \equiv \sqrt{V^2 - \Omega^2}$. The survival amplitude $\mathcal{A}(t)$ assuming that the initial state of the system is given by Eq. (5.61), reads

$$\begin{aligned} \mathcal{A}(t) &= \langle \psi_0 | e^{-i\hat{\mathcal{H}}_{\text{int}}^{\text{eff}}t} | \psi_0 \rangle = e^{-Vt} \left[\cosh(Gt) + \frac{V}{G} \sinh(Gt) \right] \\ &= \frac{1}{2} \left(1 + \frac{V}{G} \right) e^{-(V-G)t} + \frac{1}{2} \left(1 - \frac{V}{G} \right) e^{-(V+G)t}. \end{aligned} \quad (5.64)$$

Using the above equation, and its expansion in the parameter Ω/V for large V , one can show that the survival probability is proportional to the factor $\exp\left(-\frac{\Omega^2}{V}t\right)$, which leads to an effective decay rate of the form $\gamma_{\text{eff}}(V) = \Omega^2/V$. The appearance of the coupling V in the denominator of the exponent, and hence in the denominator of the effective decay rate may seem counter-intuitive at first glance. It suggests that the depletion of the initial state $|+\rangle$ is slower as V increases. The reason behind this counter-intuitive phenomenon is the QZE. A larger V entails a more "effective" measurement of the initial state, leading eventually to the halting of the decay in the $V \rightarrow \infty$ limit. Contrary to the previous investigated scenario where active measurements were performed at very short intervals, here the measurements are attributed to a passive coupling and therefore they can be viewed as "continuous". Note that since the apparatus is coupled to the lower state $|-\rangle$, in order to see the QZE one must prepare the initial state of the system to the state $|+\rangle$ (or in some superposition involving $|+\rangle$). If the system was initially prepared in $|-\rangle$, increasing the coupling V would result to faster depletion of the initial state.

5.4 Single-qubit coupled to an external environment

In this section we provide a formulation that enables us to describe the dynamics of a single-qubit system coupled to an external environment that is characterized by an

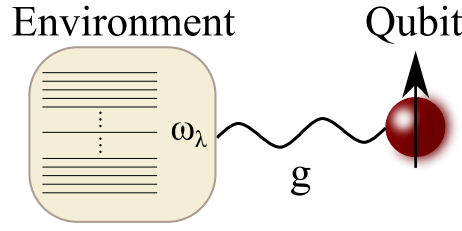


FIGURE 5.1: Schematic representation of a single-qubit coupled to an external environment with a coupling strength g .

arbitrary spectral density. This formulation, although simple, constitutes the basis for the extension of our studies to even more complex systems involving a larger number qubits or environments, as the ones investigated in the following chapters of the thesis.

Consider a two-level system (qubit) coupled with an environment (reservoir) with spectral density $J(\omega)$. The coupling strength is denoted by g and without loss of generality we assume that it is a real number. A schematic representation of the system is depicted in Fig. 5.1. The Hamiltonian of the compound system (qubit + reservoir) consists of three parts, i.e. the qubit Hamiltonian $\hat{\mathcal{H}}_S$, the bosonic environment Hamiltonian $\hat{\mathcal{H}}_E$, and the interaction Hamiltonian $\hat{\mathcal{H}}_I$, describing the interaction between the two subsystems ($\hbar = 1$):

$$\hat{\mathcal{H}} = \hat{\mathcal{H}}_S + \hat{\mathcal{H}}_E + \hat{\mathcal{H}}_I, \quad (5.65a)$$

$$\hat{\mathcal{H}}_S = \omega_g |g\rangle \langle g| + \omega_e |e\rangle \langle e|, \quad (5.65b)$$

$$\hat{\mathcal{H}}_E = \sum_{\lambda} \omega_{\lambda} \hat{a}_{\lambda}^{E\dagger} \hat{a}_{\lambda}^E, \quad (5.65c)$$

$$\hat{\mathcal{H}}_I = \sum_{\lambda} g(\omega_{\lambda}) \left(\hat{a}_{\lambda}^E \hat{\sigma}^+ + \hat{a}_{\lambda}^{E\dagger} \hat{\sigma}^- \right), \quad (5.65d)$$

where ω_g and ω_e are the energies of the ground and excited state of the qubit, respectively, ω_{λ} is the energy of the λ^{th} mode of the environment, $\hat{\sigma}^+ = |e\rangle \langle g|$ and $\hat{\sigma}^- = |g\rangle \langle e|$, are the qubit raising and lowering operators, respectively, while \hat{a}_{λ}^E and $\hat{a}_{\lambda}^{E\dagger}$ are the bosonic annihilation and creation operators of the environment.

The wavefunction of the compound system reads:

$$|\Psi(t)\rangle = c(t) |\psi_Q\rangle + \sum_{\lambda} c_{\lambda}^E(t) |\psi_{\lambda}^E\rangle, \quad (5.66)$$

where,

$$|\psi_Q\rangle \equiv |e\rangle |0\rangle_E, \quad (5.67a)$$

$$|\psi_{\lambda}^E\rangle \equiv |g\rangle |00 \dots 01_{\lambda} 0 \dots 00\rangle_E. \quad (5.67b)$$

The time-dependent Schrödinger equation after adoption of the amplitude transformations $c(t) = e^{-i\omega_e t} \tilde{c}(t)$ and $c_{\lambda}^E(t) = e^{-i(\omega_g + \omega_{\lambda})t} \tilde{c}_{\lambda}^E(t)$, leads to the following set of

equations:

$$\frac{d\tilde{c}(t)}{dt} = -i \sum_{\lambda} g(\omega_{\lambda}) e^{-i\Delta_{\lambda}t} \tilde{c}_{\lambda}^E(t), \quad (5.68a)$$

$$\frac{d\tilde{c}_{\lambda}^E(t)}{dt} = -ig(\omega_{\lambda}) e^{+i\Delta_{\lambda}t} \tilde{c}(t), \quad (5.68b)$$

where $\Delta_{\lambda} \equiv \omega_{\lambda} - (\omega_e - \omega_g) \equiv \omega_{\lambda} - \omega_{eg}$ is the detuning between the energy of the λ^{th} mode of the environment and the excitation energy of qubit. Formal integration of Eq. (5.68b) under the initial condition $\tilde{c}_{\lambda}^E(0) = 0$ and substitution back to Eq. (5.68a), yields:

$$\frac{d\tilde{c}(t)}{dt} = - \int_0^t \sum_{\lambda} [g(\omega_{\lambda})]^2 e^{-i\Delta_{\lambda}(t-t')} \tilde{c}(t') dt'. \quad (5.69)$$

We can now replace the sum over all the modes of the environment by a frequency integral, according to the relation $\sum_{\lambda} [g(\omega_{\lambda})]^2 \rightarrow \int d\omega J(\omega)$, where $J(\omega)$ is the spectral density of the environment, leading to:

$$\frac{d\tilde{c}(t)}{dt} = - \int_0^t R(t-t') \tilde{c}(t') dt', \quad (5.70)$$

where $R(t)$ is defined via

$$R(t) \equiv \int_0^{\infty} J(\omega) e^{-i\Delta t} d\omega. \quad (5.71)$$

and $\Delta \equiv \omega - \omega_{eg}$. Taking the Laplace transform of Eq. (5.70) assuming that the qubit is initially at its excited state, i.e. $c(0) = \tilde{c}(0) = 1$, we get:

$$sF(s) = 1 - B(s)F(s) \quad (5.72)$$

where $F(s)$ is the Laplace transform of the tilde amplitude $\tilde{c}(t)$ and $B(s)$ is the Laplace transform of $R(t)$. Solving Eq. (5.72) for $F(s)$ leads to:

$$F(s) = \frac{1}{s + B(s)} \quad (5.73)$$

The time dependence of $\tilde{c}(t)$ can be obtained by taking the inverse Laplace transform of $F(s)$, which can be calculated after specification of $J(\omega)$, calculation of the function $R(t)$ and its Laplace transform $B(s)$. The advantage of this method is that it does not make any restriction on the form of $J(\omega)$ and therefore it enables the study of various type of external reservoirs. In the special case of Markovian reservoirs, $B(s)$ is by definition a slowly varying function of s and it can be roughly approximated by a constant whose real part represents the decay rate to the environment and its imaginary part an energy shift of the qubit energy [26]. For other types of environmental spectral densities, the calculation of the functions $R(t)$ and $B(s)$ is necessary in order to find the inverse Laplace transform of $F(s)$. The specifics of these calculations for various types of non-Markovian reservoirs is presented in Appendix B.

5.5 Exceptional points in open quantum systems

Open quantum systems are, by definition, quantum-mechanical systems that interact with one or more external systems, usually characterized by large degrees of

freedom. As such, they are inevitably subject to quantum dissipation and therefore the information contained in the system is constantly leaking to the larger system(s). Open quantum systems are often described in terms of non-Hermitian Hamiltonians, which can be found after tracing out the degrees of freedom of the larger system(s). An interesting feature of some of these non-Hermitian Hamiltonians is the presence of "exceptional points" (EPs), i.e. a special class of degeneracies that occur in the spectrum of non-Hermitian Hamiltonians [284]. Unlike conventional Hermitian systems, which possess a real spectrum, non-Hermitian systems can exhibit complex eigenvalues. EPs correspond to the specific parameter values where two or more eigenvalues coalesce, leading to important effects in the system's dynamics and response.

At an EP, not only do the eigenvalues merge, but the corresponding eigenvectors become degenerate as well. This nontrivial degeneracy gives rise to exceptional point phenomena, such as unconventional behavior in the system's energy levels and unique quantum phase transitions [285]. Additionally, the eigenvectors associated with EPs exhibit interesting topological properties, leading to sensitivity to external perturbations in the system [286–288]. For N^{th} order EPs, i.e. EPs that mark the coalescence of N eigenvalues, the sensitivity in the response of the system to small perturbations in parameter space has been confirmed to become more pronounced as N is increased [288–290].

Through the seminal works of C. Bender et al. [291–295], an important connection between the physics of non-Hermitian Hamiltonians and parity-time (\mathcal{PT}) symmetry was revealed, as the boundary between the unbroken and broken \mathcal{PT} symmetry of such Hamiltonians [296, 297] was found to be marked by the presence of EPs [298–301]. The concept of EPs has been explored in various physical systems, including atomic, molecular, and optical (AMO) systems [302–305], photonic systems [298, 299], condensed matter systems [306–308] as well as systems used in information science research [309]. In what follows we explore the physics of exceptional points in the simplest possible general system, i.e. a two-level system, as presented in the work of W. D. Heiss in 2012 [310].

We begin by considering a two-level system described by a 2×2 Hamiltonian of the form:

$$\hat{\mathcal{H}}(\lambda) = \hat{\mathcal{H}}_0 + \lambda \hat{\mathcal{V}} = \begin{pmatrix} \omega_1 & 0 \\ 0 & \omega_2 \end{pmatrix} + \lambda \begin{pmatrix} \varepsilon_1 & \delta_1 \\ \delta_2 & \varepsilon_2 \end{pmatrix}, \quad (5.74)$$

where ω_k and ε_k determine the non-interacting resonance energies of the system, $E_k = \omega_k + \lambda \varepsilon_k$, ($k = 1, 2$). Due to the non-zero interaction matrix elements δ_k , the two levels do not cross but repel each other. We should note that the Hamiltonian $\hat{\mathcal{H}}(\lambda)$ is in general non-Hermitian; it only becomes Hermitian in the special case where all ω_k , ε_k and λ are real and $\delta_1 = \delta_2^*$. There exist two special values of λ that result in the coalescence of the two eigenvalues, namely:

$$\lambda_1 = \frac{-i(\omega_1 - \omega_2)}{i(\varepsilon_1 - \varepsilon_2) + 2\sqrt{\delta_1 \delta_2}}, \quad (5.75a)$$

$$\lambda_2 = \frac{-i(\omega_1 - \omega_2)}{i(\varepsilon_1 - \varepsilon_2) - 2\sqrt{\delta_1 \delta_2}}. \quad (5.75b)$$

Those values of λ mark the positions of the two EPs of the system. The eigenenergies of the system in terms of λ for $\delta_k \neq 0$, read

$$E_{1,2}(\lambda) = \frac{1}{2} \left[\omega_1 + \omega_2 + \lambda(\varepsilon_1 + \varepsilon_2) \pm \sqrt{(\varepsilon_1 - \varepsilon_2)^2 + 4\delta_1\delta_2} \sqrt{(\lambda - \lambda_1)(\lambda - \lambda_2)} \right], \quad (5.76)$$

and the eigenvalues at the EPs are

$$E(\lambda_{1,2}) = \frac{\varepsilon_1\omega_2 - \varepsilon_2\omega_1 \mp i\sqrt{\delta_1\delta_2}(\omega_1 + \omega_2)}{\varepsilon_1 - \varepsilon_2 \mp 2i\sqrt{\delta_1\delta_2}}. \quad (5.77)$$

The corresponding eigenvector (up to a factor) for $\lambda = \lambda_1$, is:

$$|\varphi_1\rangle = \begin{pmatrix} \frac{+i\delta_1}{\sqrt{\delta_1\delta_2}} \\ 1 \end{pmatrix}, \quad (5.78)$$

and for $\lambda = \lambda_2$,

$$|\varphi_1\rangle = \begin{pmatrix} \frac{-i\delta_1}{\sqrt{\delta_1\delta_2}} \\ 1 \end{pmatrix}, \quad (5.79)$$

while the corresponding left-hand eigenvectors for $\lambda = \lambda_1$ and $\lambda = \lambda_2$, are

$$\langle\tilde{\varphi}_1| = \begin{pmatrix} \frac{+i\delta_2}{\sqrt{\delta_1\delta_2}} & 1 \end{pmatrix}, \quad (5.80)$$

and

$$\langle\tilde{\varphi}_2| = \begin{pmatrix} \frac{-i\delta_2}{\sqrt{\delta_1\delta_2}} & 1 \end{pmatrix}, \quad (5.81)$$

respectively. It is easy to check that the norm $\langle\tilde{\varphi}_k|\varphi_k\rangle$ vanishes for $k = 1, 2$ (self-orthogonality [311]) and it is that vanishing that enables the reduction of a higher-dimensional problem to two dimensions in the vicinity of an EP, as discussed in [312]. We should note that the existence of only one eigenvector with vanishing norm is based on the fact that the Hamiltonian of the system is not diagonalizable for $\lambda = \lambda_1$ or $\lambda = \lambda_2$. For $\lambda = \lambda_1$, the Jordan decomposition of the Hamiltonian is:

$$\hat{\mathcal{H}}(\lambda_1) = \hat{S} \begin{pmatrix} E(\lambda_1) & 0 \\ 0 & E(\lambda_1) \end{pmatrix} \hat{S}^{-1} \quad (5.82)$$

where

$$\hat{S} = \begin{pmatrix} \frac{i\delta_1}{\sqrt{\delta_1\delta_2}} & \frac{2i\sqrt{\delta_1\delta_2}-\varepsilon_1+\varepsilon_2}{(\omega_1-\omega_2)\delta_2} \\ 1 & 0 \end{pmatrix}, \quad (5.83)$$

while similar expressions hold for $\lambda = \lambda_2$. Note that the second column of \hat{S} is usually referred to as an associate vector that obeys the equation $(\hat{\mathcal{H}}(\lambda_1) - E(\lambda_1))|\psi_{\text{assoc}}\rangle = |\varphi_1\rangle$. If one (or both) δ_k is (are) zero then there is level crossing ($\lambda_1 = \lambda_2$). If only one among δ_1 and δ_2 are zero then the Hamiltonian is not diagonalizable at the crossing point, in which case the Jacobian form is non-diagonal and only one eigenvector exists at the crossing point. However this crossing point is not associated with a presence of an EP since there is no square root singularity in λ .

At an EP, the square root singularity has been shown to affect also the Green's function and the scattering matrix describing a particular problem. For example, in the system considered above, the Green's function (and scattering matrix), in addition to the familiar first-order pole, has also a second-order pole [313]. At $\lambda = \lambda_1$ the

Green's function reads:

$$(E - \hat{\mathcal{H}}(\lambda_1))^{-1} = \frac{1}{E - E(\lambda_1)} \begin{pmatrix} 1 & 0 \\ 0 & 1 \end{pmatrix} + \frac{i\sqrt{\delta_1\delta_2}\lambda_1}{[E - E(\lambda_1)]^2} \begin{pmatrix} 1 & i\sqrt{\frac{\delta_1}{\delta_2}} \\ i\sqrt{\frac{\delta_2}{\delta_1}} & -1 \end{pmatrix} \quad (5.84)$$

with an analogous expression holding for $\lambda = \lambda_2$. The first term of Eq. (5.84) resembles the conventional expression at a non-singular point of the spectrum, while the presence of the second term is a consequence of the singular spectral point and it can give rise to dramatic effects in the vicinity of the EP [314].

The particular dependence of the eigenvalues of Eq. (5.76) on λ has several physical consequences, with the main of them being discussed below. First, in the vicinity of an EP, the spectrum is strongly dependent on the interaction parameter. This is reflected on the fact that the derivative of the eigenvalues and the eigenvectors with respect to λ diverges at the position of the EP. Second, when λ_1 or λ_2 is encircled in the complex λ -plane we observe the interchange of the two energy levels, which is attributed to the complex topology of the intersecting Riemann sheets of the eigenvalues in the complex λ -plane. Third, we know that at some finite distance from an EP, there exist two linearly independent eigenvectors $|\psi_1\rangle$ and $|\psi_2\rangle$, as well as their left-hand companions $\langle\tilde{\psi}_1|$ and $\langle\tilde{\psi}_2|$, normalized according to $\langle\tilde{\psi}_k|\psi_k\rangle$, ($k = 1, 2$). However, when we enforce the normalization exactly in the position of an EP (where $\langle\tilde{\psi}_k|\psi_k\rangle$ vanishes), the component of the eigenvectors tend to infinity as they are proportional to the factor $1/(\lambda - \lambda_k)^{1/4}$. Encircling of an EP (for example counterclockwise) results to the generation of the following pattern of normalized eigenvectors:

$$|\psi_1\rangle \rightarrow -|\psi_2\rangle \rightarrow -|\psi_1\rangle \rightarrow |\psi_2\rangle \rightarrow |\psi_1\rangle, \quad (5.85)$$

from which the pattern when starting from the state $|\psi_2\rangle$ follows accordingly [315, 316]. The fourth root behaviour is reflected on the fact that four rounds are needed to reach back to the initial state. Finally, when the eigenfunctions $|\psi_1\rangle$ and $|\psi_2\rangle$ coalesce, they become independent of parameters for $\delta_1 = \delta_2$, and, up to a normalization factor, assume the form $\begin{pmatrix} \pm i \\ 1 \end{pmatrix}$. The phase difference between the two components, i.e. $\pi/2$, can be different if, for example, we choose $\delta_1 = \delta_2^*$, in which case time reversal symmetry is broken.

Chapter 6

Entanglement dynamics of two interacting qubits coupled with a common non-Markovian environment

In this chapter, we study the steady state entanglement between two qubits interacting asymmetrically with a common non-Markovian reservoir [317]. We explore the conditions for steady state entanglement maximization, for various initial two-qubit states, by examining the behaviour of the steady state concurrence (SSC) in the qubit-reservoir couplings space. We uncover the cases in which SSC is favored by the asymmetric coupling configuration, demonstrating at the same time its great sensitivity to the value of the coupling between the two qubits. The phenomenon of entanglement instability is also predicted in the case where the latter becomes larger than the couplings between each qubit and the non-Markovian reservoir.

6.1 Overview of the existing literature

Protecting and controlling the quantum correlations generated between individual quantum systems is one of the major tasks of our century, since such correlations are the basic resources in quantum information and quantum computing [318]. Among these quantum correlations, entanglement, which expresses the non-separability of the quantum state of a compound system, has attracted extensive attention over the past few years. Even though the achievements on the study of entanglement generation between individual parts of a compound system have been truly remarkable so far, the main difficulty of preserving the entanglement in realistic configurations is associated with the fact that the coupling of such systems to their environment leads to dissipation and therefore loss of the quantum correlations, most often in times much shorter than those needed for implementing quantum information tasks.

A key realization in the study of the dynamics of entanglement in open quantum systems, is that the entanglement between two qubits interacting with two independent Markovian environments may reduce to zero after a finite time, despite the fact that the single-qubit coherence is decaying asymptotically to zero. This phenomenon predicted by Yu and Eberly [319–321], remained known as "entanglement sudden death" (ESD) and has been also verified experimentally [322, 323]. In the zero-temperature limit, ESD has been shown to occur for certain classes of initial two-qubit states [324], while finite temperature models indicate that even for the rest of those classes of initial states, ESD will eventually occur after a finite time [325].

Since the discovery of ESD, a number of studies focused on the role of non-Markovianity [24] of the surrounding environments on the entanglement dynamics of a system of qubits [326–334]. The main result of these studies, is that non-Markovian reservoirs may lead to the effect of entanglement revivals for finite times after the occurrence of ESD, while the inclusion of finite temperature may accelerate the decay of entanglement and induce ESD even in the non-Markovian regime [335, 336]. At the same time, works on the dynamics of the entanglement between two qubits coupled to independent structured environments, with the case of photonic band-gap materials serving as a prototype [337], revealed the possibility of achieving entanglement trapping and therefore effective hindering of ESD [338, 339].

The situation however may change drastically in the case where the qubits are interacting with a common reservoir [340–352]. As has been shown in such a configuration, there exists a class of initial two-qubit states that eventually lead to non-zero steady state values of entanglement after a finite time that depends on the relevant parameters of the system [353]. For the rest of the initial two-qubit states that do not lead to finite values of entanglement in the steady state of the system, effective strategies of entanglement preservation based on the Quantum Zeno effect have been proposed [354]. From the viewpoint of entanglement, a relatively interesting scenario arises when one considers two qubits coupled asymmetrically to a common non-Markovian environment [353–357]. Depending on the choice of the initial two-qubit state, this asymmetry in the coupling strengths between each individual qubit and the environment has been shown to potentially lead to larger two-qubit concurrence values beyond the maximum values obtained in the symmetric coupling case [353–355], although details on the conditions of observing this enhancement are still under investigation.

6.2 Theoretical description of the system

Our system consists of two identical interacting qubits coupled asymmetrically to a common non-Markovian reservoir, as depicted in Fig. 6.1. The Hamiltonian of the compound system (two qubits + reservoir) consists of three parts, namely the two-qubit Hamiltonian, $\hat{\mathcal{H}}_S$, the Hamiltonian describing the evolution of the environment, $\hat{\mathcal{H}}_E$ and the Hamiltonian of the interaction between the environment and each individual qubit, $\hat{\mathcal{H}}_I$, i.e.

$$\hat{\mathcal{H}} = \hat{\mathcal{H}}_S + \hat{\mathcal{H}}_E + \hat{\mathcal{H}}_I, \quad (6.1)$$

where,

$$\hat{\mathcal{H}}_S = \omega_e \sum_{i=1}^2 |e\rangle_i \langle e| + \omega_g \sum_{i=1}^2 |g\rangle_i \langle g| + \frac{\mathcal{J}}{2} (\sigma_1^+ \sigma_2^- + \sigma_1^- \sigma_2^+), \quad (6.2a)$$

$$\hat{\mathcal{H}}_E = \sum_{\lambda} \omega_{\lambda} a_{\lambda}^{\dagger} a_{\lambda}, \quad (6.2b)$$

$$\hat{\mathcal{H}}_I = \sum_{i=1}^2 \sum_{\lambda} g_i(\omega_{\lambda}) (a_{\lambda} \sigma_i^+ + a_{\lambda}^{\dagger} \sigma_i^-). \quad (6.2c)$$

In the above set of equations, ω_g and ω_e are the energies ($\hbar = 1$) of the ground and the excited state of the identical qubits, respectively, \mathcal{J} is the strength of the qubit-qubit interaction and $g_i(\omega_{\lambda})$, ($i = 1, 2$), the qubit-environment coupling strength. The creation and annihilation operators of the λ -mode of the bosonic environment

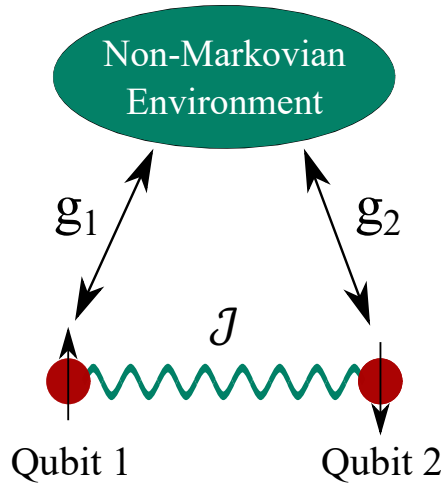


FIGURE 6.1: Schematic representation of the system at study. Two identical interacting qubits are coupled to a common non-Markovian environment with different coupling strengths.

are denoted by a_λ^\dagger and a_λ , respectively, while the qubit raising and lowering operators are given by $\sigma_i^+ = |e\rangle_i\langle g|$ and $\sigma_i^- = |g\rangle_i\langle e|$, ($i = 1, 2$).

In the single-excitation case, at any time $t > 0$, the wavefunction of the compound system can be expressed as a linear superposition of the vectors:

$$|\psi_1\rangle \equiv |e\rangle_1 |g\rangle_2 |0\rangle_E, \quad (6.3a)$$

$$|\psi_2\rangle \equiv |g\rangle_1 |e\rangle_2 |0\rangle_E, \quad (6.3b)$$

$$|\psi^\lambda\rangle \equiv |g\rangle_1 |g\rangle_2 |00\dots 01_\lambda 0\dots 00\rangle_E, \quad (6.3c)$$

according to the following expression:

$$|\Psi(t)\rangle = c_1(t) |\psi_1\rangle + c_2(t) |\psi_2\rangle + \sum_\lambda c^\lambda(t) |\psi^\lambda\rangle. \quad (6.4)$$

By adopting the amplitude transformation $c_i(t) = e^{-i(\omega_e + \omega_g)t} \tilde{c}_i(t)$, ($i = 1, 2$) and $c^\lambda(t) = e^{-i(2\omega_g + \omega_\lambda)t} \tilde{c}^\lambda(t)$, one can easily show that the equations of motion of the tilde amplitudes according to the time-dependent Schrödinger equation, reduce to:

$$i \frac{d\tilde{c}_1(t)}{dt} = \frac{\mathcal{J}}{2} \tilde{c}_2(t) + \sum_\lambda g_1(\omega_\lambda) e^{-i\Delta_\lambda t} \tilde{c}^\lambda(t), \quad (6.5a)$$

$$i \frac{d\tilde{c}_2(t)}{dt} = \frac{\mathcal{J}}{2} \tilde{c}_1(t) + \sum_\lambda g_2(\omega_\lambda) e^{-i\Delta_\lambda t} \tilde{c}^\lambda(t), \quad (6.5b)$$

$$i \frac{d\tilde{c}^\lambda(t)}{dt} = g_1(\omega_\lambda) e^{i\Delta_\lambda t} \tilde{c}_1(t) + g_2(\omega_\lambda) e^{i\Delta_\lambda t} \tilde{c}_2(t), \quad (6.5c)$$

where $\Delta_\lambda = \omega_\lambda - (\omega_e - \omega_g) \equiv \omega_\lambda - \omega_{eg}$. Formal integration of Eq. (6.5c) under the assumption that $\tilde{c}^{(\lambda)}(0) = 0$ and substitution back to Eqs. (6.5a) and (6.5b), yields:

$$\frac{d\tilde{c}_1(t)}{dt} = -i\frac{\mathcal{J}}{2}\tilde{c}_2(t) - \int_0^t \sum_{\lambda} e^{-i\Delta_{\lambda}(t-t')} \left\{ [g_1(\omega_{\lambda})]^2 \tilde{c}_1(t') + g_1(\omega_{\lambda})g_2(\omega_{\lambda})\tilde{c}_2(t') \right\} dt', \quad (6.6a)$$

$$\frac{d\tilde{c}_2(t)}{dt} = -i\frac{\mathcal{J}}{2}\tilde{c}_1(t) - \int_0^t \sum_{\lambda} e^{-i\Delta_{\lambda}(t-t')} \left\{ [g_2(\omega_{\lambda})]^2 \tilde{c}_2(t') + g_1(\omega_{\lambda})g_2(\omega_{\lambda})\tilde{c}_1(t') \right\} dt'. \quad (6.6b)$$

We now replace the summation over λ by an integration according to $\sum_{\lambda} \rightarrow \int d\omega \rho(\omega)$, where $\rho(\omega)$ is the density of states (DOS) of the reservoir representing the physical environment under consideration. In what follows, we explore the case of a non-Markovian environment, with DOS given by the Lorentzian distribution:

$$\rho(\omega) = \frac{1}{\pi} \frac{\frac{\gamma}{2}}{(\omega - \omega_c)^2 + (\frac{\gamma}{2})^2}, \quad (6.7)$$

where γ and ω_c are the width and the peak of the distribution, respectively. The Lorentzian DOS is widely used in the context of non-Markovian environments due to its practicality in enabling analytical solutions in systems described by complex integro-differential equations, as well as its correspondence to many realistic physical environments. As an example, Eq. (6.7) could correspond to a high finesse leaky cavity with a damping rate γ , whose mode with frequency ω_c is near-resonant with the qubit energy difference ω_{eg} . The generalization to any type of reservoir is straightforward by choosing the relevant DOS.

If the coupling strengths $g_i(\omega_{\lambda})$, ($i = 1, 2$), vary slowly as a function of ω_{λ} in the vicinity of ω_c , then to a good approximation, they can be substituted by their value at this frequency [337]. In that case, in order to simplify the notation, we adopt the definitions $g_i \equiv g_i(\omega_c)$, $i = 1, 2$. The resulting equations are:

$$\frac{d\tilde{c}_1(t)}{dt} = -i\frac{\mathcal{J}}{2}\tilde{c}_2(t) - \int_0^t I(t-t') [g_1^2 \tilde{c}_1(t') + g_1 g_2 \tilde{c}_2(t')] dt', \quad (6.8a)$$

$$\frac{d\tilde{c}_2(t)}{dt} = -i\frac{\mathcal{J}}{2}\tilde{c}_1(t) - \int_0^t I(t-t') [g_2^2 \tilde{c}_2(t') + g_1 g_2 \tilde{c}_1(t')] dt', \quad (6.8b)$$

where

$$\begin{aligned} I(t-t') &= \int_{-\infty}^{+\infty} \rho(\omega) e^{-i(\omega - \omega_{eg})(t-t')} d\omega = \frac{\gamma}{2\pi} \int_{-\infty}^{+\infty} \frac{e^{-i(\omega - \omega_{eg})(t-t')}}{(\omega - \omega_c)^2 + (\frac{\gamma}{2})^2} d\omega \\ &= e^{-i\Delta_c(t-t')} e^{-\frac{\gamma}{2}(t-t')}, \end{aligned} \quad (6.9)$$

and $\Delta_c \equiv \omega_c - \omega_{eg}$. Note that in Eq. (6.9) we extended the lower limit of the integration over frequency from 0 to $-\infty$. Such an extension is not in general valid for any kind of DOS; it is however well justified and commonly used in the case of a Lorentzian DOS with positive peak frequency and width such that the distribution has practically negligible extension to negative frequencies. In view of Eq. (6.9), taking the Laplace transform of Eqs. (6.8a) and (6.8b), one obtains:

$$sF_1(s) = \tilde{c}_1(0) - i\frac{\mathcal{J}}{2}F_2(s) - g_1^2 \Lambda(s)F_1(s) - g_1 g_2 \Lambda(s)F_2(s), \quad (6.10a)$$

$$sF_2(s) = \tilde{c}_2(0) - i\frac{\mathcal{J}}{2}F_1(s) - g_2^2 \Lambda(s)F_2(s) - g_1 g_2 \Lambda(s)F_1(s), \quad (6.10b)$$

where $F_1(s)$ and $F_2(s)$ are the Laplace transforms of the amplitudes $\tilde{c}_1(t)$ and $\tilde{c}_2(t)$,

respectively, and $\Lambda(s) = \frac{1}{s + \frac{\gamma}{2} + i\Delta_c}$. Note that $\tilde{c}_i(0) = c_i(0)$, ($i = 1, 2$). The set of Eqs. (6.10a) and (6.10b) is now algebraic and can be easily solved for $F_1(s)$ and $F_2(s)$, the inverse Laplace of which give us the expressions of $\tilde{c}_1(t)$ and $\tilde{c}_2(t)$, respectively.

The quantity of interest is the two-qubit concurrence (see section 5.2.1) given by the expression [244],

$$C(t) = 2|c_1(t)c_2^*(t)| = 2|\tilde{c}_1(t)\tilde{c}_2^*(t)|, \quad (6.11)$$

and in particular its steady state value as a function of the coupling strengths g_1 and g_2 .

6.3 Two-qubit entanglement dynamics and the phenomenon of entanglement "instability"

Using Eq. (6.11), in Fig. 6.2 we plot the dynamics of the two-qubit concurrence for various initial two-qubit states in the non-interacting qubit case ($\mathcal{J} = 0$). In panel (a) the two qubits are interacting with the non-Markovian environment with coupling strengths $g_1/\gamma = g_2/\gamma = 1$. In this arrangement we capture the well-studied case of the entanglement dynamics in the symmetrical coupling regime [356]. The entanglement dynamics of the initial two-qubit states $|\Psi(0)\rangle_{12} = |e\rangle_1 |g\rangle_2$ and $|\Psi(0)\rangle_{12} = \frac{1}{\sqrt{2}}(|e\rangle_1 |g\rangle_2 \pm i |g\rangle_1 |e\rangle_2)$ is symmetric with respect to the $C(t) = 0.5$ straight line, while this value is at the same time the two-qubit concurrence steady state value if the system is initially prepared in those states. If the two qubits are initially disentangled, as in the case of the initial state $|\Psi(0)\rangle_{12} = |e\rangle_1 |g\rangle_2$, their interaction with the non-Markovian reservoir generates entanglement. In the symmetric coupling regime considered, the concurrence dynamics of the initial state $|\Psi(0)\rangle_{12} = |g\rangle_1 |e\rangle_2$ is exactly the same as the respective dynamics of the $|\Psi(0)\rangle_{12} = |e\rangle_1 |g\rangle_2$ state, since the two qubits are assumed to be identical. On the other hand, the concurrence resulting from initially preparing the system to the states $|\Psi(0)\rangle_{12} = \frac{1}{\sqrt{2}}(|e\rangle_1 |g\rangle_2 + |g\rangle_1 |e\rangle_2)$ and $|\Psi(0)\rangle_{12} = \frac{1}{\sqrt{2}}(|e\rangle_1 |g\rangle_2 - |g\rangle_1 |e\rangle_2)$, follows a different dynamical picture, with the concurrence dropping from 1 to 0 after some finite time in the case of the former or being preserved to the value of 1 in the case of the latter.

The situation however may change drastically in the case where the two qubits interact asymmetrically with the non-Markovian environment. In Fig. 6.2(b) we choose the values $g_1/\gamma = 0.6$ and $g_2/\gamma = 1$ for the qubit-environment coupling strengths. Note that, as mentioned in the caption of Fig. 2, so far we consider the case of $\Delta_c = 0$, i.e. we assume that the energy difference ω_{eg} of the identical qubits is exactly on resonance with the considered Lorentzian mode of the reservoir. In this coupling configuration, all of the initial states considered above, result to totally different concurrence dynamics. The coupling asymmetry affects not only the steady state value of the two-qubit concurrence but also its characteristic oscillations that are associated with the non-Markovian character of the reservoir, and therefore the ability of information exchange between the qubits and the reservoir within some finite time that depends upon the width γ . An interesting effect of this coupling asymmetry is the possibility of concurrence stabilization to a steady state value larger than the respective steady state value of the symmetric coupling configuration [353–355], as also becomes evident by comparing the dynamics of the black line in each panel of Fig. 6.2.

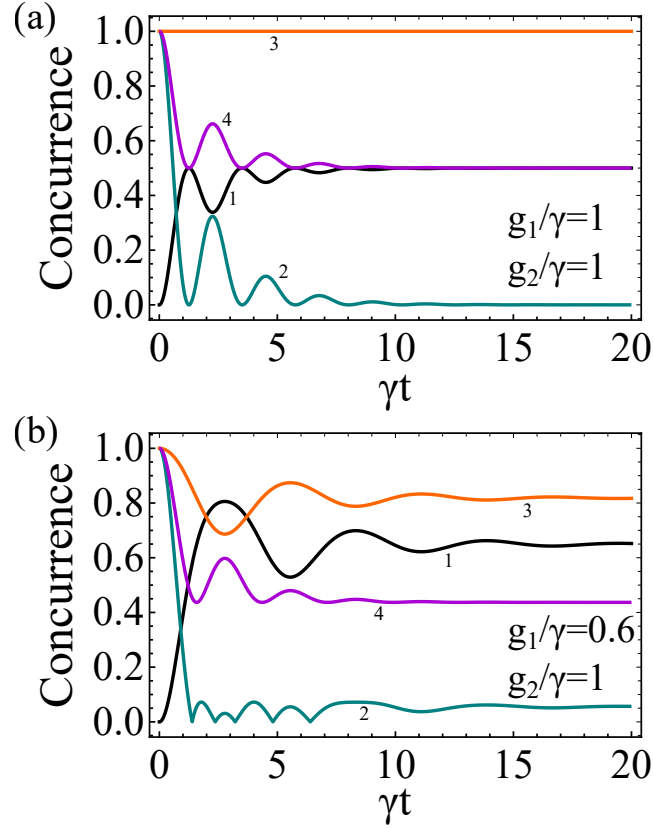


FIGURE 6.2: Dynamics of the two-qubit concurrence for various initial two-qubit states. The two-qubits are assumed to be non-interacting ($\mathcal{J} = 0$). (1) Black line: $|\Psi(0)\rangle_{12} = |e\rangle_1 |g\rangle_2$, (2) teal line: $|\Psi(0)\rangle_{12} = \frac{1}{\sqrt{2}}(|e\rangle_1 |g\rangle_2 + |g\rangle_1 |e\rangle_2)$, (3) orange line: $|\Psi(0)\rangle_{12} = \frac{1}{\sqrt{2}}(|e\rangle_1 |g\rangle_2 - |g\rangle_1 |e\rangle_2)$, (4) purple line: $|\Psi(0)\rangle_{12} = \frac{1}{\sqrt{2}}(|e\rangle_1 |g\rangle_2 \pm i |g\rangle_1 |e\rangle_2)$. In panel (a) the couplings of the qubits to the non-Markovian reservoir are $g_1/\gamma = 1$ and $g_2/\gamma = 1$, while in panel (b) $g_1/\gamma = 0.6$ and $g_2/\gamma = 1$. In both panels $\Delta_c = 0$.

These realisations naturally lead us to examine the profile of the SSC in the qubits' couplings space for various initial two-qubit states. The results for the non-interacting qubit case are presented in Fig. 6.3. Interestingly, we observe that if the two qubits are prepared initially in the state $|\Psi(0)\rangle_{12} = |e\rangle_1 |g\rangle_2$ (panel (a)), the SSC is not favored by the symmetric or the anti-symmetric coupling configuration, corresponding to the relations $g_1 = g_2$ and $g_1 = -g_2$, respectively. As becomes evident, there exists a big region of coupling combinations that result to SSC values larger than the value of 0.5 obtained with the symmetric and anti-symmetric configurations, going up to a maximum of 0.65. For the sake of comparison, the respective SSC pattern for the initial state $|\Psi(0)\rangle_{12} = |g\rangle_1 |e\rangle_2$ can be found in Fig. 6.5(a). We should note that the reason for considering also negative values for the qubit-environment couplings is that it occurs in many physical systems that one or both couplings are negative. For example, when considering two identical qubits placed in different positions inside a cavity, if the excited mode of the cavity that is near-resonant with the qubit's transition energy is other than its fundamental, then due to the sin dependence of the coupling strength to the qubit position, there exist regions of the standing wave mode where the coupling strengths are negative. By allowing the couplings to acquire negative values as well, we came across an interesting result in the case where the initial two-qubit state is

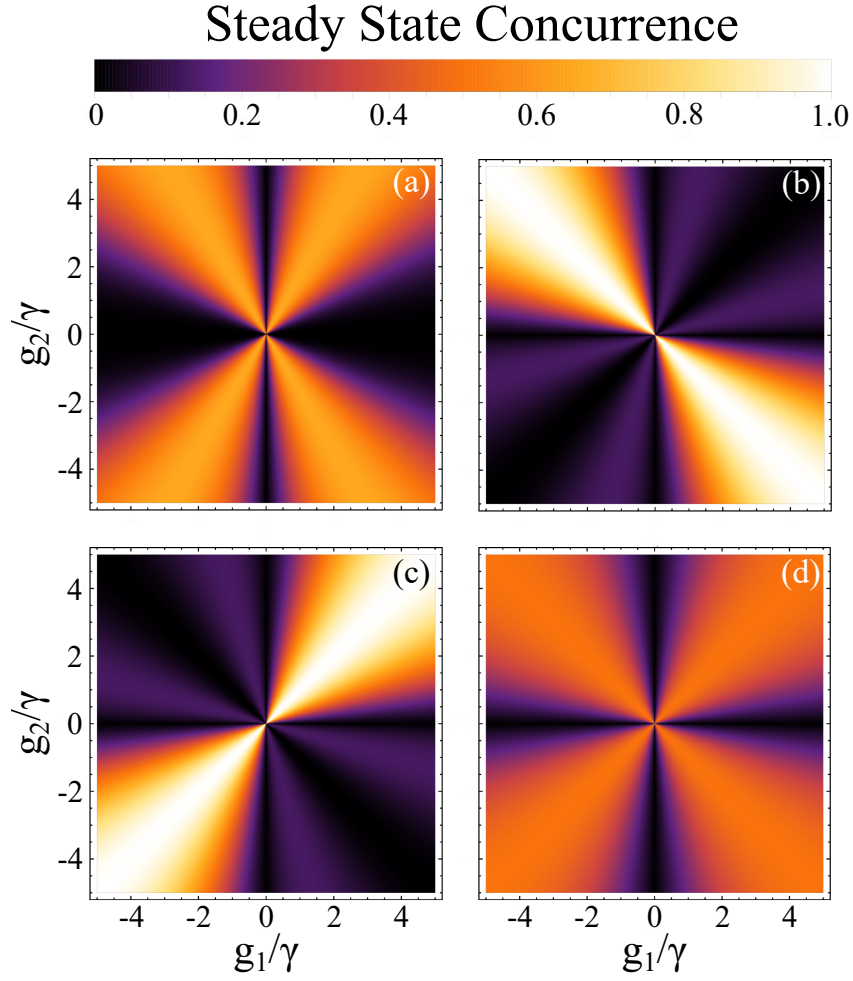


FIGURE 6.3: Steady state value of the two-qubit concurrence as a function of the qubit-environment couplings g_1 and g_2 , for various initial two-qubit states. The two-qubits are assumed to be non-interacting ($\mathcal{J} = 0$). Panel (a): $|\Psi(0)\rangle_{12} = |e\rangle_1 |g\rangle_2$, panel (b): $|\Psi(0)\rangle_{12} = \frac{1}{\sqrt{2}} (|e\rangle_1 |g\rangle_2 + |g\rangle_1 |e\rangle_2)$, panel (c): $|\Psi(0)\rangle_{12} = \frac{1}{\sqrt{2}} (|e\rangle_1 |g\rangle_2 - |g\rangle_1 |e\rangle_2)$, panel (d): $|\Psi(0)\rangle_{12} = \frac{1}{\sqrt{2}} (|e\rangle_1 |g\rangle_2 \pm i |g\rangle_1 |e\rangle_2)$. In all panels $\Delta_c = 0$.

$|\Psi(0)\rangle_{12} = \frac{1}{\sqrt{2}} (|e\rangle_1 |g\rangle_2 + |g\rangle_1 |e\rangle_2)$ (panel (b)). The steady state two-qubit concurrence may be zero along the symmetric couplings configuration, however it is maximum and equal to 1 along the anti-symmetric configuration and gets decreased as we move away from this region. On the other hand, if the two-qubits are prepared in the initial state $|\Psi(0)\rangle_{12} = \frac{1}{\sqrt{2}} (|e\rangle_1 |g\rangle_2 - |g\rangle_1 |e\rangle_2)$ (panel (c)) the SSC pattern follows exactly the opposite picture, i.e. it is favored by the symmetric configuration, while it is zero along the anti-symmetric couplings line. The physical reason behind this effect is the following: In the absence of the interaction between the two qubits, there exists a sub-radiant two-qubit state $|\Psi_{-}\rangle$ that does not exhibit decoherence as well as a super-radiant state $|\Psi_{+}\rangle$, which is orthogonal to $|\Psi_{-}\rangle$. It is easy to show that, up to a normalization constant, these states are given by the expressions $|\Psi_{-}\rangle = g_2 |e\rangle_1 |g\rangle_2 - g_1 |g\rangle_1 |e\rangle_2$ and $|\Psi_{+}\rangle = g_1 |e\rangle_1 |g\rangle_2 + g_2 |g\rangle_1 |e\rangle_2$ [353, 354]. In view of the expressions above, in the symmetrical couplings configuration $g_1 = g_2$ the sub-radiant state is $|\Psi_{-}\rangle \propto |e\rangle_1 |g\rangle_2 - |g\rangle_1 |e\rangle_2$ and the super-radiant

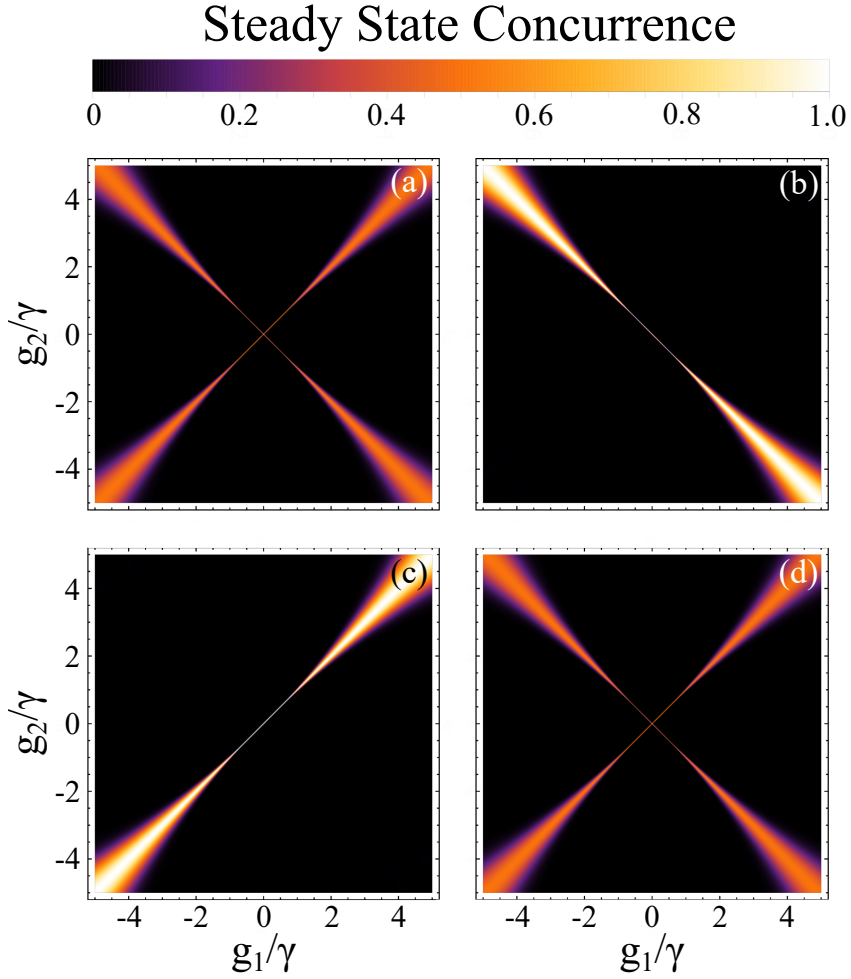


FIGURE 6.4: Steady state value of the two-qubit concurrence as a function of the qubit-environment couplings g_1 and g_2 , for various initial two-qubit states. The two-qubits are assumed to be interacting with a coupling strength $\mathcal{J}/\gamma = 1$. Panel (a): $|\Psi(0)\rangle_{12} = |e\rangle_1 |g\rangle_2$, panel (b): $|\Psi(0)\rangle_{12} = \frac{1}{\sqrt{2}} (|e\rangle_1 |g\rangle_2 + |g\rangle_1 |e\rangle_2)$, panel (c): $|\Psi(0)\rangle_{12} = \frac{1}{\sqrt{2}} (|e\rangle_1 |g\rangle_2 - |g\rangle_1 |e\rangle_2)$, panel (d): $|\Psi(0)\rangle_{12} = \frac{1}{\sqrt{2}} (|e\rangle_1 |g\rangle_2 \pm i |g\rangle_1 |e\rangle_2)$. In all panels $\Delta_c = 0$.

state is $|\Psi_+\rangle \propto |e\rangle_1 |g\rangle_2 + |g\rangle_1 |e\rangle_2$, while in the anti-symmetric couplings configuration $g_1 = -g_2$, exactly the opposite occurs. This explains the behaviour of SSC as a function of g_1 and g_2 in Figs. 6.3(b) and 6.3(c).

A paradigm of a state that results to a SSC that is favored both by the symmetric and anti-symmetric couplings configuration in the same way (with a maximum value of 0.5), is the state $|\Psi(0)\rangle_{12} = \frac{1}{\sqrt{2}} (|e\rangle_1 |g\rangle_2 \pm i |g\rangle_1 |e\rangle_2)$ (panel (d)). This state also indicates robustness in its resulting SSC when small deviations from the lines of these configurations are considered.

The situation however changes drastically if the interaction between the two qubits is nonzero. In Fig. 6.4 we examine the case of $\mathcal{J}/\gamma = 1$. Comparing Fig. 6.3 with Fig. 6.4, at least three major differences stand out. First, the resulting SSC pattern in the g_1, g_2 space is always favored by the symmetric or anti-symmetric couplings configuration, irrespective of the initial two-qubit state. The initial state will only determine the exact values of the SSC along the vicinity of the $g_1 = g_2$ and $g_1 = -g_2$ lines. Second, the initial states $|\Psi(0)\rangle_{12} = |e\rangle_1 |g\rangle_2$ panel 6.4(a)

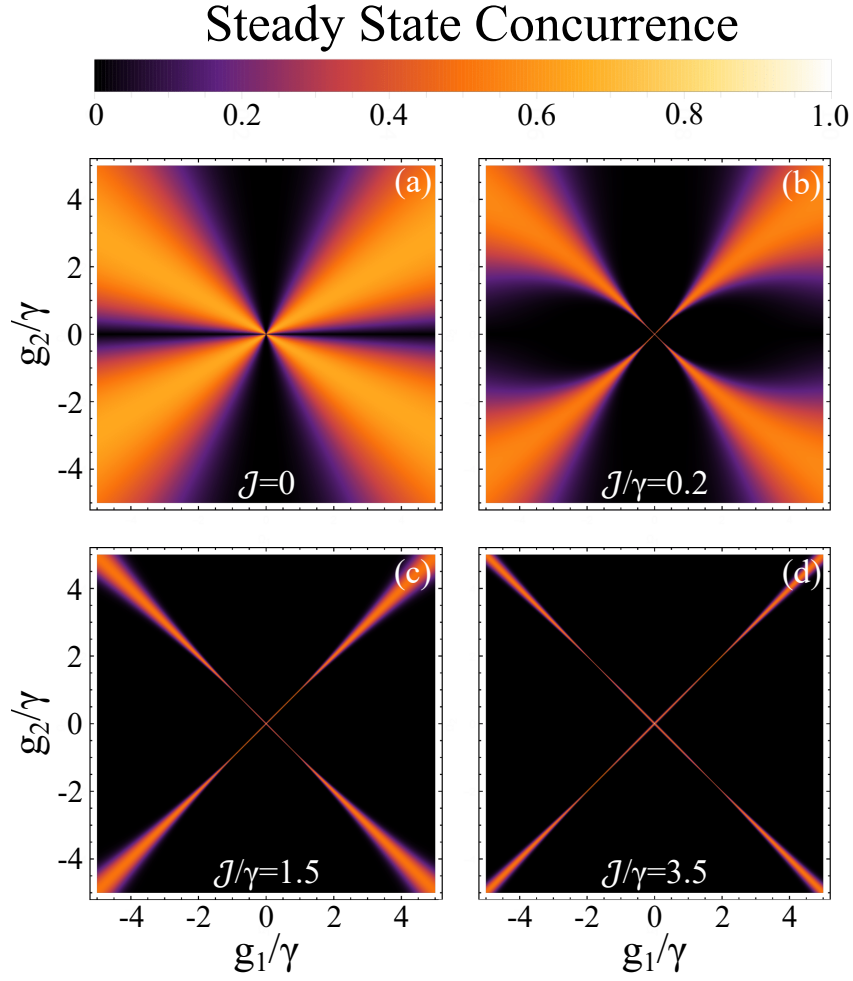


FIGURE 6.5: Steady state value of the two-qubit concurrence as a function of the qubit-environment couplings g_1 and g_2 for the initial two-qubit state $|\Psi(0)\rangle_{12} = |g\rangle_1 |e\rangle_2$. The panels correspond to different values of the qubit-qubit coupling strength \mathcal{J} . Panel (a): $\mathcal{J} = 0$, panel (b): $\mathcal{J}/\gamma = 0.2$, panel (c): $\mathcal{J}/\gamma = 1.5$, panel (d): $\mathcal{J}/\gamma = 3.5$. In all panels $\Delta_c = 0$.

and $|\Psi(0)\rangle_{12} = \frac{1}{\sqrt{2}}(|e\rangle_1 |g\rangle_2 \pm i |g\rangle_1 |e\rangle_2)$ (panel 6.4(d)) result to exactly the same SSC as a function of the qubit's couplings, despite the fact that in the absence of the qubit-qubit interaction, each state had its characteristic SSC pattern. Although not presented in Fig. 6.4, the same is true for the SSC pattern of the initial state $|\Psi(0)\rangle_{12} = |g\rangle_1 |e\rangle_2$. Third and most important, the SSC may be finite along the symmetric or anti-symmetric couplings configuration lines however it may exhibit high instability; namely, a slight deviation from the $g_1 = g_2$ and $g_1 = -g_2$ lines may result to zero SSC. This phenomenon of entanglement instability does not appear for any values of the qubit-qubit and qubit-environment couplings. In Fig. 6.5 we examine the SSC pattern of the initial state $|\Psi(0)\rangle_{12} = |g\rangle_1 |e\rangle_2$ in the qubit-environment coupling space for increasing values of \mathcal{J} . As becomes evident, the region of entanglement instability becomes larger with the increase of \mathcal{J} . More precisely, the results of Fig. 6.5 indicate that the instability occurs for absolute values of g_1 and g_2 roughly up to the value of \mathcal{J} , while the regions of finite SSC along the vicinity of the symmetric and anti-symmetric couplings configurations get increasingly wider for absolute values of g_1 and g_2 larger than \mathcal{J} .

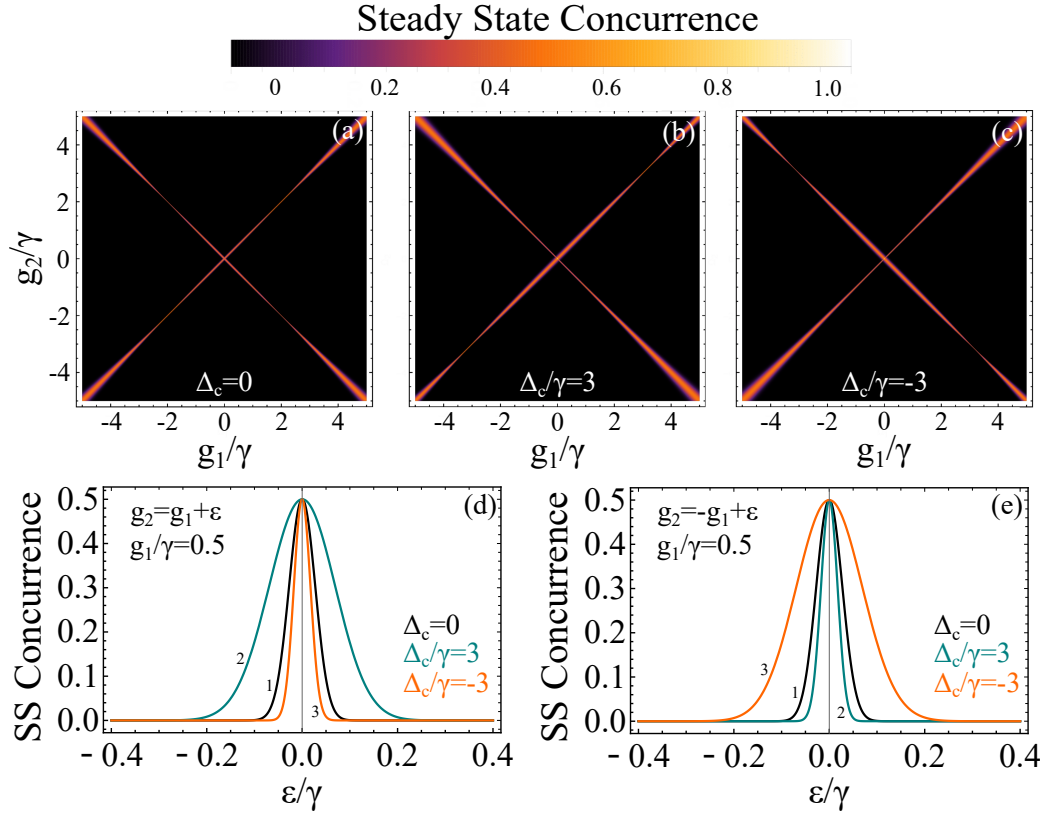


FIGURE 6.6: Effects of the detuning Δ_c on the value of the two-qubit steady state concurrence. In panels (a), (b) and (c) we study the behaviour of the value of the two-qubit steady state concurrence as a function of the qubit-environment couplings g_1 and g_2 , for various values of the detuning Δ_c and $\mathcal{J}/\gamma = 4$. Panel (a): $\Delta_c = 0$, panel (b): $\Delta_c/\gamma = 3$, panel (c): $\Delta_c/\gamma = -3$. The initial state of the two-qubit system is $|\Psi(0)\rangle_{12} = |g\rangle_1 |e\rangle_2$. In panels (d) and (e) we show how the detuning affects the SSC when small perturbations around the symmetric and anti-symmetric coupling regimes are considered, respectively. The stability of the SSC in both cases is studied for $g_1/\gamma = 0.5$. (1) Black line: $\Delta_c = 0$, (2) teal line: $\Delta_c/\gamma = 3$, (3) orange line: $\Delta_c/\gamma = -3$.

These findings expand the asymptotic analysis results of Y. Li et al. [355] who found that the only conditions for non-zero qubit's amplitudes in the steady state of the system are either the absence of the qubit-qubit coupling or the presence of equal coupling strengths between the reservoir and each qubit. While our results in Fig. 6.3 support the first statement, the results of Fig. 6.4 indicate that there exists a region of qubit-environment couplings with values slightly deviated from the vicinity of the symmetric couplings configurations that may result to finite SSC, depending on the choice of \mathcal{J} . We also showed that for certain initial two-qubit states this may be true only in the vicinity of the symmetric or anti-symmetric couplings lines, while for other states this can be true in both configurations (see Fig. 6.4). At the same time as far as the equal couplings argument is concerned, we showed that, although finite, the SSC may be highly unstable to small deviations from the $g_1 = g_2$ or $g_1 = -g_2$ lines.

Finally, in Fig. 6.6 we examine the effects of a finite detuning Δ_c on the resulting SSC pattern in the g_1, g_2 space. The initial state of the two-qubit system is chosen to be $|\Psi(0)\rangle_{12} = |g\rangle_1 |e\rangle_2$ and the value of the qubit-qubit coupling strength is $\mathcal{J}/\gamma = 4$. In Fig. 6.6(a) the peak of the Lorentzian reservoir mode coincides with the

qubit energy difference ω_{eg} , i.e. $\Delta_c = 0$, while in Figs. 6.6(b) and 6.6(c) the detunings $\Delta_c/\gamma = 3$ and $\Delta_c/\gamma = -3$ are chosen, respectively. As seen in Fig. 6.6(b), a positive detuning results to a slightly broadened region of finite SSC along the vicinity of the symmetric couplings configuration line, as long as the detuning is larger than the absolute value of the qubit-reservoir couplings. For absolute values of g_1, g_2 larger than the detuning Δ_c , the region of finite SSC along the vicinity of the symmetric couplings configuration line tends to shrink. On the other hand, a negative detuning Δ_c results to exactly the same effects but along the anti-symmetric configuration line (see Fig. 6.6(c)). In order to probe the degree of entanglement instability for various detunings, in Figs. 6.6(d) and 6.6(e) we study the behaviour of the SSC when small perturbations around the symmetric and anti-symmetric coupling regimes are considered, respectively. For that reason, we choose a fixed value for one of the qubit-reservoir couplings, i.e. $g_1/\gamma = 0.5$ and let the other coupling acquire the value $g_2 = g_1 + \varepsilon$ (Fig. 6.6(d)) or $g_2 = -g_1 + \varepsilon$ (Fig. 6.6(e)), where ε is a small change in units of frequency (energy). The SSC is then studied as a function of ε for various detunings. As becomes evident, a positive detuning Δ_c may increase the width of the resulting curve in the symmetric configuration but it also leads to a decreased width in the anti-symmetric configuration. At the same time, exactly the opposite picture holds on for negative detunings. Our results indicate that even if increasing the detuning can slightly improve the instability, it is ultimately a question of the precision one could achieve in the control and stability over the qubit-environment couplings in order to control the resulting SSC for given values of \mathcal{J} and Δ_c .

To sum up, in this chapter we studied properties of the steady state entanglement between two qubits that interact with a common non-Markovian environment. We showed that each initial two-qubit state results to a characteristic SSC pattern in the qubit-environment couplings space, with the maximum value of SSC occurring along the symmetric, the anti-symmetric or both coupling configuration lines. In some cases, as for example in the case where the initial two-qubit state is $|\Psi(0)\rangle_{12} = |e\rangle_1 |g\rangle_2$ or $|\Psi(0)\rangle_{12} = |g\rangle_1 |e\rangle_2$, the SSC may be favored by the choice of specific asymmetric coupling configurations. We additionally demonstrated the dramatic effects of the presence of a qubit-qubit interaction in the resulting SSC between the two qubits, with our results suggesting that in this case the SSC is finite only along the vicinity of the symmetric or anti-symmetric coupling configuration lines. It is also shown that, although finite, the SSC is predicted to be highly unstable as long as the interaction between the two qubits is larger than the couplings between each qubit and the non-Markovian reservoir; namely, a small deviation from the symmetric or anti-symmetric configuration could result to zero SSC. From the viewpoint of entanglement engineering, this result suggests that, if the exact tuning of the qubit-environment couplings to the symmetric or anti-symmetric configurations is difficult, these couplings should be larger than the qubit-qubit coupling in order to ensure the observation of finite two-qubit entanglement in the steady state of the system. The degree of instability was also studied as a function of the detuning between the peak of the considered Lorentzian mode of the reservoir and the qubits' transition energy, revealing interesting features that depend upon the parameters of the problem. In total, our findings complement and extend the interesting work of Yang Li et al. [355], who in contrast to earlier work have addressed the important aspect of coupling between the qubits themselves.

The physical realization of the considered system is within current experimental capabilities. The system can be experimentally realized using quantum dots (QDs) as qubits, since QDs can be coupled efficiently to optical cavities, [358–361] while their interaction is controllable by external means, making them an ideal candidate

for quantum information tasks [362–364]. Alternatively, the system can be realized using trapped ions efficiently coupled to a mode of an optical resonator, as in the case of the pioneering work of B. Casabone et al. [365], in which the entanglement generation between the two ions was investigated. Our results acquire great significance in view of the rapid developments in the field of entanglement engineering in open quantum systems.

Chapter 7

Arbitrary-length XX spin chains boundary-driven by non-Markovian environments

In this chapter we provide a recursive method of calculating the wave function of an XX spin chain coupled at both ends to non-Markovian reservoirs with arbitrary spectral density [366]. The method is based on the appropriate handling of the time-dependent Schrödinger's equations of motion in Laplace space and leads to closed-form solutions of the transformed amplitudes for arbitrary chain lengths as well as arbitrary initial conditions within the single-excitation subspace. Results on the dynamical as well as state-transfer properties of the system for various combinations of parameters are also presented. In particular, detailed quantitative comparisons for Lorentzian and Ohmic reservoirs are illustrated.

7.1 Introduction

One dimensional many-body systems such as quantum spin chains arise in many contexts throughout quantum information theory as well as condensed matter physics, due to their versatility as basic resources for the implementation of solid-state devices for quantum computing and quantum communication tasks [367]. Among these tasks, faithful quantum state transfer [253, 255, 261, 266, 274, 368–370] and long-distance entanglement [263, 371–375] have been investigated for various spin chain configurations in great detail throughout the last 20 years or so, with the research on these fields being still active.

In recent years, much interest has arisen in the study of properties of open quantum systems interacting with external environments, whose experimental realization inevitably involves decoherence and dissipation. Such systems may consist of just a pair of qubits, with focus on the effects of the environmental dissipation on the generated bipartite entanglement [320–325] as discussed in the previous chapter of the thesis, up to a whole quantum spin chain with focus on state transfer [376–379] or short- and long-distance correlations [380–383]. Extensions that account for the non-Markovian character of the surrounding environment have been also made [23, 317, 326, 384–388], revealing interesting effects associated with the memory character of the reservoir, which enable the exchange of information between the system and the environment within finite times.

At the same time, attention has been drawn to a special class of open quantum systems, i.e. the so-called boundary-driven open quantum systems [389]. These are quantum systems coupled to external environments at their edges and are usually studied for their transport [390–393] and thermodynamic properties [394–396]. For

1D boundary-driven open quantum systems, the different temperature or chemical potential between the two edge baths will cause a current flow from one bath to the other, mediated by the quantum system which can reach a non-equilibrium steady-state (NESS). The study of the transport properties of such systems, focusing on ways of controlling the associated current flows efficiently, seems therefore promising owing to potential applications in solid-state devices such as diodes or transistors [397]. On the other hand, the dynamical and quantum state transfer properties of such systems [398] are also essential from a practical perspective for the implementation of quantum information tasks.

Among the tools available for the study of open quantum systems, tensor network numerical methods based on matrix product states have proven quite efficient for the simulation of their dynamical behaviour [399, 400]. The method of matrix product states can in many cases yield analytical expressions for the expectation values of observables in the NESS of open quantum systems boundary-driven by Lindblad operators for Markovian reservoirs [401–404]. Perturbative approaches [405] as well as approaches based on quantum trajectories using numerical Monte Carlo techniques [406] have also been explored in great detail.

7.2 Theoretical formulation

Our system consists of an N qubit (spin) chain interacting with two environments E_1 and E_2 through its first and last qubit, with coupling strengths g_1 and g_2 , respectively. The interaction between each pair of neighboring qubits in the chain is denoted by \mathcal{J} . A schematic presentation of our system is depicted in Fig. 7.1. The Hamiltonian of our system $\hat{\mathcal{H}} = \hat{\mathcal{H}}_S + \hat{\mathcal{H}}_E + \hat{\mathcal{H}}_I$, consists of three parts; namely, the Hamiltonian of the XX chain $\hat{\mathcal{H}}_S$, the Hamiltonian of the two environments $\hat{\mathcal{H}}_E$ and the chain-environments interaction Hamiltonian $\hat{\mathcal{H}}_I$, given by the relations ($\hbar = 1$):

$$\hat{\mathcal{H}}_S = \omega_e \sum_{i=1}^N |e\rangle_i \langle e| + \omega_g \sum_{i=1}^N |g\rangle_i \langle g| + \sum_{i=1}^{N-1} \frac{\mathcal{J}}{2} (\sigma_i^+ \sigma_{i+1}^- + \sigma_i^- \sigma_{i+1}^+), \quad (7.1a)$$

$$\hat{\mathcal{H}}_E = \sum_{\lambda} \omega_{\lambda}^1 a_{\lambda}^{E_1 \dagger} a_{\lambda}^{E_1} + \sum_{\lambda} \omega_{\lambda}^2 a_{\lambda}^{E_2 \dagger} a_{\lambda}^{E_2}, \quad (7.1b)$$

$$\hat{\mathcal{H}}_I = \sum_{\lambda} g_1 (\omega_{\lambda}^1) (a_{\lambda}^{E_1} \sigma_1^+ + a_{\lambda}^{E_1 \dagger} \sigma_1^-) + \sum_{\lambda} g_2 (\omega_{\lambda}^2) (a_{\lambda}^{E_2} \sigma_N^+ + a_{\lambda}^{E_2 \dagger} \sigma_N^-), \quad (7.1c)$$

where ω_g and ω_e are, respectively, the energies of the ground and excited state of each spin (all spins are assumed to be identical), ω_{λ}^i , ($i = 1, 2$), is the energy of the λ -mode photon of each environment, $a_{\lambda}^{E_j}$ and $a_{\lambda}^{E_j \dagger}$, ($j = 1, 2$), are the annihilation and creation operators of each environment, respectively, and $\sigma_i^+ = |e\rangle_i \langle g|$ and $\sigma_i^- = |g\rangle_i \langle e|$, ($i = 1, \dots, N$), are the qubit raising and lowering operators, respectively.

The wavefunction of the compound system (spin chain + environments) in the single-excitation space is expressed as:

$$|\Psi(t)\rangle = \sum_{i=1}^N c_i(t) |\psi_i\rangle + \sum_{\lambda} c_{\lambda}^{E_1}(t) |\psi_{\lambda}^{E_1}\rangle + \sum_{\lambda} c_{\lambda}^{E_2}(t) |\psi_{\lambda}^{E_2}\rangle, \quad (7.2)$$

where,

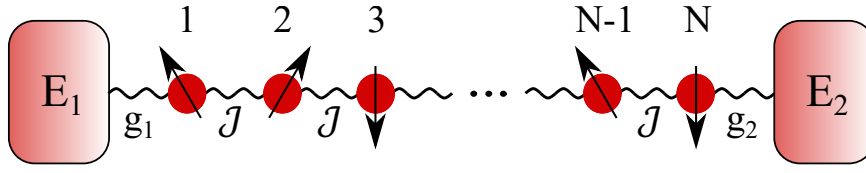


FIGURE 7.1: Schematic presentation of the system at study. A Heisenberg XX spin chain of arbitrary length is coupled to non-Markovian reservoirs at its boundaries.

$$|\psi_i\rangle = |g\rangle_1 |g\rangle_2 \cdots |g\rangle_{i-1} |e\rangle_i |g\rangle_{i+1} \cdots |g\rangle_N |0\rangle_{E_1} |0\rangle_{E_2}, \quad (7.3a)$$

$$|\psi_\lambda^1\rangle = |g\rangle_1 |g\rangle_2 \cdots |g\rangle_N |00 \dots 01_\lambda 0 \dots 00\rangle_{E_1} |0\rangle_{E_2}, \quad (7.3b)$$

$$|\psi_\lambda^2\rangle = |g\rangle_1 |g\rangle_2 \cdots |g\rangle_N |0\rangle_{E_1} |00 \dots 01_\lambda 0 \dots 00\rangle_{E_2}. \quad (7.3c)$$

For our derivation, it is useful to adopt the transformations $c_i(t) = e^{-i[\omega_e + (N-1)\omega_g]t} \tilde{c}_i(t)$, ($i = 1, \dots, N$), and $c_\lambda^{Ej}(t) = e^{-i(N\omega_g + \omega_\lambda^j)t} \tilde{c}_\lambda^{Ej}(t)$, ($j = 1, 2$), for the qubits' and environments' amplitudes. The equations of motion of the transformed amplitudes, resulting from the time-dependent Schrödinger equation, are:

$$i \frac{d\tilde{c}_1(t)}{dt} = \frac{\mathcal{J}}{2} \tilde{c}_2(t) + \sum_\lambda g_1(\omega_\lambda^1) e^{-i\Delta_\lambda^1 t} \tilde{c}_\lambda^{E1}(t), \quad (7.4a)$$

$$i \frac{d\tilde{c}_i(t)}{dt} = \frac{\mathcal{J}}{2} [\tilde{c}_{i-1}(t) + \tilde{c}_{i+1}(t)], \quad (i = 2, \dots, N-1), \quad (7.4b)$$

$$i \frac{d\tilde{c}_N(t)}{dt} = \frac{\mathcal{J}}{2} \tilde{c}_{N-1}(t) + \sum_\lambda g_2(\omega_\lambda^2) e^{-i\Delta_\lambda^2 t} \tilde{c}_\lambda^{E2}(t), \quad (7.4c)$$

$$i \frac{d\tilde{c}_\lambda^{E1}(t)}{dt} = g_1(\omega_\lambda^1) e^{i\Delta_\lambda^1 t} \tilde{c}_1(t), \quad (7.4d)$$

$$i \frac{d\tilde{c}_\lambda^{E2}(t)}{dt} = g_2(\omega_\lambda^2) e^{i\Delta_\lambda^2 t} \tilde{c}_2(t), \quad (7.4e)$$

where $\Delta_\lambda^j \equiv \omega_\lambda^j - (\omega_e - \omega_g) \equiv \omega_\lambda^j - \omega_{eg}$, ($j = 1, 2$). Formal integration of Eqs. (7.4d) and (7.4e), under the assumption that $\tilde{c}_\lambda^{E1}(0) = \tilde{c}_\lambda^{E2}(0) = 0$, and substitution back to Eqs. (7.4a) and (7.4c), yields:

$$\frac{d\tilde{c}_1(t)}{dt} = -i \frac{\mathcal{J}}{2} \tilde{c}_2(t) - \int_0^t \sum_\lambda e^{-i\Delta_\lambda^1(t-t')} [g_1(\omega_\lambda^1)]^2 \tilde{c}_1(t') dt', \quad (7.5a)$$

$$\frac{d\tilde{c}_N(t)}{dt} = -i \frac{\mathcal{J}}{2} \tilde{c}_{N-1}(t) - \int_0^t \sum_\lambda e^{-i\Delta_\lambda^2(t-t')} [g_2(\omega_\lambda^2)]^2 \tilde{c}_N(t') dt'. \quad (7.5b)$$

The summation over all possible modes of each environment can be replaced by an integration that requires the specification of the environment's spectral density $J_j(\omega_\lambda^j)$, according to $\sum_\lambda [g_j(\omega_\lambda^j)]^2 \rightarrow \int d\omega^j J_j(\omega^j)$, ($j = 1, 2$). In what follows, we

keep the spectral density of both environments arbitrary. The resulting set of differential equations then is:

$$\frac{d\tilde{c}_1(t)}{dt} = -i\frac{\mathcal{J}}{2}\tilde{c}_2(t) - \int_0^t R_1(t-t')\tilde{c}_1(t')dt', \quad (7.6a)$$

$$\frac{d\tilde{c}_i(t)}{dt} = -i\frac{\mathcal{J}}{2}[\tilde{c}_{i-1}(t) + \tilde{c}_{i+1}(t)], \quad (i = 2, \dots, N-1), \quad (7.6b)$$

$$\frac{d\tilde{c}_N(t)}{dt} = -i\frac{\mathcal{J}}{2}\tilde{c}_{N-1}(t) - \int_0^t R_2(t-t')\tilde{c}_N(t')dt', \quad (7.6c)$$

where we have introduced the definition

$$R_j(t) \equiv \int_0^\infty J_j(\omega^j) e^{-i(\omega^j - \omega_{eg})t} d\omega^j, \quad (j = 1, 2). \quad (7.7)$$

Taking now the Laplace transform of the above set of differential equations, and using the property of the convolution transform, $\mathcal{L} \left[\int_0^t f(t')g(t-t')dt' \right] = F(s)G(s)$, where $F(s)$ and $G(s)$ are the Laplace transforms of the functions $f(t)$ and $g(t)$, respectively, we obtain:

$$sF_1(s) = c_1(0) - i\frac{\mathcal{J}}{2}F_2(s) - B_1(s)F_1(s), \quad (7.8a)$$

$$sF_i(s) = c_i(0) - i\frac{\mathcal{J}}{2}[F_{i-1}(s) + F_{i+1}(s)], \quad (i = 2, \dots, N-1), \quad (7.8b)$$

$$sF_N(s) = c_N(0) - i\frac{\mathcal{J}}{2}F_{N-1}(s) - B_2(s)F_N(s), \quad (7.8c)$$

where we have used the fact that $\tilde{c}_i(0) = c_i(0)$, since $c_i(t) = e^{-i[\omega_e + (N-1)\omega_g]t}\tilde{c}_i(t)$. In the above system of algebraic equations, $F_i(s)$ is the Laplace transform of $\tilde{c}_i(t)$, ($i = 1, \dots, N$), while $B_j(s)$ is the Laplace transform of the function $R_j(t)$, ($j = 1, 2$).

The system of Eqs. (7.8) is a set of N algebraic equations that can be solved recursively as follows: First we solve Eq. (7.8a) for $F_2(s)$ and Eq. (7.8b) for $F_{i+1}(s)$ to find

$$F_2(s) = (iks)F_1(s) + (ik)B_1(s)F_1(s) - (ik)c_1(0), \quad (7.9a)$$

$$F_{i+1}(s) = -F_{i-1}(s) + (iks)F_i(s) - (ik)c_i(0), \quad (i = 2, \dots, N-1), \quad (7.9b)$$

where $k \equiv 2/\mathcal{J}$. Using these two relations, we can express each $F_i(s)$ in terms of $F_1(s)$. The first few terms up to $F_6(s)$ can be organized as follows:

$$F_2(s) = (iks)F_1(s) + (ik)B_1(s)F_1(s) - (ik)c_1(0), \quad (7.10a)$$

$$F_3(s) = [(iks)^2 - 1]F_1(s) + (iks)(ik)B_1(s)F_1(s) - (ik)[(iks)c_1(0) + c_2(0)], \quad (7.10b)$$

$$F_4(s) = [(iks)^3 - 2(iks)]F_1(s) + [(iks)^2 - 1](ik)B_1(s)F_1(s) - (ik)\left\{[(iks)^2 - 1]c_1(0) + (iks)c_2(0) - c_3(0)\right\}, \quad (7.10c)$$

$$F_5(s) = \left[(iks)^4 - 3(iks)^2 + 1 \right] F_1(s) + \left[(iks)^3 - 2(iks) \right] (ik) B_1(s) F_1(s) - (ik) \left\{ \left[(iks)^3 - 2(iks) \right] c_1(0) + \left[(iks)^2 - 1 \right] c_2(0) + (iks) c_3(0) + c_4(0) \right\}, \quad (7.10d)$$

$$F_6(s) = \left[(iks)^5 - 4(iks)^3 + 3(iks) \right] F_1(s) + \left[(iks)^4 - 3(iks)^2 + 1 \right] B_1(s) F_1(s) - (ik) \left\{ \left[(iks)^4 - 3(iks)^2 + 1 \right] c_1(0) + \left[(iks)^3 - 2(iks) \right] c_2(0) + \left[(iks)^2 - 1 \right] c_3(0) + (iks) c_4(0) + c_5(0) \right\}. \quad (7.10e)$$

Careful inspection of the above system of equations reveals that $F_i(s)$, follows a pattern of the form:

$$F_i(s) = A_i(s) F_1(s) + A_{i-1}(s) (ik) B_1(s) F_1(s) - (ik) \sum_{n=1}^{i-1} A_{i-n}(s) c_n(0), \quad (i = 2, \dots, N), \quad (7.11)$$

where $A_i(s)$ obeys the relation:

$$A_{m+2}(s) = (iks) A_{m+1}(s) - A_m(s), \quad (m = 1, \dots, N), \quad (7.12)$$

with $A_1(s) = 1$ and $A_2(s) = iks$. The m^{th} term of this sequence is given by:

$$A_m(s) = \frac{\left[(iks) + i\sqrt{k^2 s^2 + 4} \right]^m - \left[(iks) - i\sqrt{k^2 s^2 + 4} \right]^m}{2^m i \sqrt{k^2 s^2 + 4}}, \quad (m = 1, \dots, N). \quad (7.13)$$

Taking Eq. (7.11) for $i = N - 1$ and $i = N$, we obtain:

$$F_{N-1}(s) = A_{N-1}(s) F_1(s) + A_{N-2}(s) (ik) B_1(s) F_1(s) - (ik) \sum_{m=1}^{N-2} A_{N-1-m}(s) c_m(0), \quad (7.14)$$

$$F_N(s) = A_N(s) F_1(s) + A_{N-1}(s) (ik) B_1(s) F_1(s) - (ik) \sum_{m=1}^{N-1} A_{N-m}(s) c_m(0). \quad (7.15)$$

Substituting Eqs. (7.14) and (7.15) back into Eq. (7.8c) and using the relation $\sum_{m=1}^{N-1} A_{N-m}(s) c_m(0) = \sum_{m=1}^{N-2} A_{N-m}(s) c_m(0) + A_1(s) c_{N-1}(0)$, we can, after some straightforward algebraic manipulations, find that $F_1(s)$ is given by:

$$F_1(s) = \frac{ikc_N(0) - k^2[s + B_2(s)] A_1(s) c_{N-1}(0) + (ik) \sum_{m=1}^{N-2} \left\{ ik[s + B_2(s)] A_{N-m}(s) - A_{N-1-m}(s) \right\} c_m(0)}{ik[s + B_2(s)] A_N(s) - \left\{ 1 + k^2 B_1(s) [s + B_2(s)] \right\} A_{N-1}(s) - ik B_1(s) A_{N-2}(s)}. \quad (7.16)$$

The inverse Laplace transform of Eq. (7.16) provides the time evolution of the amplitude $\tilde{c}_1(t)$. The rest of the amplitudes are given by the inverse Laplace transforms of $F_i(s)$, ($i = 2, \dots, N$), which are recursively related to $F_1(s)$ through Eq. (7.11).

The analytical method we have developed above allows us to obtain the time evolution of the amplitude of any spin, for an arbitrary number of sites as well as for arbitrary initial conditions, within the single-excitation subspace, by simply calculating the inversion integral of the corresponding Laplace transform. Through our

method, the number of sites N has become an arbitrary and easily modifiable parameter entering expression (7.16). The inversion integral can be readily calculated numerically (or even analytically in some cases), after specification of the spectral density of each environment, necessary for the calculation of the Laplace transforms $B_j(s)$ of the functions $R_j(t)$.

7.3 Dynamical and state transfer properties of XX spin chains boundary-driven by non-Markovian environments

7.3.1 Lorentzian environments

As a first example, we consider the case of an XX chain boundary-driven by two non-Markovian reservoirs with Lorentzian spectral densities, given by:

$$J_j(\omega^j) = \frac{g_j^2}{\pi} \frac{\frac{\gamma_j}{2}}{\left(\omega^j - \omega_c^j\right)^2 + \left(\frac{\gamma_j}{2}\right)^2}, \quad (j = 1, 2), \quad (7.17)$$

where g_j are the coupling strengths between the edge spins and the boundary reservoirs in units of frequency, while γ_j and ω_c^j , ($j = 1, 2$), are the widths and the peak frequencies of each distribution, respectively.

As shown in Appendix B, the functions $R_j(t)$ and $B_j(s)$, for Lorentzian spectral densities, are given by the expressions

$$R_j(t) = g_j^2 e^{-i\Delta_c^j t} e^{-\frac{\gamma_j}{2} t}, \quad (j = 1, 2), \quad (7.18)$$

and

$$B_j(s) = \frac{g_j^2}{s + \frac{\gamma_j}{2} + i\Delta_c^j}, \quad (j = 1, 2). \quad (7.19)$$

Using the expression of $B_j(s)$, ($j = 1, 2$), we can easily obtain the time evolution of the amplitudes $\tilde{c}_i(t)$, i, \dots, N , using Eqns. (7.11), (7.13) and (7.16). Note that in all of our calculations, we express all couplings entering the formalism in units of the nearest neighbor coupling strength \mathcal{J} . Thus in our figures, time is measured in the dimensionless units $\mathcal{J}t$.

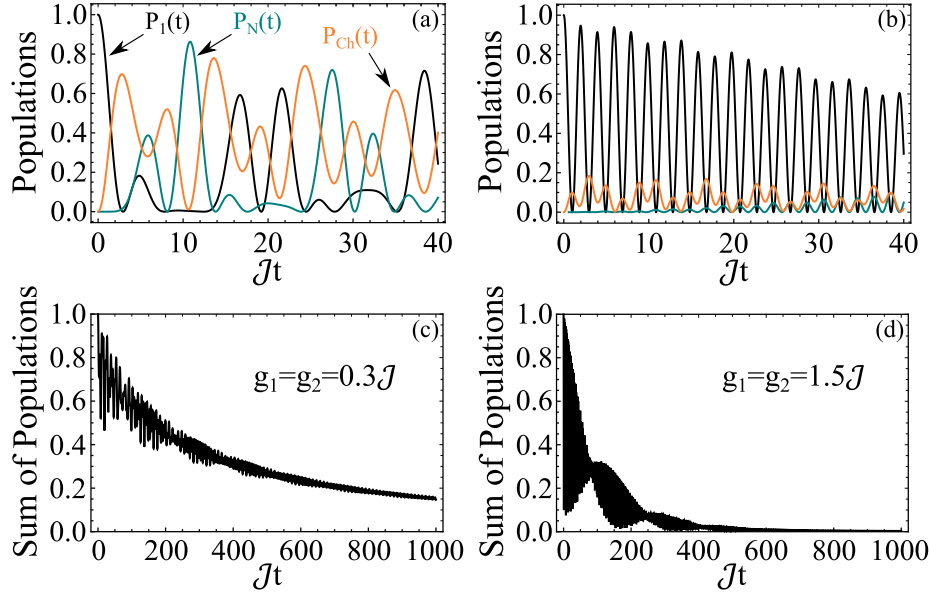


FIGURE 7.2: Dynamics of the populations of the first qubit (black line), N^{th} qubit (teal line) and channel qubits (orange line) for $c_1(0) = 1$, $N = 5$, $\gamma_1 = \gamma_2 = 0.02\mathcal{J}$, $\Delta_c^1 = \Delta_c^2 = 0$ and (a) $g_1 = g_2 = 0.3\mathcal{J}$, (b) $g_1 = g_2 = 1.5\mathcal{J}$. In panels (c) and (d) we show the long-time dynamics of the sum of all qubit populations in the spin chain for $g_1 = g_2 = 0.3\mathcal{J}$ and $g_1 = g_2 = 1.5\mathcal{J}$, respectively.

In Fig. 7.2(a) we study the dynamics of the populations of the edge as well as the intermediate spins in the $g_1, g_2 < \mathcal{J}$ case for $c_1(0) = 1$. For the intermediate qubits, we adopt the term "channel qubits", which is frequently used in quantum information protocols and represents the sum of the populations of all except the 2 edge qubits. The corresponding occupation probability is $P_{Ch}(t) = \sum_{i=2}^{N-1} |c_i(t)|^2 = \sum_{i=2}^{N-1} |\tilde{c}_i(t)|^2$. Since the coupling between the qubits is larger than the couplings between the edge spins and the reservoirs, we observe oscillations in the edge and channel qubit populations, associated with the spreading of the initial excitation throughout the whole chain. Eventually, the population will be lost due to the environmental dissipation. This can be seen through the long-time dynamical picture of the sum of all qubit populations, as in Fig. 7.2(c). On the other hand, in the case where $g_1, g_2 > \mathcal{J}$, as examined in Fig. 7.2(b), since the initial excitation is on the first qubit, the population is essentially "trapped", albeit not permanently, between the first qubit and environment 1, with only a small portion of the population leaking to the channel. In this case the exact value of g_2 is of little relevance since the population of the N^{th} site at any time t is practically negligible. As seen in Fig. 7.2(d), the strong coupling between the first qubit and the reservoir causes the total population to be lost through the reservoir much faster than in the previous case.

Although, as discussed above, the strong coupling between the environment and the edge qubits may result to population trapping (Fig. 7.2(b)), if the chain length is small (up to 5 qubits or so), the long-time dynamics of the chain reveal an oscillatory population transfer between the two edges of the chain (Fig. 7.3) along with the dissipation to the reservoirs. In that case, the population of the $N - 2$ channel qubits remains low for any time t (see inset of Figs. 7.3(a), 7.3(b) and 7.3(c)). This effect is attributed to the fact that, despite the trapping of the population that occurs between the edge qubits and the reservoirs, there is always part of the population that travels through the chain and reaches from its one end of to the other. This effect ceases

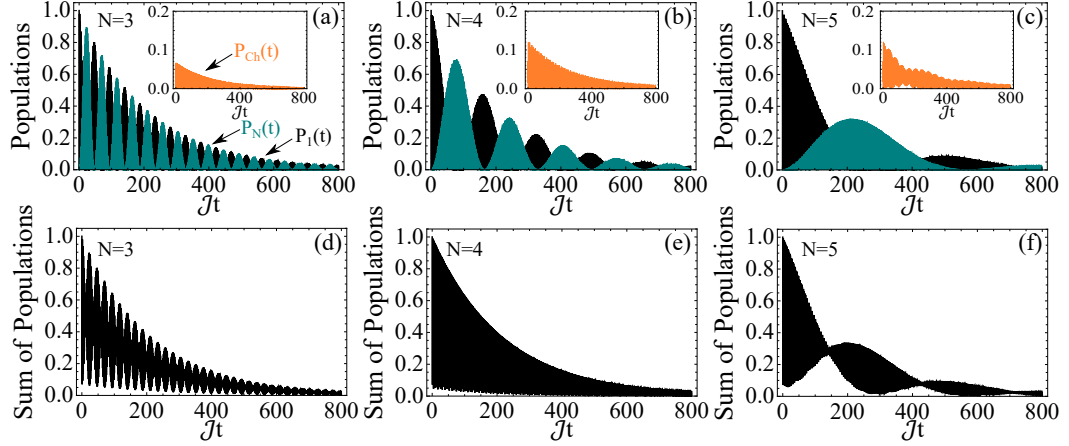


FIGURE 7.3: Long-time dynamics of the populations $P_1(t)$, $P_N(t)$, $P_{Ch}(t)$ (inset) as well as their sum, for spin chains of small length and $c_1(0) = 1$, $\gamma_1 = \gamma_2 = 0.01\mathcal{J}$, $g_1 = g_2 = 1.8\mathcal{J}$, $\Delta_c^1 = \Delta_c^2 = 0$. Panels (a) and (d): $N = 3$, panels (b) and (e): $N = 4$, panels (c) and (f): $N = 5$.

to occur for spin chains of longer length since there may be not enough oscillations between the two edges of the chain before total loss of population to the reservoirs takes place. As seen in Fig. 7.3, the frequency of these oscillation is highly sensitive to N , decreasing as the latter increases.

In Fig. 7.4 we examine the long-time dynamics of the total population for chains with odd number of sites and initial excitation on the centre of the chain, i.e. $c_{(N+1)/2}(0) = 1$. In Figs. 7.2(c) and 7.2(d) we observed that, if the initial excitation is on the first qubit, the total population of the chain decays much faster for increasing values of g_1 . This of course is also true for $c_N(0) = 1$ and increasing values of g_2 , which is also obvious from symmetry arguments. However, as seen in Fig. 7.4(a), if the initial excitation is on the centre of the chain, increasing the magnitude of the couplings between the edge spins and the corresponding environment leads to the completely opposite effect, namely a much slower decay of the total population in the long-time dynamics picture. Such an effect occurs only as long as the boundary couplings are larger than the coupling between the qubits \mathcal{J} . In the opposite regime, the increase of the boundary couplings (to values still less than \mathcal{J}) results to faster decay of the total population to the reservoirs. These results indicate that, for large boundary couplings, the evolution of the edge spins tends to freeze, alluding to a quantum Zeno effect, leading thus to an effective hindering of the total decay to the reservoirs through them. The phenomenon at hand is analyzed in more depth in the next chapter of the thesis. This hindering of the decay becomes even more pronounced for increasing chain lengths (Fig. 7.4(b)), which physically can be attributed to the increased number of pathways for the evolution of the initial excitation throughout the whole chain and therefore the smaller likelihood for the population to reach the edge spins and be lost to the reservoirs.

It may be useful at this point to note that the dissipation of the total population to the reservoirs can also be slowed down by choosing the detunings Δ_c^1 and Δ_c^2 larger than the boundary coupling constants. In that regime of parameters, the dominant modes of the Lorentzian spectral densities of the boundary reservoirs are off-resonant with the qubit frequency and do therefore damp the system less. That might be argued to be obvious. Be that as it may, the statement is valid only in the context of non-Markovian reservoirs. Because the spectral density of a non-Markovian reservoir must at some frequency exhibit a more or less pronounced

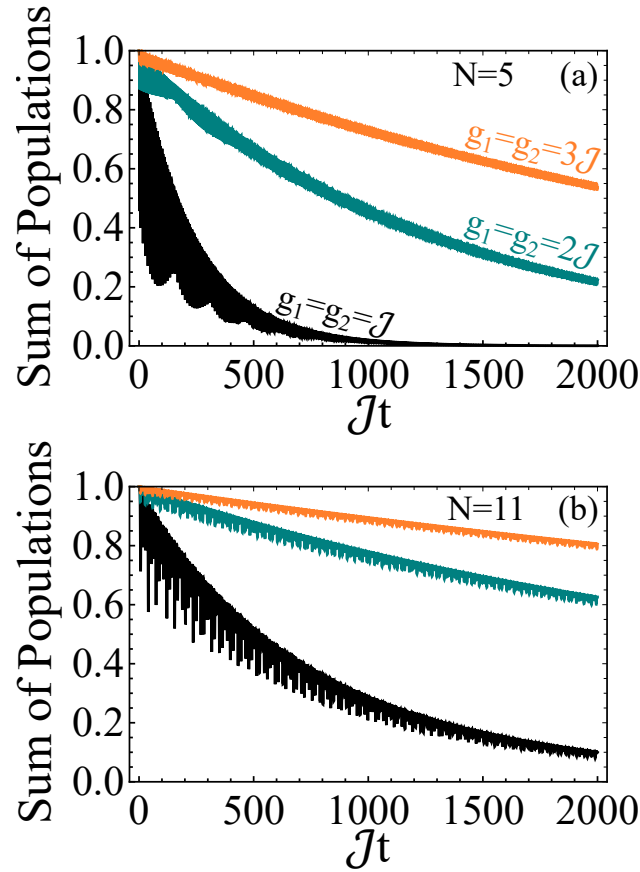


FIGURE 7.4: Long-time dynamics of the sum of all qubit populations in the spin chain with the initial excitation being on the central qubit $c_{(N+1)/2}(0) = 1$ and $\gamma_1 = \gamma_2 = 0.02J$, $\Delta_c^1 = \Delta_c^2 = 0$, (a) $N = 5$ and (b) $N = 11$. Black line: $g_1 = g_2 = J$, teal line: $g_1 = g_2 = 2J$ and orange line: $g_1 = g_2 = 3J$.

peak, as it must depart from the slowly varying, smooth spectral density which is necessary for the Markovian approximation. It could therefore be viewed as yet another feature of non-Markovian behavior.

It is also important to note that the effect in which the increased coupling constants between the edge spins and the environments act like a barrier and protect the total population of the chain from decaying to the latter, do not necessary require an initial excitation in the centre of the chain. This is just one among the choices of possible initial conditions where this phenomenon occurs. The general rule is that the initial excitation should be anywhere but the edge spins, in order to avoid the trapping of the population between the edge spins and their corresponding reservoirs, as was the case in Fig. 7.2(b). For example, the increase of g_1 and g_2 for a chain system initially prepared in the state $\frac{1}{\sqrt{N-2}} \sum_{i=2}^{N-1} |\psi_i\rangle$, will result to the same phenomenon occurring in Fig. 7.4. The details behind this phenomenon is investigated in more detail in chapter 9.

In Fig. 7.5, we study the state transfer properties between the two edge spins of the chain, in terms of the average-state fidelity [245]

$$\mathcal{F}(t) = \frac{1}{2} + \frac{|c_N(t)|^2}{6} + \frac{|c_N(t)|}{3}, \quad (7.20)$$

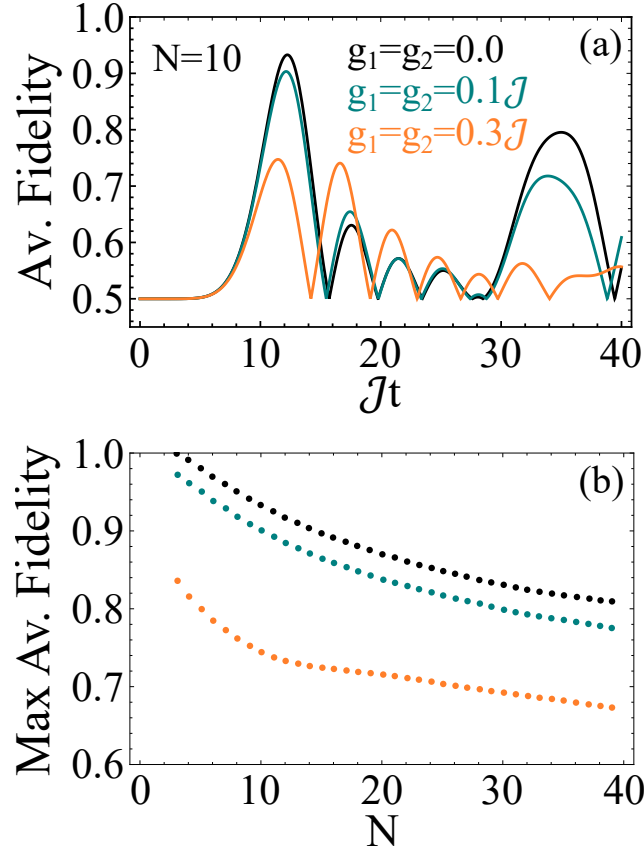


FIGURE 7.5: (a) Dynamics of the average-state fidelity of state transfer between the two edges of the spin chain for $N = 10$ and (b) Maximum average fidelity as a function of the number of spin sites N . In both panels $\gamma_1 = \gamma_2 = 0.5\mathcal{J}$, $\Delta_c^1 = \Delta_c^2 = 0$ and black line/dots: $g_1 = g_2 = 0$, teal line/dots: $g_1 = g_2 = 0.1\mathcal{J}$ and orange line/dots: $g_1 = g_2 = 0.3\mathcal{J}$.

which involves an average over all possible sender-qubit states. In Fig. 5(a) we show the dynamics of the average-state fidelity for a spin chain with $N = 10$ sites, for different values of the boundary couplings g_1 and g_2 . As becomes evident, the first peak of the average-state fidelity is very sensitive to the boundary couplings, decreasing as their values increase. At the same time subsequent peaks in time tend to increase their maximum value. The position of the first peak, indicating the transfer time is slightly decreased by increasing the boundary couplings, however larger values of the latter lead to non-faithful state transfer in general. In Fig. 7.5(b) we examine the behaviour of the maximum value of the average-state fidelity as a function of the number of spin sites for chain length up to 40 sites. As N increases, the maximum average-state fidelity tends towards lower values that depend also on the values of the boundary couplings of the edge spins with the reservoirs. Our results qualitatively agree with a similar study by Feng-Hua Ren et al. [398], where they study the state transfer properties of the same system using the dephasing and dissipation models in terms of the quantum state diffusion approach.

7.3.2 Ohmic environments

As a second example, we consider the case of boundary reservoirs characterized by Ohmic spectral densities [21, 407], according to the relation:

$$J_j(\omega^j) = \mathcal{N}_j g_j^2 \omega_c^j \left(\frac{\omega^j}{\omega_c^j} \right)^{S_j} \exp \left(-\frac{\omega^j}{\omega_c^j} \right), \quad (j = 1, 2), \quad (7.21)$$

where g_j are qubit-environment coupling constants in units of frequency, ω_c^j are the so-called Ohmic cut-off frequencies and S_j , ($j = 1, 2$), are the Ohmic parameters, characterizing whether the spectrum of the reservoirs is sub-Ohmic ($S < 1$), Ohmic ($S = 1$) or super-Ohmic ($S > 1$). \mathcal{N}_j is a normalization constant given by the relation $\mathcal{N}_j = \frac{1}{(\omega_c^j)^2 \Gamma(1+S_j)}$, where $\Gamma(z)$ is the gamma function. Note that, unlike much

of the literature, in our use of Ohmic spectral densities we found it necessary to include the normalization factor \mathcal{N}_j which renders meaningful the comparison with the Lorentzian spectral density, as discussed in the next section of the thesis.

Again, as detailed in Appendix B, the functions $R_j(t)$ and $B_j(s)$, for Ohmic spectral densities, are given by the expressions

$$R_j(t) = g_j^2 e^{i\omega_{eg}t} \left(i\omega_c^j t + 1 \right)^{-1-S_j}, \quad (j = 1, 2). \quad (7.22)$$

and

$$B_j(s) = -g_j^2 \frac{i^{1-S_j}}{\omega_c^j} e^{-iK_j(s)} [K_j(s)]^{S_j} \Gamma(-S_j, -iK_j(s)), \quad (j = 1, 2), \quad (7.23)$$

where $K_j(s) \equiv (s - i\omega_{eg}) / \omega_c^j$, ($j = 1, 2$) and $\Gamma(a, z)$ is the incomplete gamma function. In the special case where S_j are integers, it is useful to use the incomplete gamma function property

$$\Gamma(-n, z) = \frac{1}{n!} \left[\frac{e^{-z}}{z^n} \sum_{k=0}^{n-1} (-1)^k (n-k-1)! z^k + (-1)^n \Gamma(0, z) \right], \quad (7.24)$$

which holds for integer n , in order to express $B_j(s)$ in terms of $\Gamma(0, -iK_j(s))$. Using Eq. (7.23), as in the Lorentzian environments' case, we can easily calculate the Laplace inversion numerically and find the time evolution of the amplitudes $\tilde{c}_i(t)$, i, \dots, N .

In Fig. 7.6 we study the dynamics of the sum of all qubit populations in the chain for various parameters of the Ohmic reservoirs. The dynamics of this quantity provide us straightforward information of how fast the initial excitation gets lost in the two environments. As Fig. 7.6(a) indicates, by increasing the Ohmic parameters S_j , $j = 1, 2$ of the reservoirs, the sum of populations decays more slowly, indicating a slower decay of the single excitation to the environments. Physically, this effect is attributed to the fact that by increasing S_j , the spectral density distribution of the environments is mainly peaked in the vicinity of modes whose frequency is larger than the qubit frequency $\omega_{eg} = \mathcal{J}$ (see inset of Fig. 7.6(b)), and therefore by being off-resonant with the qubit frequency, they damp the system less. A similar behaviour is observed in Fig. 7.6(b), where the dynamics are shown as function of the cut-off frequencies, for Ohmic type of environments ($S_j=1$). Since for Ohmic distributions

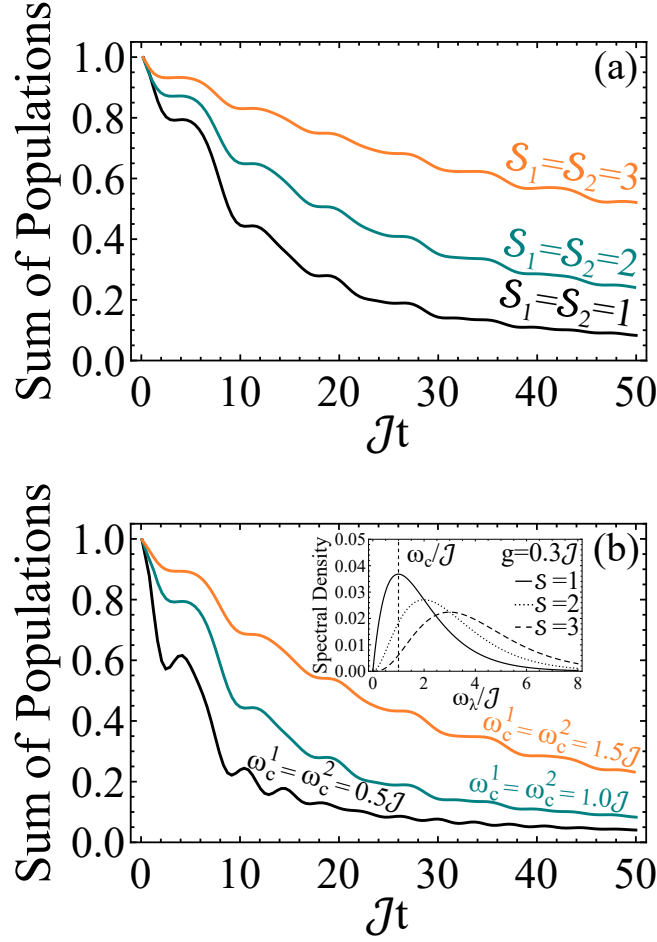


FIGURE 7.6: Dynamics of the sum of all qubit populations in a $N = 6$ qubit chain, boundary driven by reservoirs characterized by Ohmic spectral densities. The parameters used in panel (a) are $\omega_c^1 = \omega_c^2 = \mathcal{J}$, black line: $S_1 = S_2 = 1$, teal line: $S_1 = S_2 = 2$, orange line: $S_1 = S_2 = 3$, while in panel (b), $S_1 = S_2 = 1$, black line: $\omega_c^1 = \omega_c^2 = 0.5\mathcal{J}$, teal line: $\omega_c^1 = \omega_c^2 = 1.0\mathcal{J}$ and orange line: $\omega_c^1 = \omega_c^2 = 1.5\mathcal{J}$. In both panels, $g_1 = g_2 = 0.3\mathcal{J}$ and $\omega_{eg} = \mathcal{J}$ and $c_1(0) = 1$. The inset in panel (b) shows the Ohmic spectral density as a function of ω_λ for various Ohmic parameters S ($S = 1$: solid line, $S = 2$: dotted line and $S = 3$: dashed line) and $g = 0.3\mathcal{J}$ (coupling strength), $\omega_c = \mathcal{J}$ (dotted vertical line).

the peak of the distribution coincides with the cut-off frequency ω_c^j , ($j = 1, 2$), increase of the cut-off frequencies results to distributions whose modes extend mainly beyond ω_{eg} , resulting to a slower decay to the boundary environments. Note that in general, for arbitrary Ohmic parameters, the Ohmic distributions are always peaked at the frequencies $\omega_\lambda^j = S_j \omega_c^j$, ($j = 1, 2$). The characteristic oscillations observed in both panels of Fig. 7.6 are indicative of the non-Markovian character of the Ohmic boundary reservoirs, enabling the exchange of population between them and the spin chain within finite times.

In Fig. 7.7(a) we examine the dynamics of the populations of the edge as well as the channel qubits of the chain for Ohmic boundary reservoirs ($S_j=1$, ($j = 1, 2$)) in the weak boundary couplings regime $g_1, g_2 < \mathcal{J}$. The initial single-excitation is on the first qubit ($c_1(0) = 1$). The dynamics indicate oscillations between the populations of the chain damped by the two Ohmic environments. The situation however may change drastically in the strong boundary couplings regime $g_1, g_2 >$

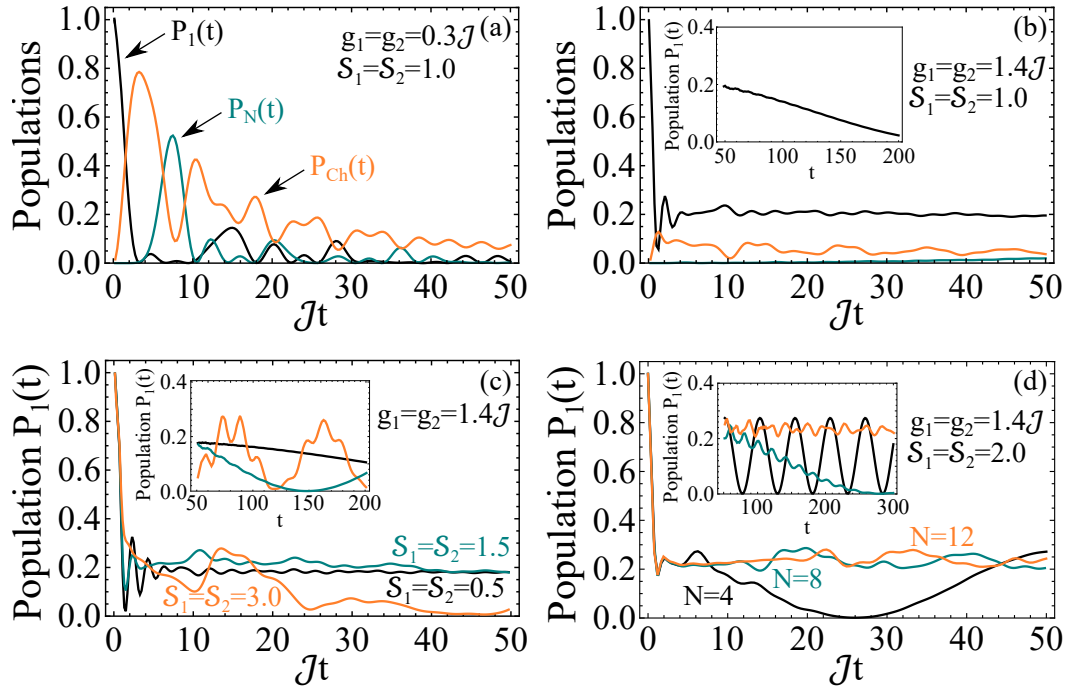


FIGURE 7.7: (a) Dynamics of the populations of the first qubit (black line), N^{th} qubit (teal line) and channel qubits (orange line) for $c_1(0) = 1$, $N = 6$, $\omega_{eg} = \mathcal{J}$, $\omega_c^1 = \omega_c^2 = \mathcal{J}$, $S_1 = S_2 = 1$ and $g_1 = g_2 = 0.3\mathcal{J}$. (b) Same as in panel (a) but for $g_1 = g_2 = 1.4\mathcal{J}$. (c) Dynamics of the population $P_1(t)$ for various values of the environmental Ohmic parameters and $c_1(0) = 1$, $N = 6$, $\omega_{eg} = \mathcal{J}$, $\omega_c^1 = \omega_c^2 = \mathcal{J}$, $g_1 = g_2 = 1.4\mathcal{J}$. Black line: $S_1 = S_2 = 0.5$, teal line: $S_1 = S_2 = 1.5$ and orange line: $S_1 = S_2 = 3.0$. (d) Dynamics of the population $P_1(t)$ for various values of the number of qubit sites and $c_1(0) = 1$, $\omega_{eg} = \mathcal{J}$, $\omega_c^1 = \omega_c^2 = \mathcal{J}$, $S_1 = S_2 = 2.0$, $g_1 = g_2 = 1.4\mathcal{J}$. Black line: $N = 4$, teal line: $N = 8$, orange line: $N = 12$. In the insets of panels (b), (c) and (d) we show the long-time dynamics of the population $P_1(t)$.

\mathcal{J} , as shown in Fig. 7.7(b). In this case the dynamics of the population $P_1(t)$ indicate a long-time stability behaviour around a finite value for times much larger than any other time scale of the system. Note that further increase of the boundary coupling constants will not result to the increase of this long-time stability value. Still, as seen in Fig. 7.7(c), this value is highly affected by the Ohmic parameters of the environments (more specifically by the Ohmic parameter of the first environment which is the one that communicates with the first qubit). In general, increase of the Ohmic parameters results to more complex behaviour as indicated by the orange line of Fig. 7.7(c). In the long-time dynamics picture, the population of the first qubit exhibits an oscillatory behaviour with a frequency that depends on the Ohmic parameter of its boundary reservoir. These non-coherent oscillations become faster for super-Ohmic reservoirs and are essentially an effect associated with the non-Markovianity of the boundary reservoirs that drive the chain, since they indicate population exchanges between the chain and the latter for very long times. Another parameter that affects considerably this oscillatory behaviour is the number of qubit sites. In Fig. 7.7(d) we plot the dynamics of $P_1(t)$ for a chain of various number of qubit sites N , boundary-driven by super-Ohmic environments with $S_j=2$, ($j = 1, 2$). For a small number of qubit sites, the long-time dynamics in the inset of Fig. 7.7(d) indicate a long-living coherent oscillatory behaviour (black line) while for chains

that consist of larger number of qubits, the population of the first qubit exhibit small non-coherent oscillations around a stabilized value (orange line). Our results are just a first glimpse on the richness of the effects one may expect from the boundary-driving of chains with Ohmic type of reservoirs.

7.3.3 Comparing Lorentzian to Ohmic environments

So far we have separately studied the cases of boundary-driven chains by reservoirs with Lorentzian and Ohmic spectral densities. As is evident throughout our formalism, the dynamics of the chain, when the boundary reservoirs are characterized by a Lorentzian spectral density, do not depend directly on the qubit frequency ω_{eg} , but on the detuning Δ_c between the latter and the peak frequency of the Lorentzian. Therefore the specification of Δ_c along with the rest of the Lorentzian and spin chain parameters is sufficient for calculating the wavefunction of the chain. However, this is not the case for Ohmic boundary reservoirs, where in order to calculate aspects of the chain dynamics, one must specify the qubit frequency ω_{eg} as well as all of the rest of the Ohmic spectral density parameters (i.e. cut-off frequency and Ohmic parameter). This direct dependence on the qubit frequency is reflected on the particular form of $B_j(s)$ for Ohmic boundary reservoirs according to Eq. (7.23). In all of our calculations involving Ohmic boundary reservoirs, in the regime of the parameters we have explored, all couplings are not significantly larger than the qubit frequency or the cut-off frequencies ω_c^j , ($j = 1, 2$).

In Fig. 7.8, we provide a comparative evaluation of the effect of the two spectral densities. In Fig. 7.8(a), we have chosen both distributions to be peaked exactly on resonance with the qubit frequency $\omega_{eg} = 3\mathcal{J}$. Although the freedom in the choice of the parameters of each distribution, results to many possible lineshapes of their spectral densities, the general tendency for typical parameters of the two distributions is that Ohmic distributions are usually wider than Lorentzian distributions. In Fig. 7.8(b) we use the distributions of Fig. 7.8(a) as spectral densities of the boundary reservoirs and study the dynamics of the sum of all qubit populations in a $N = 7$ chain for various values of the boundary couplings g_j , ($j = 1, 2$), and initial excitation in the center of the chain. The solid lines correspond to Lorentzian boundary reservoirs while the dashed lines correspond to Ohmic. As also argued in the discussion of Fig. 7.4, since the initial excitation is not on the edge qubits of the chain and the boundary couplings are larger than the qubit-qubit coupling \mathcal{J} , increasing the values of g_j , ($j = 1, 2$), results to slower dissipation of the total excitation in the environments. Comparison between the solid (Lorentzian) and dashed (Ohmic) lines, reveals two major differences: First, the dynamics of the total population in the boundary-driven chain by Lorentzian reservoirs is more sensitive to the increase of the boundary couplings compared to the Ohmic-driven chain. Moreover, for the particular combination of parameters chosen, the total excitation in the chain tends to live longer in Lorentzian-driven chains compared to Ohmic-driven ones, which can be attributed to the much broader profile of the Ohmic spectral density compared to the Lorentzian one. Second, it is evident that the dynamics of the sum of all qubit populations exhibit more vivid oscillations in the Lorentzian case compared to the Ohmic one. Such oscillations are indicative of the non-Markovian character of the boundary-reservoirs and therefore the exchange of populations between the chain and the reservoirs within finite times. Even if both types of reservoirs are non-Markovian, the Ohmic spectral density of Fig. 7.8(a) tends to be substantially

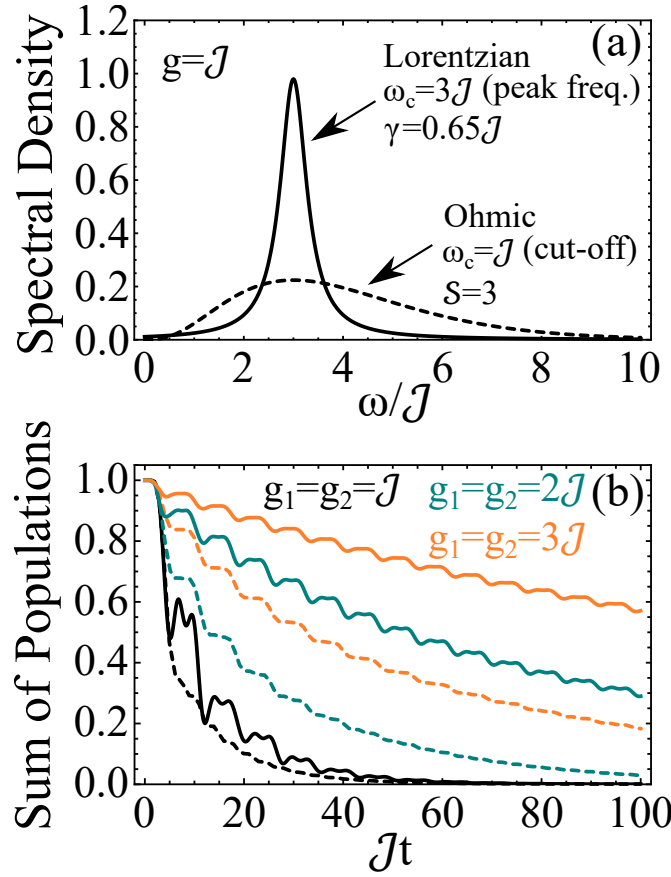


FIGURE 7.8: (a) Spectral density of a Lorentzian distribution with peak frequency $\omega_c = 3J$, width $\gamma = 0.65J$ and $g = J$ (solid line) compared with an Ohmic distribution with Ohmic parameter $S = 3$, cut-off frequency $\omega_c = J$ and $g = J$ (dashed line). (b) Dynamics of the sum of all qubit populations in a $N = 7$ chain and initial excitation in the center of the chain ($c_{(N+1)/2}(0) = 1$), for various coupling strengths between the boundary reservoirs and the edge qubits. Black line: $g_1 = g_2 = J$, teal line: $g_1 = g_2 = 2J$ and orange line: $g_1 = g_2 = 3J$. The solid lines corresponds to Lorentzian boundary reservoirs, while the dashed lines correspond to Ohmic. The rest of the parameters (except the coupling strengths) correspond to the parameters of panel (a). The qubit frequency is chosen to be resonant with the peak frequency of the two distributions, namely $\omega_{eg} = 3J$.

flatter than the Lorentzian spectral density, resembling thus a Markovian-like environment for which no significant oscillations are expected between the chain and its boundaries.

Finally, before concluding, we should note that the dynamics of the average-state fidelity of the state transfer between the edges of a chain boundary-driven by Ohmic reservoirs, display a behaviour more or less qualitatively similar to the corresponding average-state fidelity dynamics of a boundary-driven chain by Lorentzian reservoirs, shown in Fig. 7.5.

To sum up, in this chapter we presented a formalism for the systematic way of calculating the wavefunction of an arbitrary length XX spin chain, boundary-driven by non-Markovian environments of arbitrary spectral density. The theory was cast in terms of Schrödinger's equations of motion, within the single-excitation subspace, and leads to closed form solutions for the Laplace transforms of the amplitudes, for arbitrary initial conditions, using a recursive method. The inversion integrals can

be easily calculated numerically (or even analytically in some cases), upon specification of the spectral density of each environment. The calculation of the wavefunction of the chain within the single-excitation subspace enables the study of a number of interesting properties of the system. As an illustration of the potential of the approach, we have considered Lorentzian and Ohmic spectral densities for the boundary environments and studied aspects of the dynamical, as well as of the state transfer properties of the system. Our results demonstrate the memory effects of the non-Markovian environments. The concomitant information exchange between the latter and the spin chain, give rise to a plethora of interesting effects such as population trapping, oscillations between the populations of the edge spins or the protection of the spin populations against dissipation, for increased values of the boundary couplings.

One aspect of our results that turns out to be revealing and somewhat surprising has to do with the comparative analysis of the dynamics of the chain under two quite different reservoirs; namely Lorentzian and Ohmic. We adopt the general notion that any reservoir, with spectral density not smoothly and slowly varying as a function of energy (frequency), within an extended range around the resonance with the qubit, is non-Markovian. This entails some degree of memory, which in turn implies that the loss into the reservoir would not be monotonic. In much of the work and approaches on non-Markovian reservoirs, it is the Lorentzian that has served as a typical illustration. Physically, that behavior should be expected for a Lorentzian spectral density as it exhibits a well-defined peak. But so does an Ohmic, as well as a superohmic spectral density. However, our direct quantitative comparison of the effect of a Lorentzian spectral density versus that of a superohmic, reveals effects of an almost qualitative difference between the two; the effect of the superohmic resembles an almost Markovian-like reservoir, which implies a much lower degree of non-Markovianity. This concrete example complements earlier general formulations of measures of non-Markovian behavior [408].

Our work was motivated by the rapidly growing interest in the field of boundary-driven open quantum systems and in particular the need for the development of the necessary analytical or numerical tools for the study of their properties. The results provide the background for a number of extensions, such as accounting for different spin chain configurations, as well as the theoretical description of the system, within our formal development, beyond the single-excitation. It would in addition be interesting to investigate whether the behavior for long times of the edge qubits, which communicate directly with the boundary reservoirs (Fig. 7.7), could be useful in the survival of long-distance quantum correlations, for chains consisting of large number of qubit sites, boundary-driven by Ohmic reservoirs. It should, however, be kept in mind that, from the standpoint of state transfer and quantum information processing, the single-excitation scheme is sufficient. Nevertheless, from the standpoint of statistical mechanics properties of spin chains connected to non-Markovian environments, extension of the approach beyond the single-excitation subspace is necessary, although this represents a compelling and much challenging task within the context of our formalism.

Extension of our work to different spin chain configurations would provide further insight into the dynamics of systems boundary driven by non-Markovian environments. On that issue, our approach avails itself to the evaluation of the degree of non-Markovianity of various spectral densities. In the present chapter, by comparing the effects of Lorentzian to Ohmic environments, as manifested in the time evolution of the system and the concomitant dissipation, we have noted some qualitative features attributable to non-Markovianity. There are, however, quantitative

measures of non-Markovianity, as discussed for example in [408]. Given that there are more than one relevant measures [409], it is the purpose of the next chapter to explore those aspects in the context of our formalism and provide a quantitative tool of evaluating non-Markovianity in open quantum systems damped by various non-Markovian reservoirs.

Chapter 8

Non-Markovianity in the time evolution of open quantum systems assessed by means of quantum state distance

In the previous chapter we studied the dynamical and state transfer properties of an arbitrary length spin XX chain driven by non-Markovian reservoirs at both ends. Through a formulation in terms of the wave-function, combined with Laplace transform, we were able to obtain results for chains of arbitrary length, i.e. number of sites, and for environments characterized by different spectral densities such as Lorentzian and Ohmic. Guided by the behaviour of the excitation dynamics, we effectively assessed the qualitative differences of the system from that driven by a Markovian reservoir which is known to entail monotonic decay. That assessment, indirect as it was, can only be considered qualitative, although it did provide a glimpse of the similarities between these two non-Markovian cases. Yet, there are a number of technical measures aiming at a quantitative assessment of the difference between the states of a quantum system, as it evolves under coupling to different external causes; in this case reservoirs. The difference between the evolution under a given reservoir from that under a Markovian one, should therefore provide a quantitative measure for what, following standard terminology [408, 410], we shall refer to as non-Markovianity" (NM). The term degree of Markovianity (DM) can also be found in the literature, meant to indicate the similarity to the evolution under a Markovian reservoir. Although we have modelled the reservoirs in terms of an infinite collection of bosons, less common but essentially equivalent possible modelling in terms of fermions can be found in the literature [411]. By its nature, our system consists of fermions which could also be handled via the Jordan-Wigner transformation [262, 412]. The route we have chosen has been dictated by simplicity and usefulness in state transfer problems.

8.1 General description of our methodology

Having examined much of the existing literature on the issue, we have come to the realization that our scheme provides excellent territory for the quantitative study of non-Markovianity. The relevant literature is vast, ranging from general formal considerations [413–418] to examples in small specific systems [419–422], including methods for the estimation of NM using machine learning tools [423]. The advantage of our system stems from the combination of a realistic arrangement of an XX chain of mutually interacting qubits, with a reservoir of arbitrary spectral density

coupled to one end. In the previous chapter of the thesis, we had considered a chain coupled to reservoirs at both ends. Although the present quantitative study could as easily address that arrangement, since our objective is the comparative study of non-Markovian reservoirs, we have chosen to consider the same system with only one end qubit coupled to a variety of reservoirs, so as to focus on the role of the reservoir. We calculate first the time evolution of the system under each reservoir, one of which is Markovian. In the second step, we calculate the difference of the state of the system evolved under a given non-Markovian reservoir from the state evolved under the Markovian one. The time evolution of that difference is what we refer to as the NM of the given reservoir.

We have chosen to address the issue in terms of perhaps the most direct notion, namely the quantum state distance (QSD). A variety of measures appropriate as tools for our task have been proposed over the years [409, 424]. Their objective is the quantification of the difference between two different quantum states of a system, which is of fundamental importance in quantum information processing [425, 426], state transfer being a case in point [398]. The most common quantity pertaining to that issue is the Fidelity (F), for which there are various expressions in the literature [427–429]. It is meant to characterize the similarity or difference between the density matrices representing the two states. Obviously it is related to the notion of distance between two quantum states, which explains why the formulation of some distance measures involve one of the F expressions. There is no unique expression or value for F, which is also the case for the QSD. In some sense, it may be matter of taste or perhaps usefulness in a particular context which value of F or QSD is adopted.

Our stated objective then is the quantitative evaluation and calibration of non-Markovianity of several non-Markovian reservoirs by means of QSD [430]. In view of the diversity of expressions for the QSD, inevitably an additional component has been injected into our task, namely, the comparative analysis of various QSD measures. Specifically, since the NM does depend on the particular QSD measure, it is important to know whether and to what extent the classification of various reservoirs in terms of NM is independent of the QSD measure employed. And this completes the road map of this chapter.

In the following section, we review various QSD measures, their properties and the modifications necessary in order to accommodate issues pertaining to open systems. In section 8.3 we describe the theoretical approach to our problem in terms of the time-dependent Schrödinger's equations of motion in Laplace space, from which one can obtain even closed form solutions for the judiciously transformed amplitudes, for chains of arbitrary length, as well as arbitrary initial conditions, within the single-excitation subspace. Using the amplitudes of the chain sites, we construct the density matrices necessary for the calculation of the various QSD measures. Finally, we present the results of our study and provide an overview as well as some concluding remarks related to our work.

8.2 Brief summary and necessary modifications of QSD measures

Before embarking on the discussion of QSD measures, a significant clarification related to our approach and treatment is necessary. As discussed in the next section, the time evolution of the system is formulated in terms of the time-dependent Schrödinger equation, from which we obtain the amplitudes of the wave-function of the system as a function of time, after having eliminated the degrees of freedom

of the reservoir. The time-dependent amplitudes are then combined to obtain the reduced density operator of the system which is needed in all expressions of QSD. The advantage of this approach is that it is applicable for any form of reservoir, sidestepping thus the need for a master equation which is not generally available, especially for non-Markovian reservoirs. There is, however, a price paid for this advantage. The resulting density operator describes only the excitation, because the populations of the ground states have been discarded in the process of eliminating the continuum of the reservoir. In other words, we retain only one part of the entire Hilbert space of the compound system. Inclusion of those infinite in number terms is computationally impossible, as it would entail keeping track of the degrees of freedom of the reservoir. The implication for the system density operator is that its trace eventually decays to zero. The situation is analogous to the treatment of the decay of a discrete state coupled to a continuum [26, 184], except that here we deal with the excitation of a chain. Thus in a real sense, the reduced density operator describes the time evolution of the excitation which as expected, in the long time limit disappears into the reservoir. Our study aims at examining the role of the form of a reservoir in that time evolution.

In books and papers, more often than not, expressions for F or QSD are assumed, either tacitly or explicitly, to involve density operators of trace equal to unity. However, since in our approach, the trace of the reduced density operator decays, the expression for the QSD needs to be modified accordingly.

To illustrate the issue, let us consider the most common and straightforward QSD measure, referred to as the trace distance. It is defined by

$$D_T \equiv \frac{1}{2} \text{Tr} |\rho - \sigma|, \quad (8.1)$$

where $|A|$, for a matrix A , stands for $\sqrt{A^\dagger A}$ which stands for the positive definite square root of the matrix under the radical symbol, with A^\dagger being the Hermitian adjoint of A . Although slight variations of the definition of the square root of a matrix can be found in the literature, we adopt the one most commonly found in the literature on quantum information [431]. Applying the above definition to the expression for the trace distance, we obtain

$$D_T = \frac{1}{2} \text{Tr} \sqrt{(\rho^\dagger \rho + \sigma^\dagger \sigma - \rho^\dagger \sigma - \sigma^\dagger \rho)}. \quad (8.2)$$

Since the density operators under the radical are Hermitian, the expression for the trace distance shown in Eq. (8.2) reduces to

$$D_T = \frac{1}{2} \text{Tr} (\rho - \sigma), \quad (8.3)$$

which is one of the possible square roots. It so happens that the trace of that root is identically zero for matrices normalized to unity. However, in our case the traces of the density operators are time-dependent, decaying to zero in the long time limit. Consequently the trace distance is also time-dependent in a fashion depending on the relevant reservoirs, as calculated through Eq. (8.2).

Let us consider now another expression for QSD, namely the Hellinger measure D_H , defined as

$$D_H^2 \equiv \text{Tr} (\sqrt{\rho} - \sqrt{\sigma})^2, \quad (8.4)$$

which upon expanding the square becomes

$$D_H^2 = \text{Tr } \rho + \text{Tr } \sigma - 2 \text{Tr } (\sqrt{\rho} \sqrt{\sigma}), \quad (8.5)$$

where the invariance of the trace under cyclic permutation of the factors has been used. If the density operators are and remain normalized to unity, Eq. (8.5) reduces to $D_H^2 = 2 [1 - \text{Tr } (\sqrt{\rho} \sqrt{\sigma})]$, leading to the expression

$$D_H = \sqrt{2} [1 - \text{Tr } (\sqrt{\rho} \sqrt{\sigma})]^{1/2}, \quad (8.6)$$

for the Hellinger distance measure, which typically is the expression cited for this QSD measure. However, in order to account for our case, following Eq. (8.5), we have:

$$D_H = [\text{Tr } \rho + \text{Tr } \sigma - 2 \text{Tr } (\sqrt{\rho} \sqrt{\sigma})]^{1/2}. \quad (8.7)$$

If the density operators tend to zero as $t \rightarrow \infty$, in that limit, Eq. (8.7) correctly yields zero for the distance between the two states, as they both decay. On the other hand, Eq. (8.6) would lead to the value $\sqrt{2}$ which on physical grounds, is at best problematic, as it does not account for the decay of the traces of the density operators.

There is one more measure that we employ in our calculations. It is known as the Bures distance measure, usually denoted by D_B . Since it is typically defined in terms of one of the expressions for F , we list below the three most common expressions, labelled for our convenience F_1 , F_2 and F_3 . They are:

$$F_1(\rho, \sigma) = \left(\text{Tr } \sqrt{\sqrt{\rho} \sigma \sqrt{\rho}} \right)^2, \quad (8.8a)$$

$$F_2(\rho, \sigma) = \text{Tr } \sqrt{\sqrt{\rho} \sigma \sqrt{\rho}} = \sqrt{F_1(\rho, \sigma)}, \quad (8.8b)$$

$$F_3(\rho, \sigma) = \text{Tr } (\rho \sigma). \quad (8.8c)$$

The Bures QSD is usually defined as $D_B^2(\rho, \sigma) \equiv 2 [1 - \sqrt{F_1(\rho, \sigma)}]$, which, in view of Eq. (8.8b) above, can be simply written as

$$D_B^2(\rho, \sigma) = 2 [1 - F_2(\rho, \sigma)], \quad (8.9)$$

from which we obtain

$$D_B(\rho, \sigma) = \sqrt{2} \left[1 - \text{Tr } \sqrt{\sqrt{\rho} \sigma \sqrt{\rho}} \right]^{1/2}. \quad (8.10)$$

Again, this expression is valid as long as the traces of both density operators remain equal to one, because if in any distance measure we set $\rho = \sigma$, we should obtain zero. This condition is satisfied as long as $\text{Tr } \rho = \text{Tr } \sigma = 1$ for all times. But if the traces decay to zero, for the case $\rho = \sigma$ we would obtain the nonphysical value $\sqrt{2}$. This contradiction is amended if the above expression is modified as shown in the following equation:

$$D_B(\rho, \sigma) = \sqrt{2} \left[\frac{1}{2} (\text{Tr } \rho + \text{Tr } \sigma) - \text{Tr } \sqrt{\sqrt{\rho} \sigma \sqrt{\rho}} \right]^{1/2}. \quad (8.11)$$

This is the expression we are using for the Bures QSD in this chapter. In the long time limit and in the presence of dissipation, the modified Bures distance tends to zero as it should. Part of our investigation addresses the rate with which the various QSD measures tend to their final value. We are in addition interested in the consistency of the character of NM obtained by different measures. For whatever it is worth, it seems to us that one could as well define a QSD measure through an extension of Eq. (8.9), by inserting any of the expressions for F .

8.3 Theoretical formulation

As discussed in section 8.2, all expressions for QSD measures involve the density matrices ρ and σ of the quantum states whose distance is to be calculated. In general, the temporal evolution of the density matrix of a system coupled to an external environment is given by the solution of a master equation, obtained after tracing out the environmental degrees of freedom from the density matrix of the compound system (system + environment) [26]. Despite the ongoing progress in the derivation of closed form expressions for master equations of quantum systems coupled to non-Markovian reservoirs [228, 432–435], such expressions are usually obtained for special cases of environmental spectral densities under certain approximations and often are too complicated to be handled even numerically. Consequently, an attempt to quantify the degree of non-Markovianity in systems coupled to environments with a variety of possible spectral densities using numerical solutions of the respective master equations would be pointless -if possible at all- for certain forms of environmental spectral densities, such as those studied in this work.

To address this difficulty, we have developed an approach enabling the calculation of the amplitudes of the wavefunction of the open system, from which we then construct its density matrix. This formulation has been described in detail in the previous chapter of the thesis, where it was used to calculate aspects of the dynamics of a XX chain boundary-driven by non-Markovian environments. As demonstrated below, one of the advantages of this approach is its applicability to any possible form of environmental spectral density, as well as an arbitrary number of qubits in the chain.

The system under consideration consists of N identical qubits in a one-dimensional configuration coupled to each other via a nearest-neighbor coupling \mathcal{J} . The N^{th} qubit of the chain is coupled, via a coupling strength g , to an external environment of an arbitrary spectral density $J(\omega)$. Our goal is to assess the degree of non-Markovianity of that system by means of the QSD between its density matrix and the density matrix of the same system of N qubits, with the N^{th} qubit coupled to a Markovian environment. The Markovian environment is known to induce a shift of the energy of the last qubit, as well as a decay [26]. We neglect the shift, as it is of no significance in the issue of dissipation and denote the decay by γ_M . The problem is studied using several QSD measures, for various forms of non-Markovian spectral densities $J(\omega)$. Hereafter, we denote the density matrix of the Markovian open system by $\sigma(t)$ and the density matrix of the non-Markovian open system by $\rho(t)$. A schematic presentation of the systems under study and our methodology is depicted in Fig. 8.1.

The Hamiltonian of the compound system $\mathcal{H} = \mathcal{H}_S + \mathcal{H}_E + \mathcal{H}_I$, consists of three parts; namely, the Hamiltonian of the XX chain \mathcal{H}_S , the Hamiltonian of the environment coupled to N^{th} (last) qubit of the chain \mathcal{H}_E , and the chain-environment interaction Hamiltonian \mathcal{H}_I , given by the relations ($\hbar = 1$):

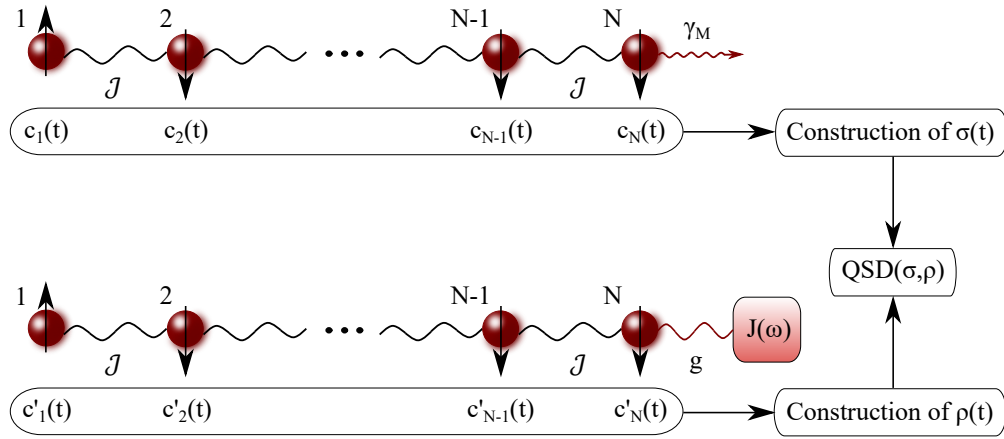


FIGURE 8.1: Schematic representation of the system at study and our methodology. A chain of an arbitrary number of coupled qubits is interacting with an external reservoir at its one end. The system is studied for two different cases of external reservoirs, namely for a Markovian and a non-Markovian reservoir with spectral density $J(\omega)$. Through our methodology we calculate the qubit amplitudes in the single-excitation subspace via which we construct the density matrix of the chain for each case. The QSD between the two density matrices is then calculated using various measures, allowing us to assess the degree of non-Markovianity of the system for different types of spectral densities $J(\omega)$.

$$\mathcal{H}_S = \omega_e \sum_{i=1}^N |e\rangle_{ii} \langle e| + \omega_g \sum_{i=1}^N |g\rangle_{ii} \langle g| + \sum_{i=1}^{N-1} \frac{\mathcal{J}}{2} (\sigma_i^+ \sigma_{i+1}^- + \sigma_i^- \sigma_{i+1}^+), \quad (8.12a)$$

$$\mathcal{H}_E = \sum_{\lambda} \omega_{\lambda} a_{\lambda}^E a_{\lambda}^{E\dagger}, \quad (8.12b)$$

$$\mathcal{H}_I = \sum_{\lambda} g(\omega_{\lambda}) (a_{\lambda}^E \sigma_N^+ + a_{\lambda}^{E\dagger} \sigma_N^-), \quad (8.12c)$$

where ω_g and ω_e are, respectively, the energies of the ground and excited state of each spin (all of which are assumed identical), ω_{λ} is the energy of the λ -mode of the environment consisting of an infinite number of bosons, a_{λ}^E and $a_{\lambda}^{E\dagger}$, are the bosonic annihilation and creation operators of the environment, and $\sigma_i^+ = |e\rangle_{ii} \langle g|$ and $\sigma_i^- = |g\rangle_{ii} \langle e|$, $i = 1, \dots, N$ are the qubit raising and lowering operators, respectively.

The wavefunction of the compound system in the single-excitation space is expressed as:

$$|\Psi(t)\rangle = \sum_{i=1}^N c_i(t) |\psi_i\rangle + \sum_{\lambda} c_{\lambda}^E(t) |\psi_{\lambda}^E\rangle, \quad (8.13)$$

where,

$$|\psi_i\rangle \equiv |g\rangle_1 |g\rangle_2 \dots |g\rangle_{i-1} |e\rangle_i |g\rangle_{i+1} \dots |g\rangle_N |0\rangle_E, \quad (8.14a)$$

and

$$|\psi_{\lambda}^E\rangle \equiv |g\rangle_1 |g\rangle_2 \dots |g\rangle_N |00\dots 01_{\lambda} 0\dots 00\rangle_E. \quad (8.14b)$$

8.3.1 Markovian system: construction of $\sigma(t)$

As already noted above, a Markovian environment (i.e. an environment with slowly varying spectral density) interacting with a two-level quantum system (qubit) within the Born approximation, induces a shift as well as a decay in the energy of the latter. Formally, this result is obtained by tracing the environmental degrees of freedom out of the density matrix of the compound system, a procedure found in many quantum optics and open quantum systems textbooks [12, 26]. In our problem, the Markovian environment will only affect the energy of the last qubit (N^{th} qubit) of the chain. Neglecting the shift and keeping the decay rate γ_M , the time dependent Schrödinger equation (TDSE) for the chain amplitudes reads:

$$i \frac{dc_i(t)}{dt} = [\omega_e + (N-1)\omega_g] c_i(t) + \frac{\mathcal{J}}{2} [c_{i-1}(t) + c_{i+1}(t)], \quad i = 1, \dots, N-1, \quad (8.15a)$$

$$i \frac{dc_N(t)}{dt} = [\omega_e + (N-1)\omega_g - i\frac{\gamma_M}{2}] c_N(t) + \frac{\mathcal{J}}{2} c_{N-1}(t) \quad (8.15b)$$

where, in order to compress notation in our equations, we allowed i to run from 1 to $N-1$ in Eq. (8.15a), noting that $c_{i-1}(t) = 0$ for $i = 1$, because qubit 1 is coupled only to qubit 2. To simplify the set of Eqs. (8.15), it is useful to introduce the amplitude transformations $c_i(t) = e^{-i[\omega_e + (N-1)\omega_g]t} \tilde{c}_i(t)$, $i = 1, \dots, N-1$ and $c_N(t) = e^{-i[\omega_e + (N-1)\omega_g - i\frac{\gamma_M}{2}]t} \tilde{c}_N(t)$, in terms of which the equations become:

$$\frac{d\tilde{c}_i(t)}{dt} = -i\frac{\mathcal{J}}{2} [\tilde{c}_{i-1}(t) + \tilde{c}_{i+1}(t)], \quad i = 1, \dots, N-1, \quad (8.16a)$$

$$\frac{d\tilde{c}_N(t)}{dt} = -i\frac{\mathcal{J}}{2} e^{\frac{\gamma_M}{2}t} \tilde{c}_{N-1}(t) \quad (8.16b)$$

where, as above, $\tilde{c}_{i-1}(t) = 0$ for $i = 1$. The above set of N coupled linear differential equations can be readily solved numerically to yield the time dependence of the tilde amplitudes of the chain sites. The density matrix $\sigma(t)$ of the chain can then be constructed in terms of the site amplitudes as shown in the following equation:

$$\sigma(t) = \sum_{i,j}^N c_i(t) c_j^*(t) |\psi_i\rangle \langle \psi_j| \quad (8.17)$$

8.3.2 Non-Markovian system (construction of $\rho(t)$)

The construction of $\rho(t)$, i.e. the density matrix of the chain with the last qubit interacting with a non-Markovian reservoir, is a subtler task because the memory effects of the reservoir make the equation of the last qubit amplitude more complicated. In the previous chapter of the thesis, we examined the dynamics of XX chain boundary driven by non-Markovian reservoirs. On the basis of the approach developed therein, as applied to the present system, we outline here the basic procedure to obtain the amplitudes of the chain sites. In order to discriminate the amplitudes from those of the Markovian damped chain, we denote them by $c'_i(t)$, $i = 1, \dots, N$.

Adopting the amplitude transformations $c'_i(t) = e^{-i[\omega_e + (N-1)\omega_g]t} \tilde{c}'_i(t)$, $i = 1, \dots, N$ and $c'^E_\lambda(t) = e^{-i(N\omega_g + \omega_\lambda)t} \tilde{c}'^E_\lambda(t)$, the time-dependent Schrödinger's equation yields:

$$i \frac{d\tilde{c}'_i(t)}{dt} = \frac{\mathcal{J}}{2} [\tilde{c}'_{i-1}(t) + \tilde{c}'_{i+1}(t)], \quad i = 1, \dots, N-1, \quad (8.18a)$$

$$i \frac{d\tilde{c}'_N(t)}{dt} = \frac{\mathcal{J}}{2} \tilde{c}'_{N-1}(t) + \sum_{\lambda} g(\omega_{\lambda}) e^{-i\Delta_{\lambda}t} \tilde{c}'_{\lambda}{}^E(t), \quad (8.18b)$$

$$i \frac{d\tilde{c}'_{\lambda}{}^E(t)}{dt} = g(\omega_{\lambda}) e^{i\Delta_{\lambda}t} \tilde{c}'_N(t), \quad (8.18c)$$

where $\Delta_{\lambda} \equiv \omega_{\lambda} - (\omega_e - \omega_g) \equiv \omega_{\lambda} - \omega_{eg}$ and $\tilde{c}'_{i-1}(t) = 0$ for $i = 1$. Formal integration of Eq. (8.18c), under the initial condition $\tilde{c}'_{\lambda}{}^E(0) = 0$, and substitution into Eq. (8.18b), yields:

$$\frac{d\tilde{c}'_N(t)}{dt} = -i \frac{\mathcal{J}}{2} \tilde{c}'_{N-1}(t) - \int_0^t \sum_{\lambda} e^{-i\Delta_{\lambda}(t-t')} [g(\omega_{\lambda})]^2 \tilde{c}'_N(t') dt'. \quad (8.19)$$

The summation over the environmental modes is at this point replaced by an integration which requires the specification of the environment's spectral density $J(\omega)$, according to the relation $\sum_{\lambda} [g(\omega_{\lambda})]^2 \rightarrow \int d\omega J(\omega)$. The resulting set of differential equations then becomes:

$$\frac{d\tilde{c}'_i(t)}{dt} = -i \frac{\mathcal{J}}{2} [\tilde{c}'_{i-1}(t) + \tilde{c}'_{i+1}(t)], \quad i = 1, \dots, N-1, \quad (8.20a)$$

$$\frac{d\tilde{c}'_N(t)}{dt} = -i \frac{\mathcal{J}}{2} \tilde{c}'_{N-1}(t) - \int_0^t R(t-t') \tilde{c}'_N(t') dt', \quad (8.20b)$$

where

$$R(t) \equiv \int_0^{\infty} J(\omega) e^{-i(\omega - \omega_{eg})t} d\omega. \quad (8.21)$$

The second term in Eq. (8.20b) reflects the possibility for the excitation to be transferred from the N^{th} qubit to the non-Markovian reservoir and vice versa.

Taking the Laplace transform of Eqs. (8.20) and following the procedure presented in the previous chapter of the thesis, we find that the Laplace transform $F_1(s)$ of the tilde amplitude $\tilde{c}'_1(t)$ is given by the expression:

$$F_1(s) = \frac{ikc'_N(0) - k^2[s+B(s)]A_1(s)c'_{N-1}(0) + (ik) \sum_{m=1}^{N-2} \left\{ ik[s+B(s)]A_{N-m}(s) - A_{N-1-m}(s) \right\} c'_m(0)}{ik[s+B(s)]A_N(s) - [1+s+B(s)]A_{N-1}(s)}. \quad (8.22)$$

where $k \equiv \frac{2}{\mathcal{J}}$, $B(s)$ is the Laplace transform of the function $R(t)$ and $A_m(s)$ is given by the following expression:

$$A_m(s) \equiv \frac{\left[(iks) + i\sqrt{k^2s^2 + 4} \right]^m - \left[(iks) - i\sqrt{k^2s^2 + 4} \right]^m}{2^m i \sqrt{k^2s^2 + 4}}, \quad m = 1, \dots, N. \quad (8.23)$$

The Laplace transforms $F_i(s)$ of the remaining qubit amplitudes are connected to $F_1(s)$ via the relation:

$$F_i(s) = A_i(s)F_1(s) - (ik) \sum_{n=1}^{i-1} A_{i-n}(s)c'_n(0), \quad i = 2, \dots, N, \quad (8.24)$$

where we used the fact that $\tilde{c}'_i(0) = c'_i(0)$ for every $i = 1, \dots, N$. The effectiveness of this method rests on the fact that it allows the derivation of closed form expressions for the Laplace transforms of the tilde amplitudes for an arbitrary number of qubits N , an arbitrary spectral density $J(\omega)$ for the environment that interacts with the

N^{th} qubit of the chain, as well as arbitrary initial conditions. The Laplace inversion integrals can be readily calculated numerically (or even analytically in some cases) upon specification of these parameters to yield the tilde amplitudes of the chain sites, in terms of which we can calculate $c'_i(t)$, $i = 1, \dots, N$, and thus construct the density matrix for the chain via the relation:

$$\rho(t) = \sum_{i,j}^N c'_i(t) c'^*_j(t) |\psi_i\rangle \langle \psi_j| \quad (8.25)$$

By construction, the density operators given by Eqs. (8.17) and (8.25) are Hermitian, with a time-dependence that leads to a decaying trace, for reasons discussed in section 8.2. Specific types of non-Markovian reservoirs, such as Lorentzian [21, 317], Lorentzian squared [436] and Ohmic [407, 437] are employed in order to assess the effect of non-Markovianity on the chain in each case. The analytical derivations of the functions $R(t)$ and $B(s)$ for these types of reservoirs are given in Appendix B.

8.4 Quantitative evaluation of non-Markovianity for various non-Markovian reservoirs

The stated objective of this section is the quantitative assessment of NM of non-Markovian reservoirs in a realistic context provided by a spin chain. As outlined in the previous sections, we have chosen to assess NM in terms of QSD measures between the state of the chain coupled to various reservoirs. An obviously suitable for the purpose quantity is the QSD between the density operator of the chain evolved under a Markovian from that evolved under a non-Markovian reservoir. From a physical standpoint, it stands to reason that the larger the values of the QSD, irrespective of the measure under consideration, the less Markovian the system's evolution will be, which means more pronounced non-Markovianity. Given that reservoirs by definition involve certain parameters, characterising their properties, in addition to the system-reservoir coupling constant, a decision has to be made as to the choice of parameters that make the value of QSD most meaningful. It is rather obvious that a direct comparison between, for example, an evolution under a Markovian reservoir with damping rate γ_M and a Lorentzian one with arbitrarily chosen parameters g , γ and Δ_c would be pointless. We suggest that, for the comparison to be meaningful, a feature common to the effect of all reservoirs entering the comparison should be adopted. With that in mind, we note that for all reservoirs the excitation of all qubits will eventually decay to zero. Since initially the excitation is in the first qubit, without claim to uniqueness, we have chosen the parameters of the various reservoirs such that the half life of the excitation of the first qubit is approximately the same to its half life under a Markovian reservoir with a given γ_M . This convention leaves a freedom on the choice of the parameter g , which expresses the coupling strength between the last qubit of the chain and the non-Markovian reservoir, and consequently it regulates the frequency of population exchange between the two. In both the single-qubit as well as the many-qubit cases, and for all non-Markovian reservoirs considered, we fix the parameter g at the value $g = 1$, i.e. we measure all parameters in units of g . Note that the parameters that determine the lifetime of the excitation in the chain are chosen such that the period of population oscillations between the last qubit and the reservoir is smaller than this lifetime.

8.4.1 Single qubit

We begin our analysis by considering the simplest case of a single qubit coupled to a variety of non-Markovian reservoirs. These results serve as a point of reference in the comparative analysis of the interplay between non-Markovianity and qubit-qubit interaction, as reflected in the evolution of the QSD measures as a function of the time.

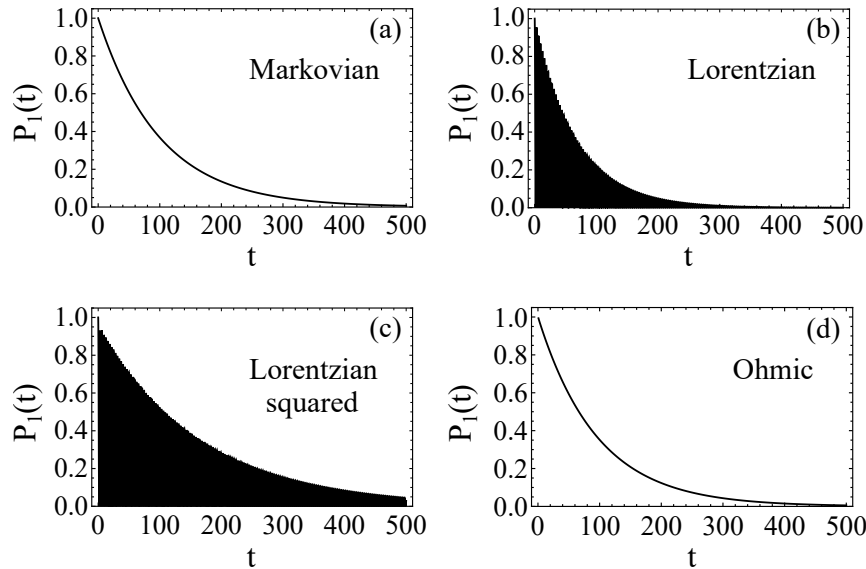


FIGURE 8.2: Dynamics of the excitation survival probability of a single qubit coupled to various types of reservoirs: (a) Markovian reservoir with $\gamma_M = 0.01$, (b) Lorentzian reservoir with $g = 1$, $\gamma = 0.03$ and $\Delta_c = 0$, (c) Lorentzian squared reservoir with $g = 1$, $\gamma = 0.3$ and $\Delta_c = 0$, (d) Ohmic reservoir with $g = 1$, $S = 1.5$, $\omega_c = 8$ and qubit frequency $\omega_{eg} = 10$.

In Fig. 8.2 we plot the time dynamics of the single qubit excitation survival probability for various types of reservoirs. In particular, we examine the cases of Markovian, Lorentzian, Lorentzian squared and Ohmic reservoirs, with the parameters of each non-Markovian reservoir chosen as described above. The Lorentzian and Lorentzian squared spectral densities result in general to fast oscillations in the single-qubit survival of excitation dynamics, indicating the exchange of the excitation between the qubit and the environment within finite times. The high frequency of these oscillations is attributed to a large coupling strength g compared to the Lorentzian and Lorentzian-squared widths γ . As g is decreased the frequency of oscillations tends also to decrease. Note that the Markovian limit would be captured by increasing γ but at the same time keeping the ratio g^2/γ constant. The Ohmic spectral distribution tends in general to be much broader than the Lorentzian and Lorentzian squared distributions, leading to a qubit excitation survival probability that resembles more the respective survival probability of the excitation for the Markovian case.

The QSD measures between the Markovian-damped single-qubit system and the non-Markovian ones are presented in Fig. 8.3. In all three of the non-Markovian reservoirs under consideration, the coupling strength g between the single-qubit and the reservoir has been kept the same. As expected, all QSD measures are zero for $t = 0$, as well as in the long time limit, as there is practically no excitation left in the open system.

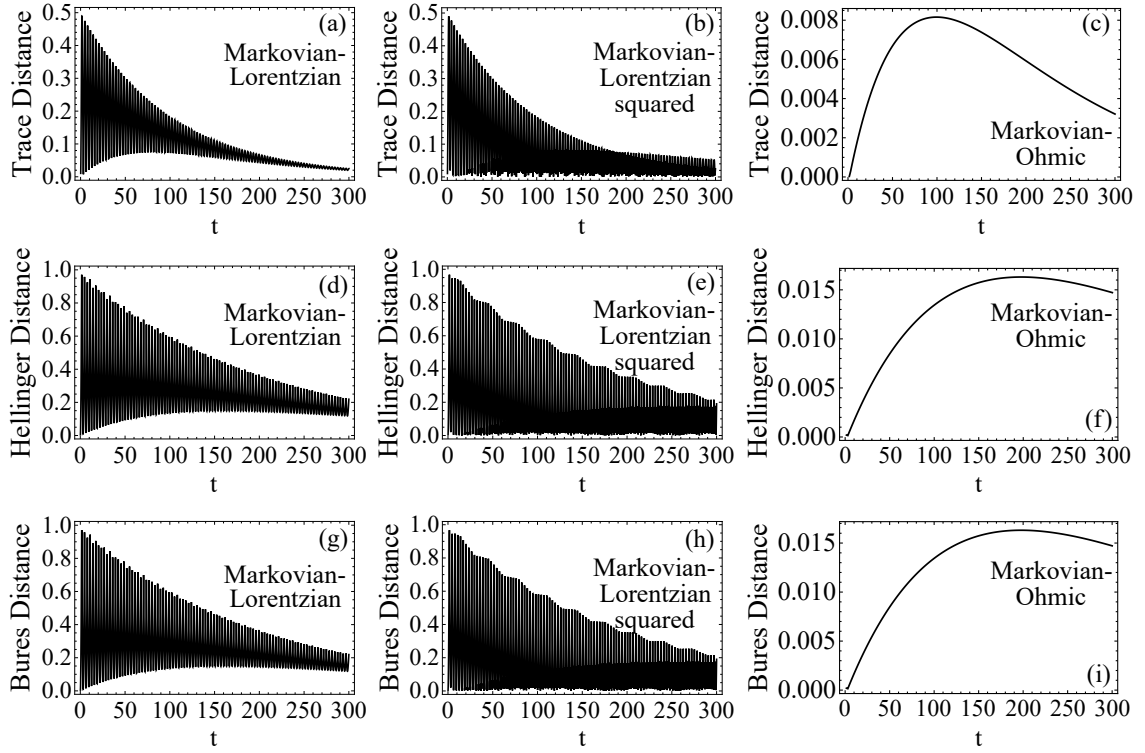


FIGURE 8.3: QSD measures between the Markovian-damped and the non-Markovian-damped system using various types of non-Markovian reservoirs in the single-qubit case. The types of reservoirs chosen and their parameters are: Markovian reservoir with $\gamma_M = 0.01$, Lorentzian reservoir with $g = 1$, $\gamma = 0.03$ and $\Delta_c = 0$, Lorentzian squared reservoir with $g = 1$, $\gamma = 0.3$ and $\Delta_c = 0$, Ohmic reservoir with $g = 1$, $S = 1.5$, $\omega_c = 8$ and qubit frequency $\omega_{eg} = 10$. (a) Markovian-Lorentzian Trace Distance, (b) Markovian-Lorentzian-squared Trace Distance, (c) Markovian-Ohmic Trace Distance, (d) Markovian-Lorentzian Hellinger Distance, (e) Markovian-Lorentzian-squared Hellinger Distance, (f) Markovian-Ohmic Hellinger Distance, (g) Markovian-Lorentzian Bures Distance, (h) Markovian-Lorentzian-squared Bures Distance, (i) Markovian-Ohmic Bures Distance.

We focus first on the comparison of the degrees of non-Markovianity, for different types of non-Markovian reservoirs, resulting from the same QSD measure. The trace distance between the Markovian and the Lorentzian damped system (Fig. 8.3(a)) exhibits rapid oscillations between two bounds, whose values change over time. The upper bound is initially at its maximum value and over time decreases to zero, whereas the lower bound initially increases, reaches a maximum, after which it decreases merging with the upper bound, tending eventually to zero for long times. The dynamics of the trace distance between the Markovian and the Lorentzian-squared damped system (Fig. 8.3(b)) also exhibit rapid oscillations, following a trend similar to the Markovian-Lorentzian case, with the exception that the lower bound can be zero within finite times, indicating that, at those instants, the Lorentzian-squared damped system resembles the Markovian-damped one. The oscillations in both Figs. 8.3(a) and 8.3(b) are indicative of the fast excitation exchange between the qubit and the non-Markovian reservoirs. In Fig. 8.3(c) we plot the trace distance between the Markovian-damped and the Ohmic-damped qubit state as a function of time. Clearly, the behaviour of the trace distance dynamics in this case differs

substantially from the dynamics of the Markovian-Lorentzian and the Markovian-Lorentzian-squared cases, in that it does not exhibit any oscillations, reaches a maximum after some finite time before decreasing, with the overall values of the trace distance remaining much smaller than the respective values in panels (a) and (b) of Fig. 8.3. We may therefore safely conclude that, under the prescribed conditions on parameters, the Ohmic-damped single qubit system displays the lowest character of NM.

In addition to the trace distance, we have calculated QSD's in terms of two other relevant measures, namely the Hellinger and Bures measures, with the results shown in Fig. 8.3. The overall behavior bears significant similarity to that of the trace distance, with some non-negligible quantitative differences. Note that all Markovian-Lorentzian and Markovian-Lorentzian-squared QSD measures tend to zero as we tune the Lorentzian and Lorentzian-squared parameters to the Markovian limit. In Fig. 8.3, the oscillations reflecting the exchange of excitation between qubit and reservoir are still present in both measures for the Markovian-Lorentzian and Markovian-Lorentzian-squared cases, whereas they are absent for the Markovian-Ohmic one. However both of these measures produce generally slower decrease of the QSD from the respective trace distance measure. For example, in terms of the trace distance, the value of the QSD between Lorentzian and Markovian in the vicinity of $t = 100$ hovers around 0.15, whereas the Hellinger and Bures measures indicate values around a mean of 0.4. Moreover, the oscillations of the QSD for the Markovian obtained from these two measures are damped much more slowly than the oscillations in the trace distance. The Ohmic case seems to follow the same trend, in that these two measures produce larger values for the QSD and a much slower evolution towards the expected value of 0. In summary, for all three non-Markovian reservoirs in the single qubit case, the trace distance is found to show faster decay of non-Markovianity than the Hellinger and Bures measures do. It is also worth noting that, despite the non-trivial formal difference of the expressions for the Hellinger and Bures QSD (Eqs. (8.7) and (8.11)), they lead to practically the same dynamics, indicating the same NM effect.

8.4.2 Five mutually interacting qubits

The merit of our approach rests with the possibility to obtain straightforwardly the Laplace transforms of the qubits tilde state amplitudes for an arbitrary number of qubits N , because N appears in our equations as a modifiable parameter. Having calibrated the measures of QSD in characterising non-Markovianity in the simplest set-up of a single qubit, in this section we explore the role of non-Markovianity in the more realistic situation of a chain involving qubit-qubit interaction. For a concrete quantitative analysis, we have chosen five qubits in an XX chain with nearest neighbor coupling \mathcal{J} . The calculation follows the approach presented in section 8.3, with the initial excitation in qubit 1 and the last qubit 5 coupled to the reservoir. The question now is how the non-Markovianity of the reservoir affects the exchange of excitation between the qubits, as manifested in the evolution of QSD between the Markovian and the various non-Markovian reservoirs.

In a set-up of this type, the crucial parameter is \mathcal{J} , as it controls the communication between qubits, which typically is the dominant aspect in applications. In order to remain within a realistic scenario, we have chosen the Markovian damping rate γ_M much smaller than \mathcal{J} , keeping the choice of the parameters of the non-Markovian reservoirs as in the previous section, so that the initial excitation of the first qubit decays on a time scale approximately the same for all reservoirs. At first,

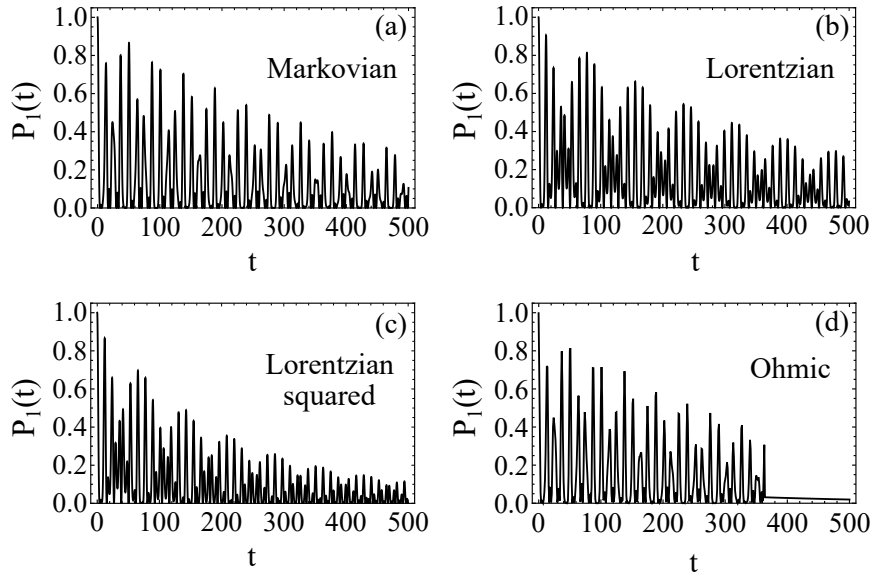


FIGURE 8.4: Dynamics of the excitation survival probability of the first qubit of a chain consisting of $N = 5$ qubits with qubit-qubit coupling $\mathcal{J} = 1$. The initial excitation is chosen to be on the first qubit while the last qubit of the chain is coupled to various types of reservoirs: (a) Markovian reservoir with $\gamma_M = 0.01$, (b) Lorentzian reservoir with $g = 1$, $\gamma = 0.03$ and $\Delta_c = 0$, (c) Lorentzian squared reservoir with $g = 1$, $\gamma = 0.3$ and $\Delta_c = 0$, (d) Ohmic reservoir with $g = 1$, $S = 1.5$, $\omega_c = 8$ and qubit frequency $\omega_{eg} = 10$.

we calculate the time evolution of the excitation probability of the first qubit for all of the reservoirs under consideration, with the results shown in Fig. 8.4. The glaring difference between the single-qubit dynamics in Fig. 8.2 and the $N = 5$ dynamics of the first qubit excitation in Fig. 8.4, is the appearance of oscillations in the dynamics of the latter, indicating the exchange of population between the qubits of the chain. In the cases of Lorentzian and Lorentzian squared reservoirs, such oscillations are superimposed on the oscillations between the last qubit and the reservoir, resulting to the characteristic oscillatory dynamics of $P_1(t)$ depicted in Figs. 8.4(b) and 8.4(c). For the Markovian case (Fig. 8.4(a)) the oscillations are due solely to the coupling between the qubits, because as we have seen in the case of the single qubit (Fig. 8.2(a)) the Markovian damping is monotonic. Again, for the Ohmic-damped case, the dynamics of the first qubit population (Fig. 8.4(d)) bears strong similarity to the Markovian-damped chain, with a rather unexpected exception, in that the oscillations are found to collapse abruptly after a finite time, a behaviour that has been also reported in previous works involving qubits coupled to Ohmic reservoirs [366, 438].

We consider now the dynamics of the QSD measures exploring the non-Markovianity of the three reservoirs in the context of a chain of $N = 5$ interacting qubits, with the results shown in Fig. 8.5. First we note that the time scales of decay for all QSD measures are longer than the respective time scales in the single-qubit case of Fig. 8.3. This behaviour was to be expected, since the excitation is now spread over the whole chain and naturally it takes more time to be lost in the reservoir. At the same time, the values of the QSD measures are in general larger than the respective values of Fig. 8.3, indicating that the NM of the open system is affected by the number of qubits in the chain. The Markovian-Lorentzian and Markovian-Lorentzian-squared

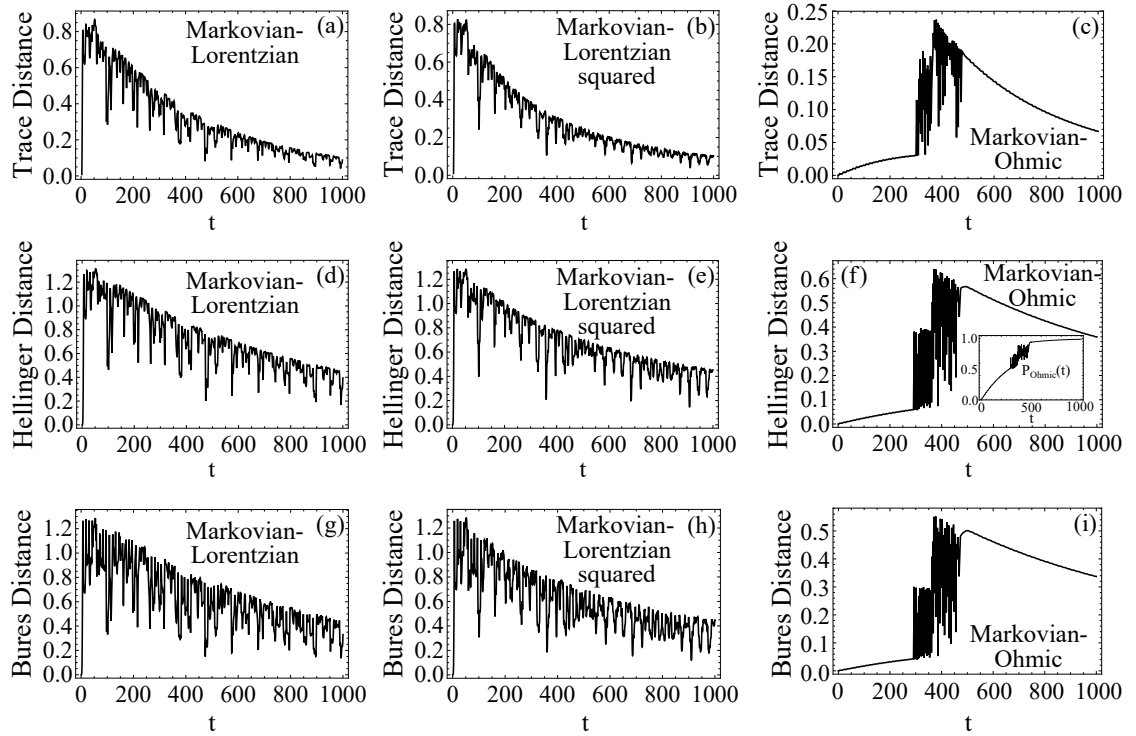


FIGURE 8.5: QSD measures between the Markovian-damped and the non-Markovian-damped system using various types of non-Markovian reservoirs for the case of $N = 5$ qubits with qubit-qubit coupling $\mathcal{J} = 1$. The types of reservoirs chosen and their parameters are: Markovian reservoir with $\gamma_M = 0.01$, Lorentzian reservoir with $g = 1$, $\gamma = 0.03$ and $\Delta_c = 0$, Lorentzian squared reservoir with $g = 1$, $\gamma = 0.3$ and $\Delta_c = 0$, Ohmic reservoir with $g = 1$, $S = 1.5$, $\omega_c = 8$ and qubit frequency $\omega_{eg} = 10$. (a) Markovian-Lorentzian Trace Distance, (b) Markovian-Lorentzian-squared Trace Distance, (c) Markovian-Ohmic Trace Distance, (d) Markovian-Lorentzian Hellinger Distance, (e) Markovian-Lorentzian-squared Hellinger Distance, (f) Markovian-Ohmic Hellinger Distance, (g) Markovian-Lorentzian Bures Distance, (h) Markovian-Lorentzian-squared Bures Distance, (i) Markovian-Ohmic Bures Distance. In the inset of panel (f) we show the dynamics of the probability of finding the excitation in the Ohmic environment for the case of $N = 5$ qubits. The time window where the probability dynamics abruptly become oscillatory coincides with the time window where the Markovian-Ohmic QSD measures follow the same behaviour.

QSD measures are seen to display an overall similar behaviour. This similarity requires some clarification, as it is a bit misleading. Recall that the values of the parameters for the Lorentzian and Lorentzian-squared spectral densities have been chosen according to the criterion explained in the discussion of Fig. 8.1. As a consequence, the comparison is not between a Lorentzian and its square. However, in detailed calculations we have found that an open system damped by a Lorentzian squared reservoir would display much larger NM character compared to the same system damped by a Lorentzian with the same parameters (g , γ and Δ_c). In fact, under those conditions, the excitation throughout the chain for the Lorentzian squared case remains constant for a time so long that it practically resembles a steady state for the timescales considered in our work. All QSD measures we examined (Trace distance, Hellinger distance and Bures distance) exhibit dynamics following the same trend, although the exact distance values may differ in general between different measures.

As clearly seen in Fig. 8.5, the Hellinger and Bures distances display minor differences in their dynamical behaviour for all of the reservoirs studied.

A rather interesting phenomenon appears in the dynamical behaviour of the QSD measures in the case of the Ohmic-damped chain. In contrast to the single-qubit case, the interplay between qubit-qubit and qubit- Ohmic reservoir interactions gives rise to an intricate behavior in the dynamics for all of the Markovian-Ohmic QSD measures considered. The dynamics are initially smooth for all QSD measures with the distance being zero at $t = 0$ and slowly increasing afterwards. However, there is a time when they suddenly change and exhibit rapid oscillations. These rapid oscillations appear only in a time window which is the same for all QSD measures considered. Beyond that time window, the dynamics are smoothed out with the distance slowly decaying back to zero. The time window of that sudden modification of the behaviour of the QSD measures coincides with the time window within which the total probability of finding the excitation in the Ohmic reservoir, exhibits similar behaviour (see inset of Fig. 8.5(f)). Changes in the dynamical behaviour of the system can be also observed through abrupt changes in the dynamics of the qubit excitations of the chain, as also reported in [366]. In summary, the qubit-qubit interaction is found to enhance the NM obtained in all QSD measures. Conversely, this may be interpreted as an enhancement of the excitation storage in the chain due to the non-Markovian character of the reservoir.

To sum up, the work in this chapter was undertaken with the purpose of evaluating the NM of some typical non-Markovian reservoirs, by means of the most common QSD measures, some of which required a slight modification owing to the character of the density operators involved. In order to offer an analysis connected with a realistic system typical in quantum information processing, we chose an XX chain of interacting qubits with a reservoir connected to one end of the chain. QSD measures require the density matrices of the systems under consideration. Since non-Markovian reservoirs do not in general lend themselves to descriptions in terms of a master equation, we employed an approach developed in chapter 7, based on the solution of the Schrödinger equation, in which the amplitudes of the excitation of the sites as a function of time are obtained by means of Laplace transform. With those amplitudes in hand we construct the density matrix of the system which is necessary for the calculation of the desired QSD measure.

As a measure of NM we have chosen the distance of the quantum state of our system as evolved under a given non-Markovian reservoir from the state evolved under a Markovian one. A meaningful comparison required the judicious choice of the parameters entering the expressions of the spectral densities of the reservoirs involved in each QSD calculation. Given the flexibility of our approach as to the number of qubits it can handle, we studied first the case of a single-qubit coupled to a reservoir, so as to have a frame for the evaluation of the interplay between qubit-qubit interaction and qubit-reservoir. The results from the single qubit analysis showed that the Hellinger and Bures measures indicated slightly higher character of NM for all three reservoirs than the trace distance measure did. On the other hand, all three measures have indicated significantly lower character of NM for the Ohmic reservoir, in comparison to the Lorentzian or Lorentzian squared. Moreover, the absence of any noticeable back-flow of excitation from the Ohmic reservoir to the qubit suggests that the Ohmic reservoir behaves practically in a Markovian fashion.

As noted in section 8.4, the Lorentzian and Lorentzian squared reservoirs, on the basis of all three measures, were found to exhibit essentially the same character of NM. This might seem counter intuitive, because inspection of the relevant formal expressions in the appendix suggests that the squared Lorentzian is more peaked

than the Lorentzian with the same parameters, which would imply a higher character of NM. However, the Lorentzian squared employed in all of our comparative calculations (Figs. 8.2-8.5) was not the square of the accompanying Lorentzian, owing to the adjustment of the parameters explained in section 8.4. If we calculate the evolution of the qubit excitation dynamics and evaluate the character of NM for a Lorentzian and a Lorentzian squared spectral density characterized by the same parameters (g , γ and Δ_c), we do indeed find more back-flow and higher NM character for the Lorentzian squared, which brings up an interesting issue in reservoir engineering. If in any open system subjected to dissipation through a Lorentzian reservoir, it were possible to modify the reservoir to the square of the Lorentzian, dissipation would slow down significantly. Our consideration of the Lorentzian squared spectral density is not a mere mathematical exercise. It was inspired by the observation of non-Lorentzian line shapes [436, 439], including the Lorentzian squared, albeit in different physical context.

The results for the case of five interacting qubits chain bear similarities to as well as differences from the single-qubit case. The similarity is seen in the NM by the three QSD measures which produce more or less similar values, with the value of the trace distance somewhat lower than the values of the Hellinger and Bures measures. In other words, the three measures provide mutually compatible results. However, the measures of the NM for all three reservoirs for the chain are noticeably higher than those for the single-qubit. Moreover, for the Ohmic reservoir, the QSD obtained by all three measures is not only quantitatively but even qualitatively different from that of the single qubit. The smooth dynamics obtained in the single qubit case, is in this case interrupted by a region of abrupt oscillations, within a certain time window in which the dynamics of the probability of finding the excitation in the Ohmic environment was found to exhibit the same behaviour. However, the stunning difference between the single and five qubit cases lies in the retention of population distributed among the interacting qubits and the much slower decay of the excitation for all of the reservoirs in the latter case, which is compatible with the consistently higher measures of NM reported in our work. It can then be argued that the exchange of excitation between the qubits slows down the dissipation which implies that the larger the number of the qubit the slower the loss into the reservoir. Perhaps the most significant message conveyed by the comparison of the single-qubit and chain of interacting qubits results is that the NM is not independent of the quantum system in the context of which it is evaluated.

In closing, we believe that the appropriate modifications of the QSD measures, that extend their use to non-trace-preserving processes and the detailed analysis of their applicability to a qubit chain system, have revealed subtle aspects of non-Markovianity. Extension of our approach and analysis to other open systems can be expected to offer new insights into the performance of protocols pertaining to quantum information technology tasks as well as to the statistical mechanics of spin chains. Even for the single chain coupled to non-Markovian reservoirs, issues such as the dynamics of entanglement, and the NM beyond single excitation represent potentially fruitful territory for exploration.

Chapter 9

Coalescence of non-Markovian dissipation, quantum Zeno effect, and non-Hermitian physics in a simple realistic quantum system

In chapter 7 we developed a theoretical framework in terms of the time-dependent Schrödinger equation, which provided analytical closed-form solutions of the Laplace transforms of the amplitudes of an XX qubit chain, enabling the study of various cases of environmental spectral densities. In this chapter we apply this formulation in a simple case consisting of two qubits, one of which is coupled to an external reservoir, but focus on different aspects of the system, namely, dynamical aspects associated with the presence of exceptional points and their connection to the quantum Zeno effect (QZE) [440].

As we described in section 5.5, diagonalization of the effective Hamiltonian describing an open quantum system is the usual method of tracking its exceptional points (EPs). Although, such a method is successful for tracking EPs in Markovian systems, it may be problematic in non-Markovian systems where a closed expression of the effective Hamiltonian describing the open system may not exist. In this chapter we provide an alternative method of tracking EPs in open quantum systems, using an experimentally measurable quantity, namely the effective decay rate of a qubit. Moreover we investigate the link between the peaked structure of the effective decay rate of the qubit that interacts indirectly with the environment, and the onset of the QZE, revealing the connections between the latter and the presence of exceptional points. Our treatment and results reveal an intricate interplay between non-Markovian dynamics, the QZE and non-Hermitian physics.

9.1 Introduction

As argued in chapter 7, the dissipative dynamics of open quantum systems coupled to non-Markovian reservoirs is a multifaceted field of fundamental, as well as practical importance [23, 24] that pertain to a broad class of problems, ranging from quantum information processing to non-equilibrium statistical mechanics. The effective Hamiltonian describing an open quantum system is by necessity non-Hermitian, which brings up its possible connection with non-Hermitian physics [293], exceptional points [310] and related questions, in that field of wide-ranging interest and activity. In both of those fields and from different angles, the QZE has been found to be a major participant. Having initially entered physics as a curiosity, it has been

found to play an uncanny role in the protection against dissipation [441, 442]. Although research in each one of the above three fields has been active for many years, the synergy of phenomena related to those fields does not seem to have been noticed, let alone explored. The work presented in chapter 7 on quantum dissipation in non-Markovian environments has steered us to a type of problem in which that synergy has been found to be astonishingly revelatory. The treatment of that problem and its consequences is the purpose of the present chapter. Before embarking on the discussion of formulation, computation and results, we need to provide a brief outline of the background and past activity in related works.

As far as the QZE is concerned, a number of studies have pointed out the potential role of the QZE in the protection of quantum information between correlated qubits [354, 443–445]. The results suggest that repeated projective measurements on a system of entangled qubits can lead to the preservation of entanglement, independently of the state in which the system is initially encoded. This effect appears when the state of the system evolves in a multidimensional sub-space, usually referred to as the Zeno subspace [281, 446]. Although fast repeated projective measurements directly on the system may freeze its evolution, this method may be somewhat restrictive for the implementation of quantum information processing tasks, where additional operations on the system may be necessary. An alternative approach relies on "indirect" measurements, where the apparatus does not act directly on the system, but detects a signal mediated by some field with which it interacts [447]. That work has, however, given rise to serious reservations as to the possibility of the occurrence of the QZE in such configurations [448–452]. On the other hand, as also discussed in section 5.3, it has been demonstrated that the QZE does not necessarily require projective measurements, as it may also be induced through continuous strong couplings [453–457].

In recent work [458], W. Wu and H.-Q. Lin have investigated the QZE in dissipative systems beyond the Markov, the rotating-wave and the perturbative approximations, in the context of a spin-boson model which describes the interaction between a spin system and a bosonic bath. Their study suggested that the non-Markovian character of the bath may be favorable for the accessibility of the QZE in such systems, as it may prolong the quantum Zeno time and lead to multiple Zeno-anti-Zeno crossover phenomena.

At the same time, the transitions to the quantum Zeno regime have been recently shown to be linked with the \mathcal{PT} symmetry breaking of the non-Hermitian Hamiltonian which describes the open quantum system [459–463]. As detailed in section 5.5, the boundary between the unbroken and broken \mathcal{PT} symmetry of a Hamiltonian describing an open quantum system [296, 297] is marked by the presence of exceptional points [298–301] where two or more eigenvalues coalesce, while their corresponding eigenvectors become parallel. It has also been demonstrated that the onset of the QZE is marked by a cascade of transitions in the system dynamics, as the strength of a continuous partial measurement on the open system is increased [464].

Tracking of EPs in open quantum systems is of crucial importance, since the system appears to exhibit enhanced sensitivity in their vicinity [286–288]. Although in open Markovian systems, tracking EPs through diagonalization of the corresponding effective Hamiltonian is a rather easy theoretical task, that method is rather problematic in non-Markovian systems, for which it may not even be possible to construct an effective Hamiltonian describing the open system. In that case, alternative methods capable of tracking EPs indirectly, without the need of finding the eigenvalues of the open system, should be sought, which served as a motivation for

this work. Based on a comparative analysis with the case of a Markovian reservoir, for which the system is diagonalizable, in what follows we argue that the effective decay rate may be used as a quantity of reference for tracking the onset of the QZE in an non-Markovian open quantum system, as well as its EPs.

9.2 Description of the system under consideration

Our system consists of two non-identical qubits and an environment characterized by a specific spectral density $J(\omega)$. The two qubits are interacting with a coupling strength \mathcal{J} while the environment is interacting with the second qubit with a coupling strength g . Without loss of generality, we assume that the coupling strengths \mathcal{J} and g are real numbers. A schematic representation of our system is depicted in Fig. 9.1.

The Hamiltonian of our system $\hat{\mathcal{H}} = \hat{\mathcal{H}}_S + \hat{\mathcal{H}}_E + \hat{\mathcal{H}}_I$ consists of three parts; namely, the Hamiltonian $\hat{\mathcal{H}}_S$ which describes our system of qubits and their mutual interaction, the Hamiltonian of the bosonic environment $\hat{\mathcal{H}}_E$ and the interaction Hamiltonian $\hat{\mathcal{H}}_I$ which describes the interaction between the second qubit and the environment. These three Hamiltonian terms are given by the expressions ($\hbar = 1$):

$$\hat{\mathcal{H}}_S = \omega_g |g\rangle_{11} \langle g| + \omega_e |e\rangle_{11} \langle e| + \omega'_g |g\rangle_{22} \langle g| + \omega'_e |e\rangle_{22} \langle e| + \mathcal{J} (\hat{\sigma}_1^+ \hat{\sigma}_2^- + \hat{\sigma}_1^- \hat{\sigma}_2^+), \quad (9.1a)$$

$$\hat{\mathcal{H}}_E = \sum_{\lambda} \omega_{\lambda} \hat{a}_{\lambda}^{E\dagger} \hat{a}_{\lambda}^E, \quad (9.1b)$$

$$\hat{\mathcal{H}}_I = \sum_{\lambda} g(\omega_{\lambda}) \left(\hat{a}_{\lambda}^E \hat{\sigma}_2^+ + \hat{a}_{\lambda}^{E\dagger} \hat{\sigma}_2^- \right), \quad (9.1c)$$

where ω_g and ω_e are the energies of the ground and excited state of first qubit, respectively, ω'_g and ω'_e are the energies of the ground and excited state of second qubit, respectively, ω_{λ} is the energy of the λ^{th} mode of the environment, $\hat{\sigma}_j^+ = |e\rangle_{jj} \langle g|$ and $\hat{\sigma}_j^- = |g\rangle_{jj} \langle e|$, $j = 1, 2$, are the qubit raising and lowering operators, respectively, while \hat{a}_{λ}^E and $\hat{a}_{\lambda}^{E\dagger}$ are the quantum annihilation and creation operators of the environment.

The wavefunction of the whole system in the single-excitation space can be expressed as

$$|\Psi(t)\rangle = c_1(t) |\psi_1\rangle + c_2(t) |\psi_2\rangle + \sum_{\lambda} c_{\lambda}^E(t) |\psi_{\lambda}^E\rangle, \quad (9.2)$$

where,

$$|\psi_1\rangle = |e\rangle_1 |g\rangle_2 |0\rangle_E, \quad (9.3a)$$

$$|\psi_2\rangle = |g\rangle_1 |e\rangle_2 |0\rangle_E, \quad (9.3b)$$

$$|\psi_{\lambda}^E\rangle = |g\rangle_1 |g\rangle_2 |00 \dots 01_{\lambda} 0 \dots 00\rangle_E. \quad (9.3c)$$

By adopting the following transformations for the qubit and environment amplitudes; namely, $c_1(t) = e^{-i(\omega'_g + \omega_e)t} \tilde{c}_1(t)$, $c_2(t) = e^{-i(\omega_g + \omega'_e)t} \tilde{c}_2(t)$ and $c_{\lambda}^E(t) =$

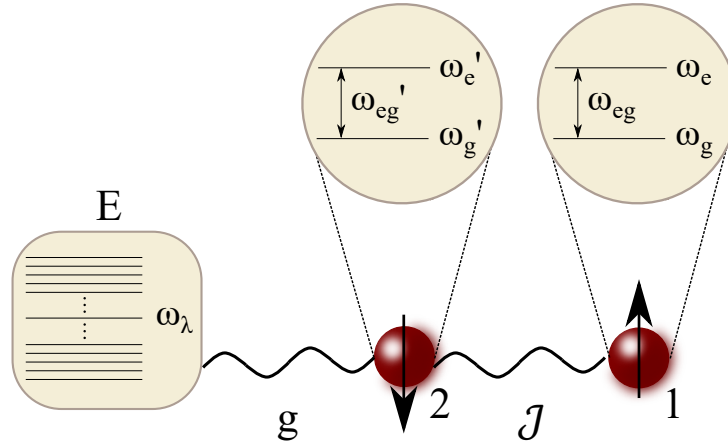


FIGURE 9.1: Schematic representation of the system at study. Two non-identical qubits are interacting with a coupling strength \mathcal{J} , while one of them is also coupled to an external environment E via a coupling g .

$e^{-i(\omega_g + \omega'_g + \omega_\lambda)t} \tilde{c}_\lambda^E(t)$, using the time-dependent Schrödinger equation (TDSE) leads to the following equations of motion of the tilde amplitudes:

$$\frac{d\tilde{c}_1(t)}{dt} = -i\mathcal{J}\tilde{c}_2(t)e^{-i\varepsilon t}, \quad (9.4a)$$

$$\frac{d\tilde{c}_2(t)}{dt} = -i\mathcal{J}\tilde{c}_1(t)e^{+i\varepsilon t} - i\sum_\lambda g(\omega_\lambda) e^{-i\Delta_\lambda t} \tilde{c}_\lambda^E(t), \quad (9.4b)$$

$$\frac{d\tilde{c}_\lambda^E(t)}{dt} = -ig(\omega_\lambda) e^{+i\Delta_\lambda t} \tilde{c}_2(t), \quad (9.4c)$$

where $\varepsilon \equiv (\omega'_e - \omega'_g) - (\omega_e - \omega_g) \equiv \omega'_{eg} - \omega_{eg}$ is the difference between the two qubit energies and $\Delta_\lambda \equiv \omega_\lambda - (\omega'_e - \omega'_g) \equiv \omega_\lambda - \omega'_{eg}$ is the detuning between the energy of the λ^{th} mode of the environment and the excitation energy of the second qubit.

By following the exact same procedure as the one described in chapter 7 (elimination of the continuum, substitution of the summation over k by integration, Laplace transform of resulting equations), we readily obtain

$$sF_1(s) = c_1(0) - i\mathcal{J}F_2(s + i\varepsilon), \quad (9.5a)$$

$$sF_2(s) = c_2(0) - i\mathcal{J}F_1(s - i\varepsilon) - B(s)F_2(s), \quad (9.5b)$$

where $F_1(s)$ and $F_2(s)$ are the Laplace transforms of the tilde amplitudes $\tilde{c}_1(t)$ and $\tilde{c}_2(t)$, respectively, while $B(s)$ is the Laplace transform of $R(t)$, defined again as:

$$R(t) \equiv \int_0^\infty J(\omega) e^{-i(\omega - \omega'_{eg})t} d\omega. \quad (9.6)$$

Note that we also used the fact that the tilde amplitudes are equal to the amplitudes at $t = 0$. Although the set of Eqs. (9.5) can be solved for arbitrary initial conditions, for the purposes of our study we focus on the expression of $F_1(s)$ for initial excitation

on the first qubit, i.e. $c_1(0) = 1$ and $c_2(0) = 0$. In that case, we can easily show that $F_1(s)$ is given by the following expression:

$$F_1(s) = \frac{1}{s + \frac{\mathcal{J}^2}{s + i\varepsilon + B(s + i\varepsilon)}}. \quad (9.7)$$

Before proceeding with the calculation of the inversion integral, to obtain the time dependence of $\tilde{c}_1(t)$, we need to specify the spectral density function of the environment, so that we can derive $R(t)$ according to Eq. (9.6) and hence the expression of its Laplace transform $B(s)$. Special cases of environments with Markovian, Lorentzian or Ohmic spectral densities are studied in what follows, revealing the regions of parameters that affect the onset of the quantum Zeno regime. As also noted before, the derivation of the functions $R(t)$ and $B(s)$ for various types of non-Markovian reservoirs is provided in Appendix B.

It is important to note that our formalism can be used to explore much more complex systems, involving arbitrary number of qubits and/or environments. A rather interesting result arises if we consider a system in which the qubit 1 of Fig. 9.1 does not interact directly with only one qubit (qubit 2) but with an arbitrary number of qubits N , each one of which is coupled to its own environment. Using our formulation we can show that, if all of the qubits are identical and the surrounding environments are characterized by the same spectral density, the Laplace transform of the tilde amplitude of the first qubit is given by:

$$F_1(s) = \frac{1}{s + \frac{N\mathcal{J}^2}{s + B(s)}}. \quad (9.8)$$

This equation is essentially the same with Eq. (9.7) for $\varepsilon = 0$ (identical qubits), with the exception of a factor of N multiplying \mathcal{J}^2 , where N is the number of qubits interacting with qubit 1. In other words, the system consisting of a qubit (qubit 1) interacting with N qubits that communicate with N respective environments with identical spectral densities can be effectively considered equivalent to a two-qubit + one environment system (Fig. 9.1) with a "collective coupling" $\sqrt{N}\mathcal{J}$ between the two qubits.

On the other hand, if all of the N qubits that interact with qubit 1 are communicating with a common environment, it is straightforward to show that $F_1(s)$ acquires the form:

$$F_1(s) = \frac{1}{s + \frac{N\mathcal{J}^2}{s + NB(s)}}, \quad (9.9)$$

where the factor of N now multiplies both \mathcal{J}^2 and $B(s)$.

9.3 Exceptional points and the onset of the quantum Zeno regime

9.3.1 Markovian environment

The coupling of a system to a reservoir, within the Born (weak coupling) approximation is Markovian, if in addition the spectral density of the reservoir, as a function of energy, is smooth and slowly varying, in the extended vicinity of the system transition energy. A formulation in terms of a Lindblad master equation, for the

time evolution of the reduced density operator of the system, leads to a set of linear differential equations. In those equations the diagonal matrix elements involve damping coefficients proportional to the square of the constant coupling the system to the reservoir. Whereas, the off-diagonal matrix elements, in the absence of other dephasing interactions, involve damping constants one half of that for the respective diagonal matrix element [26]. In fact, in an N -level ladder system, the damping of an off-diagonal matrix element connecting two decaying levels is one half of the sum of the respective diagonal damping constants. The spontaneous decay of an excited atomic state in open space and the loss of a cavity mode coupled to a bosonic reservoir are two well-known examples. In both cases, the reservoir is bosonic, representing the standard model for dissipation in a quantum system. The derivation and time evolution of the system reduced density operator are standard textbook material that can be found in any book on quantum optics [26] or quantum electrodynamics [465].

In this chapter, we are dealing with two interacting qubits, one of which is coupled to reservoirs of various spectral densities. It can be viewed as a basic component of a chain of qubits, in which case the end qubits are often referred to as boundaries. Our system is generic, in the sense that we do not assume any specific physical realization of the qubits. They could be quantum dots, two-level cold atoms, superconducting josephson, etc. The results and predictions of our analysis would therefore be applicable to a chain of any physical qubit realization. The nature of the coupling constants entering our formulation would then depend on the realization. The general structure of the equations would, however, be the same. The relative magnitude of the coupling constants employed in our analysis merits a comment, as it is of significance. Viewing the two-qubit system as a basic component of a chain of a vehicle for information transfer [366], the parameter \mathcal{J} is of controlling importance. It is for that reason that the magnitude of all other parameters is defined in relation to \mathcal{J} .

Although for a Markovian reservoir the dynamics are amenable to a description in terms of a master equation, for non-Markovian reservoirs such a formulation is not possible. Given our emphasis on non-Markovian cases, we have developed the formalism in terms of the amplitudes of the Schrödinger equation, described in the previous section. From the solutions for the amplitudes, if needed, the corresponding expressions for the density matrix elements are readily constructed.

Returning to the Markovian case, using well known results outlined above, all we need to do is add to the transition energy of the second qubit the imaginary part $-i\tilde{\gamma}/2$, where $\tilde{\gamma}$ is the decay rate of that qubit, due to the coupling to the Markovian reservoir. It bears repeating that $\tilde{\gamma}$ is proportional to the square of the coupling constant $g(\omega_\lambda)$, evaluated at the transition energy of the qubit, as dictated by the delta function in the identity $\lim_{\varepsilon \rightarrow 0^+} \frac{1}{x \pm i\varepsilon} = \mathbb{P} \frac{1}{x} \mp i\pi\delta(x)$ employed in the elimination of the degrees of freedom of the reservoir. There is nothing phenomenological about this procedure, in which well-known textbook rigorous results are invoked. Note that since $\varepsilon \equiv \omega'_{eg} - \omega_{eg}$, the decay term $-i\tilde{\gamma}/2$ in the transition energy of the second qubit is also transferred to ε . Making the substitution $\varepsilon \rightarrow \varepsilon - i\tilde{\gamma}/2$ in the expression of $F_1(s)$ for $B(s) = 0$ (the effects of the Markovian reservoir are taken into account through the substitution) in Eq. (9.7), we obtain

$$F_1(s) = \frac{s + (\tilde{\gamma}/2 + i\varepsilon)}{s^2 + (\tilde{\gamma}/2 + i\varepsilon)s + \mathcal{J}^2}. \quad (9.10)$$

The Laplace inversion of Eq. (9.10) provides the time evolution of the tilde amplitude of qubit 1. An insightful expression can be obtained in the case of identical

qubits ($\varepsilon = 0$), where the Laplace inversion yields:

$$\begin{aligned} \tilde{c}_1(t) = e^{-\tilde{\gamma}t/4} & \left[\cos \left(\frac{t}{4} \sqrt{(4\mathcal{J})^2 - \tilde{\gamma}^2} \right) \right. \\ & \left. + \frac{\tilde{\gamma}}{\sqrt{(4\mathcal{J})^2 - \tilde{\gamma}^2}} \sin \left(\frac{t}{4} \sqrt{(4\mathcal{J})^2 - \tilde{\gamma}^2} \right) \right], \quad \tilde{\gamma} \neq 4\mathcal{J} \end{aligned} \quad (9.11)$$

and $\tilde{c}_1(t) = e^{-\mathcal{J}t} (1 + \mathcal{J}t)$, for $\tilde{\gamma} = 4\mathcal{J}$. It is interesting to observe that for $\tilde{\gamma} \ll 4\mathcal{J}$, the tilde amplitude of the first qubit follows an oscillatory behaviour with frequency equal to $\frac{\sqrt{(4\mathcal{J})^2 - \tilde{\gamma}^2}}{4}$ along with an exponential decay. As $\tilde{\gamma}$ approaches the value $4\mathcal{J}$ the oscillations tend to disappear, and when $\tilde{\gamma} = 4\mathcal{J}$, the oscillatory part $\left[\cos \left(\frac{t}{4} \sqrt{(4\mathcal{J})^2 - \tilde{\gamma}^2} \right) + \frac{\tilde{\gamma}}{\sqrt{(4\mathcal{J})^2 - \tilde{\gamma}^2}} \sin \left(\frac{t}{4} \sqrt{(4\mathcal{J})^2 - \tilde{\gamma}^2} \right) \right]$ reduces to a form which is linear on time, i.e. $(1 + \mathcal{J}t)$. In the $\tilde{\gamma} \gg 4\mathcal{J}$ limit, using the identities $\cos(ix) = \cosh x$ and $\sin(ix) = i \sinh x$, it is straightforward to show that $\tilde{c}_1(t) \rightarrow 1$. Although this result may seem counter-intuitive at first glance, it can be interpreted in terms of the QZE, i.e. a strong coupling between the second qubit and the Markovian environment causes the second qubit to freeze in its ground state, preventing qubit 1 from transferring population to qubit 2 and hence to the environment. Therefore the population of the first qubit becomes protected against dissipation. Note that for this scheme to work, it is crucial not to have an initially populated second qubit, because in that case, the part of population of the second qubit would quickly dissipate due to the strong coupling between the latter and the environment.

Diagonalization of $\hat{\mathcal{H}}_S$ after the substitution $\omega'_e \rightarrow \omega'_e - i\tilde{\gamma}/2$ leads to the following four eigenvalues:

$$\lambda_1 = \omega_g + \omega'_g, \quad (9.12a)$$

$$\lambda_2 = \omega_e + \omega'_e - i\tilde{\gamma}/2, \quad (9.12b)$$

$$\lambda_3 = \frac{1}{2} \left(\omega_g + \omega'_g + \omega_e + \omega'_e - i\tilde{\gamma}/2 \right) - \frac{1}{4} \sqrt{(4\mathcal{J})^2 - (\tilde{\gamma} + 2i\varepsilon)^2}, \quad (9.12c)$$

$$\lambda_4 = \frac{1}{2} \left(\omega_g + \omega'_g + \omega_e + \omega'_e - i\tilde{\gamma}/2 \right) + \frac{1}{4} \sqrt{(4\mathcal{J})^2 - (\tilde{\gamma} + 2i\varepsilon)^2}. \quad (9.12d)$$

Note that since we focus on the single-excitation subspace we only need to consider the eigenvalues λ_3 and λ_4 . Equivalently, if we diagonalized $\hat{\mathcal{H}}_S$ in the single-excitation subspace, which would be essentially a 2×2 matrix, its eigenvalues are λ_3 and λ_4 .

In Fig. 9.2(a) we plot the imaginary part of the eigenvalues λ_3 and λ_4 as a function of $\tilde{\gamma}$ for various values of the energy difference between the two qubits ε . As shown, in the case of identical qubits ($\varepsilon = 0$), the imaginary parts of the two eigenvalues coalesce at $\tilde{\gamma} = 4\mathcal{J}$ and they split for $\tilde{\gamma} > 4\mathcal{J}$. The point $\tilde{\gamma} = 4\mathcal{J}$ is an exceptional point and marks the boundary between the unbroken and the broken \mathcal{PT} symmetry of the Hamiltonian. At the exceptional point, both the real and the

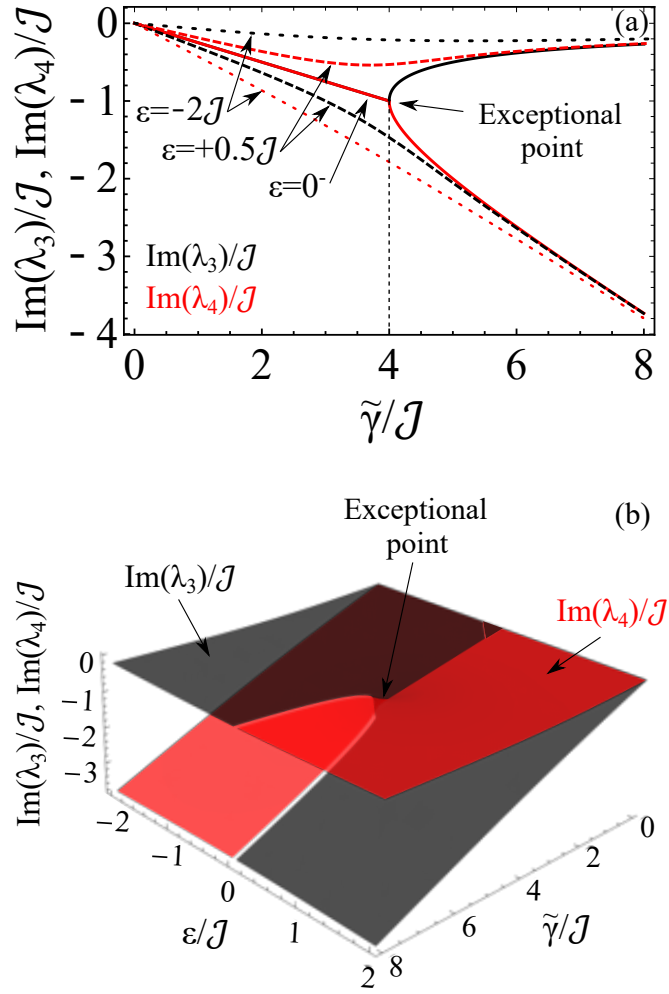


FIGURE 9.2: (a) Imaginary parts of the eigenvalues λ_3 (black) and λ_4 (red) as a function of $\tilde{\gamma}$ for various values of the energy difference between the two qubits ε . Solid line: $\varepsilon = 0$, dashed line: $\varepsilon = -2J$, dotted line: $\varepsilon = 0.5J$. The vertical dashed line indicates the position of the exceptional point for $\varepsilon = 0^-$, i.e. $\tilde{\gamma} = 4J$. (b) Imaginary parts of the eigenvalues λ_3 (black) and λ_4 (red) in the ε - γ plane.

imaginary parts of λ_3 and λ_4 coalesce, while the corresponding eigenvectors $|\phi_3\rangle$ and $|\phi_4\rangle$ given by the expressions below, become parallel.

$$|\phi_3\rangle = |g\rangle_1 |e\rangle_2 + \frac{1}{2J} \left[-(\varepsilon - i\tilde{\gamma}/2) - \frac{1}{2} \sqrt{(4J)^2 - (\tilde{\gamma} + 2i\varepsilon)^2} \right] |e\rangle_1 |g\rangle_2, \quad (9.13a)$$

$$|\phi_4\rangle = |g\rangle_1 |e\rangle_2 + \frac{1}{2J} \left[-(\varepsilon - i\tilde{\gamma}/2) + \frac{1}{2} \sqrt{(4J)^2 - (\tilde{\gamma} + 2i\varepsilon)^2} \right] |e\rangle_1 |g\rangle_2. \quad (9.13b)$$

For $\varepsilon \neq 0$, the imaginary parts of λ_3 and λ_4 are different for any value of $\tilde{\gamma} \neq 0$ and therefore no exceptional point exists in that case. It is interesting to note that there is an abrupt interchange between the values of $\text{Im}(\lambda_3)$ and $\text{Im}(\lambda_4)$ as ε approaches zero. This behaviour can be explained by visualizing these quantities in

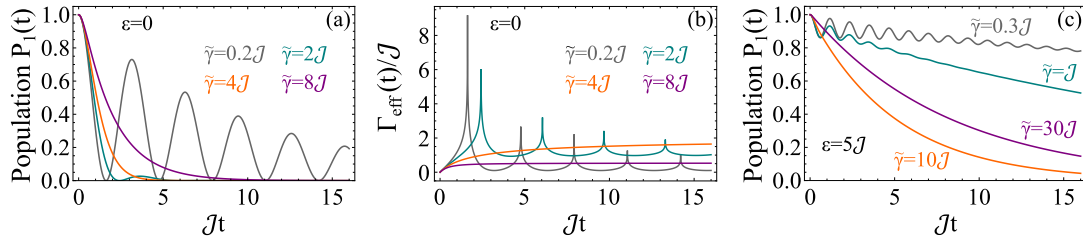


FIGURE 9.3: (a) Population of qubit 1 in the configuration of Fig. 9.1, as a function of the time for various values of $\tilde{\gamma}$ and $\varepsilon = 0$. Gray line¹: $\tilde{\gamma} = 0.2J$, teal line²: $\tilde{\gamma} = 2J$, orange line³: $\tilde{\gamma} = 4J$ and purple line⁴: $\tilde{\gamma} = 8J$. (b) Time dynamics of the effective decay Γ_{eff} using the same parameters with those of panel (a). (c) Population of qubit 1, as a function of the time for various values of $\tilde{\gamma}$ and $\varepsilon = 5J$. Gray line¹: $\tilde{\gamma} = 0.3J$, teal line²: $\tilde{\gamma} = J$, orange line³: $\tilde{\gamma} = 10J$ and purple line⁴: $\tilde{\gamma} = 30J$.

the $\varepsilon - \tilde{\gamma}$ plane, as shown in Fig. 9.2(b). This abrupt change is based on the complex eigenvalue topology of the involved intersecting Riemann sheets across the $\varepsilon = 0$ surface. The particular topology also suggests that the directionality of the motion in the $\varepsilon - \gamma$ space, when encircling the exceptional point, with starting points on different Riemann sheets, plays an important role on the final outcome.

In Fig. 9.3(a) we show the time population dynamics of the first qubit of the configuration depicted in Fig. 9.1. The population dynamics are studied for various values of $\tilde{\gamma}$ and $\varepsilon = 0$ (identical qubits). For small values of $\tilde{\gamma}$ such that $\tilde{\gamma} \ll 4J$ (gray line), the population exhibits damped oscillations indicative of the transfer of the excitation to the second qubit along with the environmental dissipation. As $\tilde{\gamma}$ is increased the oscillations become increasingly damped and less frequent (teal line), while at the critical coupling $\tilde{\gamma} = 4J$ where the exceptional point lies, the oscillations disappear and the population dynamics are given by the expression $P_1(t) = e^{-2Jt} (1 + Jt)^2$ (orange line). For increasing values of $\tilde{\gamma}$ the population retains its non-oscillatory behaviour and becomes increasingly protected against dissipation through the QZE (purple line). In the limit $\tilde{\gamma} \gg 4J$, as also our analytical study suggests, the population of the first qubit remains essentially frozen in its initial value. Strictly speaking complete freezing occurs in the limit of infinite $\tilde{\gamma}$, which is of only mathematical interest, as it is the range of finite but large values, in the sense of the above inequality, that are of realistic relevance.

The same conclusions can be deduced by studying the effective decay rate of the probability $P_1(t)$, an important and widely used tool in the context of QZE in open quantum systems, defined as:

$$\Gamma_{\text{eff}}(t) \equiv -\frac{1}{t} \ln[P_1(t)], \quad (9.14a)$$

which leads to

$$P_1(t) = e^{-\Gamma_{\text{eff}}(t)t}, \quad (9.14b)$$

indicating a decay rate with a time dependent exponent. In Fig. 9.3(b) we show the time dynamics of the effective decay rate $\Gamma_{\text{eff}}(t)$ using parameters identical to those of Fig. 9.3(a). Clearly, for $\tilde{\gamma} < 4J$, the effective decay rate exhibits peaks associated with the population oscillations between the two qubits, whose frequency depends upon $\tilde{\gamma}$. The time between subsequent peaks increases, as $\tilde{\gamma}$ is increased, while each subsequent peak is less pronounced compared to the preceding one. For $\tilde{\gamma} \geq 4J$, the effective decay rate does not exhibit any peak, and its value tends to decrease as

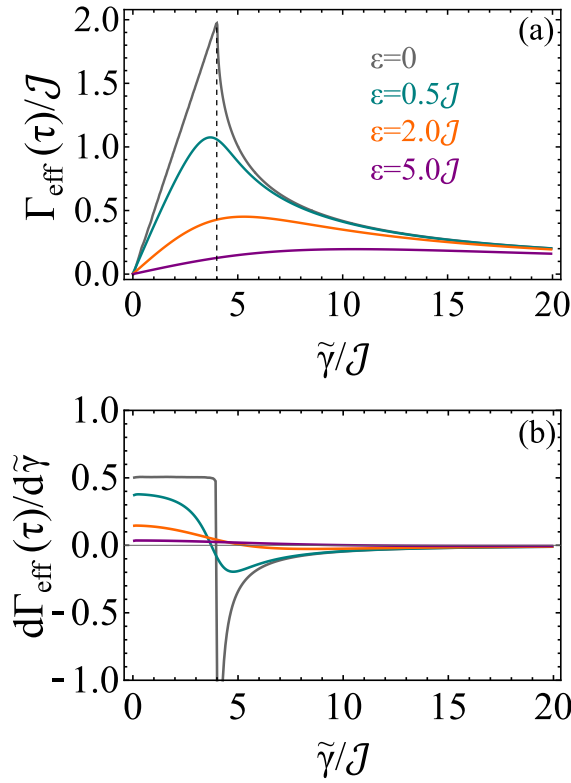


FIGURE 9.4: (a) Effective decay rate for times τ much larger than any other timescale of the system, as function of $\tilde{\gamma}$, for various qubit energy differences ε . The vertical dashed line at $\tilde{\gamma} = 4J$ indicates the position of the peak for $\varepsilon = 0$. Gray line¹: $\varepsilon = 0$, teal line²: $\varepsilon = 0.5J$, orange line³: $\varepsilon = 2.0J$ and purple line⁴: $\varepsilon = 5.0J$. (b) Derivative of the effective decay rate for times τ much larger than any other timescale of the system, with respect to $\tilde{\gamma}$, as a function of $\tilde{\gamma}$. The parameters are the same with those of panel (a).

$\tilde{\gamma}$ is increased.

However, the situation is quite different if the two qubits are non-identical, as is the case in Fig. 9.3(c) where $\varepsilon = 5J$. As also Fig. 9.3(c) suggests, we do not expect any qualitative transition on the system's response as $\tilde{\gamma}$ approaches and exceeds the value $\tilde{\gamma} = 4J$. In this case, what determines the dissipation behaviour is the ratio of ε to $\tilde{\gamma}$. In other words, as $\tilde{\gamma}$ is increased the dissipation of $P_1(t)$ is also increased. But if $\tilde{\gamma}$ becomes sufficiently larger than ε , the picture changes with the population of the first qubit becoming increasingly robust against dissipation. Again, even for $\varepsilon \neq 0$, in the limit where $\tilde{\gamma}$ is much larger than J and ε , the QZE "freezes" the dynamics of the second qubit, inducing thus a hindering of the decay of the first qubit population.

As is also evident from Fig. 9.3(b), in the long-time limit, the effective decay rate $\Gamma_{\text{eff}}(t)$ tends to stabilize to a finite non-zero value. The results of Fig. 9.3(c) become much clearer if we plot $\Gamma_{\text{eff}}(\tau)$ as a function of $\tilde{\gamma}$, where τ is defined to be a time much larger than any other timescale of the system. This quantity informs us about the onset of the QZE since it indicates the coupling $\tilde{\gamma}$ where the decay becomes maximum and decreases thereafter. As seen in Fig. 9.4(a), for $\varepsilon = 0$ and increasing $\tilde{\gamma}$, the decay is also increased until the point $\tilde{\gamma} = 4J$ where it becomes maximum. As $\tilde{\gamma}$ crosses the value $4J$ there is an abrupt change in the behaviour of the decay as also suggested by Fig. 9.4(b) where we show the derivative of the effective decay rate with respect to $\tilde{\gamma}$. In view of the analysis of Fig. 9.2, the sharp peak at $\tilde{\gamma} = 4J$

does therefore indicate the position of the exceptional point.

On the other hand, for finite ε , i.e. non-identical qubits, although the effective decay rate calculated at large times also exhibits a maximum, the curve around the maximum is smooth. In this case, according to Fig. 9.2, we should not expect any exceptional points at any coupling strength $\tilde{\gamma}$. For increasing ε , the decay rate as a function of $\tilde{\gamma}$ exhibits an increased width, which indicates that it takes a larger coupling window to cross the maximum and move from regions of increasing dissipation to the quantum Zeno regime, in compatibility with Fig. 9.3(c).

Our results suggest that the onset of the QZE is not -necessarily- associated with a presence of an exceptional point but with a peaked structure of the effective decay rate as a function of the coupling strength between the second qubit and the environment. The presence of an exceptional point on the other hand always indicates an abrupt phase transition from the anti-Zeno to the Zeno regime and is associated with a sharp peak of the effective decay rate as a function of $\tilde{\gamma}$. The link between these sharp peaks and the presence of EPs has also been pointed out in a recent paper by P. Kumar et al. [460]. The sharpness of the peak can be easily identified through discontinuities of the first derivative of the effective decay rate with respect to $\tilde{\gamma}$ as in Fig. 9.4(b). Therefore, if the quantity $\Gamma_{\text{eff}}(\tau)$ could be measured as a function of $\tilde{\gamma}$ for τ much larger than any other timescale of the system, it could be argued that by just studying its peak structure, the presence of an EP could be identified. As will get clear, this method appears to be very useful in cases of systems where explicit expressions of effective Hamiltonians do not exist and therefore no diagonalization is possible.

9.3.2 Lorentzian environment

In order to obtain the time dependence of the tilde amplitude $\tilde{c}_1(t)$ for a Lorentzian boundary environment, one needs to calculate the function $R(t)$ via Eq. (9.6) for a Lorentzian spectral density $J(\omega)$ and find its Laplace transform $B(s)$, necessary for the inversion of the Laplace transform $F_1(s)$. As shown in Appendix B, the function $B(s)$ for a Lorentzian spectral density distribution with positive peak frequency and negligible extension to negative frequencies is:

$$B(s) = \frac{g^2}{s + \frac{\gamma}{2} + i\Delta_c}, \quad (9.15)$$

where, g is the coupling strength constant between the second qubit and the environment, γ is the width of the distribution and $\Delta_c \equiv \omega_c - \omega'_{eg}$ is the detuning between the peak frequency ω_c of the distribution and the qubit frequency ω'_{eg} of the second qubit. Substitution of Eq. (9.15) back to Eq. (9.7) leads to an expression involving a third order polynomial with respect to s in the denominator. Although the Laplace inversion can be carried out analytically, the resulting expression of $\tilde{c}_1(t)$ is too lengthy to be insightful.

In contrast to the previous case of a Markovian spectral density, now it is not possible to develop an effective Hamiltonian characterizing the open quantum system by eliminating the reservoir degrees of freedom. This inability is associated with the non-Markovian character of the Lorentzian spectral density, which enables information exchange between the system and the environment within finite times. Therefore an attempt to find the eigenenergies of the open system as a probe of its exceptional points seems ineffectual. Based, however, on the results of the previous subsection, deduced from the study of the effective decay rate maxima, in comparison to what we know from the spectrum of the non-Hermitian Hamiltonian and

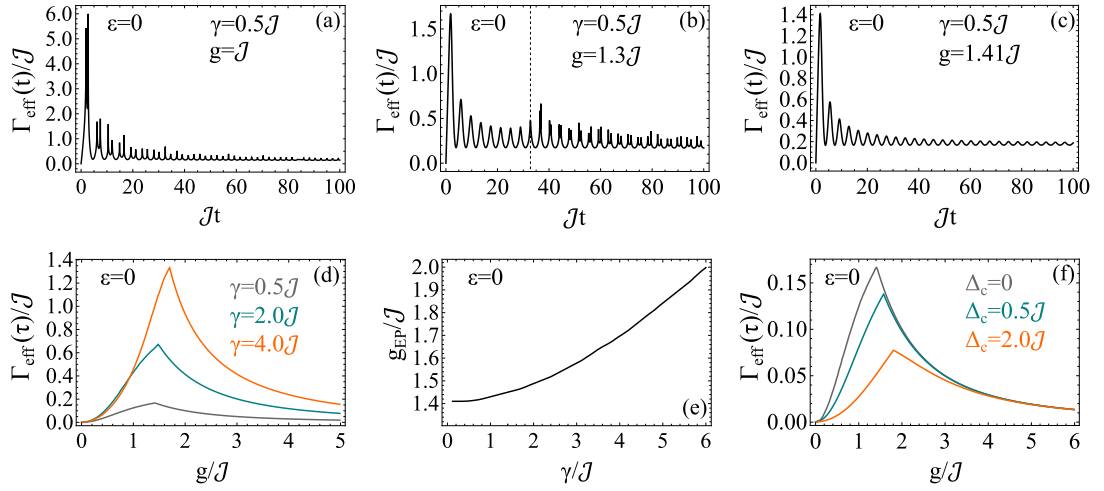


FIGURE 9.5: (a) Time dynamics of the effective decay rate for $\varepsilon = 0$ (identical qubits) and a Lorentzian boundary environment with parameters $\gamma = 0.5J$, $g = J$ and $\Delta_c = 0$. (b) Same as panel (a) but for $g = 1.3J$. The vertical dashed line indicates the time up to which the decay rate oscillations are smooth. (c) Same as panel (a) but for $g = 1.41J$. (d) Effective decay rate for times τ much larger than any other timescale of the system, as function of g , for various Lorentzian widths γ , $\varepsilon = 0$ and $\Delta_c = 0$. Gray line¹: $\gamma = 0.5J$, teal line²: $\gamma = 2J$ and orange line³: $\gamma = 4J$. (e) Location of the exceptional point g_{EP} as a function of γ for $\varepsilon = 0$ and $\Delta_c = 0$. (f) Effective decay rate for times τ much larger than any other timescale of the system, as function of g , for various values of the detuning Δ_c between the Lorentzian peak and the qubit frequency of the second qubit. The parameters used are: $\varepsilon = 0$ and $\gamma = 0.5J$. Gray line¹: $\Delta_c = 0$, teal line²: $\Delta_c = 0.5J$ and orange line³: $\Delta_c = 2.0J$.

its exceptional points, we can track the EPs of the system damped by a Lorentzian reservoir.

In Fig. 9.5(a) we plot the effective decay rate of the first qubit as a function of the time for $\varepsilon = 0$, $\gamma = 0.5J$, $\Delta_c = 0$ and $g = J$. Based on the form of the peaked structure of $\Gamma_{\text{eff}}(\tau)$ as a function of g for τ much larger than any other timescale of the system, we expect an exceptional point at $g = 1.41J$ (see Fig. 9.5(d), gray line). For g smaller than the position of the exceptional point, which we will denote by g_{EP} hereafter, the effective decay rate as a function of the time exhibits sharp peaks indicative of the transfer of populations between the two qubits. Note that, contrary to the Markovian reservoir case, part of the excitation can now be transferred from the open system to the environment and vice versa, within finite times. As g is increased towards the value g_{EP} , the sharp peaks begin to be gradually substituted by smooth oscillations (Fig. 9.5(b)) up to $g = g_{\text{EP}}$ at which point the $\Gamma_{\text{eff}}(t)$ dynamics exhibit only smooth oscillations, as in Fig. 9.5(c). Note that for $g \geq g_{\text{EP}}$, the system lies in the region where the QZE starts to inhibit the evolution of the second qubit. As a result, as g increases, the population of the second qubit becomes increasingly negligible and the smooth oscillations of the effective decay rate of the first qubit reflect oscillations directly between the latter and the environment.

In Fig. 9.5(d) we show how the effective decay rate at long times τ behaves as a function of g for various Lorentzian widths and $\varepsilon = 0$. As expected, on physical grounds, the decay rate is overall increased as γ increases. At the same time the sharp peak of the curve which indicates the position of the exceptional point, moves towards larger g . The dependence between the position of the exceptional point g_{EP}

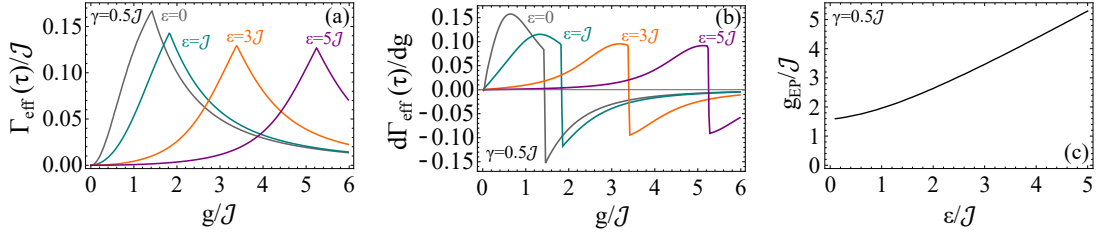


FIGURE 9.6: (a) Effective decay rate for times τ much larger than any other timescale of the system, as function of g , for various energy differences ε between the two qubits, $\gamma = 0.5J$ and $\Delta_c = 0$ (Lorentzian boundary reservoir). Gray line: $\varepsilon = 0$, teal line: $\varepsilon = J$, orange line: $\varepsilon = 3J$ and purple line: $\varepsilon = 5J$. (b) Derivative of the effective decay rate for times τ much larger than any other timescale of the system, with respect to g , as a function of g , for various ε . The values of the parameters are chosen the same as with panel (a). (c) Location of the exceptional point as a function of ε for $\gamma = 0.5J$ and $\Delta_c = 0$.

and the Lorentzian width γ , is depicted in Fig. 9.5(e). At the same time the maximum of the curve is also affected by the value of detuning between the Lorentzian peak and the qubit frequency of the second qubit (Fig. 9.5(f)). In view of the above results, we can confidently argue that the positions of the exceptional points in the case of a Lorentzian reservoir show great sensitivity to the values of the Lorentzian parameters γ and Δ_c .

For the results of Fig. 9.5 we have assumed that $\varepsilon = 0$, i.e. the two identical qubits. In Fig. 9.6 we examine the effects of a non-zero energy difference between the two qubits on the QZE onset for Lorentzian reservoirs. In Fig. 9.6(a) we plot the effective decay rate at long times τ as a function of the qubit-environment coupling strength g for various values of ε . As ε is increased, the position of the maximum of the curve tends towards larger coupling strengths, as was the case for a Markovian-damped open system (see Fig. 9.4). There are however two striking differences. First, in the Markovian case the value of ε affected significantly the width of the effective decay curve whereas for Lorentzian reservoirs, the increase of ε results roughly to a displacement of the curve towards larger g . Second and most important, in the Markovian case, for any value of ε , the effective decay rate exhibited a smooth maximum, except the case $\varepsilon = 0$ where the peak was sharp (see derivative in Fig. 9.4(b)), and was marked by the presence of an exceptional point. On the other hand, for a Lorentzian reservoir, the peak of the effective decay rate is sharp for any value of ε . This result can be verified upon inspection of the discontinuities of the effective decay rate derivative with respect to g as a function of g for various values of ε (Fig. 9.6(b)). Therefore, the maxima points of the effective decay rate mark the existence of exceptional points for any value of ε in the case of a Lorentzian reservoir. The dependence of the positions of such points as a function of ε is depicted in Fig. 9.6(c).

9.3.3 Ohmic environment

In this subsection, we examine the case of a reservoir characterized by an Ohmic spectral density [407]. In that case $J(\omega)$ is given by:

$$J(\omega) = \mathcal{N} g^2 \omega_c \left(\frac{\omega}{\omega_c} \right)^S \exp \left(-\frac{\omega}{\omega_c} \right), \quad (9.16)$$

where ω_c is the so-called Ohmic cut-off frequency and S the Ohmic parameter, characterizing whether the spectrum of the reservoir is sub-Ohmic ($S < 1$), Ohmic ($S = 1$) or super-Ohmic ($S > 1$). \mathcal{N} is a normalization constant given by the relation $\mathcal{N} = \frac{1}{(\omega_c)^2 \Gamma(1+S)}$, where $\Gamma(z)$ is the gamma function.

The corresponding function $B(s)$ which is the Laplace transform of the function $R(t)$, as shown in Appendix B, is found to be:

$$B(s) = -g^2 \frac{i^{1-S}}{\omega_c} e^{-iK(s)} [K(s)]^S \Gamma(-S, -iK(s)), \quad (9.17)$$

where $K(s) \equiv (s - i\omega_{eg}) / \omega_c$ and $\Gamma(a, z)$ is the incomplete gamma function. Substitution of Eq. (9.17) back to Eq. (9.7) leads to an expression of $F_1(s)$ whose inverse Laplace transform can be calculated numerically to yield the time dependence of $\tilde{c}_1(t)$.

In Fig. 9.7 we plot the effective decay rate of the first qubit at long times τ , as a function of the qubit-reservoir coupling strength g , for various combinations of the remaining parameters. In Fig. 9.7(a) we examine the effects of varying the Ohmic parameter S on the behaviour of the effective decay rate profile in the case of identical qubits ($\varepsilon = 0$). The effective decay rate is now found to exhibit a peak for any value of S . But it is not sharp, i.e. the first derivative of the effective decay rate with respect to g , as a function of g , does not exhibit a discontinuity at the position of the peak. Although this suggests that the QZE occurs for any value of S , it is not accompanied by the presence of an EP. The onset of the QZE (position of the maximum) decreases as the Ohmic parameter is increased. At the same time, the overall decay rate decreases as S is increased, which can be interpreted in terms of the form of the Ohmic spectral density distribution as a function of S . In particular, for fixed ω_c and increasing S , the distribution tends to flatten, causing more dominant modes of the distribution to be off-resonance from the qubit frequency, thus damping the system less efficiently. The difference between the effects of the Ohmic and Lorentzian distributions can be attributed to the fact that the flattening of the distribution and the position of its peak is controlled by different parameters in the two cases. For the Lorentzian, they are γ and Δ_c (for fixed ω_{eg}), respectively, whereas for an Ohmic distribution, both of them depend on the Ohmic parameters S and ω_c . Note that the Ohmic distribution exhibits a peak at the frequency $S\omega_c$.

In Fig. 9.7(b) we have kept the Ohmic parameter fixed to the value $S = 2$ and examined the behaviour of the effective decay rate, as a function of the cut-off frequency of the distribution. The results indicate that the onset of the QZE occurs for larger qubit-environment couplings g , as the cut-off frequency is increased. Again, the effective decay rate shows no evidence for the presence of EPs, for any combination of the Ohmic parameters. The values of the decay rate decrease, as ω_c is increased, owing to the flattening of the distribution for fixed S and increasing ω_c , along the lines of interpretation in the previous paragraph.

Finally, in Fig. 9.7(c) we examine the behaviour of the effective decay rate for various values of the energy difference between the two qubits. Interestingly, contrary to the case of identical qubits, when $\varepsilon \neq 0$, the effective decay rate is maximum at $g = 0$ and decreases as g is increased. This result indicates that the system lies in the QZE regime for any value of g .

To sum up, in this chapter we investigated a method of tracking EPs in non-Markovian open quantum systems, for which a closed form expression of an effective Hamiltonian describing the open system may not exist. In that case, the EPs

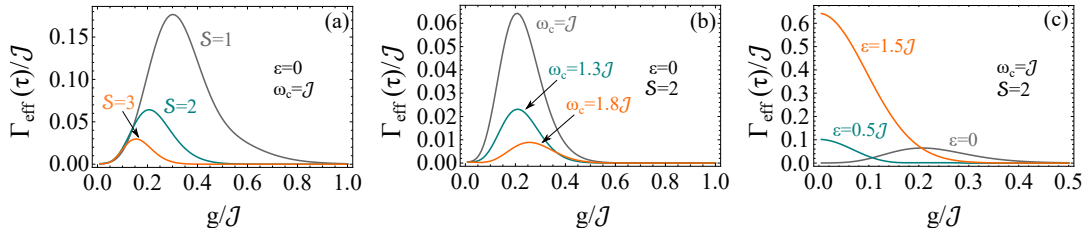


FIGURE 9.7: (a) Effective decay rate for times τ much larger than any other timescale of the system, as function of g , for various Ohmic parameters \mathcal{S} , $\omega_c = \mathcal{J}$, $\varepsilon = 0$ and $\omega_{eg} = 6\mathcal{J}$. Gray line: $\mathcal{S} = 1$, teal line: $\mathcal{S} = 2$, orange line: $\mathcal{S} = 3$. (b) Effective decay rate for times τ much larger than other timescale of the system, as function of g , for various cut-off frequencies ω_c , $\mathcal{S} = 2$, $\varepsilon = 0$ and $\omega_{eg} = 6\mathcal{J}$. Gray line: $\omega_c = \mathcal{J}$, teal line: $\omega_c = 1.3\mathcal{J}$, orange line: $\omega_c = 1.8\mathcal{J}$. (c) Effective decay rate for times τ much larger than other timescale of the system, as function of g , for various energy differences ε between the two qubits, $\mathcal{S} = 2$, $\omega_c = \mathcal{J}$ and $\omega_{eg} = 6\mathcal{J}$. Gray line: $\varepsilon = 0$, teal line: $\varepsilon = 0.5\mathcal{J}$, orange line: $\varepsilon = 1.5\mathcal{J}$.

of the system cannot be found by following the usual procedure of Hamiltonian diagonalization, as would have been the case for a quantum system damped by one or more Markovian reservoirs. Although our theory in this chapter deals with the simple case of two non-identical qubits, one of which interacts with a reservoir of arbitrary spectral density, our method is readily generalizable to any number of qubits and reservoirs.

The method is based upon studying the behaviour of the effective decay rate of the first qubit as a function of the coupling between the environment and the second qubit. We first studied the case of Markovian damping where the system is diagonalizable and we compared the effective decay rate analysis with the analysis in terms of the eigenvalues/eigenenergies of the open system. The results indicated that although a peak of the effective decay rate term is always associated with the onset of the QZE, if the peak is sharp (i.e. if the first derivative of the effective decay rate with respect to g , as a function of g exhibits a discontinuity), the system has an EP at the position of the peak.

We have further examined the cases of reservoirs characterized by Lorentzian, as well as Ohmic spectral densities. For Lorentzians, we have shown that the system will always have a single EP, for any combination of the parameters of the spectral density, i.e. its width and the detuning of its peak from the qubit frequency. The position of the EP (g_{EP}) has been found to shift towards higher values as γ increases for fixed Δ_c or as Δ_c increases for fixed γ . Interestingly, in contrast to the case of Markovian damping where the EP exists only for identical qubits ($\varepsilon = 0$), for a Lorentzian reservoir, an EP is always present irrespective of the value of ε . On the other hand, for reservoirs with an Ohmic spectral density, our results indicate that, although the system has a critical coupling marking the onset of the QZE (peak of the effective decay rate curve), this onset is not accompanied by the presence of an EP (i.e. the peak is not sharp), for any combination of the Ohmic parameters. The position of this onset was found to move towards smaller values of g , as the Ohmic parameter \mathcal{S} is increased or as the Ohmic cut-off frequency ω_c is decreased. For $\varepsilon \neq 0$ the effective decay rate is maximum at $g = 0$, decreasing monotonically as g is increased. Therefore, in the case of two non-identical qubits and an Ohmic environment, the system will lie within the QZE regime, for any value of g .

We believe that the significance of our results rests upon the synthesis of EPs in

the presence of non-Markovian dissipation. Although both aspects represent problems of extensive current research activity, their combined effect in the same quantum system has hardly been explored. Yet, the dynamics of open quantum systems associated with the presence of EPs or/and the regions of the onset of the QZE beyond Markovianity is of great significance in a plethora of realistic situations, many of practical interest. Our method can account for any form of the boundary environment's spectral density and can easily be generalized to open quantum systems consisting of qubits and environments interacting in more complex arrangements. The drastic differences in the effective decay rate of the first qubit as a function of g , between a boundary environment of Lorentzian spectral density from that of Ohmic, raises the profound question: What are the necessary conditions that an arbitrary spectral density should satisfy, in order to entail the existence of EPs for certain regions of parameters? Whether these conditions are related to symmetries of the spectral density profile or other features remains to be examined in future work, with possibly quite impactful implications. Be that as it may, the contrast between the effect of a Lorentzian and an Ohmic spectral density on the EPs in our system, illustrates the resistance of non-Markovian distribution to general classifications.

Chapter 10

The non-Hermitian landscape of autoionization

In this final chapter of the thesis we investigate the phenomenon of single-resonance autoionization viewed from the viewpoint of non-Hermitian physics. We report on the existence of exceptional points (EPs) and provide analytical expressions for their positions in parameter space, in terms of the Fano asymmetry parameter. We additionally propose a reliable method for the experimental determination of EPs, based solely on information about their ionization probability as a function of the system parameters. The links between EPs, the maxima of the asymmetric profile and the effective decay rate of the ground state are investigated in detail. Quantitative numerical examples pertaining to the doubly excited $2s2p(^1P)$ state of Helium confirm the validity of our formulation and results [466].

10.1 Brief introductory overview

Autoionization (AI) belongs to a broad class of quantum phenomena involving discrete states (resonances) embedded in continua into which they decay. Examples, among others, are the Breit-Wigner resonance in nuclear physics [467], in particle physics [468, 469], in photonics [470] and of course in atoms and molecules [471, 472], where the continuum is ionization or even dissociation; hence the term autoionization. The literature on autoionization spans a vast range of topics, including the time-dependent formation of the autoionization profile [473–477], strong driving of autoionizing resonances (ARs) [478–484], the dynamics of doubly-resonant autoionization [485, 486], and the effects of phase [487, 488] and statistical fluctuations [130, 489–491] of the laser field on the process.

ARs can be excited by radiation absorption or collisions and are infinite in number, with the spacing between them decreasing with increasing excitation energy. Yet, there are cases in which one or more resonances are separated in energy by significantly more than their width, qualifying as isolated resonances, with the doubly excited $2s2p(^1P)$ state of Helium being the prototype of an isolated AR, which continues revealing novel aspects, as attested by the ongoing streams of papers to this day [480–484]. It is in addition a perfect example of an open quantum system, with its dynamics governed by a non-Hermitian effective Hamiltonian. Surprisingly, the natural connection of AI to non-Hermitian physics, a field in the process of explosive activity, has escaped attention.

As we described in section 5.5, non-Hermitian physics and its connection to parity-time (\mathcal{PT}) symmetry, was introduced as an axiomatic theory in the seminal papers of C. Bender et al. [291–295]. Soon thereafter, it was pointed out that effective Hamiltonians describing the dynamics of open quantum systems, inevitably

are non-Hermitian [492]. Several approaches for understanding phenomena related to quasi-bound states embedded in continua using complex spectral analysis have been presented in the past, applied to various systems such as two-channel quantum wires [493, 494], semi-infinite superlattices with embedded impurities [495], discrete states coupled to continua containing Van Hove singularities at their threshold [496], as well as systems involving laser-induced population trapping via strong coupling of ARs in atoms [302].

10.2 Theoretical formulation

We begin by considering an atom whose ground state $|g\rangle$ is coupled to an isolated autoionizing resonance $|a\rangle$ through a linearly polarized field with frequency ω , as well as a continuum of states denoted by $|E\rangle$, both coupled to $|g\rangle$ and $|a\rangle$. The wavefunction of the system at times $t \geq 0$ is given by:

$$|\psi(t)\rangle = c_g(t) |g\rangle + c_a(t) |a\rangle + \int dE c_E(t) |E\rangle. \quad (10.1)$$

Introducing the transformations $\tilde{c}_g(t) = c_g(t)e^{i\omega_g t}$, $\tilde{c}_a(t) = c_a(t)e^{i(\omega_g + \omega)t}$ and $\tilde{c}_E(t) = c_E(t)e^{i(\omega_g + \omega)t}$ in the time-dependent Schrödinger equation, eliminating as usual the continuum adiabatically and adopting the rotating-wave approximation, as detailed in Appendix C, we show that the dynamics of the system under the above conditions, are described by the effective Hamiltonian ($\hbar = 1$):

$$\hat{\mathcal{H}}_{\text{eff}} \equiv \begin{bmatrix} S_g - i\frac{\gamma}{2} & \tilde{\Omega} \left(1 - \frac{i}{q}\right) \\ \tilde{\Omega} \left(1 - \frac{i}{q}\right) & -\Delta - i\frac{\Gamma}{2} \end{bmatrix}, \quad (10.2)$$

where S_g and γ are, respectively, the light-induced shift and the direct into the continuum ionization rate of the ground state, Γ is the autoionization rate of quasi-bound state $|a\rangle$, $\tilde{\Omega}$ the generalized Rabi frequency of the $|g\rangle \longleftrightarrow |a\rangle$ transition (see SM), and q the Fano asymmetry parameter [497], expressing the relative strength of the direct transition from $|g\rangle$ to the continuum compared to the transition to $|a\rangle$. $\Delta \equiv \omega - (\omega_a - F_a - \omega_g)$ is the detuning between the frequency of the driving field and the frequency of the $|g\rangle \longleftrightarrow |a\rangle$ transition, including the self-energy shift F_a of $|a\rangle$. Note that the asymmetry parameter is related to the parameters of $\hat{\mathcal{H}}_{\text{eff}}$ through the strict equation $q^2 = 4\tilde{\Omega}^2/(\gamma\Gamma)$ (See Appendix C). The light-induced shift of the ground state is hereafter neglected as it is of no relevance to our study. A schematic representation of our system is depicted in Fig. 10.1.

The effective Hamiltonian of Eq. (10.2) is obviously non-Hermitian, not only due to the presence of the diagonal decay terms in the energies of the ground state and $|a\rangle$, but also due to the presence of non-zero imaginary parts in the off-diagonal terms reflecting the driving of the $|g\rangle \longleftrightarrow |a\rangle$ transition. Diagonalization of $\hat{\mathcal{H}}_{\text{eff}}$ leads to the following set of eigenvalues:

$$\lambda_{1,2} = -\frac{1}{2} \left[\Delta + i\frac{(\gamma + \Gamma)}{2} \right] \pm \frac{1}{4} \sqrt{16 \left(1 - \frac{i}{q}\right)^2 \tilde{\Omega}^2 - (\gamma - \Gamma + 2i\Delta)^2}. \quad (10.3)$$

At first sight, owing to the presence of imaginary parts in the radicands, the spectra of $\hat{\mathcal{H}}_{\text{eff}}$ appear not to exhibit EPs. However, if the detuning is set to $\Delta = \Delta^s \equiv 2q\gamma\Gamma/(\Gamma - \gamma)$, $\gamma \neq \Gamma$ and we eliminate γ via the relation $\gamma = 4\tilde{\Omega}^2/(q^2\Gamma)$, we obtain:

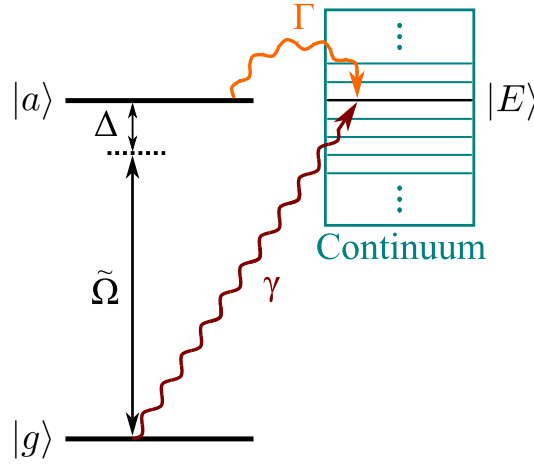


FIGURE 10.1: Schematic representation of the system at study. The ground state $|g\rangle$ of an atom that is ionized with a rate γ , is coupled to an AR $|a\rangle$ via a linearly polarized field that drives the $|g\rangle \leftrightarrow |a\rangle$ transition with a generalized Rabi frequency $\tilde{\Omega}$. The frequency of the driving field is detuned by Δ from the energy separation of the two states and the AR decays into the continuum with an autoionization rate Γ .

$$\lambda_{1,2} = \frac{4\tilde{\Omega}^2 q \Gamma}{4\tilde{\Omega}^2 - q^2 \Gamma^2} - i \left(\frac{\tilde{\Omega}^2}{q^2 \Gamma} + \Gamma/4 \right) \pm \frac{1}{4q|q|\Gamma} \sqrt{-\left(\frac{4\tilde{\Omega}^2 + q^2 \Gamma^2}{4\tilde{\Omega}^2 - q^2 \Gamma^2} \right)^2 [16\tilde{\Omega}^4 - 8\tilde{\Omega}^2 \Gamma^2 q^2 (1 + 2q^2) + q^4 \Gamma^4]}, \quad \tilde{\Omega} \neq \frac{|q|\Gamma}{2} \quad (10.4)$$

Observe now that choosing $\Delta = \Delta^s$ results to a set of eigenvalues with real radicands. Note that Eq. (10.4) holds for $\tilde{\Omega} \neq |q|\Gamma/2$ which is equivalent to $\gamma \neq \Gamma$. For $\tilde{\Omega} = |q|\Gamma/2$, i.e. $\gamma = \Gamma$, the radicand is complex for every value of Δ . The details of the physical significance of Δ^s for our system will become clear later. We should also note that the value of Δ^s resulting to real radicands depend on the intensity of the driving field, which in turn determines the value of $\tilde{\Omega}$. The relation between Δ^s and $\tilde{\Omega}$ is $\frac{\Delta^s(\tilde{\Omega})}{\Gamma} = \frac{8q\left(\frac{\tilde{\Omega}}{\Gamma}\right)^2}{q^2 - 4\left(\frac{\tilde{\Omega}}{\Gamma}\right)^2}$, $\tilde{\Omega} \neq |q|\Gamma/2$, which results upon substitution of $\gamma = 4\tilde{\Omega}^2/(q^2\Gamma)$ in the expression $\Delta^s \equiv 2q\gamma\Gamma/(\Gamma - \gamma)$, $\gamma \neq \Gamma$.

We are interested in the values of the coupling $\tilde{\Omega}$ that nullify the radicands of Eq. (10.4). The radicands become zero when

$$16\tilde{\Omega}^4 - 8\tilde{\Omega}^2 \Gamma^2 q^2 (1 + 2q^2) + q^4 \Gamma^4 = 0, \quad (10.5)$$

and the positive roots of the above equation are

$$\frac{\tilde{\Omega}_{\pm}}{\Gamma} = \frac{1}{2} \left(|q| \sqrt{1 + q^2} \pm q^2 \right). \quad (10.6)$$

It is easy to verify that for both $\tilde{\Omega} = \tilde{\Omega}_+$ and $\tilde{\Omega} = \tilde{\Omega}_-$, given that $\Delta = \Delta^s$, the eigenvectors of $\hat{\mathcal{H}}_{\text{eff}}$ coalesce, respectively, to the states $|\psi_+\rangle = (-i|g\rangle + |a\rangle)/\sqrt{2}$ and $|\psi_-\rangle = (i|g\rangle + |a\rangle)/\sqrt{2}$. Therefore the points $(\tilde{\Omega}_{\pm}, \Delta_{\pm}^s)$ in parameter space, where $\Delta_{\pm}^s \equiv \Delta^s(\tilde{\Omega}_{\pm})$, are EPs of $\hat{\mathcal{H}}_{\text{eff}}$.

10.3 Exceptional points in single-resonance autoionization

Interestingly, the EPs of the system measured in units of the autoionization width Γ , depend solely on the asymmetry parameter q , and there are two for any given value of the latter (Fig. 10.2). Note that the value of q for a given AR is fixed, as it depends solely upon the corresponding matrix elements of the transitions involved in the process. In particular, for the process involving the driving of the $1s^2(^1S) \longleftrightarrow 2s2p(^1P)$ transition in Helium and the associated autoionization of the $2s2p(^1P)$ AR, it is well established that $q \approx -2.79$ [490, 498].

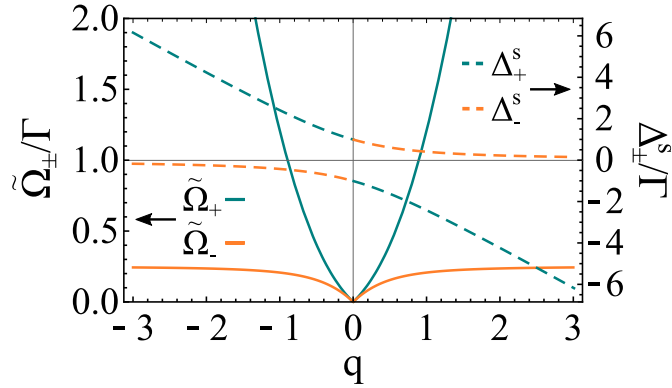


FIGURE 10.2: Dependence of the exceptional points $(\tilde{\Omega}_{\pm}, \tilde{\Delta}_{\pm}^s)$ on the asymmetry parameter q . Solid teal line: $\tilde{\Omega}_+$, dashed teal line: $\tilde{\Delta}_+^s$, solid orange line: $\tilde{\Omega}_-$ and dashed orange line: $\tilde{\Delta}_-^s$. For each value of q there exist two exceptional points.

Focusing hereafter on that isolated AR, we note that for $q = -2.79$, according to Eq. (10.6) and the relation between Δ^s and $\tilde{\Omega}$, the theory indicates the existence of two EPs at the positions $(\tilde{\Omega}_-, \Delta_-^s) = (0.2424\Gamma, -0.1738\Gamma)$ and $(\tilde{\Omega}_+, \Delta_+^s) = (8.0265\Gamma, 5.7538\Gamma)$ in parameter space. In Fig. 10.3 we plot the real and imaginary parts of the eigenvalues as a function of $\tilde{\Omega}$ and Δ for $q = -2.79$ and indeed confirm the coalescence of the eigenvalues at the above positions in parameter space.

As noted above, tuning Δ to Δ^s is essential in order to ensure that the radicands appearing in the expressions of the eigenvalues become real. We can get a glimpse on the physical significance of Δ^s in the vicinity of an EP, by solving the time-dependent Schrödinger equation using the effective Hamiltonian $\hat{\mathcal{H}}_{\text{eff}}$, and plotting the ionization probability of the atom $(P(t) = 1 - |c_g(t)|^2 - |c_a(t)|^2)$ as a function of the detuning for $\tilde{\Omega} = \tilde{\Omega}_-$ (Fig. 10.4). Note that the ionization probability is calculated on $t = T$, where T is the interaction time between the atom and the driving field. As expected, the ionization profile is asymmetric, transforming gradually to a "window" profile for sufficiently large interaction times, a phenomenon labelled "time saturation" in [478], reconfirmed most recently in [482]. Interestingly, the position of the maximum of the asymmetric profile, denoted by Δ_m , which is initially increasing as T increases, eventually stabilizes at Δ_-^s , as shown in the inset of Fig. 10.4. Therefore, for $\tilde{\Omega} = \tilde{\Omega}_-$, $\Delta^s(\tilde{\Omega}_-) \equiv \Delta_-^s$ is the detuning which maximizes the ionization probability (to unity) for sufficiently large interaction times, which for the field intensity considered, translates to $T \approx 20\Gamma^{-1}$ or larger. It is important to note that this occurs only by tuning the parameters of the system to the exceptional point $(\tilde{\Omega}_-, \Delta_-^s)$. For example, if we choose an intensity such that $\tilde{\Omega} = 0.1\tilde{\Omega}_-$, the position of the maximum of the asymmetric profile stabilizes to $\Delta_m \approx -0.195\Gamma$, whereas $\Delta^s(0.1\tilde{\Omega}_-) = -0.0016\Gamma$.

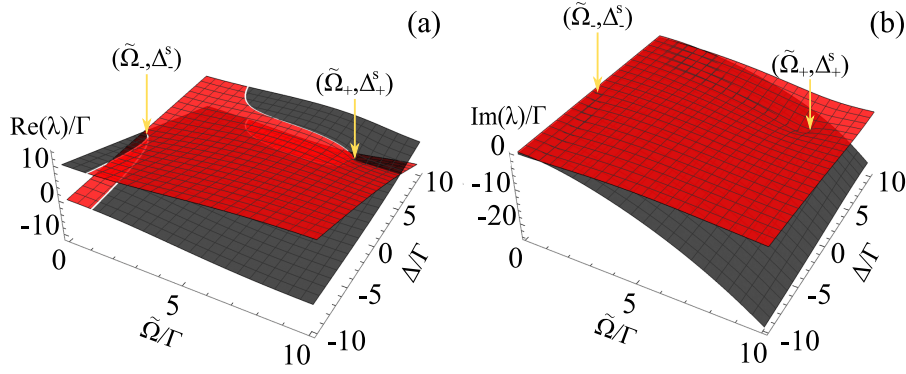


FIGURE 10.3: (a) Real and (b) imaginary parts of the eigenvalues λ_1 (red surface) and λ_2 (black surface) as a function of the parameters $\tilde{\Omega}$ and Δ , for $q = -2.79$. The yellow arrows mark the positions of the exceptional points at $(\tilde{\Omega}, \Delta) = (\tilde{\Omega}_-, \Delta_-^s) = (0.2424\Gamma, -0.1738\Gamma)$ and $(\tilde{\Omega}, \Delta) = (\tilde{\Omega}_+, \Delta_+^s) = (8.0265\Gamma, 5.7538\Gamma)$, where the real and imaginary parts of the eigenvalues coalesce.

Although in most cases, the EPs of a system can be explored theoretically through diagonalization of the relevant effective Hamiltonian, the experimental determination of EPs most often is quite a challenging task, since in general the eigenenergies of a Hamiltonian are not amenable experimentally. Therefore one needs to identify EPs indirectly by studying their footprints on system observables. To that end, we employ a quantity widely used in the context of the Quantum Zeno effect in open quantum systems, namely, the effective decay rate of a state [440], defined as $\Gamma_{\text{eff}}^j(t) \equiv -\frac{1}{t} \ln[P_j(t)]$, $j = g, a$, where $P_j(t) = |c_j(t)|^2$ is the population of state $|j\rangle$, $j = g, a$. The effective decay rate provides information about how the couplings between a given state and a set of other states or a continuum, modify the time evolution of that state's population. It turns out that the effective decay rate of the ground state, which can be readily determined experimentally, is remarkably sensitive to the EPs of our system, pinpointing their positions in parameter space.

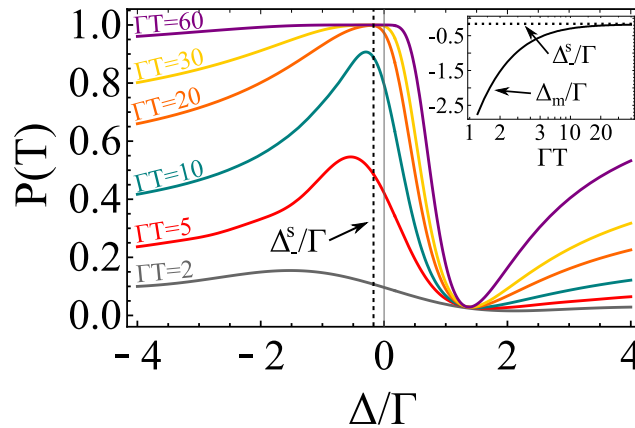


FIGURE 10.4: Ionization probability as a function of Δ for various interaction times T , $q = -2.79$ and $\tilde{\Omega} = \tilde{\Omega}_- = 0.2424\Gamma$. The vertical dashed line marks the position of the detuning $\Delta_-^s = -0.1738\Gamma$. Inset: Position of the peak of the asymmetric profile (Δ_m) as a function of the interaction time T (logarithmic scale) for $q = -2.79$ and $\tilde{\Omega} = \tilde{\Omega}_-$. The horizontal dotted line marks the position of the detuning Δ_-^s .

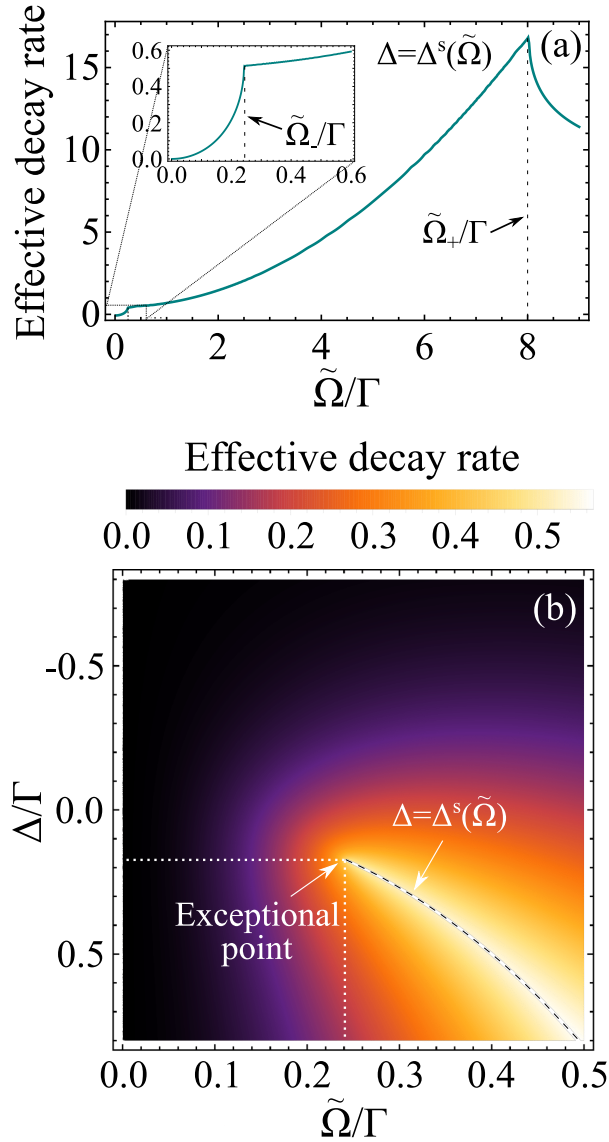


FIGURE 10.5: (a) Effective decay rate of the ground state as a function of $\tilde{\Omega}$ for $q = 2.79$ and $\Delta = \Delta^s$. The dashed lines mark the positions of the exceptional points at $\tilde{\Omega} = \tilde{\Omega}_- = 0.2424\Gamma$ and $\tilde{\Omega} = \tilde{\Omega}_+ = 8.0265\Gamma$. (b) Effective decay rate of the ground state as a function of $\tilde{\Omega}$ and Δ for $q = -2.79$. The curved dashed line marks the $\Delta = \Delta^s(\tilde{\Omega})$ curve, over which the effective decay rate is maximum. An exceptional point lies at the position $(\tilde{\Omega}, \Delta) = (\tilde{\Omega}_-, \Delta_-) = (0.2424\Gamma, -0.1738\Gamma)$.

In Fig. 10.5(a) we plot the effective decay rate of the ground state as a function of $\tilde{\Omega}$ for $\Delta = \Delta^s(\tilde{\Omega})$, which implies setting each time the detuning to a different value, depending on the value of $\tilde{\Omega}$ considered. Note that the effective decay rate is calculated at an interaction time $t = T$, which should be sufficiently large for the rate to be no longer modified with further increase of T . For $q = -2.79$, the effective decay rate is stabilized for $T \approx 20\Gamma^{-1}$ or larger, which is the same time scale as the one discussed in the results of Fig. 4. At such time scales it is easy to show that the population of $|a\rangle$ is practically negligible. Therefore the effective decay rate of the ground state is directly related to the measurable ionization probability $P(t)$, because $\Gamma_{\text{eff}}^g(t) \equiv -\frac{1}{t} \ln[P_g(t)] \cong \frac{1}{t} \ln[1 - P(t)]$. Clearly, the effective decay rate of the ground state provides direct evidence for the positions of the EPs of the system (Fig. 10.5(a)), in agreement with our theoretical predictions based on diagonalization of $\hat{\mathcal{H}}_{\text{eff}}$.

A short note regarding the experimental detection of the EPs related to the autoionization of the Helium $2s2p(^1P)$ AR, is in place at this point. The EP at $(\tilde{\Omega}, \Delta) = (\tilde{\Omega}_-, \Delta_-^s) = (0.2424\Gamma, -0.1738\Gamma)$ lies in a parameter region that is well within the current capabilities of synchrotron sources and seeded Free-electron lasers [499, 500] of short wavelength radiation, sufficient intensity and small bandwidth that can excite the AR. However, the EP at $(\tilde{\Omega}, \Delta) = (\tilde{\Omega}_+, \Delta_+^s) = (8.0265\Gamma, 5.7538\Gamma)$ would require a source of high intensity, as it lies in the strong field regime where $\tilde{\Omega} > \Gamma$ [478]. Although the required intensity, which is estimated to be around 1.3×10^{16} W/cm², is available with current Free-electron laser sources, issues such as intensity fluctuations [209, 501] known to affect the excitation of ARs [130, 489–491] and large bandwidth need to be addressed. Their interplay with EPs pose interesting followup studies.

Finally, in Fig. 10.5(b) we plot the effective decay rate of the ground state as a function of $\tilde{\Omega}$ and Δ at the vicinity of the EP that lies in the weak field regime. The effective decay rate maxima lie on the $\Delta = \Delta^s(\tilde{\Omega})$ line (curved dashed line) over which the eigenvalues have real radicands. At the tip of this maxima curve we find the weak field EP at the position $(\tilde{\Omega}, \Delta) = (\tilde{\Omega}_-, \Delta_-^s) = (0.2424\Gamma, -0.1738\Gamma)$ in parameter space.

In summary, we have unveiled the existence of EPs in single-resonance autoionization and provided analytical expressions for their positions in parameter space, in terms of the Fano asymmetry parameter. We have further demonstrated the connection between EPs and the maxima of the asymmetric ionization profile, through a numerical study of the $2s2p(^1P)$ resonance in Helium and proposed a reliable method for the observation of EPs, based solely on information about the ionization probability as a function of the parameters of the system, well within the capabilities of current radiation sources. Our results lead to further questions related to the role of pulse shape or field fluctuations in the observation of EPs in autoionization, as well as questions related to the influence of neighboring ARs, beyond the single-resonance autoionization. At the same time, the investigation of potentially impactful effects related to phase changes associated with the encircling of EPs in the parameter space of autoionization, based on the complex topology of the Riemann surfaces in the vicinity of the latter, is a further challenging issue. Overall, our results offer new insights into the interplay between autoionization and non-Hermitian \mathcal{PT} physics, opening up a novel and potentially fruitful territory for further exploration.

Appendix A

Photon statistics enhancement of e^-e^+ pair production

In this appendix we prove that in the zero intensity limit, the number of e^-e^+ pairs created by the standing wave field that results from the collision of two counter-propagating FEL beams with Gaussian amplitude fluctuations, is $2N_0!$ times larger than the respective number of pairs created by a field of the form $\mathcal{E}\cos(\omega t)$, i.e.

$$\lim_{I \rightarrow 0^+} \frac{\tilde{N}(I)}{N(I)} = 2N_0!, \quad (\text{A.1})$$

where

$$\tilde{N}(I) = 2 \int_0^\infty N(I') \frac{e^{-I'/I}}{I} dI'. \quad (\text{A.2})$$

The number of e^-e^+ created by the $\mathcal{E}\cos(\omega t)$ field in the $\gamma \ll 1$ and $\gamma \gg 1$ limits, corresponding to the tunneling and multi-photon regimes, respectively, are:

$$N(I) = 2^{-3/2} N_0^4 \left(\frac{I}{I_c} \right)^{5/4} \times \exp \left[-\pi \sqrt{\frac{I_c}{I}} \left(1 - \frac{1}{2N_0^2 \left(\frac{I}{I_c} \right)} \right) \right] \left(\frac{\omega\tau}{2\pi} \right), \quad \gamma \ll 1, \quad (\text{A.3a})$$

$$N(I) \approx 2\pi N_0^{3/2} \left(\frac{8}{N_0 e} \right)^{-2N_0} \left(\frac{I}{I_c} \right)^{N_0} \left(\frac{\omega\tau}{2\pi} \right), \quad \gamma \gg 1, \quad (\text{A.3b})$$

where I is the intensity, e is Euler's constant, $I_c = 4.65 \times 10^{29} \text{ W/cm}^2$ is the intensity corresponding to \mathcal{E}_c and $N_0 = \frac{2mc^2}{\hbar\omega}$ is the minimum number photons needed for vacuum pair creation to occur at a given frequency.

Since γ is inversely proportional to the square root of the intensity, and the integration in Eq. (A.2) extends over infinity, we divide the integral into two parts, corresponding to the multi-photon and the tunneling regimes, respectively. The intensity boundary between these two regimes (I_b) is set to be the intensity corresponding to $\gamma = 1$. Note that, even if practically such a sharp boundary between the two regimes does not exist, the exact value of this intensity boundary does not need to be well-defined for the purposes of our proof, since when taking the limit of the intensity to zero in Eq (A.1), the final result does not depend on its choice.

In view of the above, we write:

$$\begin{aligned} \lim_{I \rightarrow 0^+} \frac{\tilde{N}(I)}{N(I)} &= \lim_{I \rightarrow 0^+} \frac{2 \int_0^\infty N(I') \frac{e^{-I'/I}}{I} dI'}{N(I)} \\ &= 2 \left[\lim_{I \rightarrow 0^+} \frac{\int_0^{I_b} N(I') e^{-I'/I} dI'}{N(I) I} + \lim_{I \rightarrow 0^+} \frac{\int_{I_b}^\infty N(I') e^{-I'/I} dI'}{N(I) I} \right]. \end{aligned} \quad (\text{A.4})$$

The two terms in the right-hand side of Eq. (A.4) can now be calculated using Eqs. (A.3a) and (A.3b) for the number of created pairs in the tunneling and the multi-photon regime, respectively. Note that, in the limit of zero intensities, the number of created pairs appearing in the denominator of both terms in Eq. (A.4) is always given by Eq. (A.3b). By substituting the respective expressions for the number of created pairs of each regime back in Eq. (A.4), one can show that in the $I \rightarrow 0^+$ limit, the second term goes to zero. For the first term we have:

$$\begin{aligned} \lim_{I \rightarrow 0^+} \frac{\int_0^{I_b} N(I') e^{-I'/I} dI'}{N(I) I} &= \lim_{I \rightarrow 0^+} \frac{\int_0^{I_b} I'^{N_0} e^{-I'/I} dI'}{I^{N_0+1}} = \lim_{I \rightarrow 0^+} \left[-\Gamma \left(N_0 + 1, \frac{I'}{I} \right) \right]_{0^+}^{I_b} = \\ &= \lim_{I \rightarrow 0^+} \left\{ \lim_{I' \rightarrow 0^+} \Gamma \left(N_0 + 1, \frac{I'}{I} \right) - \Gamma \left(N_0 + 1, \frac{I_b}{I} \right) \right\}, \end{aligned} \quad (\text{A.5})$$

where $\Gamma(s, x)$ is the upper incomplete gamma function. The first term in the right-hand side of Eq. (A.5) is

$$\begin{aligned} \lim_{I \rightarrow 0^+} \lim_{I' \rightarrow 0^+} \Gamma \left(N_0 + 1, \frac{I'}{I} \right) &= \lim_{I \rightarrow 0^+} \Gamma(N_0 + 1, 0) \\ &= \lim_{I \rightarrow 0^+} \Gamma(N_0 + 1) = \lim_{I \rightarrow 0^+} N_0! = N_0!, \end{aligned} \quad (\text{A.6})$$

while for the second one we can show that it approaches zero by using the asymptotic expansion of the upper incomplete gamma function

$$\Gamma(s, z) \sim z^{s-1} e^{-z} \sum_{k=0}^{\infty} \frac{\Gamma(s)}{\Gamma(s-k)} z^{-k}, \quad (\text{A.7})$$

in the $I \rightarrow 0^+$ limit. Therefore Eq. (A.5) becomes

$$\lim_{I \rightarrow 0^+} \frac{\int_0^{I_a} N(I') e^{-I'/I} dI'}{N(I) I} = N_0!, \quad (\text{A.8})$$

which upon substitution back to Eq. (A.4) finally proves Eq. (A.1):

$$\lim_{I \rightarrow 0^+} \frac{\tilde{N}(I)}{N(I)} = 2N_0!$$

Appendix B

Derivation of the functions $R(t)$ and $B(s)$ for special types of non-Markovian reservoirs

In this appendix we provide the analytical derivation of the function

$$R(t) \equiv \int_0^\infty J(\omega) e^{-i(\omega - \omega_{eg})t} d\omega, \quad (\text{B.1})$$

and its Laplace transform $B(s)$ for various forms of non-Markovian spectral densities $J(\omega)$.

B.1 Lorentzian spectral density

For reservoirs characterized by Lorentzian spectral densities, $J(\omega)$ is given by:

$$J(\omega) = \frac{g^2}{\pi} \frac{\frac{\gamma}{2}}{(\omega - \omega_c)^2 + (\frac{\gamma}{2})^2}, \quad (\text{B.2})$$

where g is the qubit-reservoir coupling strength, while γ and ω_c is the width and the peak of the distribution, respectively. An approximation that considerably simplifies analytically the calculation of the function $R(t)$ is the extension of the lower limit of the integration over frequency from 0 to $-\infty$. Note that such extension is not in general valid for any spectral density; it is however well justified in the case of a Lorentzian with positive peak frequency and width such that the distribution has practically negligible extension to negative frequencies. The necessary condition for this approximation is $\gamma \ll \omega_c$. In this case the frequency integral can be calculated analytically, yielding:

$$R(t) = g^2 e^{-i\Delta_c t} e^{-\frac{\gamma}{2}t}, \quad (\text{B.3})$$

where $\Delta_c \equiv \omega_c - \omega_{eg}$. The Laplace transforms of $R(t)$ is then given by the expression:

$$B(s) = \frac{g^2}{s + \frac{\gamma}{2} + i\Delta_c}. \quad (\text{B.4})$$

B.2 Lorentzian squared spectral density

The Lorentzian squared spectral density is a special case of a broader set of spectral densities referred as powers of Lorentzian and are given by the form:

$$J(\omega) = g^2 \mathcal{N}_n \frac{\left(\frac{\gamma}{2}\right)^{2n-1}}{\left[(\omega - \omega_c)^2 + \left(\frac{\gamma}{2}\right)^2\right]^n}, \quad (\text{B.5})$$

where \mathcal{N}_n is an appropriate normalization factor that depends upon the non-zero integer n . For $n = 1$ we capture the case of the Lorentzian spectral density, while for $n = 2$ we capture the Lorentzian squared spectral density given by:

$$J(\omega) = \frac{2g^2}{\pi} \frac{\left(\frac{\gamma}{2}\right)^3}{\left[(\omega - \omega_c)^2 + \left(\frac{\gamma}{2}\right)^2\right]^2}, \quad (\text{B.6})$$

Following the same procedure as with the case of the Lorentzian, we find that the function $R(t)$ is given by:

$$R(t) = g^2 \left(1 + \frac{\gamma t}{2}\right) e^{-i\Delta_c t} e^{-\frac{\gamma}{2}t}. \quad (\text{B.7})$$

Notice that Eq. (B.7) is the same as Eq. (B.3) with an addition of a multiplication factor $\left(1 + \frac{\gamma t}{2}\right)$. The Laplace transform of Eq. (B.7) reads:

$$B(s) = g^2 \frac{(s + \gamma + i\Delta_c)}{(s + \frac{\gamma}{2} + i\Delta_c)^2}. \quad (\text{B.8})$$

B.3 Ohmic spectral density

The Ohmic spectral density is given by the expression:

$$J(\omega) = \mathcal{N} g^2 \omega_c \left(\frac{\omega}{\omega_c}\right)^{\mathcal{S}} \exp\left(-\frac{\omega}{\omega_c}\right), \quad (\text{B.9})$$

where \mathcal{S} is the Ohmic parameter, characterizing whether the spectrum of the reservoir is sub-Ohmic ($\mathcal{S} < 1$), Ohmic ($\mathcal{S} = 1$) or super-Ohmic ($\mathcal{S} > 1$), ω_c is the Ohmic cut-off frequency and \mathcal{N} is a normalization constant given by the relation $\mathcal{N} = \frac{1}{(\omega_c)^2 \Gamma(1+\mathcal{S})}$, where $\Gamma(z)$ is the gamma function. Substituting Eq. (B.9) back to the expression of $R(t)$ and calculation of the frequency integral yields:

$$R(t) = g^2 e^{i\omega_{eg}t} (i\omega_c t + 1)^{-1-\mathcal{S}}. \quad (\text{B.10})$$

The Laplace transform of $R(t)$ can then be calculated analytically, yielding:

$$B(s) = -g^2 \frac{i^{1-\mathcal{S}}}{\omega_c} e^{-iK(s)} [K(s)]^{\mathcal{S}} \Gamma(-\mathcal{S}, -iK(s)), \quad (\text{B.11})$$

where $K(s) \equiv (s - i\omega_{eg}) / \omega_c$ and $\Gamma(a, z)$ is the incomplete gamma function.

Appendix C

Derivation of the effective Hamiltonian $\hat{\mathcal{H}}_{\text{eff}}$

Our system consists of a ground state $|g\rangle$ coupled to an isolated quasi-bound resonance $|a\rangle$ through a linearly polarized field with frequency ω , as well as a continuum of states denoted by $|E\rangle$, coupled both to $|g\rangle$ and $|a\rangle$. The field that drives the $|g\rangle \longleftrightarrow |a\rangle$ and $|g\rangle \longleftrightarrow |E\rangle$ transitions is of the form $E(t) = \frac{1}{2} [\mathcal{E}e^{-i\omega t} + \mathcal{E}^*e^{i\omega t}]$.

The Hamiltonian of the system $\hat{\mathcal{H}} = \hat{\mathcal{H}}_0 + \hat{\mathcal{V}} + \hat{\mathcal{D}}$ consists of three parts; namely, the free-atom Hamiltonian $\hat{\mathcal{H}}_0$ with $\hat{\mathcal{H}}_0|j\rangle = \omega_j|j\rangle$, $j = g, a, E$, the configuration interaction $\hat{\mathcal{V}}$ that couples the discrete autoionizing resonance to the continuum, as well as the dipole interaction $\hat{\mathcal{D}}$ that couples both $|g\rangle$ and $|a\rangle$ to the continuum, given by the relation $\hat{\mathcal{D}} = \wp E(t)$, where $\wp = \vec{\wp} \cdot \hat{e}$ is the projection of the electric dipole moment operator on the polarization direction of the electric field amplitude, denoted by \hat{e} . Note that throughout our calculations we set $\hbar = 1$.

The wavefunction of the system at times $t \geq 0$ is given by:

$$|\psi(t)\rangle = c_g(t)|g\rangle + c_a(t)|a\rangle + \int dE c_E(t)|E\rangle \quad (\text{C.1})$$

The time-dependent Schrödinger equation (TDSE) in view of Eq. (C.1) reduce to the following set of equations:

$$i\partial_t c_g(t) = \omega_g c_g(t) + \mathcal{D}_{ga} c_a(t) + \int dE \mathcal{D}_{gE} c_E(t) \quad (\text{C.2a})$$

$$i\partial_t c_a(t) = \omega_a c_a(t) + \mathcal{D}_{ga}^* c_g(t) + \int dE \mathcal{V}_{aE} c_E(t) \quad (\text{C.2b})$$

$$i\partial_t c_E(t) = \omega_E c_E(t) + \mathcal{D}_{gE}^* c_g(t) + \mathcal{V}_{aE}^* c_a(t) \quad (\text{C.2c})$$

where we adopted the notation $\partial_t \equiv \frac{\partial}{\partial t}$. Introducing the slowly varying amplitudes according to the transformations $\tilde{c}_g(t) = c_g(t)e^{i\omega_g t}$, $\tilde{c}_a(t) = c_a(t)e^{i(\omega_g + \omega)t}$ and $\tilde{c}_E(t) = c_E(t)e^{i(\omega_g + \omega)t}$, the above set of equations become:

$$i\partial_t \tilde{c}_g(t) = \mathcal{D}_{ga} e^{-i\omega t} \tilde{c}_a(t) + \int dE \mathcal{D}_{gE} e^{-i\omega t} \tilde{c}_E(t) \quad (\text{C.3a})$$

$$i\partial_t \tilde{c}_a(t) = (\omega_a - \omega_g - \omega) \tilde{c}_a(t) + \mathcal{D}_{ga}^* e^{i\omega t} \tilde{c}_g(t) + \int dE \mathcal{V}_{aE} \tilde{c}_E(t) \quad (\text{C.3b})$$

$$i\partial_t \tilde{c}_E(t) = (\omega_E - \omega_g - \omega) \tilde{c}_E(t) + \mathcal{D}_{gE}^* e^{i\omega t} \tilde{c}_g(t) + \mathcal{V}_{aE}^* \tilde{c}_a(t) \quad (\text{C.3c})$$

We now eliminate the continuum adiabatically by setting $\partial_t \tilde{c}_E(t) = 0$, treating it as a sink. Under this assumption Eq. (C.3c) leads to:

$$\tilde{c}_E(t) = \frac{\mathcal{D}_{gE}^* e^{i\omega t}}{\omega_g + \omega - \omega_E} \tilde{c}_g(t) + \frac{\mathcal{V}_{aE}^*}{\omega_g + \omega - \omega_E} \tilde{c}_a(t) \quad (\text{C.4})$$

Substitution of Eq. (C.4) back to Eqs. (C.3a) and (C.3b), yields:

$$i\partial_t \tilde{c}_g(t) = \mathcal{D}_{ga} e^{-i\omega t} \tilde{c}_a(t) + \int dE \frac{|\mathcal{D}_{gE}|^2}{\omega_g + \omega - \omega_E} \tilde{c}_g(t) + \int dE \frac{\mathcal{V}_{aE}^* \mathcal{D}_{gE} e^{-i\omega t}}{\omega_g + \omega - \omega_E} \tilde{c}_a(t) \quad (\text{C.5a})$$

$$\begin{aligned} i\partial_t \tilde{c}_a(t) = & (\omega_a - \omega_g - \omega) \tilde{c}_a(t) + \int dE \frac{\mathcal{V}_{aE} \mathcal{D}_{gE}^* e^{i\omega t}}{\omega_g + \omega - \omega_E} \tilde{c}_g(t) + \\ & \mathcal{D}_{ga}^* e^{i\omega t} \tilde{c}_g(t) + \int dE \frac{|\mathcal{V}_{aE}|^2}{\omega_g + \omega - \omega_E} \tilde{c}_a(t) \end{aligned} \quad (\text{C.5b})$$

By substituting the matrix elements $\mathcal{D}_{ga} = \wp_{ga} E(t)$ and $\mathcal{D}_{gE} = \wp_{gE} E(t)$ of the dipole interaction operator in the above set of equations and adopting the rotating-wave approximation (RWA) which implies the neglect of the fast-oscillating anti-resonant time-dependent exponentials, we obtain:

$$i\partial_t \tilde{c}_g(t) = \int dE \frac{|\Omega_{gE}|^2}{\omega_g + \omega - \omega_E} \tilde{c}_g(t) + \left(\Omega_{ga} + \int dE \frac{\mathcal{V}_{aE}^* \Omega_{gE}}{\omega_g + \omega - \omega_E} \right) \tilde{c}_a(t) \quad (\text{C.6a})$$

$$i\partial_t \tilde{c}_a(t) = \left(\Omega_{ga}^* + \int dE \frac{\mathcal{V}_{aE} \Omega_{gE}^*}{\omega_g + \omega - \omega_E} \right) \tilde{c}_g(t) + \left[(\omega_a - \omega_g - \omega) + \int dE \frac{|\mathcal{V}_{aE}|^2}{\omega_g + \omega - \omega_E} \right] \tilde{c}_a(t) \quad (\text{C.6b})$$

where we have introduced the definitions $\Omega_{ga} \equiv \frac{1}{2} \wp_{ga} \mathcal{E}^*$ and $\Omega_{gE} \equiv \frac{1}{2} \wp_{gE} \mathcal{E}^*$. The above set of equations is simplified considerably by using the identity

$$\lim_{\eta \rightarrow 0^+} \frac{1}{\omega_g + \omega - \omega_E + i\eta} = \mathbb{P} \frac{1}{\omega_g + \omega - \omega_E} - i\pi \delta(\omega_g + \omega - \omega_E) \quad (\text{C.7})$$

where \mathbb{P} denotes the principal value part and $\delta(x)$ is the Dirac delta function. In view of Eq. (C.7), Eqs. (C.6) can ultimately be written as:

$$i\partial_t \tilde{c}_g(t) = \left(S_g - i\frac{\gamma}{2} \right) \tilde{c}_g(t) + \tilde{\Omega}_{ga} \left(1 - \frac{i}{q} \right) \tilde{c}_a(t) \quad (\text{C.8a})$$

$$i\partial_t \tilde{c}_a(t) = \tilde{\Omega}_{ag} \left(1 - \frac{i}{q} \right) \tilde{c}_g(t) - \left(\Delta + i\frac{\Gamma}{2} \right) \tilde{c}_a(t) \quad (\text{C.8b})$$

where $S_g \equiv \mathbb{P} \int dE \frac{|\Omega_{gE}|^2}{\omega_g + \omega - \omega_E}$ and $\gamma \equiv 2\pi |\Omega_{gE}|^2 \Big|_{\omega_E = \omega_g + \omega}$ are, respectively, the light-induced shift and the ionization rate of the ground state, whereas $F_a \equiv \mathbb{P} \int dE \frac{|\mathcal{V}_{aE}|^2}{\omega_g + \omega - \omega_E}$ and $\Gamma \equiv 2\pi |\mathcal{V}_{aE}|^2 \Big|_{\omega_E = \omega_g + \omega}$ are, respectively, the self-energy shift and the autoionization rate of the state $|a\rangle$. Moreover, $\tilde{\Omega}_{ga} \equiv \Omega_{ga} + \mathbb{P} \int dE \frac{\mathcal{V}_{aE}^* \Omega_{gE}}{\omega_g + \omega - \omega_E}$ is the generalized

Rabi frequency of the $|g\rangle \longleftrightarrow |a\rangle$ transition, $q \equiv \frac{\tilde{\Omega}_{ga}}{\pi\Omega_{gE}\mathcal{V}_{aE}^*}$ is the Fano asymmetry parameter and $\Delta \equiv \omega - (\omega_a - F_a - \omega_g)$ is the detuning between the frequency of the driving field and the frequency of the $|g\rangle \longleftrightarrow |a\rangle$ transition, including the self-energy shift of state $|a\rangle$.

The set of Eqs. (C.8) can be written as:

$$i\partial_t \begin{bmatrix} \tilde{c}_g(t) \\ \tilde{c}_a(t) \end{bmatrix} = \hat{\mathcal{H}}_{\text{eff}} \begin{bmatrix} \tilde{c}_g(t) \\ \tilde{c}_a(t) \end{bmatrix} \quad (\text{C.9})$$

with

$$\hat{\mathcal{H}}_{\text{eff}} \equiv \begin{bmatrix} S_g - i\frac{\gamma}{2} & \tilde{\Omega} \left(1 - \frac{i}{q}\right) \\ \tilde{\Omega} \left(1 - \frac{i}{q}\right) & -\Delta - i\frac{\Gamma}{2} \end{bmatrix} \quad (\text{C.10})$$

where in order to simplify notation we have introduced the definition $\tilde{\Omega} \equiv \tilde{\Omega}_{ga}$. $\hat{\mathcal{H}}_{\text{eff}}$ is the effective Hamiltonian governing the dynamics of our system under the adiabatic elimination of the continuum and RWA approximations. Combining the definitions of γ , Γ and $\tilde{\Omega}$ given above, we obtain $q^2 = 4\tilde{\Omega}^2/(\gamma\Gamma)$ which is independent of intensity and provides a very useful relation between the parameters of the effective Hamiltonian.

List of publications

PhD publications

1. **G. Mouloudakis** and P. Lambropoulos, Phys. Rev. A **102**, 023713 (2020) ([191])
2. **G. Mouloudakis** and P. Lambropoulos, Physics Letters B **811**, 135987 (2020) ([223])
3. **G. Mouloudakis** and P. Lambropoulos, Photonics **8**, 72 (2021) ([183])
Chosen for journal cover of Photonics **8** (3): <https://www.mdpi.com/2304-6732/8/3>
4. **G. Mouloudakis** and P. Lambropoulos, Quantum Information Processing **20**, 1-15 (2021) ([317])
5. **G. Mouloudakis**, T. Ilias, and P. Lambropoulos, Phys. Rev. A **105**, 012429 (2022) ([366])
6. **G. Mouloudakis** and P. Lambropoulos, Phys. Rev. A **106**, 053709 (2022) ([440])
7. **G. Mouloudakis**, I. Stergou, and P. Lambropoulos, Physica Scripta **98**, 085111 (2023) ([430])
8. **G. Mouloudakis** and P. Lambropoulos, Phys. Rev. A **108**, 063104 (2023) ([466])

Other publications

9. **G. Mouloudakis** and P. Lambropoulos, J. Phys. B: At. Mol. Opt. Phys. **51**, 1 01LT01 (2017) ([489])
10. **G. Mouloudakis** and P. Lambropoulos, Eur. Phys. J. D **72**, 226 (2018) ([490])
11. **G. Mouloudakis** and P. Lambropoulos, Phys. Rev. A **97**, 0543413 (2018) ([176])
12. **G. Mouloudakis** and P. Lambropoulos, Phys. Rev. A **99**, 063419 (2019) ([177])
13. K. Mouloudakis, F. Vouzinas, A. Margaritakis, A. Koutsimpela, **G. Mouloudakis**, V. Koutrouli, M. Skotiniotis, G. P. Tsironis, M. Loulakis, M. W. Mitchell, G. Vasilakis, and I. K. Kominis, Phys. Rev. A **108**, 052822 (2023) ([502])

Bibliography

- [1] M. O. Scully and M. S. Zubairy, *Quantum optics*, 1999.
- [2] A. Steane, “Quantum computing”, *Reports on Progress in Physics* **61**, 117 (1998).
- [3] N. Gisin, G. Ribordy, W. Tittel, and H. Zbinden, “Quantum cryptography”, *Reviews of modern physics* **74**, 145 (2002).
- [4] B. Wolter, M. G. Pullen, M. Baudisch, M. Sclafani, M. Hemmer, A. Senftleben, C. D. Schröter, J. Ullrich, R. Moshhammer, and J. Biegert, “Strong-field physics with mid-ir fields”, *Physical Review X* **5**, 021034 (2015).
- [5] A. Georges and P. Lambropoulos, “Saturation and stark splitting of an atomic transition in a stochastic field”, *Physical Review A* **20**, 991 (1979).
- [6] A. Georges, P. Lambropoulos, and P. Zoller, “Saturation and stark splitting of resonant transitions in strong chaotic fields of arbitrary bandwidth”, *Physical Review Letters* **42**, 1609 (1979).
- [7] R. J. Glauber, “Coherent and incoherent states of the radiation field”, *Physical Review* **131**, 2766 (1963).
- [8] R. J. Glauber, “The quantum theory of optical coherence”, *Physical Review* **130**, 2529 (1963).
- [9] P. G. O’Shea and H. P. Freund, “Free-electron lasers: status and applications”, *Science* **292**, 1853–1858 (2001).
- [10] K. Vogel, V. Akulin, and W. P. Schleich, “Quantum state engineering of the radiation field”, *Physical review letters* **71**, 1816 (1993).
- [11] D. F. Walls, “Squeezed states of light”, *nature* **306**, 141–146 (1983).
- [12] H.-P. Breuer, F. Petruccione, et al., *The theory of open quantum systems* (Oxford University Press on Demand, 2002).
- [13] F. Flamini, N. Spagnolo, and F. Sciarrino, “Photonic quantum information processing: a review”, *Reports on Progress in Physics* **82**, 016001 (2018).
- [14] R. Kapral, “Quantum dynamics in open quantum-classical systems”, *Journal of Physics: Condensed Matter* **27**, 073201 (2015).
- [15] W. R. Frensley, “Boundary conditions for open quantum systems driven far from equilibrium”, *Reviews of Modern Physics* **62**, 745 (1990).
- [16] M. Mohseni, Y. Omar, G. S. Engel, and M. B. Plenio, *Quantum effects in biology* (Cambridge University Press, 2014).
- [17] I. Rotter and J. Bird, “A review of progress in the physics of open quantum systems: theory and experiment”, *Reports on Progress in Physics* **78**, 114001 (2015).
- [18] S. J. Devitt, W. J. Munro, and K. Nemoto, “Quantum error correction for beginners”, *Reports on Progress in Physics* **76**, 076001 (2013).

- [19] P. W. Shor, "Fault-tolerant quantum computation", in Proceedings of 37th conference on foundations of computer science (IEEE, 1996), pp. 56–65.
- [20] N. Gisin and R. Thew, "Quantum communication", *Nature photonics* **1**, 165–171 (2007).
- [21] U. Weiss, *Quantum dissipative systems* (World Scientific, 2012).
- [22] S. Schirmer and X. Wang, "Stabilizing open quantum systems by markovian reservoir engineering", *Physical Review A* **81**, 062306 (2010).
- [23] H.-P. Breuer, E.-M. Laine, J. Piilo, and B. Vacchini, "Colloquium: non-markovian dynamics in open quantum systems", *Reviews of Modern Physics* **88**, 021002 (2016).
- [24] I. De Vega and D. Alonso, "Dynamics of non-markovian open quantum systems", *Reviews of Modern Physics* **89**, 015001 (2017).
- [25] C. P. Koch, "Controlling open quantum systems: tools, achievements, and limitations", *Journal of Physics: Condensed Matter* **28**, 213001 (2016).
- [26] P. Lambropoulos and D. Petrosyan, *Fundamentals of quantum optics and quantum information* (Springer, 2007).
- [27] C. Gerry and P. Knight, "Quantum superpositions and schrödinger cat states in quantum optics", *American Journal of Physics* **65**, 964–974 (1997).
- [28] S. Pirandola, J. Eisert, C. Weedbrook, A. Furusawa, and S. L. Braunstein, "Advances in quantum teleportation", *Nature photonics* **9**, 641–652 (2015).
- [29] M. J. Klein, "Max planck and the beginnings of the quantum theory", *Archive for History of Exact Sciences* **1**, 459–479 (1961).
- [30] U. L. Andersen, T. Gehring, C. Marquardt, and G. Leuchs, "30 years of squeezed light generation", *Physica Scripta* **91**, 053001 (2016).
- [31] P. Knight and V. Bužek, "Squeezed states: basic principles", *Quantum Squeezing*, 3–32 (2004).
- [32] R. Schnabel, "Squeezed states of light and their applications in laser interferometers", *Physics Reports* **684**, 1–51 (2017).
- [33] H. Yonezawa and A. Furusawa, "Continuous-variable quantum information processing with squeezed states of light", *Optics and Spectroscopy* **108**, 288–296 (2010).
- [34] H. Grote, K. Danzmann, K. Dooley, R. Schnabel, J. Slutsky, and H. Vahlbruch, "First long-term application of squeezed states of light in a gravitational-wave observatory", *Physical review letters* **110**, 181101 (2013).
- [35] R. S. Bondurant and J. H. Shapiro, "Squeezed states in phase-sensing interferometers", *Physical Review D* **30**, 2548 (1984).
- [36] H. Vahlbruch, S. Chelkowski, K. Danzmann, and R. Schnabel, "Quantum engineering of squeezed states for quantum communication and metrology", *New Journal of Physics* **9**, 371 (2007).
- [37] M. Reid and D. Walls, "Generation of squeezed states via degenerate four-wave mixing", *Physical Review A* **31**, 1622 (1985).
- [38] R. Loudon and P. L. Knight, "Squeezed light", *Journal of modern optics* **34**, 709–759 (1987).
- [39] C. Gerry and P. Knight, "Nonclassical light", *Introductory Quantum Optics* (Cambridge University Press (Cambridge), 2004) p, 150–194 (2004).

- [40] S. Wang, X.-Y. Zhang, and H.-Y. Fan, "Oscillation behaviour in the photon-number distribution of squeezed coherent states", *Chinese Physics B* **21**, 054206 (2012).
- [41] S. Chumakov, A. B. Klimov, and J. Sanchez-Mondragon, "General properties of quantum optical systems in a strong-field limit", *Physical Review A* **49**, 4972 (1994).
- [42] P. á. Corkum and F. Krausz, "Attosecond science", *Nature physics* **3**, 381–387 (2007).
- [43] D. Gotta, "Precision spectroscopy of light exotic atoms", *Progress in Particle and Nuclear Physics* **52**, 133–195 (2004).
- [44] S. Y. Kruchinin, F. Krausz, and V. S. Yakovlev, "Colloquium: strong-field phenomena in periodic systems", *Reviews of Modern Physics* **90**, 021002 (2018).
- [45] C. Winterfeldt, C. Spielmann, and G. Gerber, "Colloquium: optimal control of high-harmonic generation", *Reviews of Modern Physics* **80**, 117 (2008).
- [46] M. Lewenstein, P. Balcou, M. Y. Ivanov, A. L'huillier, and P. B. Corkum, "Theory of high-harmonic generation by low-frequency laser fields", *Physical Review A* **49**, 2117 (1994).
- [47] P.-M. Paul, E. S. Toma, P. Breger, G. Mullot, F. Augé, P. Balcou, H. G. Muller, and P. Agostini, "Observation of a train of attosecond pulses from high harmonic generation", *Science* **292**, 1689–1692 (2001).
- [48] J. Li, J. Lu, A. Chew, S. Han, J. Li, Y. Wu, H. Wang, S. Ghimire, and Z. Chang, "Attosecond science based on high harmonic generation from gases and solids", *Nature Communications* **11**, 2748 (2020).
- [49] M. Y. Ivanov, M. Spanner, and O. Smirnova, "Anatomy of strong field ionization", *Journal of Modern Optics* **52**, 165–184 (2005).
- [50] J. H. Eberly, J. Javanainen, and K. Rzażewski, "Above-threshold ionization", *Physics reports* **204**, 331–383 (1991).
- [51] T. Brabec, M. Côté, P. Boulanger, and L. Ramunno, "Theory of tunnel ionization in complex systems", *Physical review letters* **95**, 073001 (2005).
- [52] M. Wollenhaupt, A. Assion, D. Liese, C. Sarpe-Tudoran, T. Baumert, S. Zamith, M. A. Bouchène, B. Girard, A. Flettner, U. Weichmann, et al., "Interferences of ultrashort free electron wave packets", *Physical review letters* **89**, 173001 (2002).
- [53] C. Lin, A.-T. Le, Z. Chen, T. Morishita, and R. Lucchese, "Strong-field rescattering physics—self-imaging of a molecule by its own electrons", *Journal of Physics B: Atomic, Molecular and Optical Physics* **43**, 122001 (2010).
- [54] R. J. Levis, G. M. Menkir, and H. Rabitz, "Selective bond dissociation and rearrangement with optimally tailored, strong-field laser pulses", *Science* **292**, 709–713 (2001).
- [55] F. Lépine, M. Y. Ivanov, and M. J. Vrakking, "Attosecond molecular dynamics: fact or fiction?", *Nature Photonics* **8**, 195–204 (2014).
- [56] C. N. Cohen-Tannoudji, "The autler-townes effect revisited", *Amazing Light*, 109–123 (1996).
- [57] M. Fushitani, "Applications of pump-probe spectroscopy", *Annual Reports Section "C"(Physical Chemistry)* **104**, 272–297 (2008).

- [58] P. A. George, J. Strait, J. Dawlaty, S. Shivaraman, M. Chandrashekhara, F. Rana, and M. G. Spencer, "Ultrafast optical-pump terahertz-probe spectroscopy of the carrier relaxation and recombination dynamics in epitaxial graphene", *Nano letters* **8**, 4248–4251 (2008).
- [59] C. P. Koch, T. Klüner, and R. Kosloff, "A complete quantum description of an ultrafast pump-probe charge transfer event in condensed phase", *The Journal of chemical physics* **116**, 7983–7996 (2002).
- [60] K. Sharp and J. J. Skinner, "Pump-probe molecular dynamics as a tool for studying protein motion and long range coupling", *Proteins: Structure, Function, and Bioinformatics* **65**, 347–361 (2006).
- [61] H. Liu, L. Wong, S. Wang, S. Tang, and X. Zhang, "Ultrafast insulator–metal phase transition in vanadium dioxide studied using optical pump–terahertz probe spectroscopy", *Journal of Physics: Condensed Matter* **24**, 415604 (2012).
- [62] J. Dynes, M. Frogley, M. Beck, J. Faist, and C. Phillips, "Ac stark splitting and quantum interference with intersubband transitions in quantum wells", *Physical review letters* **94**, 157403 (2005).
- [63] N. B. Delone and V. P. Krainov, "Ac stark shift of atomic energy levels", *Physics-Uspekhi* **42**, 669 (1999).
- [64] J. R. Rubbmark, M. M. Kash, M. G. Littman, and D. Kleppner, "Dynamical effects at avoided level crossings: a study of the landau-zener effect using rydberg atoms", *Physical Review A* **23**, 3107 (1981).
- [65] T. Ricketts, L. Yatsenko, S. Steuerwald, T. Halfmann, B. Shore, N. Vitanov, and K. Bergmann, "Efficient adiabatic population transfer by two-photon excitation assisted by a laser-induced stark shift", *The Journal of Chemical Physics* **113**, 534–546 (2000).
- [66] F. Sauter, "Über das verhalten eines elektrons im homogenen elektrischen feld nach der relativistischen theorie diracs", *Zeitschrift für Physik* **69**, 742–764 (1931).
- [67] J. Schwinger, "On gauge invariance and vacuum polarization", *Physical Review* **82**, 664 (1951).
- [68] F. V. Bunkin and I. Tugov, "The possibility of electron-positron pair production in vacuum when laser radiation is focussed", in *Doklady akademii nauk*, Vol. 187, 3 (Russian Academy of Sciences, 1969), pp. 541–544.
- [69] E. Brézin and C. Itzykson, "Pair production in vacuum by an alternating field", *Physical Review D* **2**, 1191 (1970).
- [70] V. S. Popov, "Production of e^+e^- pairs in an alternating external field", *Soviet Journal of Experimental and Theoretical Physics Letters* **13**, 195 (1971).
- [71] V. Popov, *Pair production in a varying external field (quasiclassical approximation)*. Tech. rep. (Inst. of Theoretical and Experimental Physics, Moscow, 1971).
- [72] V. Popov, *Resonant pair production in a strong electric field*, tech. rep. (Inst. of Theoretical and Experimental Physics, Moscow, 1973).
- [73] N. Narozhnyi and A. Nikishov, "Pair production by a periodic electric field", *Soviet Journal of Experimental and Theoretical Physics* **38**, 427 (1974).
- [74] V. Mostepanenko and V. Frolov, "Production of particles from vacuum by a uniform electric-field with periodic time-dependence", *SOVIET JOURNAL OF NUCLEAR PHYSICS-USSR* **19**, 451–456 (1974).

- [75] M. Marinov and V. Popov, "Electron-positron pair creation from vacuum induced by variable electric field", *Fortschritte der Physik* **25**, 373–400 (1977).
- [76] T. Tschentscher, C. Bressler, J. Grünert, A. Madsen, A. P. Mancuso, M. Meyer, A. Scherz, H. Sinn, and U. Zastra, "Photon beam transport and scientific instruments at the european xfel", *Applied Sciences* **7**, 592 (2017).
- [77] K. Tiedtke, A. Azima, N. Von Bargen, L. Bittner, S. Bonfigt, S. Düsterer, B. Faatz, U. Frühling, M. Gensch, C. Gerth, et al., "The soft x-ray free-electron laser flash at desy: beamlines, diagnostics and end-stations", *New journal of physics* **11**, 023029 (2009).
- [78] C. Bostedt, S. Boutet, D. M. Fritz, Z. Huang, H. J. Lee, H. T. Lemke, A. Robert, W. F. Schlotter, J. J. Turner, and G. J. Williams, "Linac coherent light source: the first five years", *Reviews of Modern Physics* **88**, 015007 (2016).
- [79] M. Yabashi, H. Tanaka, and T. Ishikawa, "Overview of the sacra facility", *Journal of synchrotron radiation* **22**, 477–484 (2015).
- [80] I. Tsohantjis, S. Moustazis, and I. Ploumistakis, "On electron–positron pair production using a two level on resonant multiphoton approximation", *Physics Letters B* **650**, 249–256 (2007).
- [81] A. Melissinos, "Quantum aspects of beam physics", in *Proceedings of the 15th advanced icfa beam dynamics workshop, monterey, ca* (1998), pp. 4–9.
- [82] P. Chen, "Quantum aspects of beam physics", in *Proceedings of the 1999 particle accelerator conference* (cat. no. 99ch36366), Vol. 1 (IEEE, 1999), pp. 224–228.
- [83] P. Chen and T. Tajima, "Testing unruh radiation with ultraintense lasers", *Physical Review Letters* **83**, 256 (1999).
- [84] T. Tajima, "Fundamental physics with an x-ray free electron laser.", *Plasma Physics Reports* **29** (2003).
- [85] V. S. Popov, "Schwinger mechanism of electron-positron pair production by the field of optical and x-ray lasers in vacuum", *Journal of Experimental and Theoretical Physics Letters* **74**, 133–138 (2001).
- [86] V. Popov, "The schwinger effect and possibilities for its observation using optical and x-ray lasers", *Journal of Experimental and Theoretical Physics* **94**, 1057–1069 (2002).
- [87] A. Ringwald, "Pair production from vacuum at the focus of an x-ray free electron laser", *Physics Letters B* **510**, 107–116 (2001).
- [88] R. Alkofer, M. Hecht, C. D. Roberts, S. Schmidt, and D. Vinnik, "Pair creation and an x-ray free electron laser", *Physical Review Letters* **87**, 193902 (2001).
- [89] H. Avetissian, A. Avetissian, G. Mkrtchian, and K. V. Sedrakian, "X-ray free electron laser for electron–positron pair production on the nuclei", *Nuclear Instruments and Methods in Physics Research Section A: Accelerators, Spectrometers, Detectors and Associated Equipment* **507**, 582–586 (2003).
- [90] I. Smetanin and K. Nakajima, "Quantum effects in laser-beam compton interaction and stimulated electron-positron annihilation in a strong field", *Laser and Particle Beams* **22**, 479–484 (2004).
- [91] I. Ploumistakis, S. Moustazis, and I. Tsohantjis, "Towards laser based improved experimental schemes for multiphoton $e^+ e^-$ pair production from vacuum", *Physics Letters A* **373**, 2897–2900 (2009).

- [92] A. Ringwald, "Boiling the vacuum with an x-ray free electron laser", in *Quantum aspects of beam physics 2003* (World Scientific, 2004), pp. 149–163.
- [93] A. Hartin, A. Ringwald, and N. Tapia, "Measuring the boiling point of the vacuum of quantum electrodynamics", *Physical Review D* **99**, 036008 (2019).
- [94] C. Roberts, S. Schmidt, and D. Vinnik, "Quantum effects with an x-ray free-electron laser", *Physical review letters* **89**, 153901 (2002).
- [95] L. Granz, O. Mathiak, S. Villalba-Chávez, and C. Müller, "Electron-positron pair production in oscillating electric fields with double-pulse structure", *Physics Letters B* **793**, 85–89 (2019).
- [96] A. Di Piazza, E. Lötstedt, A. Milstein, and C. Keitel, "Barrier control in tunneling e^+e^- photoproduction", *Physical review letters* **103**, 170403 (2009).
- [97] R. Schützhold, H. Gies, and G. Dunne, "Dynamically assisted schwinger mechanism", *Physical review letters* **101**, 130404 (2008).
- [98] O. Olugh, Z. Li, and B. Xie, "Dynamically assisted pair production for various polarizations", *Physics Letters B* **802**, 135259 (2020).
- [99] A. Otto, D. Seipt, D. Blaschke, B. Kämpfer, and S. A. Smolyansky, "Lifting shell structures in the dynamically assisted schwinger effect in periodic fields", *Physics Letters B* **740**, 335–340 (2015).
- [100] G. Torgrimsson, "Thermally versus dynamically assisted schwinger pair production", *Physical Review D* **99**, 096007 (2019).
- [101] Z.-L. Li, H.-B. Sang, and B.-S. Xie, "Enhanced electron-positron pair production of a vacuum in a strong laser pulse field by frequency variation", *Chinese Physics Letters* **30**, 071201 (2013).
- [102] I. Sitiwaldi and B.-S. Xie, "Modulation effect in multiphoton pair production", *Physics Letters B* **768**, 174–179 (2017).
- [103] T. Heinzl, A. Ilderton, and M. Marklund, "Finite size effects in stimulated laser pair production", *Physics Letters B* **692**, 250–256 (2010).
- [104] C. Kohlfürst, H. Gies, and R. Alkofer, "Effective mass signatures in multiphoton pair production", *Physical Review Letters* **112**, 050402 (2014).
- [105] C. Kohlfürst and R. Alkofer, "Ponderomotive effects in multiphoton pair production", *Physical Review D* **97**, 036026 (2018).
- [106] H. Avetissian, A. Avetissian, G. Mkrtchian, and K. V. Sedrakian, "Electron-positron pair production in the field of superstrong oppositely directed laser beams", *Physical Review E* **66**, 016502 (2002).
- [107] G. R. Mocken, M. Ruf, C. Müller, and C. H. Keitel, "Nonperturbative multiphoton electron-positron-pair creation in laser fields", *Physical Review A* **81**, 022122 (2010).
- [108] Z. Li, D. Lu, B. Shen, L. Fu, J. Liu, and B. Xie, "Mass shift effects in nonperturbative multiphoton pair production for arbitrary polarized electric fields", *arXiv preprint arXiv:1410.6284* (2014).
- [109] C. Müller, K. Hatsagortsyan, M. Ruf, S. Müller, H. Hetzheim, M. Kohler, and C. Keitel, "Relativistic nonperturbative above-threshold phenomena in strong laser fields", *Laser physics* **19**, 1743–1752 (2009).
- [110] K. Z. Hatsagortsyan, C. Müller, and C. H. Keitel, "Nonperturbative multiphoton processes and electron-positron pair production", in *Aip conference proceedings*, Vol. 827, 1 (American Institute of Physics, 2006), pp. 442–447.

- [111] C. Kohlfürst, “Effect of time-dependent inhomogeneous magnetic fields on the particle momentum spectrum in electron-positron pair production”, *Physical Review D* **101**, 096003 (2020).
- [112] M. Makris, P. Lambropoulos, and A. Mihelič, “Theory of multiphoton multi-electron ionization of xenon under strong 93-ev radiation”, *Physical review letters* **102**, 033002 (2009).
- [113] G. Breit and J. A. Wheeler, “Collision of two light quanta”, *Physical Review* **46**, 1087 (1934).
- [114] D. Burke, R. Field, G. Horton-Smith, J. Spencer, D. Walz, S. Berridge, W. Bugg, K. Shmakov, A. Weidemann, C. Bula, et al., “Positron production in multiphoton light-by-light scattering”, *Physical Review Letters* **79**, 1626 (1997).
- [115] C. Bamber, S. Boege, T. Koffas, T. Kotseroglou, A. Melissinos, D. Meyerhofer, D. Reis, W. Ragg, C. Bula, K. McDonald, et al., “Studies of nonlinear qed in collisions of 46.6 gev electrons with intense laser pulses”, *Physical Review D* **60**, 092004 (1999).
- [116] H. R. Reiss, “Production of electron pairs from a zero-mass state”, *Physical Review Letters* **26**, 1072 (1971).
- [117] A. Nikishov and V. Ritus, “Quantum processes in the field of a plane electromagnetic wave and in a constant field i ”, *Sov. Phys. JETP* **19**, 529–541 (1964).
- [118] H. Hu, C. Müller, and C. H. Keitel, “Complete qed theory of multiphoton trident pair production in strong laser fields”, *Physical review letters* **105**, 080401 (2010).
- [119] A. Ilderton, “Trident pair production in strong laser pulses”, *Physical review letters* **106**, 020404 (2011).
- [120] C. Müller, “Nonlinear bethe–heitler pair creation with attosecond laser pulses at the lhc”, *Physics Letters B* **672**, 56–60 (2009).
- [121] T.-O. Müller and C. Müller, “Spin correlations in nonperturbative electron–positron pair creation by petawatt laser pulses colliding with a tev proton beam”, *Physics Letters B* **696**, 201–206 (2011).
- [122] K. Krajewska, C. Müller, and J. Kamiński, “Bethe–heitler pair production in ultrastrong short laser pulses”, *Physical Review A* **87**, 062107 (2013).
- [123] A. Georges and P. Lambropoulos, “Aspects of resonant multiphoton processes”, in *Advances in electronics and electron physics*, Vol. 54 (Elsevier, 1980), pp. 191–240.
- [124] F. Edition, A. Papoulis, and S. U. Pillai, *Probability, random variables, and stochastic processes*, 2002.
- [125] J. R. Klauder and E. C. G. Sudarshan, *Fundamentals of quantum optics* (Courier Corporation, 2006).
- [126] G. Nikolopoulos and P. Lambropoulos, “Effects of free-electron-laser field fluctuations on the frequency response of driven atomic resonances”, *Physical Review A* **86**, 033420 (2012).
- [127] G. Nikolopoulos and P. Lambropoulos, “Frequency response of an atomic resonance driven by weak free-electron-laser fluctuating pulses”, *Journal of Physics B: Atomic, Molecular and Optical Physics* **46**, 164010 (2013).

- [128] S. Przhibelskii, "Mean value and fluctuations of population of a two-level system excited by intense nonmonochromatic radiation", *Optics and Spectroscopy* **42**, 8–13 (1977).
- [129] P. Elyutin, "Linear susceptibility of a three-level system in a strong nonmonochromatic radiation field", *Optics and Spectroscopy* **43**, 318–321 (1977).
- [130] T. Katravulapally and L. Nikolopoulos, "Perturbative theory of statistically averaged atomic dynamics in fluctuating laser fields", *Physical Review A* **102**, 053111 (2020).
- [131] P. Kochan and H. Carmichael, "Photon-statistics dependence of single-atom absorption", *Physical Review A* **50**, 1700 (1994).
- [132] H. Carmichael, A. Lane, and D. Walls, "Resonance fluorescence in a squeezed vacuum", *Journal of Modern Optics* **34**, 821–840 (1987).
- [133] Z. Ficek and B. Sanders, "Resonance fluorescence of a two-level atom in an off-resonance squeezed vacuum", *Journal of Physics B: Atomic, Molecular and Optical Physics* **27**, 809 (1994).
- [134] M. Ferguson, Z. Ficek, and B. Dalton, "Resonance fluorescence spectra of three-level atoms in a squeezed vacuum", *Physical Review A* **54**, 2379 (1996).
- [135] A. Joshi and S. V. Lawande, "Time-dependent spectrum of a strongly driven two-level atom in the squeezed vacuum", *Physical Review A* **41**, 2822 (1990).
- [136] A. Joshi and R. Puri, "Sideband correlations in resonance fluorescence from two-level atoms in a squeezed vacuum", *Physical Review A* **43**, 6428 (1991).
- [137] A. Parkins, "Rabi sideband narrowing via strongly driven resonance fluorescence in a narrow-bandwidth squeezed vacuum", *Physical Review A* **42**, 4352 (1990).
- [138] A. Parkins, "Resonance fluorescence of a two-level atom in a two-mode squeezed vacuum", *Physical Review A* **42**, 6873 (1990).
- [139] R. Tanaś, "Master equation approach to the problem of two-level atom in a squeezed vacuum with finite bandwidth", *Optics and Spectroscopy* **87**, 676–682 (1999).
- [140] S. Tesfa, "Coherently driven two-level atom coupled to a broadband squeezed vacuum", *Journal of Modern Optics* **54**, 1759–1777 (2007).
- [141] H. Ritsch and P. Zoller, "Atomic transitions in finite-bandwidth squeezed light", *Physical review letters* **61**, 1097 (1988).
- [142] H. Ritsch and P. Zoller, "Systems driven by colored squeezed noise: the atomic absorption spectrum", *Physical Review A* **38**, 4657 (1988).
- [143] Z. Ficek and P. Drummond, "Three-level atom in a broadband squeezed vacuum field. ii. applications", *Physical Review A* **43**, 6258 (1991).
- [144] Z. Ficek and P. Drummond, "Three-level atom in a broadband squeezed vacuum field. i. general theory", *Physical Review A* **43**, 6247 (1991).
- [145] P. Zoller, "Ac stark splitting in double optical resonance and resonance fluorescence by a nonmonochromatic chaotic field", *Physical Review A* **20**, 1019 (1979).
- [146] A. Georges, "Resonance fluorescence in markovian stochastic fields", *Physical Review A* **21**, 2034 (1980).

- [147] K. Y. Spasibko, D. A. Kopylov, V. L. Krutyanskiy, T. V. Murzina, G. Leuchs, and M. V. Chekhova, "Multiphoton effects enhanced due to ultrafast photon-number fluctuations", *Physical Review Letters* **119**, 223603 (2017).
- [148] L. Zhang, Y. Lu, D. Zhou, H. Zhang, L. Li, and G. Zhang, "Superbunching effect of classical light with a digitally designed spatially phase-correlated wave front", *Physical Review A* **99**, 063827 (2019).
- [149] L. Zhang, D. Zhou, Y. Lu, H. Zhang, and G. Zhang, "Super-bunched focusing with chirped random-phase gratings", *Photonics Research* **8**, 503–510 (2020).
- [150] R. Slusher, L. Hollberg, B. Yurke, J. Mertz, and J. Valley, "Observation of squeezed states generated by four-wave mixing in an optical cavity", *Physical review letters* **55**, 2409 (1985).
- [151] H. P. Yuen, "Two-photon coherent states of the radiation field", *Physical Review A* **13**, 2226 (1976).
- [152] M. Xiao, L.-A. Wu, and H. J. Kimble, "Precision measurement beyond the shot-noise limit", *Physical review letters* **59**, 278 (1987).
- [153] P. Grangier, R. Slusher, B. Yurke, and A. LaPorta, "Squeezed-light-enhanced polarization interferometer", *Physical review letters* **59**, 2153 (1987).
- [154] C. M. Caves, "Quantum-mechanical noise in an interferometer", *Physical Review D* **23**, 1693 (1981).
- [155] B. P. Abbott, R. Abbott, T. Abbott, M. Abernathy, F. Acernese, K. Ackley, C. Adams, T. Adams, P. Addesso, R. Adhikari, et al., "Observation of gravitational waves from a binary black hole merger", *Physical review letters* **116**, 061102 (2016).
- [156] A. Kozhekin, K. Mølmer, and E. Polzik, "Quantum memory for light", *Physical Review A* **62**, 033809 (2000).
- [157] J. Appel, E. Figueroa, D. Korystov, M. Lobino, and A. Lvovsky, "Quantum memory for squeezed light", *Physical review letters* **100**, 093602 (2008).
- [158] T. Li, F. Li, C. Altuzarra, A. Classen, and G. S. Agarwal, "Squeezed light induced two-photon absorption fluorescence of fluorescein biomarkers", *Applied Physics Letters* **116**, 254001 (2020).
- [159] B. Lawrie, R. Pooser, and P. Maksymovych, "Squeezing noise in microscopy with quantum light", *Trends in Chemistry* **2**, 683–686 (2020).
- [160] P. Lambropoulos, C. Kikuchi, and R. K. Osborn, "Coherence and two-photon absorption", *Physical Review* **144**, 1081 (1966).
- [161] M. Glodz and J. Krasinski, "The two-quanta absorption of the 623.8 nm line of the cw he-ne laser by 3, 4-benzopyrene solid solution in methyl methacrylate polymer", *Lett. Nuovo Cim* **6**, 566–568 (1973).
- [162] J. Kasiński, S. Chudzyński, W. Majewski, and M. Głódź, "Experimental dependence of two-photon absorption efficiency on statistical properties of laser light", *Optics Communications* **12**, 304–306 (1974).
- [163] J. Kasiński, B. Karczewski, W. Majewski, and M. Głódź, "Dependence of two-photon absorption efficiency on the relative intensities of two modes simultaneously generated by a cw laser", *Optics Communications* **15**, 409–411 (1975).
- [164] P. Lambropoulos, "Topics on multiphoton processes in atoms", in *Advances in atomic and molecular physics*, Vol. 12 (Elsevier, 1976), pp. 87–164.

- [165] J. Krasinski and S. Dinev, "Influence of nonlinear effects on the statistical properties of a high power density laser beam", *Optics Communications* **18**, 424–426 (1976).
- [166] M. Teich and G. Wolga, "Multiple-photon processes and higher order correlation functions", *Physical Review Letters* **16**, 625 (1966).
- [167] Y. Shen, "Quantum statistics of nonlinear optics", *Physical Review* **155**, 921 (1967).
- [168] F. Shiga and S. Imamura, "Experiment on relation between two-photon absorption and coherence of light", *Physics Letters A* **25**, 706–707 (1967).
- [169] P. Lambropoulos, "Field-correlation effects in two-photon processes", *Physical Review* **168**, 1418 (1968).
- [170] B. Mollow, "Two-photon absorption and field correlation functions", *Physical Review* **175**, 1555 (1968).
- [171] G. Agarwal, "Field-correlation effects in multiphoton absorption processes", *Physical Review A* **1**, 1445 (1970).
- [172] M. Teich, R. Abrams, and W. Gandrud, "Photon-correlation enhancement of shg at $10.6\ \mu\text{m}$ ", *Optics Communications* **2**, 206–208 (1970).
- [173] J. Debethune, "Quantum correlation functions for radiation fields with stationary independent modes", *Nuovo Cimento B Serie* **12**, 101–117 (1972).
- [174] S. Dixit and P. Lambropoulos, "New photon-correlation effects in near-resonant multiphoton ionization", *Physical Review Letters* **40**, 111 (1978).
- [175] S. N. Dixit and P. Lambropoulos, "Photon correlation effects in resonant multiphoton ionization", *Physical Review A* **21**, 168 (1980).
- [176] G. Mouloudakis and P. Lambropoulos, "Revisiting photon-statistics effects on multiphoton ionization", *Physical Review A* **97**, 053413 (2018).
- [177] G. Mouloudakis and P. Lambropoulos, "Revisiting photon-statistics effects on multiphoton ionization. ii. connection to realistic systems", *Physical Review A* **99**, 063419 (2019).
- [178] T. Lamprou, I. Lontos, N. Papadakis, and P. Tzallas, "A perspective on high photon flux nonclassical light and applications in nonlinear optics", *High power laser science and engineering* **8**, e42 (2020).
- [179] C. Lecompte, G. Mainfray, C. Manus, and F. Sanchez, "Experimental demonstration of laser temporal coherence effects on multiphoton ionization processes", *Physical Review Letters* **32**, 265 (1974).
- [180] C. Lecompte, G. Mainfray, C. Manus, and F. Sanchez, "Laser temporal-coherence effects on multiphoton ionization processes", *Physical Review A* **11**, 1009 (1975).
- [181] J. Gea-Banacloche, "Two-photon absorption of nonclassical light", *Physical review letters* **62**, 1603 (1989).
- [182] C. S. Muñoz and D. Jaksch, "Squeezed lasing", *Physical Review Letters* **127**, 183603 (2021).
- [183] G. Mouloudakis and P. Lambropoulos, "Squeezed coherent states in double optical resonance", in *Photonics*, Vol. 8, 3 (MDPI, 2021), p. 72.
- [184] M. L. Goldberger and K. M. Watson, *Collision theory* (Courier Corporation, 2004).

- [185] C. Cohen-Tannoudji, J. Dupont-Roc, and G. Grynberg, *Atom-photon interactions: basic processes and applications* (John Wiley & Sons, 1998).
- [186] W. Schleich and J. A. Wheeler, "Oscillations in photon distribution of squeezed states and interference in phase space", *Nature* **326**, 574–577 (1987).
- [187] S. H. Autler and C. H. Townes, "Stark effect in rapidly varying fields", *Physical Review* **100**, 703 (1955).
- [188] N. Vitanov, B. Shore, L. Yatsenko, K. Böhmer, T. Halfmann, T. Rickes, and K. Bergmann, "Power broadening revisited: theory and experiment", *Optics communications* **199**, 117–126 (2001).
- [189] O. Hosten, N. J. Engelsen, R. Krishnakumar, and M. A. Kasevich, "Measurement noise 100 times lower than the quantum-projection limit using entangled atoms", *Nature* **529**, 505–508 (2016).
- [190] R. M. Whitley and C. Stroud Jr, "Double optical resonance", *Physical Review A* **14**, 1498 (1976).
- [191] G. Mouloudakis and P. Lambropoulos, "Pairing superbunching with compounded nonlinearity in a resonant transition", *Physical Review A* **102**, 023713 (2020).
- [192] F. Wu, R. Grove, and S. Ezekiel, "Investigation of the spectrum of resonance fluorescence induced by a monochromatic field", *Physical Review Letters* **35**, 1426 (1975).
- [193] H. Eicher, "Third-order susceptibility of alkali metal vapors", *IEEE Journal of Quantum Electronics* **11**, 121–130 (1975).
- [194] M. Aymar, E. Luc-Koenig, and F. C. Farnoux, "Theoretical investigation on photoionization from rydberg states of lithium, sodium and potassium", *Journal of Physics B: Atomic and Molecular Physics* **9**, 1279 (1976).
- [195] S. Hussain, M. Saleem, and M. Baig, "Angular momentum dependence of photoionization cross sections from the excited states of lithium", *Physical Review A* **74**, 052705 (2006).
- [196] R. J. Wolff and S. P. Davis, "Direct measurement of atomic lifetimes of cesium and sodium", *JOSA* **58**, 490–495 (1968).
- [197] R. W. Boyd, J. G. Dodd, J. Krasinski, and C. Stroud, "Disk-shaped heat-pipe oven used for lithium excited-state lifetime measurements", *Optics Letters* **5**, 117–119 (1980).
- [198] F. Krausz and M. Ivanov, "Attosecond physics", *Reviews of modern physics* **81**, 163 (2009).
- [199] P. Avan and C. Cohen-Tannoudji, "Two-level atom saturated by a fluctuating resonant laser beam. calculation of the fluorescence spectrum", *Journal of Physics B: Atomic and Molecular Physics* **10**, 155 (1977).
- [200] M. Citron, H. Gray, C. W. Gabel, and C. Stroud Jr, "Experimental study of power broadening in a two-level atom", *Physical Review A* **16**, 1507 (1977).
- [201] C. Mavroyannis, "Two-photon resonance fluorescence", *Optics Communications* **26**, 453–456 (1978).
- [202] D. A. Holm and M. Sargent, "Theory of two-photon resonance fluorescence", *Optics letters* **10**, 405–407 (1985).
- [203] M. Alexanian and S. K. Bose, "Two-photon resonance fluorescence", *Physical Review A* **74**, 063418 (2006).

- [204] Y. Li, S. Krinsky, J. W. Lewellen, K.-J. Kim, V. Sajaev, and S. V. Milton, "Characterization of a chaotic optical field using a high-gain, self-amplified free-electron laser", *Physical review letters* **91**, 243602 (2003).
- [205] P. Finetti, H. Höppner, E. Allaria, C. Callegari, F. Capotondi, P. Cinquegrana, M. Coreno, R. Cucini, M. B. Danailov, A. Demidovich, et al., "Pulse duration of seeded free-electron lasers", *Physical Review X* **7**, 021043 (2017).
- [206] O. Y. Gorobtsov, G. Mercurio, F. Capotondi, P. Skopintsev, S. Lazarev, I. A. Zaluzhnyy, M. B. Danailov, M. Dell'Angela, M. Manfredda, E. Pedersoli, et al., "Seeded x-ray free-electron laser generating radiation with laser statistical properties", *Nature communications* **9**, 4498 (2018).
- [207] B. S. Xie, Z. L. Li, and S. Tang, "Electron-positron pair production in ultra-strong laser fields", *Matter and Radiation at Extremes* **2**, 225–242 (2017).
- [208] A. Di Piazza, C. Müller, K. Hatsagortsyan, and C. H. Keitel, "Extremely high-intensity laser interactions with fundamental quantum systems", *Reviews of Modern Physics* **84**, 1177 (2012).
- [209] E. Saldin, E. Schneidmiller, and M. Yurkov, "Statistical and coherence properties of radiation from x-ray free-electron lasers", *New Journal of Physics* **12**, 035010 (2010).
- [210] R. Bonifacio, L. De Salvo, P. Pierini, N. Piovella, and C. Pellegrini, "Spectrum, temporal structure, and fluctuations in a high-gain free-electron laser starting from noise", *Physical review letters* **73**, 70 (1994).
- [211] V. Ayvazyan, N. Baboi, I. Bohnet, R. Brinkmann, M. Castellano, P. Castro, L. Catani, S. Choroba, A. Cianchi, M. Dohlus, et al., "Generation of gw radiation pulses from a vuv free-electron laser operating in the femtosecond regime", *Physical review letters* **88**, 104802 (2002).
- [212] V. Ayvazyan, J.-P. Carneiro, P. Castro, B. Faatz, A. Fateev, J. Feldhaus, C. Gerth, V. Gretchko, B. Grigoryan, U. Hahn, et al., "Study of the statistical properties of the radiation from a vuv sase fel operating in the femtosecond regime", *Nuclear Instruments and Methods in Physics Research Section A: Accelerators, Spectrometers, Detectors and Associated Equipment* **507**, 368–372 (2003).
- [213] O. Y. Gorobtsov, G. Mercurio, G. Brenner, U. Lorenz, N. Gerasimova, R. Kurta, F. Hieke, P. Skopintsev, I. Zaluzhnyy, S. Lazarev, et al., "Statistical properties of a free-electron laser revealed by hanbury brown–twiss interferometry", *Physical Review A* **95**, 023843 (2017).
- [214] X. M. Zhao, M. Gulley, H. Bryant, C. E. Strauss, D. J. Funk, A. Stintz, D. Rislove, G. Kyrala, W. Ingalls, and W. Miller, "Nonresonant excess photon detachment of negative hydrogen ions", *Physical review letters* **78**, 1656 (1997).
- [215] L. Nikolopoulos and P. Lambropoulos, "Above-threshold ionization of negative hydrogen", *Physical Review A* **56**, 3106 (1997).
- [216] L. Nikolopoulos and P. Lambropoulos, "Time-dependent nonperturbative theory of h- in a strong laser field", *Physical review letters* **82**, 3771 (1999).
- [217] P. Lambropoulos, "Mechanisms for multiple ionization of atoms by strong pulsed lasers", *Physical review letters* **55**, 2141 (1985).
- [218] G. Troup and H. Perlman, "Pair production in a vacuum by an alternating field", *Physical Review D* **6**, 2299 (1972).

- [219] A. Di Piazza, "Pair production at the focus of two equal and oppositely directed laser beams: the effect of the pulse shape", *Physical Review D* **70**, 053013 (2004).
- [220] I. A. Aleksandrov and C. Kohlfürst, "Pair production in temporally and spatially oscillating fields", *Physical Review D* **101**, 096009 (2020).
- [221] H. Avetissian, "Zhetf 74, 21 (1988); hk avetissian, ak avetissian, et. al", *Sov. Phys. JETP* **72**, 26 (1991).
- [222] H. Avetissian, A. Avetissian, A. K. Bagdasarian, and K. V. Sedrakian, "Non-linear $e^+ e^-$ pair production in a plasma by a strong electromagnetic wave", *Physical Review D* **54**, 5509 (1996).
- [223] G. Mouloudakis and P. Lambropoulos, "Multi-photon enhancement of the schwinger pair production mechanism under strong fel radiation", *Physics Letters B* **811**, 135987 (2020).
- [224] V. Popov, "Imaginary-time method in quantum mechanics and field theory.", *Physics of Atomic Nuclei* **68** (2005).
- [225] E. Schneidmiller, V. Balandin, W. Decking, M. Dohlus, N. Golubeva, D. Noelle, M. Yurkov, I. Zagorodnov, G. Geloni, Y. Li, et al., "Feasibility studies of the 100 keV undulator line of the european XFEL", in 39th int. free electron laser conf.(fel'19), hamburg, germany (2019).
- [226] E. Schneidmiller, V. Balandin, W. Decking, M. Dohlus, N. Golubeva, D. Noelle, M. Yurkov, I. Zagorodnov, G. G. Geloni, Y. Li, et al., "Considerations for the ultrahard x-ray undulator line of the european XFEL", *Proc. IPAC'19*, 1732–1735 (2019).
- [227] E. Cartlidge, *The light fantastic*, 2018.
- [228] F. Shibata, Y. Takahashi, and N. Hashitsume, "A generalized stochastic liouville equation. non-markovian versus memoryless master equations", *Journal of Statistical Physics* **17**, 171–187 (1977).
- [229] S. Chaturvedi and F. Shibata, "Time-convolutionless projection operator formalism for elimination of fast variables. applications to brownian motion", *Zeitschrift für Physik B Condensed Matter* **35**, 297–308 (1979).
- [230] F. Shibata and T. Arimitsu, "Expansion formulas in nonequilibrium statistical mechanics", *Journal of the Physical Society of Japan* **49**, 891–897 (1980).
- [231] D. P. DiVincenzo, "Quantum computation", *Science* **270**, 255–261 (1995).
- [232] M. Schlosshauer, "Quantum decoherence", *Physics Reports* **831**, 1–57 (2019).
- [233] A. Streltsov, G. Adesso, and M. B. Plenio, "Colloquium: quantum coherence as a resource", *Reviews of Modern Physics* **89**, 041003 (2017).
- [234] D. Dong and I. R. Petersen, "Quantum control theory and applications: a survey", *IET control theory & applications* **4**, 2651–2671 (2010).
- [235] V. B. Braginsky, V. B. Braginskii, and F. Y. Khalili, *Quantum measurement* (Cambridge University Press, 1995).
- [236] D. Aharonov and M. Ben-Or, "Fault-tolerant quantum computation with constant error", in *Proceedings of the twenty-ninth annual ACM symposium on theory of computing* (1997), pp. 176–188.
- [237] S. Endo, S. C. Benjamin, and Y. Li, "Practical quantum error mitigation for near-future applications", *Physical Review X* **8**, 031027 (2018).

- [238] A. Einstein, B. Podolsky, and N. Rosen, "Can quantum-mechanical description of physical reality be considered complete?", *Physical review* **47**, 777 (1935).
- [239] J. S. Bell, "On the einstein podolsky rosen paradox", *Physics Physique Fizika* **1**, 195 (1964).
- [240] A. Aspect, P. Grangier, and G. Roger, "Experimental realization of einstein-podolsky-rosen-bohm gedankenexperiment: a new violation of bell's inequalities", *Physical review letters* **49**, 91 (1982).
- [241] H. Ollivier and W. H. Zurek, "Quantum discord: a measure of the quantumness of correlations", *Physical review letters* **88**, 017901 (2001).
- [242] R. Uola, A. C. Costa, H. C. Nguyen, and O. Gühne, "Quantum steering", *Reviews of Modern Physics* **92**, 015001 (2020).
- [243] R. Horodecki, P. Horodecki, M. Horodecki, and K. Horodecki, "Quantum entanglement", *Reviews of modern physics* **81**, 865 (2009).
- [244] W. K. Wootters, "Entanglement of formation of an arbitrary state of two qubits", *Physical Review Letters* **80**, 2245 (1998).
- [245] G. M. Nikolopoulos, I. Jex, et al., *Quantum state transfer and network engineering* (Springer, 2014).
- [246] W. K. Wootters and W. H. Zurek, "The no-cloning theorem", *Physics Today* **62**, 76–77 (2009).
- [247] D. Matsukevich and A. Kuzmich, "Quantum state transfer between matter and light", *Science* **306**, 663–666 (2004).
- [248] A. Parkins and H. Kimble, "Quantum state transfer between motion and light", *Journal of Optics B: Quantum and Semiclassical Optics* **1**, 496 (1999).
- [249] C. Roos, "Controlling the quantum state of trapped ions", (2000).
- [250] F. Mei, G. Chen, L. Tian, S.-L. Zhu, and S. Jia, "Robust quantum state transfer via topological edge states in superconducting qubit chains", *Physical Review A* **98**, 012331 (2018).
- [251] X. Li, Y. Ma, J. Han, T. Chen, Y. Xu, W. Cai, H. Wang, Y. Song, Z.-Y. Xue, Z.-q. Yin, et al., "Perfect quantum state transfer in a superconducting qubit chain with parametrically tunable couplings", *Physical Review Applied* **10**, 054009 (2018).
- [252] F. W. Strauch and C. J. Williams, "Theoretical analysis of perfect quantum state transfer with superconducting qubits", *Physical Review B* **78**, 094516 (2008).
- [253] N. Y. Yao, L. Jiang, A. V. Gorshkov, Z.-X. Gong, A. Zhai, L.-M. Duan, and M. D. Lukin, "Robust quantum state transfer in random unpolarized spin chains", *Physical Review Letters* **106**, 040505 (2011).
- [254] J. Zhang, N. Rajendran, X. Peng, and D. Suter, "Iterative quantum-state transfer along a chain of nuclear spin qubits", *Physical Review A* **76**, 012317 (2007).
- [255] J. I. Cirac, P. Zoller, H. J. Kimble, and H. Mabuchi, "Quantum state transfer and entanglement distribution among distant nodes in a quantum network", *Physical Review Letters* **78**, 3221 (1997).
- [256] L.-M. Duan, M. D. Lukin, J. I. Cirac, and P. Zoller, "Long-distance quantum communication with atomic ensembles and linear optics", *Nature* **414**, 413–418 (2001).

- [257] C. Portmann and R. Renner, "Security in quantum cryptography", *Reviews of Modern Physics* **94**, 025008 (2022).
- [258] A. G. Fowler, M. Mariantoni, J. M. Martinis, and A. N. Cleland, "Surface codes: towards practical large-scale quantum computation", *Physical Review A* **86**, 032324 (2012).
- [259] D. Kielpinski, C. Monroe, and D. J. Wineland, "Architecture for a large-scale ion-trap quantum computer", *Nature* **417**, 709–711 (2002).
- [260] V. Kostak, G. Nikolopoulos, and I. Jex, "Perfect state transfer in networks of arbitrary topology and coupling configuration", *Physical Review A* **75**, 042319 (2007).
- [261] D. Petrosyan, G. M. Nikolopoulos, and P. Lambropoulos, "State transfer in static and dynamic spin chains with disorder", *Physical Review A* **81**, 042307 (2010).
- [262] J. B. Parkinson and D. J. Farnell, *An introduction to quantum spin systems*, Vol. 816 (Springer, 2010).
- [263] S. Bose, "Quantum communication through an unmodulated spin chain", *Physical review letters* **91**, 207901 (2003).
- [264] G. M. Nikolopoulos, D. Petrosyan, and P. Lambropoulos, "Coherent electron wavepacket propagation and entanglement in array of coupled quantum dots", *Europhysics Letters* **65**, 297 (2004).
- [265] G. M. Nikolopoulos, D. Petrosyan, and P. Lambropoulos, "Electron wavepacket propagation in a chain of coupled quantum dots", *Journal of Physics: Condensed Matter* **16**, 4991 (2004).
- [266] M. Christandl, N. Datta, A. Ekert, and A. J. Landahl, "Perfect state transfer in quantum spin networks", *Physical review letters* **92**, 187902 (2004).
- [267] M. Christandl, N. Datta, T. C. Dorlas, A. Ekert, A. Kay, and A. J. Landahl, "Perfect transfer of arbitrary states in quantum spin networks", *Physical Review A* **71**, 032312 (2005).
- [268] R. J. Cook and B. W. Shore, "Coherent dynamics of n-level atoms and molecules. iii. an analytically soluble periodic case", *Physical Review A* **20**, 539 (1979).
- [269] M.-H. Yung, "Quantum speed limit for perfect state transfer in one dimension", *Physical Review A* **74**, 030303 (2006).
- [270] A. D. Greentree, J. H. Cole, A. Hamilton, and L. C. Hollenberg, "Coherent electronic transfer in quantum dot systems using adiabatic passage", *Physical Review B* **70**, 235317 (2004).
- [271] D. Petrosyan and P. Lambropoulos, "Coherent population transfer in a chain of tunnel coupled quantum dots", *Optics Communications* **264**, 419–425 (2006).
- [272] K. Bergmann, H. Theuer, and B. Shore, "Coherent population transfer among quantum states of atoms and molecules", *Reviews of Modern Physics* **70**, 1003 (1998).
- [273] B. Shore, K. Bergmann, J. Oreg, and S. Rosenwaks, "Multilevel adiabatic population transfer", *Physical Review A* **44**, 7442 (1991).
- [274] A. K. Pavlis, G. M. Nikolopoulos, and P. Lambropoulos, "Evaluation of the performance of two state-transfer hamiltonians in the presence of static disorder", *Quantum Information Processing* **15**, 2553–2568 (2016).

- [275] C. Keele and A. Kay, "Combating the effects of disorder in quantum state transfer", *Physical Review A* **105**, 032612 (2022).
- [276] D. Burgarth, "Quantum state transfer and time-dependent disorder in quantum chains", *The European Physical Journal Special Topics* **151**, 147–155 (2007).
- [277] S. Yang, A. Bayat, and S. Bose, "Spin-state transfer in laterally coupled quantum-dot chains with disorders", *Physical Review A* **82**, 022336 (2010).
- [278] S. Pascazio, "All you ever wanted to know about the quantum zeno effect in 70 minutes", *Open Systems & Information Dynamics* **21**, 1440007 (2014).
- [279] H. Nakazato, M. Namiki, and S. Pascazio, "Temporal behavior of quantum mechanical systems", *International Journal of Modern Physics B* **10**, 247–295 (1996).
- [280] P. Facchi and S. Pascazio, "Quantum zeno and inverse quantum zeno effects", *Progress in Optics* **42**, 147–218 (2001).
- [281] P. Facchi and S. Pascazio, "Quantum zeno dynamics: mathematical and physical aspects", *Journal of Physics A: Mathematical and Theoretical* **41**, 493001 (2008).
- [282] B. Misra and E. G. Sudarshan, "The zeno's paradox in quantum theory", *Journal of Mathematical Physics* **18**, 756–763 (1977).
- [283] P. A. Mello, "The von neumann model of measurement in quantum mechanics", in *Aip conference proceedings*, Vol. 1575, 1 (American Institute of Physics, 2014), pp. 136–165.
- [284] W. Heiss, "Exceptional points of non-hermitian operators", *Journal of Physics A: Mathematical and General* **37**, 2455 (2004).
- [285] W. Heiss, M. Müller, and I. Rotter, "Collectivity, phase transitions, and exceptional points in open quantum systems", *Physical Review E* **58**, 2894 (1998).
- [286] W. Chen, Ş. Kaya Özdemir, G. Zhao, J. Wiersig, and L. Yang, "Exceptional points enhance sensing in an optical microcavity", *Nature* **548**, 192–196 (2017).
- [287] M. I. Rosa, M. Mazzotti, and M. Ruzzene, "Exceptional points and enhanced sensitivity in pt-symmetric continuous elastic media", *Journal of the Mechanics and Physics of Solids* **149**, 104325 (2021).
- [288] X.-g. Wang, G.-h. Guo, and J. Berakdar, "Enhanced sensitivity at magnetic high-order exceptional points and topological energy transfer in magnonic planar waveguides", *Physical Review Applied* **15**, 034050 (2021).
- [289] C. Zeng, Y. Sun, G. Li, Y. Li, H. Jiang, Y. Yang, and H. Chen, "Enhanced sensitivity at high-order exceptional points in a passive wireless sensing system", *Optics express* **27**, 27562–27572 (2019).
- [290] H. Hodaei, A. U. Hassan, S. Wittek, H. Garcia-Gracia, R. El-Ganainy, D. N. Christodoulides, and M. Khajavikhan, "Enhanced sensitivity at higher-order exceptional points", *Nature* **548**, 187–191 (2017).
- [291] C. M. Bender and S. Boettcher, "Real spectra in non-hermitian hamiltonians having p t symmetry", *Physical review letters* **80**, 5243 (1998).
- [292] C. M. Bender, S. Boettcher, and P. N. Meisinger, "Pt-symmetric quantum mechanics", *Journal of Mathematical Physics* **40**, 2201–2229 (1999).
- [293] C. M. Bender, "Making sense of non-hermitian hamiltonians", *Reports on Progress in Physics* **70**, 947 (2007).

- [294] C. M. Bender, D. C. Brody, and H. F. Jones, “Must a hamiltonian be hermitian?”, *American Journal of Physics* **71**, 1095–1102 (2003).
- [295] C. M. Bender, “Introduction to \mathcal{PT} -symmetric quantum theory”, *Contemporary physics* **46**, 277–292 (2005).
- [296] R. El-Ganainy, K. G. Makris, M. Khajavikhan, Z. H. Musslimani, S. Rotter, and D. N. Christodoulides, “Non-hermitian physics and \mathcal{PT} symmetry”, *Nature Physics* **14**, 11–19 (2018).
- [297] C. E. Rüter, K. G. Makris, R. El-Ganainy, D. N. Christodoulides, M. Segev, and D. Kip, “Observation of parity–time symmetry in optics”, *Nature physics* **6**, 192–195 (2010).
- [298] M.-A. Miri and A. Alu, “Exceptional points in optics and photonics”, *Science* **363**, eaar7709 (2019).
- [299] Ş. K. Özdemir, S. Rotter, F. Nori, and L. Yang, “Parity–time symmetry and exceptional points in photonics”, *Nature materials* **18**, 783–798 (2019).
- [300] S. Garmon and G. Ordóñez, “Characteristic dynamics near two coalescing eigenvalues incorporating continuum threshold effects”, *Journal of Mathematical Physics* **58** (2017).
- [301] S. Garmon, T. Sawada, K. Noba, and G. Ordóñez, “Characteristic influence of exceptional points in quantum dynamics”, in *Journal of physics: conference series*, Vol. 2038, 1 (IOP Publishing, 2021), p. 012011.
- [302] A. Magunov, I. Rotter, and S. Strakhova, “Laser-induced resonance trapping in atoms”, *Journal of Physics B: Atomic, Molecular and Optical Physics* **32**, 1669 (1999).
- [303] R. El-Ganainy, M. Khajavikhan, and L. Ge, “Exceptional points and lasing self-termination in photonic molecules”, *Physical Review A* **90**, 013802 (2014).
- [304] T. Goldzak, A. A. Mailybaev, and N. Moiseyev, “Light stops at exceptional points”, *Physical review letters* **120**, 013901 (2018).
- [305] C. Wang, W. R. Sweeney, A. D. Stone, and L. Yang, “Coherent perfect absorption at an exceptional point”, *Science* **373**, 1261–1265 (2021).
- [306] J. Zhang, B. Peng, Ş. K. Özdemir, K. Pichler, D. O. Krimer, G. Zhao, F. Nori, Y.-x. Liu, S. Rotter, and L. Yang, “A phonon laser operating at an exceptional point”, *Nature Photonics* **12**, 479–484 (2018).
- [307] R. Hanai and P. B. Littlewood, “Critical fluctuations at a many-body exceptional point”, *Physical Review Research* **2**, 033018 (2020).
- [308] D. J. Luitz and F. Piazza, “Exceptional points and the topology of quantum many-body spectra”, *Physical Review Research* **1**, 033051 (2019).
- [309] M. Yang, L. Zhu, Q. Zhong, R. El-Ganainy, and P.-Y. Chen, “Spectral sensitivity near exceptional points as a resource for hardware encryption”, *Nature Communications* **14**, 1145 (2023).
- [310] W. Heiss, “The physics of exceptional points”, *Journal of Physics A: Mathematical and Theoretical* **45**, 444016 (2012).
- [311] N. Moiseyev, *Non-hermitian quantum mechanics* (Cambridge University Press, 2011).
- [312] W. Heiss and H. Harney, “The chirality of exceptional points”, *The European Physical Journal D-Atomic, Molecular, Optical and Plasma Physics* **17**, 149–151 (2001).

- [313] E. Hernández, A. Jáuregui, and A. Mondragón, “Degeneracy of resonances in a double barrier potential”, *Journal of Physics A: Mathematical and General* **33**, 4507 (2000).
- [314] W. Heiss and R. Nazmitdinov, “Resonance scattering and singularities of the scattering function”, *The European Physical Journal D* **58**, 53–56 (2010).
- [315] W. Heiss, “Phases of wave functions and level repulsion”, *The European Physical Journal D-Atomic, Molecular, Optical and Plasma Physics* **7**, 1–4 (1999).
- [316] H. Mehri-Dehnavi and A. Mostafazadeh, “Geometric phase for non-hermitian hamiltonians and its holonomy interpretation”, *Journal of Mathematical Physics* **49** (2008).
- [317] G. Mouloudakis and P. Lambropoulos, “Entanglement instability in the interaction of two qubits with a common non-markovian environment”, *Quantum Information Processing* **20**, 1–15 (2021).
- [318] M. M. Wilde, *Quantum information theory* (Cambridge university press, 2013).
- [319] T. Yu and J. Eberly, “Finite-time disentanglement via spontaneous emission”, *Physical Review Letters* **93**, 140404 (2004).
- [320] T. Yu and J. Eberly, “Quantum open system theory: bipartite aspects”, *Physical review letters* **97**, 140403 (2006).
- [321] J. Eberly and T. Yu, “The end of an entanglement”, *Science* **316**, 555–557 (2007).
- [322] M. P. Almeida, F. de Melo, M. Hor-Meyll, A. Salles, S. Walborn, P. S. Ribeiro, and L. Davidovich, “Environment-induced sudden death of entanglement”, *science* **316**, 579–582 (2007).
- [323] J. Laurat, K. Choi, H. Deng, C. Chou, and H. Kimble, “Heralded entanglement between atomic ensembles: preparation, decoherence, and scaling”, *Physical review letters* **99**, 180504 (2007).
- [324] P. Marek, J. Lee, and M. S. Kim, “Vacuum as a less hostile environment to entanglement”, *Physical Review A* **77**, 032302 (2008).
- [325] A. Al-Qasimi and D. F. James, “Sudden death of entanglement at finite temperature”, *Physical Review A* **77**, 012117 (2008).
- [326] B. Bellomo, R. L. Franco, and G. Compagno, “Non-markovian effects on the dynamics of entanglement”, *Physical Review Letters* **99**, 160502 (2007).
- [327] X. Xiao, M.-F. Fang, Y.-L. Li, K. Zeng, and C. Wu, “Robust entanglement preserving by detuning in non-markovian regime”, *Journal of Physics B: Atomic, Molecular and Optical Physics* **42**, 235502 (2009).
- [328] Z. Xu and M. Feng, “Sudden death and birth of entanglement beyond the markovian approximation”, *Physics Letters A* **373**, 1906–1910 (2009).
- [329] Y. Zhang, Z. Man, and Y. Xia, “Non-markovian effects on entanglement dynamics in lossy cavities”, *The European Physical Journal D* **55**, 173–179 (2009).
- [330] Q.-J. Tong, J.-H. An, H.-G. Luo, and C. Oh, “Mechanism of entanglement preservation”, *Physical Review A* **81**, 052330 (2010).
- [331] B. Bellomo, G. Compagno, R. L. Franco, A. Ridolfo, and S. Savasta, “Entanglement dynamics of two independent cavity-embedded quantum dots”, *Physica Scripta* **2011**, 014004 (2011).

- [332] Z.-X. Man, Y.-J. Xia, and N. B. An, "Enhancing entanglement of two qubits undergoing independent decoherences by local pre-and postmeasurements", *Physical Review A* **86**, 052322 (2012).
- [333] C. Wang and Q.-H. Chen, "Exact dynamics of quantum correlations of two qubits coupled to bosonic baths", *New Journal of Physics* **15**, 103020 (2013).
- [334] H.-M. Zou, M.-F. Fang, B.-Y. Yang, Y.-N. Guo, W. He, and S.-Y. Zhang, "The quantum entropic uncertainty relation and entanglement witness in the two-atom system coupling with the non-markovian environments", *Physica Scripta* **89**, 115101 (2014).
- [335] H.-M. Zou and M.-F. Fang, "Discord and entanglement in non-markovian environments at finite temperatures", *Chinese Physics B* **25**, 090302 (2016).
- [336] B. Bellomo, R. L. Franco, and G. Compagno, "Entanglement dynamics of two independent qubits in environments with and without memory", *Physical Review A* **77**, 032342 (2008).
- [337] P. Lambropoulos, G. M. Nikolopoulos, T. R. Nielsen, and S. Bay, "Fundamental quantum optics in structured reservoirs", *Reports on Progress in Physics* **63**, 455 (2000).
- [338] B. Bellomo, R. L. Franco, S. Maniscalco, and G. Compagno, "Entanglement trapping in structured environments", *Physical Review A* **78**, 060302 (2008).
- [339] B. Bellomo, R. L. Franco, S. Maniscalco, and G. Compagno, "Two-qubit entanglement dynamics for two different non-markovian environments", *Physica Scripta* **2010**, 014014 (2010).
- [340] D. Braun, "Creation of entanglement by interaction with a common heat bath", *Physical review letters* **89**, 277901 (2002).
- [341] J. Ma, Z. Sun, X. Wang, and F. Nori, "Entanglement dynamics of two qubits in a common bath", *Physical Review A* **85**, 062323 (2012).
- [342] Z.-X. Man, Y.-J. Xia, and N. B. An, "Manipulating entanglement of two qubits in a common environment by means of weak measurements and quantum measurement reversals", *Physical Review A* **86**, 012325 (2012).
- [343] L. Memarzadeh and S. Mancini, "Entanglement dynamics for qubits dissipating into a common environment", *Physical Review A* **87**, 032303 (2013).
- [344] N. B. An, "Protecting entanglement of atoms stored in a common nonperfect cavity without measurements", *Physics Letters A* **377**, 2520–2523 (2013).
- [345] S. Oh and J. Kim, "Entanglement between qubits induced by a common environment with a gap", *Physical Review A* **73**, 062306 (2006).
- [346] L. Contreras-Pulido and R. Aguado, "Entanglement between charge qubits induced by a common dissipative environment", *Physical Review B* **77**, 155420 (2008).
- [347] C. Anastopoulos, S. Shresta, and B.-L. Hu, "Non-markovian entanglement dynamics of two qubits interacting with a common electromagnetic field", *Quantum information processing* **8**, 549–563 (2009).
- [348] K. Härkönen, F. Plastina, and S. Maniscalco, "Dicke model and environment-induced entanglement in ion-cavity qed", *Physical Review A* **80**, 033841 (2009).
- [349] N. B. An, J. Kim, and K. Kim, "Nonperturbative analysis of entanglement dynamics and control for three qubits in a common lossy cavity", *Physical Review A* **82**, 032316 (2010).

- [350] N. B. An, J. Kim, and K. Kim, "Entanglement dynamics of three interacting two-level atoms within a common structured environment", *Physical Review A* **84**, 022329 (2011).
- [351] X. Zhao, J. Jing, B. Corn, and T. Yu, "Dynamics of interacting qubits coupled to a common bath: non-markovian quantum-state-diffusion approach", *Physical Review A* **84**, 032101 (2011).
- [352] C. Fleming, N. Cummings, C. Anastopoulos, and B. Hu, "Non-markovian dynamics and entanglement of two-level atoms in a common field", *Journal of Physics A: Mathematical and Theoretical* **45**, 065301 (2012).
- [353] F. Francica, S. Maniscalco, J. Piilo, F. Plastina, and K.-A. Suominen, "Off-resonant entanglement generation in a lossy cavity", *Physical Review A* **79**, 032310 (2009).
- [354] S. Maniscalco, F. Francica, R. L. Zaffino, N. L. Gullo, and F. Plastina, "Protecting entanglement via the quantum zeno effect", *Physical review letters* **100**, 090503 (2008).
- [355] Y. Li, J. Zhou, and H. Guo, "Effect of the dipole-dipole interaction for two atoms with different couplings in a non-markovian environment", *Physical Review A* **79**, 012309 (2009).
- [356] S. Golkar and M. Tavassoly, "Dynamics of entanglement protection of two qubits using a driven laser field and detunings: independent and common, markovian and/or non-markovian regimes", *Chinese Physics B* **27**, 040303 (2018).
- [357] Y.-L. Li and M.-F. Fang, "High entanglement generation and high fidelity quantum state transfer in a non-markovian environment", *Chinese Physics B* **20**, 100312 (2011).
- [358] K. Hennessy, A. Badolato, M. Winger, D. Gerace, M. Atatüre, S. Gulde, S. Fält, E. L. Hu, and A. Imamoglu, "Quantum nature of a strongly coupled single quantum dot-cavity system", *Nature* **445**, 896–899 (2007).
- [359] P. Zhang, G. Song, and L. Yu, "Optical trapping of single quantum dots for cavity quantum electrodynamics", *Photonics Research* **6**, 182–185 (2018).
- [360] H. Kim, D. Sridharan, T. C. Shen, G. S. Solomon, and E. Waks, "Strong coupling between two quantum dots and a photonic crystal cavity using magnetic field tuning", *Optics express* **19**, 2589–2598 (2011).
- [361] D. Najer, I. Söllner, P. Sekatski, V. Dolique, M. C. Löbl, D. Riedel, R. Schott, S. Starosielec, S. R. Valentin, A. D. Wieck, et al., "A gated quantum dot strongly coupled to an optical microcavity", *Nature* **575**, 622–627 (2019).
- [362] H.-R. Wei and F.-G. Deng, "Scalable quantum computing based on stationary spin qubits in coupled quantum dots inside double-sided optical microcavities", *Scientific reports* **4**, 7551 (2014).
- [363] X. Wang, M. Feng, and B. C. Sanders, "Multipartite entangled states in coupled quantum dots and cavity qed", *Physical Review A* **67**, 022302 (2003).
- [364] P. Michler, *Quantum dots for quantum information technologies*, Vol. 237 (Springer, 2017).
- [365] B. Casabone, A. Stute, K. Friebe, B. Brandstätter, K. Schüppert, R. Blatt, and T. Northup, "Heralded entanglement of two ions in an optical cavity", *Physical review letters* **111**, 100505 (2013).

- [366] G. Mouloudakis, T. Ilias, and P. Lambropoulos, "Arbitrary-length $x \times x$ spin chains boundary-driven by non-markovian environments", *Physical Review A* **105**, 012429 (2022).
- [367] S. Paganelli, S. Lorenzo, T. J. Apollaro, F. Plastina, and G. L. Giorgi, "Routing quantum information in spin chains", *Physical Review A* **87**, 062309 (2013).
- [368] C. Di Franco, M. Paternostro, and M. Kim, "Perfect state transfer on a spin chain without state initialization", *Physical review letters* **101**, 230502 (2008).
- [369] A. Gratsea, G. Nikolopoulos, and P. Lambropoulos, "Photon-assisted quantum state transfer and entanglement generation in spin chains", *Physical Review A* **98**, 012304 (2018).
- [370] M. Plenio, J. Hartley, and J. Eisert, "Dynamics and manipulation of entanglement in coupled harmonic systems with many degrees of freedom", *New Journal of Physics* **6**, 36 (2004).
- [371] L. C. Venuti, S. Giampaolo, F. Illuminati, and P. Zanardi, "Long-distance entanglement and quantum teleportation in $x \times x$ spin chains", *Physical Review A* **76**, 052328 (2007).
- [372] S. M. Giampaolo and F. Illuminati, "Long-distance entanglement in many-body atomic and optical systems", *New Journal of Physics* **12**, 025019 (2010).
- [373] S. Sahling, G. Remenyi, C. Paulsen, P. Monceau, V. Saligrama, C. Marin, A. Revcolevschi, L. Regnault, S. Raymond, and J. Lorenzo, "Experimental realization of long-distance entanglement between spins in antiferromagnetic quantum spin chains", *Nature Physics* **11**, 255–260 (2015).
- [374] M. P. Estarellas, I. D'Amico, and T. P. Spiller, "Robust quantum entanglement generation and generation-plus-storage protocols with spin chains", *Physical Review A* **95**, 042335 (2017).
- [375] F. Plastina and T. J. Apollaro, "Local control of entanglement in a spin chain", *Physical review letters* **99**, 177210 (2007).
- [376] M. B. Plenio and S. F. Huelga, "Dephasing-assisted transport: quantum networks and biomolecules", *New Journal of Physics* **10**, 113019 (2008).
- [377] Z. Lan, L. Jing, and S. Tao, "Quantum state transfer in engineered spin chain under influence of spatially distributed environment", *Communications in Theoretical Physics* **52**, 226 (2009).
- [378] Z.-M. Wang, F.-H. Ren, D.-W. Luo, Z.-Y. Yan, and L.-A. Wu, "Quantum state transmission through a spin chain in finite-temperature heat baths", *Journal of Physics A: Mathematical and Theoretical* **54**, 155303 (2021).
- [379] S. R. Clark, J. Prior, M. J. Hartmann, D. Jaksch, and M. B. Plenio, "Exact matrix product solutions in the heisenberg picture of an open quantum spin chain", *New Journal of Physics* **12**, 025005 (2010).
- [380] M. R. Pourkarimi, M. Rahnema, and H. Rooholamini, "Decoherence effect on quantum correlation and entanglement in a two-qubit spin chain", *International Journal of Theoretical Physics* **54**, 1085–1097 (2015).
- [381] Z.-Y. Sun, K.-L. Yao, W. Yao, D.-H. Zhang, and Z.-L. Liu, "Finite-temperature entanglement for low-dimensional quantum spin chains", *Physical Review B* **77**, 014416 (2008).
- [382] G. Sadiq and S. Almalki, "Entanglement dynamics in heisenberg spin chains coupled to a dissipative environment at finite temperature", *Physical Review A* **94**, 012341 (2016).

- [383] M. Rafiee, "Measurement enhances long-distance entanglement generation in spin chains with dissipative processes", *The European Physical Journal D* **72**, 1–5 (2018).
- [384] R. L. Franco, B. Bellomo, S. Maniscalco, and G. Compagno, "Dynamics of quantum correlations in two-qubit systems within non-markovian environments", *International Journal of Modern Physics B* **27**, 1345053 (2013).
- [385] T. Ramos, B. Vermersch, P. Hauke, H. Pichler, and P. Zoller, "Non-markovian dynamics in chiral quantum networks with spins and photons", *Physical Review A* **93**, 062104 (2016).
- [386] F. Liu, X. Zhou, and Z.-W. Zhou, "Memory effect and non-markovian dynamics in an open quantum system", *Physical Review A* **99**, 052119 (2019).
- [387] F. Liu, X.-X. Zhou, and Z.-W. Zhou, "Erratum: memory effect and non-markovian dynamics in an open quantum system [phys. rev. a 99, 052119 (2019)]", *Physical Review A* **100**, 019901 (2019).
- [388] Z.-M. Wang, F.-H. Ren, D.-W. Luo, Z.-Y. Yan, and L.-A. Wu, "Almost-exact state transfer by leakage-elimination-operator control in a non-markovian environment", *Physical Review A* **102**, 042406 (2020).
- [389] G. T. Landi, D. Poletti, and G. Schaller, "Nonequilibrium boundary-driven quantum systems: models, methods, and properties", *Reviews of Modern Physics* **94**, 045006 (2022).
- [390] K. Yamanaka and T. Sasamoto, "Exact solution for the lindbladian dynamics for the open xx spin chain with boundary dissipation", *SciPost Physics* **14**, 112 (2023).
- [391] E. Mascarenhas, G. Giudice, and V. Savona, "A nonequilibrium quantum phase transition in strongly coupled spin chains", *Quantum* **1**, 40 (2017).
- [392] A. Dhar, K. Saito, and P. Hänggi, "Nonequilibrium density-matrix description of steady-state quantum transport", *Physical Review E* **85**, 011126 (2012).
- [393] M. Žnidarič, "Exact large-deviation statistics for a nonequilibrium quantum spin chain", *Physical review letters* **112**, 040602 (2014).
- [394] F. Barra, "The thermodynamic cost of driving quantum systems by their boundaries", *Scientific reports* **5**, 14873 (2015).
- [395] A. Levy and R. Kosloff, "The local approach to quantum transport may violate the second law of thermodynamics", *Europhysics Letters* **107**, 20004 (2014).
- [396] G. De Chiara, G. Landi, A. Hewgill, B. Reid, A. Ferraro, A. J. Roncaglia, and M. Antezza, "Reconciliation of quantum local master equations with thermodynamics", *New Journal of Physics* **20**, 113024 (2018).
- [397] N. Li, J. Ren, L. Wang, G. Zhang, P. Hänggi, and B. Li, "Colloquium: phononics: manipulating heat flow with electronic analogs and beyond", *Reviews of Modern Physics* **84**, 1045 (2012).
- [398] F.-H. Ren, Z.-M. Wang, and Y.-J. Gu, "Quantum state transfer through a spin chain in two non-markovian baths", *Quantum Information Processing* **18**, 1–11 (2019).
- [399] D. Jaschke, M. L. Wall, and L. D. Carr, "Open source matrix product states: opening ways to simulate entangled many-body quantum systems in one dimension", *Computer Physics Communications* **225**, 59–91 (2018).

- [400] R. Finsterhölzl, M. Katzer, A. Knorr, and A. Carmele, "Using matrix-product states for open quantum many-body systems: efficient algorithms for markovian and non-markovian time-evolution", *Entropy* **22**, 984 (2020).
- [401] M. Žnidarič, "A matrix product solution for a nonequilibrium steady state of an xx chain", *Journal of Physics A: Mathematical and Theoretical* **43**, 415004 (2010).
- [402] D. Karevski, V. Popkov, and G. Schütz, "Exact matrix product solution for the boundary-driven lindblad x x z chain", *Physical review letters* **110**, 047201 (2013).
- [403] T. Prosen, "Open x x z spin chain: nonequilibrium steady state and a strict bound on ballistic transport", *Physical review letters* **106**, 217206 (2011).
- [404] T. Prosen, "Exact nonequilibrium steady state of a strongly driven open x x z chain", *Physical review letters* **107**, 137201 (2011).
- [405] M. Michel, J. Gemmer, and G. Mahler, "Heat conductivity in small quantum systems: kubo formula in liouville space", *The European Physical Journal B-Condensed Matter and Complex Systems* **42**, 555–559 (2004).
- [406] H. Wichterich, M. J. Henrich, H.-P. Breuer, J. Gemmer, and M. Michel, "Modeling heat transport through completely positive maps", *Physical Review E* **76**, 031115 (2007).
- [407] A. J. Leggett, S. Chakravarty, A. T. Dorsey, M. P. Fisher, A. Garg, and W. Zwerger, "Dynamics of the dissipative two-state system", *Reviews of Modern Physics* **59**, 1 (1987).
- [408] H.-P. Breuer, E.-M. Laine, and J. Piilo, "Measure for the degree of non-markovian behavior of quantum processes in open systems", *Physical review letters* **103**, 210401 (2009).
- [409] J. Dajka, J. Łuczka, and P. Hänggi, "Distance between quantum states in the presence of initial qubit-environment correlations: a comparative study", *Physical Review A* **84**, 032120 (2011).
- [410] E.-M. Laine, J. Piilo, and H.-P. Breuer, "Measure for the non-markovianity of quantum processes", *Physical Review A* **81**, 062115 (2010).
- [411] M. Sargent, M. Scully, and W. Lamb, "Laser physics addison-wesley", Reading, Mass (1974).
- [412] X. Zhao, W. Shi, L.-A. Wu, and T. Yu, "Fermionic stochastic schrödinger equation and master equation: an open-system model", *Physical Review A* **86**, 032116 (2012).
- [413] D. Chruściński, A. Kossakowski, and Á. Rivas, "Measures of non-markovianity: divisibility versus backflow of information", *Physical Review A* **83**, 052128 (2011).
- [414] S. Wißmann, H.-P. Breuer, and B. Vacchini, "Generalized trace-distance measure connecting quantum and classical non-markovianity", *Physical Review A* **92**, 042108 (2015).
- [415] L. Li, M. J. Hall, and H. M. Wiseman, "Concepts of quantum non-markovianity: a hierarchy", *Physics Reports* **759**, 1–51 (2018).
- [416] S. Luo, S. Fu, and H. Song, "Quantifying non-markovianity via correlations", *Physical Review A* **86**, 044101 (2012).

- [417] S. Lorenzo, F. Plastina, and M. Paternostro, “Geometrical characterization of non-markovianity”, *Physical Review A* **88**, 020102 (2013).
- [418] H.-P. Breuer, “Foundations and measures of quantum non-markovianity”, *Journal of Physics B: Atomic, Molecular and Optical Physics* **45**, 154001 (2012).
- [419] P. Haikka, J. D. Cresser, and S. Maniscalco, “Comparing different non-markovianity measures in a driven qubit system”, *Physical Review A* **83**, 012112 (2011).
- [420] A. Mortezapour, M. A. Borji, D. Park, and R. L. Franco, “Non-markovianity and coherence of a moving qubit inside a leaky cavity”, *Open Systems & Information Dynamics* **24**, 1740006 (2017).
- [421] C. Addis, B. Bylicka, D. Chruściński, and S. Maniscalco, “Comparative study of non-markovianity measures in exactly solvable one- and two-qubit models”, *Physical Review A* **90**, 052103 (2014).
- [422] M. Mannone, R. L. Franco, and G. Compagno, “Comparison of non-markovianity criteria in a qubit system under random external fields”, *Physica Scripta* **2013**, 014047 (2013).
- [423] F. F. Fanchini, G. Karpát, D. Z. Rossatto, A. Norambuena, and R. Coto, “Estimating the degree of non-markovianity using machine learning”, *Physical Review A* **103**, 022425 (2021).
- [424] Á. Rivas, S. F. Huelga, and M. B. Plenio, “Quantum non-markovianity: characterization, quantification and detection”, *Reports on Progress in Physics* **77**, 094001 (2014).
- [425] B. Bylicka, D. Chruściński, and S. Maniscalco, “Non-markovianity and reservoir memory of quantum channels: a quantum information theory perspective”, *Scientific reports* **4**, 5720 (2014).
- [426] M. Ozawa, “Entanglement measures and the hilbert–schmidt distance”, *Physics Letters A* **268**, 158–160 (2000).
- [427] R. Jozsa, “Fidelity for mixed quantum states”, *Journal of modern optics* **41**, 2315–2323 (1994).
- [428] A. Uhlmann, “Fidelity and concurrence of conjugated states”, *Physical Review A* **62**, 032307 (2000).
- [429] P. E. Mendonça, R. d. J. Napolitano, M. A. Marchioli, C. J. Foster, and Y.-C. Liang, “Alternative fidelity measure between quantum states”, *Physical Review A* **78**, 052330 (2008).
- [430] G. Mouloudakis, I. Stergou, and P. Lambropoulos, “Non-markovianity in the time evolution of open quantum systems assessed by means of quantum state distance”, *Physica Scripta* (2023).
- [431] M. A. Nielsen and I. L. Chuang, *Quantum computation and quantum information* (Cambridge university press, 2010).
- [432] H. Shen, M. Qin, X.-M. Xiu, and X. Yi, “Exact non-markovian master equation for a driven damped two-level system”, *Physical Review A* **89**, 062113 (2014).
- [433] L. Ferialdi, “Exact non-markovian master equation for the spin-boson and jaynes-cummings models”, *Physical Review A* **95**, 020101 (2017).
- [434] S. Maniscalco and F. Petruccione, “Non-markovian dynamics of a qubit”, *Physical Review A* **73**, 012111 (2006).
- [435] B. Vacchini, “Non-markovian master equations from piecewise dynamics”, *Physical Review A* **87**, 030101 (2013).

- [436] E. R. Whipple, "The lorentzian-squared environmental broadening model in mössbauer spectra", *Nuclear Instruments and Methods* **180**, 241–248 (1981).
- [437] H.-M. Zou, R. Liu, D. Long, J. Yang, and D. Lin, "Ohmic reservoir-based non-markovianity and quantum speed limit time", *Physica Scripta* **95**, 085105 (2020).
- [438] M. Abdi and M. B. Plenio, "Analog quantum simulation of extremely sub-ohmic spin-boson models", *Physical Review A* **98**, 040303 (2018).
- [439] D. Pellegrino, D. Balestri, N. Granichi, M. Ciardi, F. Intonti, F. Pagliano, A. Y. Silov, F. W. Otten, T. Wu, K. Vynck, et al., "Non-lorentzian local density of states in coupled photonic crystal cavities probed by near-and far-field emission", *Physical Review Letters* **124**, 123902 (2020).
- [440] G. Mouloudakis and P. Lambropoulos, "Coalescence of non-markovian dissipation, quantum zeno effect, and non-hermitian physics in a simple realistic quantum system", *Physical Review A* **106**, 053709 (2022).
- [441] W. M. Itano, D. J. Heinzen, J. J. Bollinger, and D. J. Wineland, "Quantum zeno effect", *Physical Review A* **41**, 2295 (1990).
- [442] K. Koshino and A. Shimizu, "Quantum zeno effect by general measurements", *Physics reports* **412**, 191–275 (2005).
- [443] S.-C. Wang, Y. Li, X.-B. Wang, and L. C. Kwek, "Operator quantum zeno effect: protecting quantum information with noisy two-qubit interactions", *Physical Review Letters* **110**, 100505 (2013).
- [444] A. Nourmandipour, M. K. Tavassoly, and M. Rafiee, "Dynamics and protection of entanglement in n-qubit systems within markovian and non-markovian environments", *Physical Review A* **93**, 022327 (2016).
- [445] A. Nourmandipour, M. Tavassoly, and M. Bolorizadeh, "Quantum zeno and anti-zeno effects on the entanglement dynamics of qubits dissipating into a common and non-markovian environment", *JOSA B* **33**, 1723–1730 (2016).
- [446] P. Facchi and S. Pascazio, "Quantum zeno subspaces", *Physical review letters* **89**, 080401 (2002).
- [447] K. Koshino and A. Shimizu, "Quantum zeno and anti-zeno effects by indirect measurement with finite errors", *Physical Review A* **67**, 042101 (2003).
- [448] M. Hotta and M. Morikawa, "Impossibility of distant indirect measurement of the quantum zeno effect", *Physical Review A* **69**, 052114 (2004).
- [449] M. Makris and P. Lambropoulos, "Quantum zeno effect by indirect measurement: the effect of the detector", *Physical Review A* **70**, 044101 (2004).
- [450] S. Wallentowitz and P. Toschek, "Comment on "impossibility of distant indirect measurement of the quantum zeno effect"", *Physical Review A* **72**, 046101 (2005).
- [451] M. Ozawa, "Defense of "impossibility of distant indirect measurement of the quantum zeno effect"", *Physics Letters A* **356**, 411–413 (2006).
- [452] S. Wallentowitz and P. Toschek, "Comment on: "defense of 'impossibility of distant indirect measurement of the quantum zeno effect'" [phys. lett. a 356 (2006) 411]", *Physics Letters A* **367**, 420–421 (2007).
- [453] E. W. Streed, J. Mun, M. Boyd, G. K. Campbell, P. Medley, W. Ketterle, and D. E. Pritchard, "Continuous and pulsed quantum zeno effect", *Physical review letters* **97**, 260402 (2006).

- [454] L. Schulman, "Continuous and pulsed observations in the quantum zeno effect", *Physical Review A* **57**, 1509 (1998).
- [455] B. Nagels, L. Hermans, and P. Chapovsky, "Quantum zeno effect induced by collisions", *Physical review letters* **79**, 3097 (1997).
- [456] K. Mølhave and M. Drewsen, "Demonstration of the continuous quantum zeno effect in optical pumping", *Physics Letters A* **268**, 45–49 (2000).
- [457] T. Nakanishi, K. Yamane, and M. Kitano, "Absorption-free optical control of spin systems: the quantum zeno effect in optical pumping", *Physical Review A* **65**, 013404 (2001).
- [458] W. Wu and H.-Q. Lin, "Quantum zeno and anti-zeno effects in quantum dissipative systems", *Physical Review A* **95**, 042132 (2017).
- [459] J. Li, T. Wang, L. Luo, S. Vemuri, and Y. N. Joglekar, "Unification of quantum zeno–anti zeno effects and parity-time symmetry breaking transitions", *Physical Review Research* **5**, 023204 (2023).
- [460] P. Kumar, A. Romito, and K. Snizhko, "Quantum zeno effect with partial measurement and noisy dynamics", *Physical Review Research* **2**, 043420 (2020).
- [461] T. Chen, W. Gou, D. Xie, T. Xiao, W. Yi, J. Jing, and B. Yan, "Quantum zeno effects across a parity-time symmetry breaking transition in atomic momentum space", *npj Quantum Information* **7**, 78 (2021).
- [462] M. Naghiloo, M. Abbasi, Y. N. Joglekar, and K. Murch, "Quantum state tomography across the exceptional point in a single dissipative qubit", *Nature Physics* **15**, 1232–1236 (2019).
- [463] B. Dóra, D. Sticlet, and C. P. Moca, "Correlations at pt-symmetric quantum critical point", *Physical Review Letters* **128**, 146804 (2022).
- [464] K. Snizhko, P. Kumar, and A. Romito, "Quantum zeno effect appears in stages", *Physical review research* **2**, 033512 (2020).
- [465] J. J. Sakurai, *Advanced quantum mechanics* (Pearson Education India, 1967).
- [466] G. Mouloudakis and P. Lambropoulos, "Non-hermitian landscape of autoionization", *Physical Review A* **108**, 063104 (2023).
- [467] K. Kikuchi and M. Kawai, *Nuclear matter and nuclear reactions* (North-Holland Publishing Company, 1968).
- [468] J.-J. Aubert, U. Becker, P. Biggs, J. Burger, M. Chen, G. Everhart, P. Goldhagen, J. Leong, T. McCorriston, T. Rhoades, et al., "Experimental observation of a heavy particle j", *Physical Review Letters* **33**, 1404 (1974).
- [469] J.-E. Augustin, A. M. Boyarski, M. Breidenbach, F. Bulos, J. Dakin, G. Feldman, G. Fischer, D. Fryberger, G. Hanson, B. Jean-Marie, et al., "Discovery of a narrow resonance in $e^+ e^-$ annihilation", *Physical Review Letters* **33**, 1406 (1974).
- [470] M. F. Limonov, M. V. Rybin, A. N. Poddubny, and Y. S. Kivshar, "Fano resonances in photonics", *Nature Photonics* **11**, 543–554 (2017).
- [471] E. Arimondo, C. W. Clark, and W. C. Martin, "Colloquium: etto majorana and the birth of autoionization", *Reviews of Modern Physics* **82**, 1947 (2010).
- [472] M. Aymar, C. H. Greene, and E. Luc-Koenig, "Multichannel rydberg spectroscopy of complex atoms", *Reviews of Modern Physics* **68**, 1015 (1996).

- [473] M. Wickenhauser, J. Burgdörfer, F. Krausz, and M. Drescher, "Time resolved fano resonances", *Physical review letters* **94**, 023002 (2005).
- [474] T. Mercouris, Y. Komninos, and C. A. Nicolaides, "Time-dependent formation of the profile of the $he\ 2\ s\ 2\ p\ p\ o\ 1$ state excited by a short laser pulse", *Physical Review A* **75**, 013407 (2007).
- [475] T. Mercouris, Y. Komninos, and C. Nicolaides, "Erratum: time-dependent formation of the profile of the $he\ 2\ s\ 2\ p\ 1\ p\ o$ state excited by a short laser pulse [phys. rev. a 75, 013407 (2007)]", *Physical Review A* **87**, 069905 (2013).
- [476] W.-C. Chu and C. Lin, "Theory of ultrafast autoionization dynamics of fano resonances", *Physical Review A* **82**, 053415 (2010).
- [477] A. Kaldun, A. Blättermann, V. Stooß, S. Donsa, H. Wei, R. Pazourek, S. Nagele, C. Ott, C.-D. Lin, J. Burgdörfer, et al., "Observing the ultrafast buildup of a fano resonance in the time domain", *Science* **354**, 738–741 (2016).
- [478] P. Lambropoulos and P. Zoller, "Autoionizing states in strong laser fields", *Physical Review A* **24**, 379 (1981).
- [479] H. Bachau, P. Lambropoulos, and R. Shakeshaft, "Theory of laser-induced transitions between autoionizing states of he ", *Physical Review A* **34**, 4785 (1986).
- [480] C. Ott, L. Aufleger, T. Ding, M. Rebholz, A. Magunia, M. Hartmann, V. Stooß, D. Wachs, P. Birk, G. D. Borisova, et al., "Strong-field extreme-ultraviolet dressing of atomic double excitation", *Physical review letters* **123**, 163201 (2019).
- [481] A. Magunia, L. Aufleger, T. Ding, P. Rupprecht, M. Rebholz, C. Ott, and T. Pfeifer, "Bound-state electron dynamics driven by near-resonantly detuned intense and ultrashort pulsed xuv fields", *Applied Sciences* **10**, 6153 (2020).
- [482] L. Aufleger, P. Friebe, P. Rupprecht, A. Magunia, T. Ding, M. Rebholz, M. Hartmann, V. Stooß, C. Ott, and T. Pfeifer, "Pulse length effects on autoionizing states under the influence of intense xuv fields", *Journal of Physics B: Atomic, Molecular and Optical Physics* **53**, 234002 (2020).
- [483] L. Aufleger, P. Friebe, P. Rupprecht, A. Magunia, T. Ding, M. Rebholz, M. Hartmann, C. Ott, and T. Pfeifer, "Line-shape broadening of an autoionizing state in helium at high xuv intensity", *New Journal of Physics* **24**, 013014 (2022).
- [484] Y. He, H. Shi, N. Xue, A. Magunia, S. Sun, J. Ding, B. Hu, and Z. Liu, "Direct manipulation of atomic excitation with intense extreme-ultraviolet laser fields", *Physical Review A* **105**, 043113 (2022).
- [485] S. Themelis, P. Lambropoulos, and M. Meyer, "Ionization dynamics in double resonance involving autoionizing states in helium: the effect of pulse shapes", *Journal of Physics B: Atomic, Molecular and Optical Physics* **37**, 4281 (2004).
- [486] N. Karapanagioti, D. Charalambidis, C. Uiterwaal, C. Fotakis, H. Bachau, I. Sánchez, and E. Cormier, "Effects of coherent coupling of autoionizing states on multiphoton ionization", *Physical Review A* **53**, 2587 (1996).
- [487] T. Nakajima and P. Lambropoulos, "Manipulation of the line shape and final products of autoionization through the phase of the electric fields", *Physical review letters* **70**, 1081 (1993).
- [488] T. Nakajima and P. Lambropoulos, "Effects of the phase of a laser field on autoionization", *Physical Review A* **50**, 595 (1994).

- [489] G. Mouloudakis and P. Lambropoulos, "Autoionizing states driven by stochastic electromagnetic fields", *Journal of Physics B: Atomic, Molecular and Optical Physics* **51**, 01LT01 (2017).
- [490] G. Mouloudakis and P. Lambropoulos, "Effects of field fluctuations on driven autoionizing resonances", *The European Physical Journal D* **72**, 1–9 (2018).
- [491] T. Katravulapally and L. A. Nikolopoulos, "Effects of the fel fluctuations on the 2s2p li+ auto-ionization lineshape", *Atoms* **8**, 35 (2020).
- [492] I. Rotter, "A non-hermitian hamilton operator and the physics of open quantum systems", *Journal of Physics A: Mathematical and Theoretical* **42**, 153001 (2009).
- [493] H. Nakamura, N. Hatano, S. Garmon, and T. Petrosky, "Quasibound states in the continuum in a two channel quantum wire with an adatom", *Physical review letters* **99**, 210404 (2007).
- [494] S. Garmon, H. Nakamura, N. Hatano, and T. Petrosky, "Two-channel quantum wire with an adatom impurity: role of the van hove singularity in the quasibound state in continuum, decay rate amplification, and the fano effect", *Physical Review B* **80**, 115318 (2009).
- [495] T. Fukuta, S. Garmon, K. Kanki, K.-i. Noba, and S. Tanaka, "Fano absorption spectrum with the complex spectral analysis", *Physical Review A* **96**, 052511 (2017).
- [496] S. Tanaka, S. Garmon, K. Kanki, and T. Petrosky, "Higher-order time-symmetry-breaking phase transition due to meeting of an exceptional point and a fano resonance", *Physical Review A* **94**, 022105 (2016).
- [497] U. Fano, "Effects of configuration interaction on intensities and phase shifts", *Physical review* **124**, 1866 (1961).
- [498] E. Lindroth, "Calculation of doubly excited states of helium with a finite discrete spectrum", *Physical Review A* **49**, 4473 (1994).
- [499] M. Malvestuto, A. Caretta, R. Bhardwaj, S. Laterza, F. Parmigiani, A. Gessini, M. Zamolo, F. Galassi, R. Sergo, G. Cautero, et al., "The magnedyn beamline at the fermi free electron laser", *Review of Scientific Instruments* **93** (2022).
- [500] M. Labat, J. C. Cabadağ, A. Ghaith, A. Irman, A. Berlioux, P. Berteaud, F. Blache, S. Bock, F. Bouvet, F. Briquez, et al., "Seeded free-electron laser driven by a compact laser plasma accelerator", *Nature Photonics* **17**, 150–156 (2023).
- [501] I. J. B. Macias, S. Düsterer, R. Ivanov, J. Liu, G. Brenner, J. Rönsch-Schulenburg, M. K. Czwalińska, and M. V. Yurkov, "Study of temporal, spectral, arrival time and energy fluctuations of sase fel pulses", *Optics express* **29**, 10491–10508 (2021).
- [502] K. Mouloudakis, F. Vouzinas, A. Margaritakis, A. Koutsimpela, G. Mouloudakis, V. Koutrouli, M. Skotiniotis, G. Tsironis, M. Loulakis, M. Mitchell, et al., "Interspecies spin-noise correlations in hot atomic vapors", *Physical Review A* **108**, 052822 (2023).